Volume 9 • No 2 • Dec. 2021 • p-ISSN: 2410-9355 • e-ISSN: 2307-549X

ARO

The Scientific Journal of Koya University

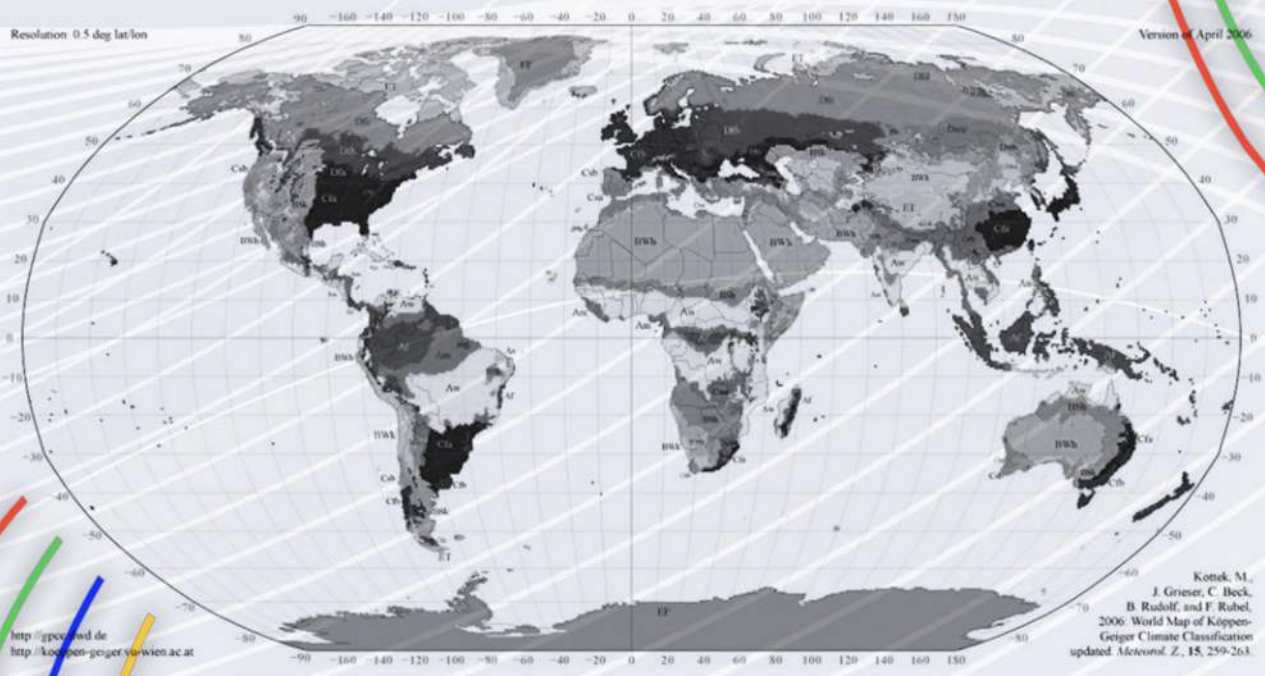

Fig. 4. Köppen-Geiger Climate Classification Map (Rubel and Kottek, 2010).

ARO - DOI: 10.14500/2307-549X
Indexed by WoS-ESCI

ARO-The Scientific Journal of Koya University

The ARO ("Today" in Hewramí Kurdish), is an international scientific journal published by the Koya University with p-ISSN: 2410-9355, e-ISSN: 2307-549X and DOI: 10.14500/2307-549X. ARO is a journal of original scientific research, global news, and commentary. The ARO Scientific Journal is a peer-reviewed, open access journal that publishes original research articles as well as review articles in areas of Science, Engineering and Technology.

ARO the Scientific Journal Office

Koya University, University Park
Danielle Mitterrand Boulevard, Koya KOY45
Kurdistan Region - F.R. Iraq

Mobile: +964 (0) 750 187 5489
E-mail: aro.journal@koyauniversity.org
url: aro.koyauniversity.org

December 2021

ARO

The Scientific Journal of Koya University

Vol IX, No 2(2021)

Contents

ARO Editorial Words

Dear readers,

Aro, the Scientific Journal of Koya University (KOU), is closing its 17th issue (Vol IX, No 2, 2021). Our journal has had an exciting and yet dynamic season. Aro, an internationally renowned scientific journal, is publishing its 17th issue in the Kurdistan Region of Iraq (KRIQ). Notably, as of February 2016, Aro has been accepted for indexing in the Emerging Sources Citation Index (ESCI), a new edition of Web of Science™. The content in this index is being considered by WoS (Clarivate Analytics) for inclusion in the Science Citation Index Expanded™ (SCIE). Aro's individual articles are currently being listed by WoS (Clarivate Analytics) using the articles' unique DOI numbers, which is a historic accomplishment for our academic community. Aro is embarking on its ninth year of leading the quality of regional scientific publications with global impact. The editorial team has worked tirelessly to maintain the novel mission and ensure that Aro's future publications have greater impact and citations. It is exciting that Aro has been awarded the DOAJ Seal listing, which indicates that his work is of trusted high quality open access scientific work. Aro's life will be even more exciting in the coming new season, as WoS (Clarivate Analytics) will examine our journal for a full permanent listing.

Aro's mission remains to provide resources, support, and advice to researchers who are in the process of publishing their scientific papers, while also providing free public access to scientific research through open online access. This is a difficult task that we hope to complete in the coming years. As a result, in the sections that follow, we'd like to share and elaborate on the core elements that make up Aro. Finding dependable and skilled reviewers, on the other hand, remains a significant challenge for us. KOU is launching Adjunct Scholar Programs, which will allow non-resident scholars to affiliate with KOU and publish in Aro.

Aro was founded with the long-term goal of making science accessible to all researchers in Kurdistan and beyond, while also covering a wide range of scholarly disciplines. Aro is an open access, peer-reviewed journal that publishes original scientific research, global news, letters and commentary, and review articles in the natural sciences and technology. You will find original research papers in a variety of fields in this issue.

The overwhelming response from researchers, academics, and professionals over the last nine years prompted us to form a larger Editorial Board to serve the greater number of submitted scientific manuscripts. It is clear, however, that having a committed and well-organized editorial board for the journal is only one side of the coin. The ability to attract submissions of high-quality research and scholarly work is the other. We thank everyone who put their faith in Aro and submitted their original research work for publication in Vol. IX, No. 2 (2021) of the journal, as well as the 36 peer-reviewers from universities around the world who worked hard to review and enable this issue of Aro.

Dilan M. Rostam
Editor-in-Chief

Wali M Hamad
Executive Publisher

Dilan M. Rostam, Salah I. Yahya, Basim M. Fadhil, Fahmi F. Muhammad, Mohammed H. Zangana, Jorge Correia, Fouad Mohammed, Jacek Binda Nadhir Al-Ansari, Howri Mansurbeg, Tara F. Tahir and Yazen A. Khaleel
Executive Editorial Board

DOI: 10.14500/2307-549X ARO p-ISSN: 2410-9355, e-ISSN: 2307-549X

Efficient Kinect Sensor-based Kurdish Sign Language Recognition Using Echo System Network

Sami F. Mirza[1], Abdulbasit K. Al-Talabani[2]

[1]Department of Computer Science, Faculty of Science, Soran University, Soran, Kurdistan Region – F.R. Iraq
[2]Department of Software Engineering, Faculty of Engineering, Koya KOY45, Kurdistan Region – F.R. Iraq

***Abstract*—Sign language assists in building communication and bridging gaps in understanding. Automatic sign language recognition (ASLR) is a field that has recently been studied for various sign languages. However, Kurdish sign language (KuSL) is relatively new and therefore researches and designed datasets on it are limited. This paper has proposed a model to translate KuSL into text and has designed a dataset using Kinect V2 sensor. The computation complexity of feature extraction and classification steps, which are serious problems for ASLR, has been investigated in this paper. The paper proposed a feature engineering approach on the skeleton position alone to provide a better representation of the features and avoid the use of all of the image information. In addition, the paper proposed model makes use of recurrent neural networks (RNNs)-based models. Training RNNs is inherently difficult, and consequently, motivates to investigate alternatives. Besides the trainable long short-term memory (LSTM), this study has proposed the untrained low complexity echo system network (ESN) classifier. The accuracy of both LSTM and ESN indicates they can outperform those in state-of-the-art studies. In addition, ESN which has not been proposed thus far for ASLT exhibits comparable accuracy to the LSTM with a significantly lower training time.**

***Index Terms*—Deep learning, Echo system network, Long short-term memory, Microsoft Kinect v2 Sensor, Recurrent neural network, Sign language.**

I. Introduction

In 2020, the World Health Organization (WHO) reported that approximately 466 million people in the world have hearing loss, of whom 34 million are children (World Health Organization, 2020). Those people who lack the ability to listen and\or speak with ordinary people may not be able to understand them. Sign language has therefore become a vital element of human communication. There are now various available sign languages such as American, British, Chinese, Russian, Indian, Persian, and Arabic Sign Language.

Kurdish sign language (KuSL) has been developed only recently. There are three different dialects in Kurdistan for the sign languages studied in deaf private schools in Kurdistan region. KuSL originated in a school for deaf students in Sulaymaniyah in 1982. Students from all Kurdish schools catering for the deaf are able to clearly understand each other using KuSL. In 2015, more than 1000 students attended classes of the deaf schools. The total number of deaf people in Iraqi Kurdistan is estimated to be in excess of 10,000 (Wikipedia, 2019,).

Automatic sign language recognition (ASLR) recognition exploits the physical (dynamic) movement of the hands, face, fingers, or entire body to translate the signs into text or speech. ASLR is a field that has been studied for various sign languages (Almasre and Al-Nuaim, 2016, Maass et al., 2002, Mahmood et al., 2018). However, few research studies have been conducted on the KuSL because it is new (Abdul et al., 2020, Hashim and Alizadeh, 2018, Mahmood et al., 2018).

In this study, we designed a model to translate KuSL into text. There are three main problems that this paper tries to investigate, one of which related to the KuSL itself, where no comprehensive dataset is available with an adequate number of samples. The other two problems related to ASLR are the complexity of the feature extraction step and the high cost of the training stage in the classification level, which negatively influence the ASLT systems' adaptability. Consequently, the questions under investigation in this paper are: (1) How to decrease the time complexity in the feature extraction step, without accuracy degrading of ASLR model? (2) How to design a high-performance model that avoid the time complexity resulted in training the large number of parameters?

In this study, Kinect sensor V2 was used to record videos of seven expert persons expressing 84 different signs (alphabets, digits and words) each with five trials. The features that fed the model were extracted from the videos as a time series representation of only the skeleton points captured by Kinect sensor V2. We have avoided extracting features from the color version of the images to reduce the complexity and proposed a feature engineering applied to the Skelton points instead, to generate more representations of these features. The study has also proposed two recurrent neural network (RNN)-based models: Long short-term memory (LSTM) and

ARO-The Scientific Journal of Koya University
Vol. IX, No.1 (2021), Article ID: ARO.10827, 9 pages
DOI: 10.14500/aro.10827
Received: 05 June 2021; Accepted: 16 August 2021
Regular research paper: Published: 13 October 2021
Corresponding author's e-mail: abdulbasit.faeq@koyauniversity.org

echo system network (ESN). The LSTM, (where weights are learned) are proposed in the literature for ASLR (Liu et al., 2016) and has recorded high performance, however, with a long computation time and complexity. Consequently, we proposed the use of an ESN which has not been used for ASLR so far and uses non-trained weights; therefore, it has a significantly lower time complexity than LSTM; however, we shall see it can achieve comparable accuracy to the LSTM.

The remainder of the paper is structured as follows: Section 2 presents a review of the literature while section 3 explains the background to the study. The adopted methodology is presented in section 4, following which the results are presented and discussed in section 5. Finally, the conclusion to the paper is presented in section 6.

II. Literature Review

In recent years, various studies have been conducted on different sign languages, such as Persian sign language (Karami et al., 2011), American sign language (Truong et al., 2016), Brazilian sign language (BSL) (Dos Santos Anjo et al., 2012), and British sign language (Liwicki and Everingham, 2009, Capilla, 2012).

Sign language recognition is much more challenging where the number of classes (signs) is high. Studies in the literature mainly used a limited number of classes (Table I). For KuSL, and to our best knowledge, the only two available studies have used 12 (Hashim and Alizadeh, 2018) and 10 signs (Mahmood et al., 2018). In this study, and to increase the validity of the proposed ASLR for KuSL, we have designed a dataset that contains 84 signs including digits, alphabets and words. In addition, we have conducted our proposed model on the Chinese Sign Language dataset (Liu et al., 2016), with 100 classes for further validation step.

The nature of the application whether it deals with static (represented in one image) or with dynamic (represented in a sequence of images) language signs, in one side and/or with discrete versus continuous input in the other side, controls the method of data collection, feature extraction, and the classification. Static signs can be easily represented in a global feature, because it has not a time series nature, for example: (Karami et al., 2011) investigated the recognition of static gestures for the Persian alphabet expressed in sign language. Overall, 32 alphabet static signs were recorded using a digital camera and a multilayer perceptron NN (MLP_NN) classifier was utilized to train the proposed model. The study achieved an accuracy of 94%. In another study of BSL, (Dos Santos Anjo et al., 2012) explored the recognition of static gestures in BSL using depth information extracted by Kinect Xbox 360. The authors worked on ten alphabets and applied image segmentation and classification using an artificial NN (ANN). The accuracy of these models was 75.4% for MLP and 67.47% for segmentation.

Regarding the dynamic signs, features should be extracted from each time step, since global features for time series-based signals may lead to lose information of sequences. Therefore, Capilla, 2012, proposed the use of dynamic time warping and utilized Kinect Xbox to translate 14 sign words and achieved an accuracy of 95.2%. In the other side, Truong et al., 2016, proposed the translation of American sign language for alphabetical text and speech using both static and dynamic inputs. ASL alphabets consist of 26 letters, 24 of which are represented statically and 2 signs (“J” and “Z”) are represented dynamically, therefore requiring gestures to be expressed. The authors used Logitech webcam to collect data and adopted two types of classification: Adaboost and Haar_Like classifiers, and they achieved accuracy of 98%.

There are three types of sign language features: Hand motion, hand position, and hand shape, and these have been

Table I
Summary of the datasets used in the literature.

Ref.	No. of Sign	No. of subjects	No. of Samples	Method	accuracy %
(Hashim and Alizadeh, 2018)	12	-		Enhancement and Segmentation	67
(Mahmood et al., 2018)	10	10	200	MLP	98
(Karami et al., 2011)	32	-	640	MLP	94
(Truong et al., 2016)	26		28000 and 11100	Adaboost, Haar_Like classifier	98
(Dos Santos Anjo et al., 2012)	10		400	MLP, Virtual Wall and Libras specific	75
(Liwicki and Everingham, 2009)	100		1000	Robust, Bootstrap and HMM	
(Capilla, 2012)	14		70	Nearest group and DTW	95.2
(Lang et al., 2012)	25			HMM and Dragonfly NITE	97
(Preeti Amatya and Gerrit Meixner, 2018)	11			DTW and VGB	65
(Chai et al., 2013)	239		1195	Kinect v2	83.5
(Kumar et al., 2018)	30	10	2700	HMM and SVM	83.7
(Almasre and Al-Nuaim, 2016)	28	4	224	Supervised learning-	-
(Li, 2012)	9	4	3600	K-Mean and Graham Scan	91
(El-Bendary et al., 2010)	15		15	MLP and MD	91.3
(Mittal et al., 2019)	35	6	3150	CNN	89.5
(Liu et al., 2016)	100 500	50 50	25,000 125,000	RNN and LSTM	86
(Lee et al., 2021)	26	100	2600	LSTM and k-Nearest-Neighbor	91.8
(Rastgoo et al., 2020)	100 45 36	10 25	10,000 100 K 81,000	Single shot detector, 2D Convolutional NN, 3D Convolutional NN, and LSTM	91
(Li et al., 2020)	2000	100	34,404	Holistic visual appearance based approach, and 2D human pose-based approach	62.6
(Gao et al., 2021)	100	50	25,000	H2SNet	0.91
(Katılmış and Karakuzu, 2021)	50	4	8000	ML-KELM	98

MLP: Multilayer perceptron, LSTM: Long short-term memory

adapted to translate Japanese sign language (Awata et al., 2017, Lee et al., 2016). We have adopted in this study the use of the skeleton position alone to reduce the complexity of feature extraction step.

Feature for time series sign language may suffer from the poor representation and\or high dimensionality and lead to increase of the classification complexity. For example, a dataset was designed using 80 Chinese sign language words and Kinect v2 was employed to exploit the RGB image, depth map, and position of the skeleton joints (Li et al., 2017). In ddition, Li et al., 2020, proposed a new large-scale word-level American sign language video dataset, and used two holistic visual appearance based approach, and 2D human pose-based approach models. The utilized dataset was collected from YouTube and contain more than 2000 words performed by 100 signers. The study achieves an accuracy of 62.63%.

In Li et al., 2021, authors present a multiscale fully convolutional NN (MFCN) based method, and extracted the detailed features of the ground object using multiscale convolution kernels. Resolving the findings of change detection (CD) can also be harmed by an imbalance of positive and negative samples. And then model has been trained by unbalanced samples. Hence, using digital globe dataset, the suggested technique was compared to six state-of-the-art CD methods. Finally, their research shows that the achieved accuracy for proposed method is higher than state of the art methods. In (Hossein and Ejaz, 2020), authors proposed a deep convolutional NNs to learn on images of Bengali sign language. Dataset has been collected by snapshot from video using webcam and then applied computer vision-based method. The dataset includes ten set of images and used 31 different signs and the total number of images are 310 Bangladesh image signs. The research achieved an accuracy of 99.8%.

To avoid using the full image-based feature recent studies utilized some devices as a feature extractor. In 2011, Microsoft produced a new device to record video and capture images called the Kinect v2 sensor, which provides RGB, Depth sensor, and 3D Skeleton (Chai et al., 2013). (Almasre and Al-Nuaim, 2016) used depth sensors in Kinect with HMM to recognize gestures and achieved an accuracy of 83.7%. In another study (Kumar et al., 2018), adopt depth sensor data to recognize hand gestures. Lang et al., 2012, and Preeti Amatya and Gerrit Meixner, 2018, propose a dynamic translation of hand gestures to text, where the data has been collected using Kinect v2 and SDK2.0 software. And most recently, leap motion device has been used on a system that is tested with 942 signed sentences using 35 different sign words of Indian Sign Language. The average accuracy of 72.3% and 89.5% has been achieved on signed sentences and isolated sign words, respectively, (Mittal et al., 2019). Kratimenos et al., 2021, employed a SMPL-X model (an extension from the Skinned Multi-Person Linear Model) to enable and extract features from hand, body and face in one RGB image and used to SLR.

Effective and up-to-date classifier for time series inputs are the RNN-based models. For example, an LSTM- based model is proposed in several projects (for example, Li et al., 2017; Liu et al., 2016) using leap motion sensors and color images in Kinect v2. In addition, Li et al. (2017) propose specific hand shape as a descriptor for hand shape, and achieve better sign recognition results, when applied to a proposed encoder-decoder LSTM model. Lee et al., 2021, provides a prototype for an ASL learning application. They applied two methods which are LSTM and k-Nearest-Neighbor for 26 ASL alphabets expressed by 100 subjects each with 100 trails, and they achieved an accuracy of 91.8%. A novel deep learning-based pipeline architecture is proposed by (Rastgoo et al., 2020) for efficient automatic hand sign language recognition from RGB input videos, based on the single shot detector, 2D convolutional NN, 3D convolutional NN, and LSTM, and dataset has been containing 10,000 RGB video from 100 Persian sign words. The achieved accuracy is 90% and 91.1% for RKS-Persian dataset and NYU dataset respectively.

However, training of LSTM as an RNN-based model is reported to be inherently difficult (Lukoševičius, 2012). As a consequent, in this paper, we have proposed ESN architecture as a new powerful approach in RNN research, where, instead of difficult learning process, it based on the property of untrained randomly initialized RNN (Čerňanský and Tiňo, 2007). We shall see in section 5 that the ESN can significantly reduce the training time and achieve results comparable to the LSTM.

Finally, and regarding the ASLR applied to KuSL, two studies have been conducted using image processing tools. First, Hashim and Alizadeh, 2018, developed an algorithm using a grid-based gesture descriptor on the hand gesture image for 12 Kurdish letters, produced following image enhancement and segmentation steps. The achieved accuracy of the proposed model was 67%. In the second study by Mahmood et al., 2018, ten words were expressed by ten people using KuSL. The classifier used was ANN_MLP and the dataset consisted of 200 images extracted from frames 16 and 30 only. The model accuracy was reported to be 98%.

Table I summarizes the datasets of some of the papers produced in sign language.

III. Background

A. Feature Extraction

In computer vision, feature extraction is utilized to capture “important” information on the selected body joints or the detection of hand gestures using image processing tools (Gilorkar and Ingle, 2014). Features can be extracted in different ways such as hand segmentation using canny edge detection (Prasad et al., 2016), scale-invariant feature transform (Pandita and Narote, 2013), Haar wavelets, Haar-like features (Chen et al., 2008), Fourier descriptors, and using Microsoft Kinect Sensor V1 and V2 (Almasre and Al-Nuaim, 2016, Awata et al., 2017, Capilla, 2012, Chai et al., 2013, Kumar et al., 2018, Lang et al., 2012, Preeti Amatya and Gerrit Meixner, 2018, Verma et al., 2013).

In this work, we used Microsoft Kinect sensor V2 to extract 25 joints from the body (Fig. 1). The sensor computes

 http://dx.doi.org/10.14500/aro.10827

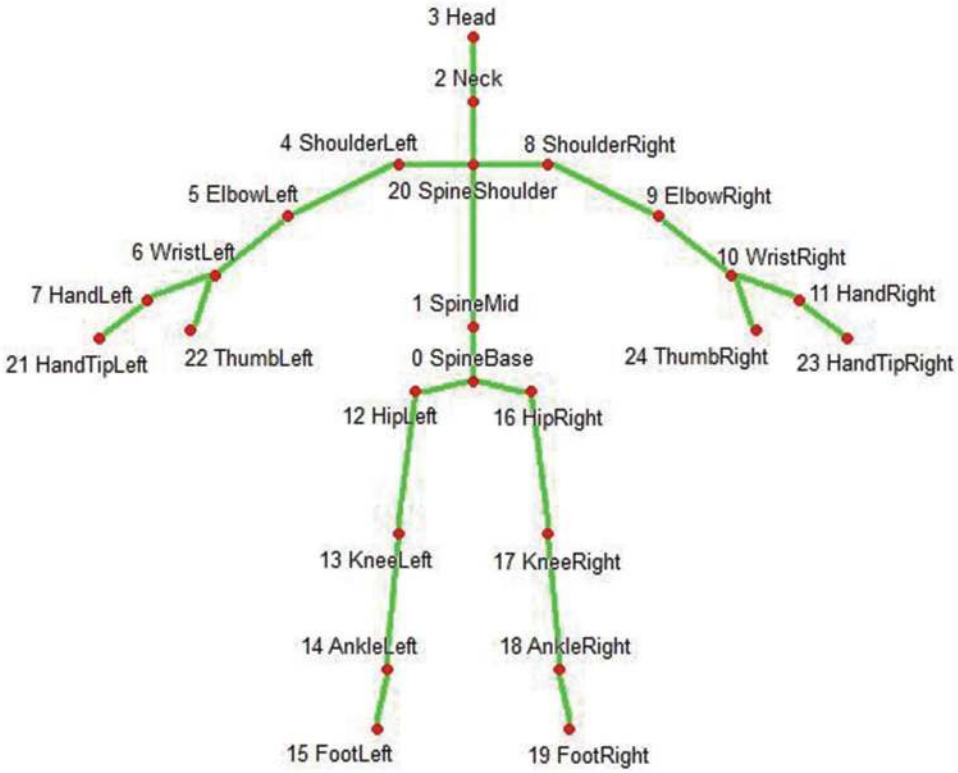

Fig. 1. Skeleton joints captured by Kinect sensor V2.

the joint position values (x, y, and z). In the current study, we extracted 15 joints representing the upper part of the body where most relevant information to the sign language is available. The extracted joints were six joints for each hand (Shoulder, Elbow, Wrist, Hand, Hand Tip, and Thumb) along with the Neck, Head, and Spine Shoulder joints. In addition, a feature engineering approach was adopted that involved determining the slope of each feature along the time steps denoted in this work as a delta feature (DF).

B. LSTM

The problem of gradient vanishing in RNN means alternative models is required. The LSTM is one of the proposed models that aim to improve the RNN. The network structure of the LSTM is complicated. The main improvement LSTM offers over RNN is its ability to capture long-term dependencies (Prabakaran and Shyamala, 2019). Therefore, LSTM adopts a structure that can overcome the problem of gradient vanishing. The LSTM is one of the deep learning classifiers that deal with time-series data such as video, voice, and vibration (Abdul et al., 2020). It takes account of the diversity of the multidimensional feature values at each time step. There are four parts in each repeating module: cell state (c), input gate (i), forget gate (f), and output gate (o) (Fig. 2).

The cell value computation at the current time c_t is represented in equation 1:

$$c_t = f_t \odot c_{t-1} + i_t \odot g_t \quad (1)$$

Where f_t is the forget gate at time t, c_{t-1} is the state of the previous cell, $\odot$ refers to an element wise multiplication, i_t is the input gate at time t, and g_t is computed using equation 4. The function of the cell state is to remember a value during the recurrent connection.

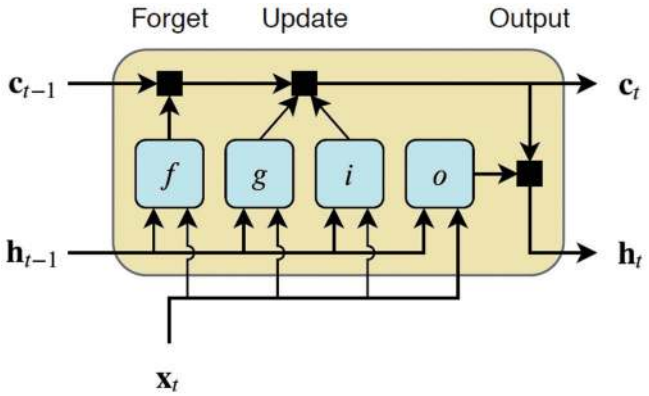

Fig. 2. The structure of the long short-term memory cell.

The following equation demonstrates how to compute, f_t, i_t, and g_t:

$$f_t = \sigma_g \left(W_f x_t + R_f h_{t-1} + b_f \right) \quad (2)$$

$$i_t = \sigma_g \left(W_i x_t + R_i h_{t-1} + b_i \right) \quad (3)$$

$$g_t = \sigma_c \left(W_g x_t + R_g h_{t-1} + b_g \right) \quad (4)$$

Where σ_g and σ_g are gate activation functions, W is the input weight, R represents the recurrent weight, and b is the bias of each component. It is also important to note that the hidden state is updated using equation (5):

$$h_t = o_t \odot \sigma_g\left(c_t\right) \tag{5}$$

Where:

$$o_t = \sigma_g\left(W_o x_t + R_o h_{t-1} + b_o\right) \tag{6}$$

crucial step in the learning process of the model consists of remembering and then forgetting the values. The updated inputs remember values in the memory whereas the forgetting gates skip the remembered input when it is no longer important. The output gate determines when the cell state produces the output value. The output of the final steps during the computation at each gate and cell state forms the input of the later steps. This enables the LSTM model to learn how to maintain its memory as a function of previous values (Jena et al., 2014).

C. Echo State Network (ESN)

ESN provide a supervised learning architecture for RNNs. It adopts a random and non-trained RNN with the input signal, thereby inducing in each neuron within this "reservoir" network a nonlinear response signal, additionally, it combines a desired output signal by a trainable linear combination of all of these response signals.

RNN is traditionally represented by the equation:

$$h(t) = f\left(x(t), h(t-1); \theta_{enc}\right) \tag{7}$$

Where $h(t)$ and $h(t\text{-}1)$ are the current and previous states, respectively, $x(t)$ is the input, $f(t)$. Is the non-linear activation function, and θ_{enc} denotes the trainable encoding parameters. Equation (7) can be rewritten as:

$$h(t) = tanh\left(W_{in} x(t) + W_r h(t-1)\right) \tag{8}$$

Thus:

$$\theta_{enc} = \left\{W_{in}, W_r\right\} \tag{9}$$

Where the matrices W_{in} and W_r are the weights of the input and recurrent connections, respectively. The collection of all states, h, is represented H= [h(1), h(2),…(h(T)], where T is the number of time steps in the sample x. To make this representation suitable for different classifiers, one representation of H can be adopted, denoted here as r(H). A possible representation r is equal to $h(T)$.

To perform the classification step, a function g(.) takes the output of the representation as an input and then maps the representation to one of the categories.

$$y = g\left(r_X; \theta_{dec}\right) \tag{10}$$

Where θ_{dec} denotes all trainable parameters in the classifier.

The traditional RNN trains all the parameters θ_{enc} and θ_{dec}. To avoid the high computational complexity of back-propagating through time, the reservoir computing approach generates the θ_{enc} weights randomly.

However, this may result in a lack of adaptability. To resolve this problem, a large recurrent layer can be used to make the reservoir generate a rich pool of diverse dynamics to model various tasks.

The reservoir capability of generalization can be improved through the processing units in the recurrent layer, the sparsity of the recurrent connections, and the spectral radius of the connection weights matrix W_r, which is set to bring the system close to stability (Bianchi et al., 2016).

The main hyper parameters that control the behavior of the reservoir are the spectral radius; the percentage of non-zero connections; the number of hidden units R; and the scaling ω of the values in W_{in} (Livi et al., 2017).

IV. Method and Materials

A. Datasets

One of the contributions of this work is to design a specific dataset for KuSL. Here, we focused on skeleton data extracted using Kinect sensor and collected metadata from the camera. The Kinect sensor v2 has two sensors for RGB-color video recording with a resolution of 1920 × 1080 pixels, the depth sensor records video at a resolution of 512 × 424 pixels (Wasenmüller and Stricker, 2016) and 3D types detect 25 joints of the body, with each joint represented in three dimensions, x, y, and z (also known as Skeleton values). This work uses the skeleton-based features. We selected 15 features, when for each one a two-dimensional position is provided. The whole dataset consists of 2940 samples, including 84 classes (35 alphabetic, 39 words, and 10 numbers [0–9]) (Table II). In this dataset, seven professional

Table II
Class label for each of Kurdish (alphabetic, words, and numbers)

Label	class	Label	class	Label	class
1	ئ	13	ها	25	ق
2	ه	14	ح	26	ر
3	ع	15	ج	27	ڕ
4	ا	16	ک	28	س
5	ب	17	خ	29	ش
6	چ	18	ل	30	ت
7	د	19	لا	31	ف
8	ی	20	ڵ	32	و
9	ێ	21	م	33	وو
10	ف	22	ن	34	ز
11	گ	23	ۆ	35	ژ
12	غ	24	پ		
36	بەڵێ	50	گران بەها	64	سارد
37	ببورە	51	هەرزان	65	سەرچاو
38	بەیارمەتیت	52	هەینی	66	سێ شەم
39	بەرامبەر	53	جوان	67	شەممە
40	بەیانی	54	کات	68	سڵاو
41	چاکەت	55	کورت	69	سپی
42	چاڵاک	56	لە تەنیشت	70	سوور
43	چۆنی	57	من	71	خواحافیز
44	چوارشەم	58	ناوت چیە	72	یەک شەم
45	دەزانم	59	نەخێر	73	زانا
46	درێژ	60	نازانم	74	زیرەک
47	دووشەم	61	نێوان		
48	ئێمە	62	پێنج شەم		
49	گەرم	63	رۆژئاوابوون		
75	سفر	79	چوار	82	حەوت
76	یەک	80	پێنج	83	هەشت
77	دوو	81	شەش	84	نۆ
78	سێ				

subjects were involved to express the signs and to record the videos, where their skeleton data has been captured. Each subject has repeated the same sign 5 times. Hence, for each class (7×5=35) samples are collected, whereas the total number of samples is 7×5×84=2940 samples.

Kurdish letters can be expressed in both dynamic and static ways. However, most of the letters are static (with no movement), just two of them are dynamic, such as (ۆ، ێ), Fig. 3. However, there are many dynamic signs in the adopted dataset in this work.

B. Feature Engineering (Delta)

Feature engineering can be applied when new features need to be produced from those available. One of the features adopted in this work was the delta of the joint positions along the time steps. The delta representation of a feature is the difference between the value of a feature in the next time step and the value of the same feature in the current time step. In this project, 15 joints were used, which were represented in two dimensions (x, y). Completing all of these computations resulted in 30 DFs, with a reduced o1-time step. To reduce the resolution and hence the computation of the samples, the time steps with odd indexes were included in the delta computation.

C. Scale Normalization

Recording videos for each participant using Kinect V2 led to some differentiating parameters. One of which was the distance from the camera to the position of the participant. The adopted camera detects a person from 1 m to 4.5 m away, and may capture images at different distances from the participant. For automatic scaling, a normalization (standardization) approach using mean and standard deviation was applied, as shown in equation (11):

$$z = \frac{x - \mu}{\sigma} \tag{11}$$

Where μ and σ are the mean and the standard deviation of the feature values in one frame.

D. The LSTM Designed Model

This work made use of two models. The first is the BiLSTM model, the structure of which consists of two BiLSTM layers (sequence to sequence and sequence to label) with the number of neurons equal to 125 and 100, respectively. In addition, we used one fully connected layer with 84 nodes (Fig. 4).

E. The ESN Model

For this work, we adopted the model developed by Bianchi et al., 2020, which is depicted in Fig. 5. Here, we employed a bi-directional representation of the signal that fed a reservoir, producing a collection of states denoted as H. High dimensional time series data significantly increases the complexity. Therefore, the dimension of $\check{H}$ was reduced using principal component analysis (PCA) to produce a low dimensional representation denoted as $\check{H}$. However,

Fig. 3. A Kurdish dynamic sign representing the word “Zirak” meaning brave.

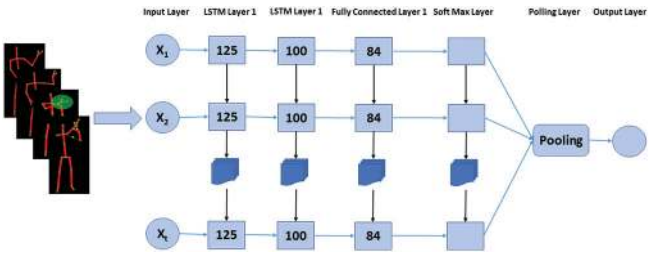

Fig. 4. Long short-term memory model structure.

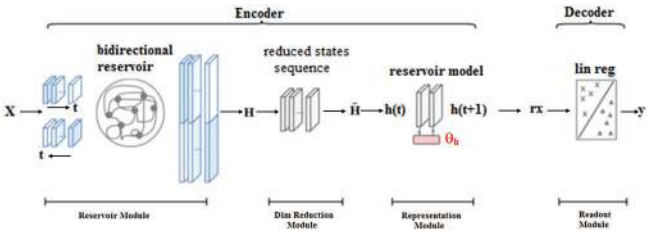

Fig. 5. Echo state network model structure (Bianchi et al., 2020).

$\check{H}$ still has two dimensions (features and time steps), thus needs to be represented in one dimension to be useful for the majority of the machine learning techniques. We have adopted a reservoir model (Bianchi et al., 2020) to produce a one-dimensional representation of $\check{H}$ to later feed the linear readout classifier. In a standard ESN, the readout is linear and is quickly trained by solving a convex optimization problem. The most important advantage of ESN that is adopted here is the low complexity because of the untrained architecture. Therefore, unlike the LSTM, we shall see in the next section how the ESN will significantly reduce the training time, with a very close accuracy to the LSTM.

V. Results and Discussion

A. LSTM Model

The experiments utilized different features for the BiLSTM, including the original feature (OF) (30 skeleton position), the Delta of the Features (DF) (30 feature), and their combination (CF) (60 features). It is important to note that the computation time using CF is extremely high;

consequently, we adopted the low resolution (LR) form of the frame representation by ignoring frames with even indexes. The normalization step was also investigated in all the experiments. To validate the parameters of the Bi-LSTM, we adopted a cross-validation approach (10% vs. 70% for validation and training, respectively, and 20% for testing the model) to tune parameters such as the number of epochs and mini-batch size.

The validation results indicate that large number epochs and small mini-batch sizes achieve better results when using our designed Kurdish dataset. Based on the available hardware in this study and to avoid extremely lengthy computation time, the optimum number of epochs in this model was found to be 250 and the batch size was 1. The small batch size may reflect the diversity of the data, which could be due to the limited number of participants and the number of samples per class in the adopted dataset. Table III displays the accuracy obtained by the BiLSTM classifier using different features. Although the results for all the experiments are similar, for 588 samples the adopted normalization step and the delta computation demonstrated a significant ability to increase the accuracy of the results. The highest accuracy (98.5%) was achieved by the normalized combination of the original and its DFs. The normalization step improved the accuracy of both OF and CF-based models, but was not able to improve the DF-based model. This could be due to the scaling that took place during the delta computation.

B. ESN Model

For the ESN model, we carried out the same experiments while using CF features without decreasing the resolution. This is because the time complexity of ESN is significantly less than that of the LSTM. In the ESN model, the main challenge lies in the parameter validation step as ESN is unstable due to the randomness of the weight initialization. However, adopting the same cross-validation approach tuned the size of the reservoir to be 590, the largest eigenvalue of the reservoir (spectral radius) as 0.2, the amount of leakage in the reservoir state update as 0.6, the percentage of nonzero connections in the reservoir (connectivity) as 0.10, the scaling of the input weights to be 0.3, the noise in the reservoir state update as 0.01, the number of transient states to be dropped as 1, and the number of epochs to be 1000. The achieved results for the ESN mode are presented in Table IV.

Unlike the LSTM, the normalization step in the ESN has not improved the accuracy of OF and CF; however, it was the combination feature in both versions that yielded the highest accuracy. The normalization pre-processing in the PCA included in the proposed ESN model therefore appeared to have an effect on the performance of the model.

It is worthy to highlight the significant lower computation time of the ESN compared to the LSTM (Fig. 6); however, a comparable accuracy has been achieved by the ESN (Fig. 7). The states in ESN are transformed into the random weight space and seem to produce good representation of the model. This may have a link to various studies that

Table III
Different feature representation with BiLSTM, where the number of epochs is 250 and batch size = 1

No	Feature	Accuracy (%)	Time (Minutes)
1	Original feature	97.7	925
2	Delta feature	98.1	912
3	Combination feature (low resolution)	96.1	488
4	The normalized original feature	98.3	939
5	The normalized delta feature	97.8	907
6	The normalized combination feature (low resolution)	98.5	

Table IV
Accuracy of ESN using different feature representation

No	Feature	Accuracy (%)	Time (Minutes)
1	Original feature	97.3	6
2	Delta feature	95.6	10
3	Combination feature	97.1	7
4	Combination feature (low resolution)	97.4	1
5	The normalized original feature	94.4	4
6	The normalized delta feature	96.4	6
7	The normalized combination feature	93.5	4
8	The normalized combination feature (low resolution)	91	1

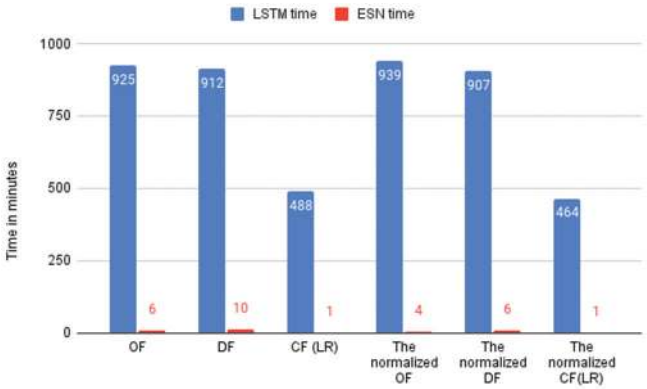

Fig. 6. Long short-term memory and echo state network training time for different set of features.

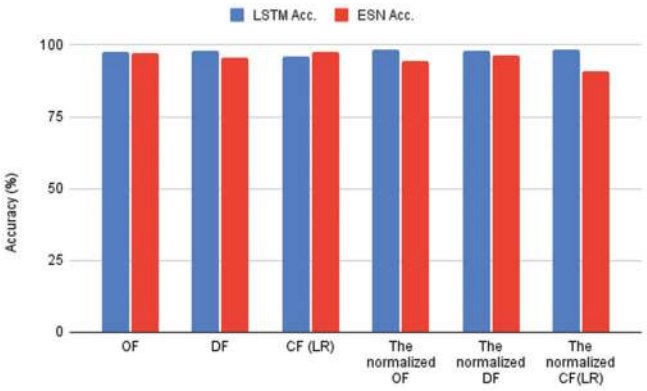

Fig. 7. Long short-term memory and echo state network accuracies for different set of features.

prove the usefulness of the random projection in many high dimensional space produced by the states of the ESN (Al-Talabani et al., 2015).

C. State of the Art Studies

In state-of-art studies, several strands of research have been conducted on a variety of styles of sign language. However, to make a comparison with our model, the dataset needs to have the skeleton version of the data available. One of the most well-known datasets which provide the skeleton version of the data and is available online is the Chinese Sign Language dataset (Liu et al., 2016). This study employed 100 Classes from this dataset, which includes 25000 samples, and adopted the use of the LSTM classifier, achieving 85% accuracy. By applying the adopted BiLSTM model to the same dataset, the accuracy increased to 95%. Similarly, when the ESN model was used, 94.6% accuracy was achieved. Additionally, in comparison with the results reviewed in Table I, we conclude that none of the reviewed works exceed our proposed BiLSTM model as the best result was 98% whereas the proposed BiLSTM achieves 98.5%. It is important to emphasize that the number of signs involved in each of the datasets presented in Table I are all smaller than our proposed dataset with the exception of (Liwicki and Everingham, 2009), which included 230 signs. However, the latter study achieved an accuracy of 83%, which is significantly less than our proposed model. It is also worthy to highlight that the proposed ESN model achieves an accuracy of (97.4%), which is comparable to the achieved results in the state-of-the-art studies, however, with significantly lower complexity.

VI. Conclusion

The skeleton points extracted by the Kinect sensor V2 have a strong ability to capture sign language-related information. Furthermore, aspects of feature engineering, such as computing the delta of the positions of each skeleton, can add complementary information to the features of skeleton positions. The nature of gesture data is that it is a time-varying signal represented in the sequence of the video frames. As it is well-known, RNN based models, especially the BiLSTM, achieve outperforming accuracy for ASLR. However, the training stage for the BiLSTM is time-consuming and may take many hours. As an alternative to reduce the complexity of the model, the ESN (where no trained weights are adopted) can achieve comparable performance and a highly significant decrease in computation time.

The high performance of ESN highlights the usefulness of transforming the gesture data on the random weight vectors adopted in the ESN. For the future, this motivates us for further investigation to link this to the random projection capability to extract valuable information for gestures. User independent ASLR, where the samples tested for a subject is not available in the training stage, can also be studied to more validation the current work.

References

Abdul, Z.K., Al-Talabani, A.K. and Ramadan, D.O., 2020. A hybrid temporal feature for gear fault diagnosis using the long short term memory. *IEEE Sensors Journal*, 20(23), pp.14444-14452.

Almasre, M.A. and Al-Nuaim, H., 2016. A real-time letter recognition model for arabic sign language using Kinect and leap motion controller v2. *International Journal of Advanced Engineering, Management and Science*, 2(5), p.239469.

Al-Talabani, A., Sellahewa, H. and Jassim, S.A., 2015. Emotion recognition from speech: Tools and challenges. Mobile multimedia/image processing, security, and applications. *International Society for Optics and Photonics*, 9497, p.94970N.

Awata, S., Sako, S. and Kitamura, T., 2017. Japanese sign language recognition based on three elements of sign using kinect v2 sensor. In: *International Conference on Human-computer Interaction*. Springer, Berlin, Germany, pp.95-102.

Bianchi, F.M., Livi, L. and Alippi, C., 2016. Investigating echo-state networks dynamics by means of recurrence analysis. *IEEE Transactions on Neural Networks and Learning Systems*, 29(2), pp.427-439.

Bianchi, F.M., Scardapane, S., Løkse, S. and Jenssen, R., 2020. Reservoir computing approaches for representation and classification of multivariate time series. *IEEE Transactions on Neural Networks and Learning Systems*, 23(5), pp.2169-2179.

Capilla, D.M., 2012. *Sign Language Translator Using Microsoft Kinect Xbox 360 tm*. Department of Electrical Engineering and Computer Science, University of Tennessee, Tennessee.

Čerňanský, M. and Tiňo, P., 2007. Comparison of echo state networks with simple recurrent networks and variable-length Markov models on symbolic sequences. In: *International Conference on Artificial Neural Networks*. Springer, Berlin, Germany, pp.618-627.

Chai, X., Li, G., Lin, Y., Xu, Z., Tang, Y., Chen, X. and Zhou, M., 2013. Sign language recognition and translation with kinect. *IEEE Conference on Automatic*, 655, p.4.

Chen, Q., Georganas, N.D. and Petriu, E.M., 2008. Hand gesture recognition using Haar-like features and a stochastic context-free grammar. *IEEE Transactions on Instrumentation and Measurement*, 57(8), pp.1562-1571.

Dos Santos Anjo, M., Pizzolato, E.B. and Feuerstack, S., 2012. *A Real-time System to Recognize Static Gestures of Brazilian Sign Language (Libras) Alphabet Using Kinect*. IHC, Citeseer, pp.259-268.

El-Bendary, N., Zawbaa, H.M., Daoud, M.S., Hassanien, A.E. and Nakamatsu, K., 2010. Arslat: Arabic sign language alphabets translator. In: *International Conference on Computer Information Systems and Industrial Management Applications*. IEEE, United States, pp.590-595.

Gao, L., Li, H., Liu, Z., Liu, Z., Wan, L. and Feng, W., 2021. RNN-transducer based Chinese sign language recognition. *Neurocomputing*, 434, pp.45-54.

Gilorkar, N.K. and Ingle, M.M., 2014. A review on feature extraction for Indian and American sign language. *International Journal of Computer Science and Information Technologies*, 5(1), pp.314-318.

Hashim, A.D. and Alizadeh, F., 2018. Kurdish sign language recognition system. *UKH Journal of Science and Engineering*, 2(1), pp.1-6.

Hossein, M.J. and Ejaz, M.S., 2020. Recognition of Bengali sign language using novel deep convolutional neural network. In: *2nd International Conference on Sustainable Technologies for Industry 4.0 (STI), 2020*. IEEE, United States, pp.1-5.

Karami, A., Zanj, B. and Sarkaleh, A.K., 2011. Persian sign language (PSL) recognition using wavelet transform and neural networks. *Expert Systems with Applications*, 38(3), pp.2661-2667.

Katilmis, Z. and Karakuzu, C., 2021. ELM based two-handed dynamic turkish sign language (TSL) word recognition. *Expert Systems with Applications*, 2021, pp.115213.

Kratimenos, A., Pavlakos, G. and Maragos, P., 2021. Independent sign language recognition with 3d body, hands, and face reconstruction. In: *ICASSP 2021-2021 IEEE International Conference on Acoustics, Speech and Signal Processing (ICASSP)*. IEEE, United States, pp.4270-4274.

Kumar, P., Saini, R., Roy, P.P. and Dogra, D.P., 2018. A position and rotation invariant framework for sign language recognition (SLR) using Kinect. *Multimedia Tools and Applications*, 77(7), pp.8823-8846.

Lang, S., Block, M. and Rojas, R., 2012. Sign language recognition using kinect. In: *International Conference on Artificial Intelligence and Soft Computing*. Springer, Berlin, Germany, pp.394-402.

Lee, C.K., Ng, K.K., Chen, C.H., Lau, H.C., Chung, S. and Tsoi, T., 2021. American sign language recognition and training method with recurrent neural network. *Expert Systems with Applications*, 167, pp.114403.

Lee, G.C., Yeh, F.H. and Hsiao, Y.H., 2016. Kinect-based Taiwanese sign-language recognition system. *Multimedia Tools and Applications*, 75(1), pp.261-279.

Li, D., Rodriguez, C., Yu, X. and Li, H., 2020. Word-level deep sign language recognition from video: A new large-scale dataset and methods comparison. *Proceedings of the IEEE/CVF Winter Conference on Applications of Computer Vision*. WACV, United States, pp.1459-1469.

Li, X., He, M., Li, H. and Shen, H., 2021. *A Combined Loss-based Multiscale Fully Convolutional Network for High-resolution Remote Sensing Image Change Detection*. IEEE Geoscience and Remote Sensing Letters, United States.

Li, X., Mao, C., Huang, S. and Ye, Z., 2017. Chinese sign language recognition based on shs descriptor and encoder-decoder lstm model. In: *Chinese Conference on Biometric Recognition*. Springer, United States, pp.719-728.

Li, Y., 2012. Hand gesture recognition using Kinect. In: *2012 IEEE International Conference on Computer Science and Automation Engineering*. IEEE, United States, pp.196-199.

Liu, T., Zhou, W. and Li, H., 2016. Sign language recognition with long short-term memory. In: *2016 IEEE International Conference on Image Processing (ICIP)*. IEEE, United States, pp.2871-2875.

Livi, L., Bianchi, F.M. and Alippi, C., 2017. Determination of the edge of criticality in echo state networks through Fisher information maximization. *IEEE Transactions on Neural Networks and Learning Systems*, 29(3), pp.706-717.

Liwicki, S. and Everingham, M., 2009. Automatic recognition of fingerspelled words in british sign language. In: *2009 IEEE Computer Society Conference on Computer Vision and Pattern Recognition Workshops*. IEEE, United States, pp.50-57.

Lukoševičius, M., 2012. A practical guide to applying echo state networks. In: *Neural Networks*: *Tricks of the Trade.* Springer, Berlin, Germany.

Maass, W., Natschläger, T. and Markram, H., 2002. Real-time computing without stable states: A new framework for neural computation based on perturbations. *Neural Computation*, 14(11), pp.2531-2560.

Mahmood, M.R., Abdulazeez, A.M. and Orman, Z., 2018. Dynamic hand gesture recognition system for kurdish sign language using two lines of features. In: *2018 International Conference on Advanced Science and Engineering (ICOASE)*. IEEE, United States, pp.42-47.

Mittal, A., Kumar, P., Roy, P.P., Balasubramanian, R. and Chaudhuri, B.B., 2019. A modified LSTM model for continuous sign language recognition using leap motion. *IEEE Sensors Journal*, 19(16), pp.7056-7063.

Pandita, S. and Narote, S., 2013. Hand gesture recognition using SIFT. *Proceedings of the IEEE International Conference on Computational Intelligence and Security*, 2(1), p.4.

Prabakaran, D. and Shyamala, R., 2019. A review on performance of voice feature extraction techniques. In: *2019 3rd International Conference on Computing and Communications Technologies (ICCCT)*. IEEE, United States, p.221-231.

Prasad, M., Kishore, P., Kumar, E.K. and Kumar, D.A., 2016. Indian sign language recognition system using new fusion based edge operator. *Journal of Theoretical and Applied Information Technology*, 88(3), p.574-583.

Preeti Amatya, K.S. and Meixner, G., 2018. Translation of sign language into text using kinect for windows v2. In: *The Eleventh International Conference on Advances in Computer-human Interactions.* ACHI, United States.

Rastgoo, R., Kiani, K. and Escalera, S., 2020. Hand sign language recognition using multi-view hand skeleton. *Expert Systems with Applications*, 150, p.113336.

Truong, V.N., Yang, C.K. and Tran, Q.V., 2016. A translator for American sign language to text and speech. In: *2016 IEEE 5th Global Conference on Consumer Electronics*. IEEE, United States, pp.1-2.

Verma, H.V., Aggarwal, E. and Chandra, S., 2013. Gesture recognition using kinect for sign language translation. In: *2013 IEEE 2nd International Conference on Image Information Processing (ICIIP-2013)*. IEEE, United States, pp.96-100.

Wasenmüller, O. and Stricker, D., 2016. Comparison of kinect v1 and v2 depth images in terms of accuracy and precision. In: *Asian Conference on Computer Vision, 2016*. Springer, United States, pp.34-45.

Wikipedia., 2019. *Kurdish Sign Language*. Available from: https://www.en.wikipedia.org/wiki/Kurdish_Sign_Language. [Last accessed on 2019 Mar 28].

World Health Organization., 2020. *Deafness and Hearing Loss*. Available from: https://www.who.int/news-room/fact-sheets/detail/deafness-and-hearing-loss. [Last accessed on 2020 Mar 01].

http://dx.doi.org/10.14500/aro.10837

Kurdish Dialect Recognition using 1D CNN

Karzan J. Ghafoor, Karwan M. Hama Rawf, Ayub O. Abdulrahman and Sarkhel H.Taher Karim

Department of Computer Science, College of Science, University of Halabja, Halabja,
Kurdistan Region - F.R. Iraq

***Abstract*—Dialect recognition (DR) is one of the most attentive topics in the speech analysis area. Machine learning algorithms have been widely used to identify dialects. In this paper, a model that based on three different 1D Convolutional Neural Network (CNN) structures is developed for Kurdish DR. This model is evaluated and CNN structures are compared to each other. The result shows that the proposed model has outperformed the state of the art. The model is evaluated on the experimental data that have been collected by the staff of Department of Computer Science at the University of Halabja. Three dialects are involved in the dataset as the Kurdish language consists of three major dialects, namely Northern Kurdish (Badini variant), Central Kurdish (Sorani variant), and Hawrami. The advantage of the CNN model is not required to concern handcraft as the CNN model is featureless. According to the results, the 1D CNN method can make predictions with an average accuracy of 95.53% on the Kurdish dialect classification. In this study, a new method is proposed to interpret the closeness of the Kurdish dialects using a confusion matrix and a non-metric multi-dimensional visualization technique. The outcome demonstrates that it is straightforward to cluster given Kurdish dialects and linearly isolated from the neighboring dialects.**

***Index Terms*—Convolution neural network; deep learning; dialect recognition; machine learning**

I. Introduction

Dialect is the language variety of a populace set up dependent on different real-life conditions (Chen, Shen, and Campbell, 2010). Every Dialect has its specific patterns of pronunciation, and there are regularly specific words or expressions that are explicitly being spoken among speakers of a specific Dialect (Najafian, *et al*. 2017, Najafian, *et al*. 2014). As of late, Dialect Recognition (DR) has become an intriguing problem for its wide applications in Speech Recognition. The adjusted Speech Recognition framework needs various tools, for example, the recognition of the dialect or the accent to standardize the speech tests for the Speech Recognition framework. For instance, Hirayama, Yoshino, Itoyama, Mori, and Okuno, (2015), build up a programmed Speech Recognition framework that accepts a mixture of various kinds of dialect.

There are many difficulties in the DR research area, for example, the assortment of speech information, which needs to display the different kinds of the examined dialect as well as languages (Diakoloukas, Digalakis, Neumeyer and Kaja, 1997). The results achieved by the researchers on DR are generally limited to the accessible collected data. To come across these challenges, we used a dataset collected by faculty members of the Computer Science Department at the University of Halabja. Subsequently, using the created algorithms beginning with the arrangement of the tested data or the classification techniques is non-persuading. Therefore, a few researches around using collected data under an explicit condition hold the important characteristics of the data. Huang and Hansen (2007) address the problem that considers the situation where no transcripts are accessible for preparing and testing data, and speakers are talking spontaneously.

Another challenge of Multi-dialect Speech Recognition is the growing adoption of smart devices. In particular, Kurdish poses an interesting challenge as the language has many dialects, and dialects do not have standard orthographic rules (Ali, 2018). Whereas the development of such a system faces the problem of the lack of annotated resources and tools, apart from the lack of standardization at all linguistic levels (phonological, morphological, syntactic, and lexical) together with the mispronunciation dictionary needed for Automatic Speech Recognition (ASR) development (Masmoudi, Bougares, Ellouze, Estève, and Belguith, 2018). To address this challenge, the study worked to reach a good result to recognize different dialects in Kurdish language. This will help to improve Speech Recognition for Kurdish dialects.

In this paper, Kurdish DR is studied and an end-to-end model is proposed based on 1D CNN for various classified Kurdish dialects including (Sorani, Badini, and Hawrami). Moreover, closeness of the dialects is presented based on a non-metric multidimensional visualization technique which is built on misclassification among the dialects.

The rest of the paper is organized as follows: Related work is presented in section II. Methodology of the proposed model is explained in section III. Experimental design and hyper parameters are clarified in sections IV and V, respectively. The result is discussed in the penultimate section (VI). Finally, conclusion of this work is pointed out in the last section (VII)

ARO-The Scientific Journal of Koya University
Vol. IX, No.2 (2021), Article ID: ARO.10837, 5 pages
DOI: 10.14500/aro.10837
Received: 21 June 2021; Accepted: 17 September 2021
Regular research paper: Published: 15 October 2021
Correspondent author's e-mail: karzan.ghafor@uoh.edu.iq

II. Related Work

In the literature, some of the studies have been focused on the feature of DR signals. Gaussian mixture model (GMM), for instance. In (Bahari, Dehak, Burget, Ali, and Glass, 2014), a positive factor analysis approach was developed for the GMM weight decomposition and conversion. Their study shows that GMM loads convey less, yet complimentary, data to GMM implies for language and DR. The Bangladeshi dialects using Mel Frequency Cepstral Coefficient (MFCC), its Delta and Delta-delta as main features and GMM to classify the characteristics of a specific dialect, by extracting the MFCCs, Deltas and Delta-deltas from the speech signal (Das, Allayear, Amin and Rahman, 2016). Whereas, in Haines, 2019, an unsupervised bottleneck feature extraction approach is proposed by Chunlei Zhang, to explain the effectiveness of the proposed methods, three datasets have been used (1) a four Chinese dialect dataset, (2) a five Arabic lingo corpus, and (3) multigene communicate challenge corpus (MGB-3) for Arabic. To overcome the utterance degrades. As it has been proposed by (Zhang, et al., 2019) an end-to-end approach to reduce recurrence varieties and extract the global context feature information vector using (CNN), Bidirectional Gated Recurrent Unit (CNN-BiGRU), which is useful to enhance the feature expression of short utterances. In another way, Experiments on ten Chinese dialects showed that the given method achieved 9.93% relative improvement in accuracy than the mainstream i-vector system. An experiment made by Huang and Hansen (2007) addresses novel advances in unsupervised TVDR in English and Spanish.

The researches of language and DR are generally using template-based and/or phonetic centered techniques. The template-based DR receives the utilization of global parameters of the speech signal playing little heed to the special attributes of the accessible phonemes identified with every dialect. This kind of research has been used by Choueiter, Zweig, and Patrick (2008) which found that an absolutely acoustic methodology dependent on a combination of heteroscedastic linear discriminant analysis and maximum mutual information training was exceptionally powerful. However, phonetic-based DR is likewise adopted and compared with acoustic and token-based DR and furthermore saw to be effective as in (Diakoloukas, Digalakis, Neumeyer, and Kaja, 1997). Another methodology embraced for DR is phonetic based recognition of dialect. A study receives a local feature that reflects the appearance of different phonemes in every language or dialect. For instance, both articles (Chen, Shen, and Campbell, 2010, Chen, Shen, Campbell, and Torres-Carrasquillo, 2011) propose supervised and unsupervised learning algorithms to find dialect discriminating phonetic rules and use these rules to apply biphones to identify dialects. Zhang and Hansen, 2018, presented an unsupervised bottleneck feature extraction approach to address the limitation of traditional bottleneck feature extraction, which is derived from the traditional bottleneck structure but trained with estimated phonetic labels.

In some research, a concealed Markov model is used to alter reference phones with dialect-specific pronunciations to describe when and how often replacements, insertions, and deletions occur. In Ying, Zhang, and Deng, 2020, anticipated an ASR system for Sichuan dialect by combining a hidden Markov model and a deep long short-term memory network which can overcomes the problem of using only captured context of a fixed number of information items compared with the deep neural network. To expand the research of DR, in this paper, we used 1D CNN to overcome the problem of feature extraction and recognition of dialects Sorani, Badini, and Hawrami.

III. Methodology

A. Data Description

Data collection is one of the basic requirements for those models developed based on the machine learning algorithm. Machine learning cannot be done without having a dataset. The utilized dataset was collected by some faculty members of the Computer Science Department in University of Halabja. All standard ways and rules were considered for the data acquisition including the consideration of various age groups and genders for those speakers who participated in the dataset. Furthermore, the geographical distribution of the speakers was considered as well. Generalization of the model can be achieved by adopting these considerations in the dataset. Three dialects were considered for the dataset as Kurdish language consists of three main dialects (Sorani, Badini, and Hawrami). Samples were recorded from TV broadcasts and debates. For each dialect, 180 different speakers were involved. Moreover, 299 samples for Sorani, 299 samples for Badini dialect, and 297 samples for Hawrami dialect were recorded. The length of each sample is only 1 s, thus 895 s are the total length of our dataset.

B. CNN

CNNs are a kind of deep neural networks which were originally proposed for 2D input. It is a powerful machine learning tool for learning features from the input raw data and outperforms the traditional machine learning models for image classification (Khan, Sohail, Zahoora, and Qureshi, 2020). One of the modifications of 2D CNNs is the 1D CNN, which has recently been applied in many applications as shown in recent researches (Kiranyaz, Ince, and Gabbouj, 2016, Acharya, et al., 2017, Ince, Kiranyaz, Eren, Askar, and Gabbouj, 2016 , and Kiranyaz, Gastli, Ben-Brahim, Al-Emadi, and Gabbouj, 2018). These researches have clarified that for certain applications, 1D CNNs are more preferable than one dimensional-based applications due to the low complexity, small number of hidden layers and neurons, and low cost of implementation. Typically, CNN models are mainly composed of two parts, feature extraction and classification. The section of feature extraction is responsible for extracting features from raw signals automatically, which normally consists of some layers such as convolution and pooling layers, and the other part (classification part) is in charge of the classification decision (Abdul, 2019).

http://dx.doi.org/10.14500/aro.10837

Furthermore, the classification part is identical to a typical Multi-Layer Perceptron and called as fully-connected layers (Kiranyaz, Ince, Hamila, and Gabbouj, 2015).

The configuration of any 1D-CNN explores some important processes as shown below:

- Initialize weights and biases
- Feed forward process applies from the input layer to the output layer to find outputs of each neuron at each layer. The process is formulated in equation (1)

$$x_k^l = b_k^l + \sum_{i=1}^{Nl-1} Conv1D\left(W_{ik}^{l-1}, s_i^{l-1}\right) \quad (1)$$

Where, x_k^l is the input, b_k^l is bias of the kth neuron at layer l, s_i^{l-1} and W_{ik}^{l-1} is the output of the th neuron at layer l–1 and the kernel from the th neuron at layer $l-1$ to the kth neuron at layer l, respectively. Moreover, *conv1D* is used to perform convolution process between W_{ik}^{l-1} and s_i^{l-1}

- Back propagation process: Start from computing delta error at the output layer and back-propagate it to the first hidden layer to compute the delta errors. The equation (2) below is delta error.

$$\frac{\partial E}{\partial_{W_{ik}^{l-1}}} = \Delta_k^t \, y_i^{l-1} \text{ and } \frac{\partial E}{\partial b_k^l} = \Delta_k^t \quad (2)$$

Where, E is the mean-squared error, y_i^{l-1} is intermediate output, and is Δ_k^t defined as delta error.

- Post-process to compute the weight and bias sensitivities.
- Update the weights and biases

IV. Experimental Design

The proposed model consists of seven layers which can be divided in two main parts, namely: Feature extraction part and classification part as shown in Fig. 1. The feature extraction part includes four sequential convolution layers, one max-pooling, and one drop layer. The convolution layers are different in size of the filters and their activation function for instance relu function is used for the first and the fourth convolution layers whereas tanh function is adopted in the second and the third convolution layer. The max-pooling layer is applied to reduce the dimension of the learned feature and the drop layer is used to overcome the overfitting problem. The classification part is responsible for classifying the learned feature from the previous part and it only consists of one fully-connected layer. Three nodes are involved in the mentioned layer because three dialects have been considered. The softmax function is usually used in a fully-connected layer for classification. More information about the structure of CNN are found in Table I.

V. Hyper Parameters

For CNN, some parameters should be tuned to obtain the optimum value to improve the performance of the model. There are some parameters of CNN that can be tuned such as number of convolution layers, number of fully-connected layers, selecting activation function, and number of epochs. Some of the mentioned parameters are tuned properly using nine folds' cross validation approach. The number of convolutional layers is tuned to four layers, where they include 20 filters for each layer. The number of fully connected layers is set as one with a number of nodes equal to the number of the classes which are three. The optimization technique adopted in this network is Adam Table II.

VI. Results And Discussion

A. DR

The length of the signal is 895 samples and divided into three classes, such as 299, 299, and 297 samples for each Sorani, Badni, and Hawrami, respectively. Based on relevant research in the literature, five-fold cross-validation is adopted

Table I
Description of the Layers

No.	Name	Description
1	Convolution Layer 1	20×5 convolutions with activation (relu), Input shape [44100×1]
2	Convolution Layer 2	20×7 convolutions with activation (tanh)
3	Convolution Layer 3	20×7 convolutions with activation (tanh)
4	Convolution Layer 4	20×3 convolutions with activation (relu),
5	Pooling	MaxPooling (9)
6	Dropout	90% dropout
7	Fully Connected1	fully connected three layers

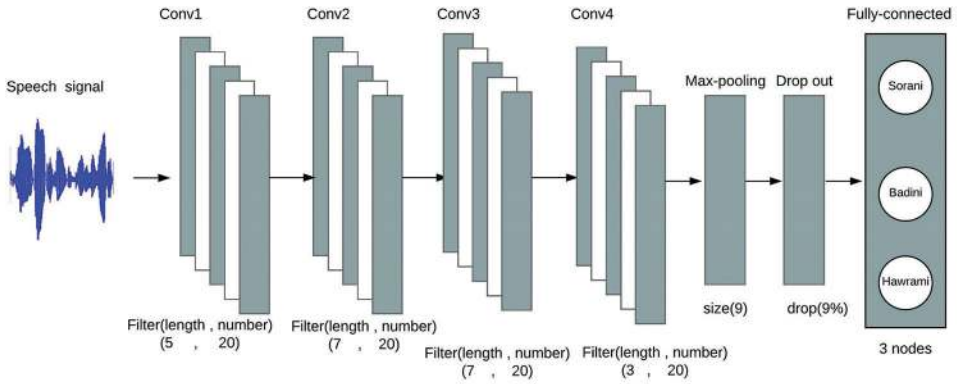

Fig. 1. Structure of the proposed model.

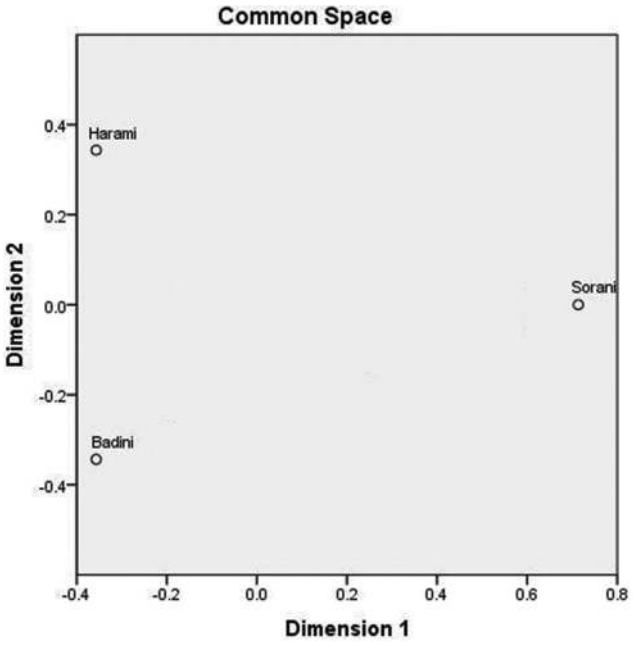

Fig. 2. Closeness of the Kurdish Dialect from each other's.

Table II
Confusion Matrices with Producer Accuracy and User Accuracy

No.	Sorani	Badini	Hawrami	Classification	Producer Accuracy (Precision)	F1-score
Sorani	53	0	2	55	96.364%	96%
Badini	1	58	1	60	96.667%	96%
Hawrami	1	3	60	64	93.75	94.%
Truth	55	61	63	179		
User Accuracy (Recall)	96.364%	95.082%	95.238%			

Table III
Accuracy of kurdish Dialect Recognition Model

Methods	Accuracy
Al-Talabani, Abdul an Ameen.	89.6
proposed model	95.5

to weigh the proposed method. The experimental result in Table III shows a significant improvement in the classification compared to the state of arts with P-value equal to 0.043 As compared to Al-Talabani's work, the study clearly shows that using MFCC feature set (95.5%) in one-dimensional CNN has greater accuracy than using MFCC feature set (71% weak accuracy) and local binary pattern (LBP)-LPC (89.6% best accuracy) fused feature set in one-dimensional LBP (Al-Talabani, Abdul, and Ameen, 2017). Moreover, Precision is 96%, 96%, and 93% for Sorani, Badni, and Hawrami and at least 95% is the proportion of actual positives which are identified correctly as illustrated in Table II.

B. Closeness of the Kurdish Dialects

The whole correct paragraph of Sub-section B should be:

The second purpose of this study is to illustrate how close the Kurdish dialect is to each other and how they impact each other in terms of the phonetic and style. A non-metric multidimensional visualization technique is applied for this purpose which is computed based on misclassification samples between dialects in such a way that a large number of misclassifications indicate high common properties between any two classes. Based on the result, Sorani Dialect has the same distance from both Badini and Hawrami; that means phonetics' Sorani is quite different from the other Dialects. But there are some similarities between Hawrami and Badini in terms of their phonetics and style. (Fig. 2 and Table III)

VII. Conclusion

In this study, 1D CNNs is proposed for Kurdish DR and presents the closeness of the Kurdish Dialects. Based on the experimental result, the performance of the proposed 1D CNN model outperforms the state of arts. Moreover, the proposed model is straightforward to apply because the model is built on the CNN which leads to carelessness about the handcraft feature, but time consumption is high as it requires to learn 23302 parameters including learning parameters of filters and learning weights for fully-connected layers. Another observation in this study is that the phonetic's Badini and Hawrami are closely related compared to the Sorani phonetic.

In addition, for future work some evaluation can be added to the study such as increasing the number of the sample, which is one of the significant points, may impact the results. Furthermore, increasing the number of classes such as Zazaki, Luri, and Bakhtyari have been changed the results and improve the evaluation of the model in the next steps.

References

Abdul, Z.K., 2019. Kurdish speaker identification based on one dimensional convolutional neural network. *Computational Methods for Differential Equations*, 7(4), pp.566-572.

Acharya, U.R., Oh, S.L., Hagiwara, Y., Tan, J.H., Adam, M., Gertych, A. and Tan, R.S., 2017. A deep convolutional neural network model to classify heartbeats. *Computers in Biology and Medicine*, 89, pp.389-396.

Ali, A., 2018. *Multi-Dialect Arabic Broadcast Speech Recognition*. [e-book] University of Edinburgh, Edinburgh p.193. Available from: https://www.era.lib.ed.ac.uk/bitstream/handle/1842/31224/Ali2018.pdf?sequence=1 and isAllowed=y [Last accessed on 2020 Dec 12].

Al-Talabani, A., Abdul Z. and Ameen, A., 2017. Kurdish dialects and neighbor languages automatic recognition. *The Scientific Journal of Koya University*, 5(1), pp.20-23.

Bahari, M.H., Dehak, N., Burget, L., Ali, A.M. and Glass, J., 2014. Non negative factor analysis of gaussian mixture model weight adaptation for language and dialect recognition. *IEEE/ACM Transactions on Audio, Speech, and Language Processing*, 22(7), pp.1117-1129.

Chen, N.F., Shen, W. and Campbell, J.P., 2010. A linguistically-informative approach to dialect recognition using dialect-discriminating context-dependent phonetic models. In: 2010 *IEEE International Conference on Acoustics, Speech and Signal Processing*, pp.5014-5017.

Chen, N.F., Shen, W., Campbell, J.P. and Torres-Carrasquillo, P.A., 2011. Informative Dialect Recognition Using Context-dependent Pronunciation

Modeling, ICASSP. In: IEEE The international Conference on Acoustics, Speech, and Signal Processing. pp.4396-4399.

Choueiter, G., Zweig, G. and Patrick, N., 2008. *An Empirical Study of Automatic Accent Classification*. Microsoft Research One Microsoft Way Redmond, WA 98052, pp.4265-4268.

Das, P.P., Allayear, S.M., Amin, R. and Rahman, Z., 2016. Bangladeshi Dialect Recognition Using Mel Frequency Cepstral Coefficient, Delta, Delta-delta and Gaussian Mixture Model. In: *Proceeding 8th International Conference on Advanced Computational Intelligence*, pp.359-364.

Diakoloukas, V., Digalakis, V., Neumeyer, L. and Kaja, J., 1997. Development of Dialect-specific Speech Recognizers Using Adaptation Methods, ICASSP. *IEEE The International Conference on Acoustics, Speech, and Signal Processing*, 2, pp.1455-1458.

Haines., Goleman, D., Boyatzis, R., Mckee, A., 2019. The meaning and process of communication. *Journal of Chemical Information and Modeling*, 53(9), pp.1689-1699.

Hirayama, N., Yoshino, K., Itoyama, K., Mori, S. and Okuno, H.G., 2015. Automatic speech recognition for mixed dialect utterances by mixing dialect language models. *IEEE/ACM Transactions on Audio, Speech, and Language Processing*, 23(2), pp.373-382.

Huang R. and Hansen, J.H.L., 2007. Unsupervised discriminative training with application to dialect classification. *IEEE/ACM Transactions on Audio, Speech, and Language Processing*, 15(8), pp.2444-2453

Ince, T., Kiranyaz, S., Eren, L. Askar, M. and Gabbouj, M., 2016. Real-time motor fault detection by 1-D convolutional neural networks. *IEEE Transactions on Industrial Electronics*, 63(11), pp.7067-7075.

Khan, A., Sohail, A., Zahoora, U. and Qureshi, A. S., 2020. *A Survey of the Recent Architectures of Deep Convolutional Neural Networks, No. 0123456789*. Springer, Netherlands.

Kiranyaz, S., Gastli, A., Ben-Brahim, L., Al-Emadi, N. and Gabbouj, M., 2019. Real-time fault detection and identification for MMC using 1-D convolutional neural networks. *IEEE Transactions on Industrial Electronics*, 66(11), pp.8760-8771.

Kiranyaz, S., Ince, T. and Gabbouj, M., 2016. Real-time patient-specific ECG classification by 1-D convolutional neural networks. *IEEE Transactions on Industrial Electronics*, 63(3), pp.664-675.

Kiranyaz, S., Ince, T., Hamila, R. and Gabbouj, M., 2015. Convolutional neural networks for patient-specific ECG classification. *Annual International Conference, IEEE Engineering in Medicine and Biology Society*, pp.2608-2611.

Masmoudi, A., Bougares, F., Ellouze, M., Estève, Y. and Belguith, L., 2018. Automatic speech recognition system for Tunisian dialect. *Language Resources and Evaluation*, 52, pp.249-267.

Najafian, M., DeMarco, A., Cox, S. and Russell, M., 2014. Unsupervised model selection for recognition of regional accented speech. *Annual Conference of the International Speech Communication Association, INTERSPEECH*, pp.2967-2971,

Najafian, M., Hsu, W., Ali, A. and Glass, J., 2017, Automatic speech recognition of Arabic multi-genre broadcast media. In: *2017 IEEE Automatic Speech Recognition and Understanding Workshop* (ASRU), pp.353-359.

Ying, W., Zhang, L. and Deng, H., 2020, Sichuan dialect speech recognition with deep LSTM network. *Frontiers of Computer Science*, 14(2), pp.378-387.

Zhang, Q. and. Hansen, J.H.L., 2018. Language/dialect recognition based on unsupervised deep learning. *IEEE/ACM Transactions on Audio, Speech, and Language Processing*, 26(5), pp.873-882.

Zhang, Q., Ma, Y., Gu, M., Jin, Y., Qi, Z., Ma, X. and Zhou, Q., 2019. End-to-End Chinese Dialects Identification in Short Utterances using CNN-BiGRU. In: 2019 *IEEE 8th Joint International Information Technology and Artificial Intelligence Conference* (ITAIC), 2019, pp. 340-344

Withania Somnifera: Correlation of Phytoconstituents with Hypolipidemic and Cardioprotective Activities

Subasini Uthirapathy[1] and Tara Fuad Tahir[2]

[1]Department of Pharmacology, Faculty of Pharmacy, Tishk International University, Erbil, Kurdistan Region - F.R. Iraq

[2]Department of Medical Microbiology, Faculty of Science and Health, Koya University, Koya KOY45, Kurdistan Region - F.R. Iraq

***Abstract*—*Withania somnifera* (WS) (Dunal) or Ashwagandha is a well-known hypolipidemic herb and antioxidant. In this study, 75% ethanolic extract of WS is attempted to evaluate the cardioprotective activity of isoproterenol-induced cardiotoxicity and hypolipidemic activity in Triton WR 1339-induced hyperlipidemia. In addition, phytochemical evaluation of the same extracts analyzed by gas chromatography–mass spectrometer (GC–MS). This study found that 7 days of therapy with WS extracts at 1000 mg/kg b.wt. reduced cholesterol by 76%, low-density lipoprotein (LDL) by 71%, and TAG by 12% ($P < 0.05$). Furthermore, it can significantly reduce cholesterol and LDL levels ($P < 0.05$). Similarly, the use of 50 mg/kg b.wt. of WS extract showed a cardioprotective effect against isoproterenol-induced cardiac toxic rats. The antioxidants glutathione, glutathione peroxidase, and catalase are increased in WS extract ($P < 0.05$), whereas the release of cardiac indicators in heart tissue is reduced ($P < 0.05$). Furthermore, a 30-day treatment with WS also reduced triacylglycerol in isoprenaline-induced cardiotoxic rats. GC–MS analysis of the methanol fraction of the Ashwagandha 70% ethanolic extract showed the presence of higher concentrations of fatty acids. In conclusion, WS showed hypolipidemic and cardioprotective activities in diseased animals induced by isoproterenol and Triton WR 1339.**

***Index Terms*—Antioxidants, Cardiac markers, Gas chromatography–mass spectrometer, Isoproterenol, Lipid, Triton WR 1339.**

I. Introduction

Withania somnifera (Dunal) (WS) is commonly known as winter cherry. It is a green shrub belonging to the Solanaceae family. Earlier references have shown that the plant preparations have anti-inflammatory (Boehm et al., 2000), anti-cancer, anti-stress, and immunomodulatory activities. WS has also shown reports of the central nervous system (CNS), endocrine (Subasini et al., 2007), and cardiovascular (Jasemi et al., 2020) diseases. Furthermore, WS preparations are thought to affect GABAergic (gamma-aminobutyric acid (GABA) (Dar et al., 2016) or cholinergic (Kumari et al., 2020) neurotransmission, which could be associated to a variety of CNS disorders. Other plant parts have been utilized to treat various diseases for a long time.

The root of WS is the central part of the plant for its treatment. WS root powder at 0.75 g and 1.5 g/rodent/day can significantly reduce the total cholesterol and triglycerides (TGLs) in plasma (Nishant and Narasimhacharya, 2006). Then, a considerable increase in plasma high-density lipoprotein (HDL) cholesterol levels, the action of 3-Hydroxy-3-Methyl-Glutaryl-CoA reductase (HMG-CoA) and liver bile acids was observed in these rats. A similar pattern was also observed in the excretion of bile acids, cholesterol, and neutral sterols in hypercholesterolemic rats with oral administration of WS. Further, a significant decrease in lipid-peroxidation occurred in WS administered hypercholesterolemia animals when compared to their normal group of rats. However, it gives an idea that WS root extract is also attractive for lowering the lipid profile (Saggam et al., 2021).

It is familiar that WS has the ability to control oxidative stress markers in the body. Conclusively, the root extract decreases lipid peroxidation and boosts superoxide dismutase (SOD) and catalase activity (Adams et al., 2002). As a result, it has free radical scavenging activity. Furthermore, the hypolipidemic (Nishant and Narasimhacharya, 2006) and antioxidant activity of WS has been demonstrated by Priscilla and Prince, 2009. We attempted to assess the cardioprotective impact, as well as hypolipidemic and antioxidant activities, in isoproterenol-induced cardiotoxicity and Triton WR 1339-induced hyperlipidemia in this research. To correlate the pharmacological activity with its active constituents, gas chromatography–mass spectrometer (GC–MS) analysis also carried out.

II. Materials and Methods

A. Chemicals and Reagents

Isoproterenol, malondialdehyde, 1,1'-diphyenyl-2-picrylhydrazyl, and 2,2'-azinobis-(3-ethyl-benzothiazoline-

ARO-The Scientific Journal of Koya University
Vol. IX, No. 2 (2021), Article ID: ARO.10844, 7 pages
DOI:10.14500/aro.10844
Received: 28 July 2021; Acceptance: 25 September 2021
Regular research paper: Published: 15 October 2021
Corresponding author's e-mail: tara.fuad@koyauniversity.org

6-sulfonic acid) were purchased from Sigma Chemical Co., St. Louis, MO, USA. Biochemical kits for the assay of cholesterol, TGLs, and HDL cholesterol were procured from Randox Laboratories. Creatine kinase (CK)-MB assay kit was purchased from SPINREACT. All the other reagents used were of analytical grade.

B. Collection and Identification of Plants

The root of WS was obtained from Madurai. The plant material was identified in the Department of Pharmacognosy, Centre for Advanced Research of the Indian System Medicine, SASTRA University, Thanjavur, Tamil Nadu, India. The voucher is saved in the same department, document number (0064).

C. Preparation of Extract

The collected plant material was dried for 15 days a room temperature. The raw materials were grinded to use it for extraction with 70% ethanol and the cold infiltration method was used.

Vacuum rotary evaporator was used to concentrate the extract 40°C. Refrigeration was used to store the concentrated extract of 3.83% as the extract yield.

D. Experimental animals

Male Wistar albino rats weighing 180–220 g were allowed to have standard pellets from Hindustan Lever Foods, Bengaluru, India, and water *ad libitum*. They are placed under normal environmental conditions. All rats experiments were performed after obtaining animal ethics approval (Authorization No. 7/SASTRA/IAEC/RPP).

E. Hypolipidemic Activity (Acute Model)

Triton WR 1339 is a non-ionic detergent which has been used to induce hyperlipidemia in animals. Animals were divided into five groups of six rats each. Group 1 animals considered as normal and were fed with standard diet. Group 2 animals received Triton WR 1339. Group 3 animals were pre-treated with atorvastatin 10 mg/kg b.wt./day (p.o.) for 7 days. Groups 4 and 5 animals were pre-treated with WS at the doses of 500 and 1000 mg/kg/day (p.o.), respectively, for 7 days. During treatment, on the 5th day, 1 h after the administration of that samples, all animals except Group 5 were injected with Triton WR 1339, intraperitoneally (i.p.) (dissolved in saline) at the single dose of 400 mg/kg b.wt. The animals were fasted for 3 h before administration of Triton WR 1339 and the fasting was continued up to 48 h after administration of Triton WR-1339. All animals were fed with water after the injection of Triton WR 1339 (Majithiya et al., 2004). The blood was collected from all animals before and after 48 h the administration of Triton WR 1339 by retro-orbital puncture under volatile (ether) anesthesia. Plasma total cholesterol, TGL, and low-density lipoprotein (LDL) by Subasini et al., 2019b, were analyzed.

F. Cardioprotective Activity (Chronic Model)

The experimental animals were divided into four groups, with six animals in each group. For the first group, normal rats were given only a standard diet. Group 2 animals received isoproterenol (ISO). Group 3 animals were pretreated with WS at a dose of 50 mg/kg body weight for 30 days without ISO. Group 4 animals were pretreated with WS 50 mg/kg body weight for 30 days with ISO. On days 31 and 32, animals in Groups 2 and 4 were injected with ISO 85 mg/kg body weight subcutaneously (s.c.) for 2 days. At the end of the study, the animals were sacrificed by cervical dislocation. Blood was collected and then plasma was separated. Heart tissue was removed immediately and washed thoroughly with saline. The cardiac tissue homogenate was prepared in 0.1 M Tris buffer (pH 7.4).

Various biochemical parameters like Creatine Kinase (CK) (Ohkawa et al., 2004), Lactate dehydrogenase (LDH) (King, 1959), Glutamate Pyruvate transaminase (GPT) (Mohun and Cook, 1957), Glutamate Oxaloacetate transaminase (GOT) (Paglia and Valentine, 1967), Thiobarbituric acid Reactive Substances (TBARS) (Ohkawa et al., 2004), Reduced Glutathione (GSH) (Moron et al., 1979), Catalase (Aebi, 1974) were estimated. The plasma concentration of total cholesterol and HDL cholesterol (HDL_C) was determined using an enzyme kit from Randox Laboratories Ltd., UK (Richmond, 1973). First, HDL_C was determined after precipitation of lipoproteins containing apolipoprotein B with dextran sulfate (Warnick et al., 1992). Next, the plasma TGL concentration and homogenate of heart triacylglycerol (TAG) concentration were analyzed by Foster (Foster and Dunn, 1973). Finally, the Friedewald equation (Friedewald et al., 1972) is used to determine the LDL cholesterol (LDL_C) concentration.

G. GC–MS Analysis

Ten milligrams of WS extract were dissolved in methanol. The methanol fraction separated from the 75% ethanol extract was injected for GC–MS analysis. The following experimental conditions to analyze the samples by GC–MS were applied on the PerkinElmer Clarus 500 GC: Elite 5 column (5% biphenyl 95% dimethylpolysiloxane), column size 30 m × 0.32 mm, gas loading – 1 ml/min of helium, column temperature from 50°C to 285°C, a speed of 10°C/min for 5 min, at 285°C, the temperature of the injector, and the detector was 290°C, and the sample is injected split mode, injection volume: 0.5 µl (2 mg/100 ml methanol solution). The total run time was 30 min. Mass spectra were acquired using a PerkinElmer-TurboMass Gold Mass Detector. Transfer line temperature – 230 °C, Source temperature – 230 °C, scan range is from 40 – 450 amu, ionization technique – Electron ionization technique. The component identification was confirmed by comparing mass spectra of compounds with available NIST and Willey mass spectral library. The quantitative composition was obtained by normalizing the peak area (Subasini et al., 2019b).

H. Statistical Analysis

The results are given Mean ±SD, and statistical significance is determined using a one-way analysis of variance using the Duncan's multiple range test. A difference of $P < 0.05$ was

considered significant and the SPSS software (version 12.0) was used for statistical analysis.

III. Results

A. Effect of WS on Triton WR 1339-Induced Hyperlipidemia

Table I shows the results of significant increasing of cholesterol, LDL, and TAG levels ($P < 0.05$) in the rats with Triton WR 1339 administration compared to normal rats. Rats pretreated with extract at 500 mg/kg b.wt. showed no significant hypolipidemic activity, but rats pre-treated with extract at 1000 mg/kg b.wt. for 7 days showed a reduction in cholesterol levels and LDL against a diseased group of rats. Treatment with atorvastatin reduced cholesterol and LDL levels significantly ($P < 0.05$) without changing TAG levels.

B. Effect of WS on Isoproterenol-induced Cardiotoxicity

Isoproterenol administration was observed to raise cholesterol, LDL significantly, and TAG levels in serum while decreasing HDL levels ($P < 0.05$). Treatment of rats with WS extract did not reverse substantially normal cholesterol, LDL, and HDL levels. At a dose of 50 mg/kg b.wt, pre-treating rats with WS extract for 30 days can dramatically reduce TAG levels ($P < 0.05$) in Table II. The level of cardiac markers was considerably higher in the serum of diseased animals and lowered in the heart homogenate ($P < 0.05$). The discharge of cardiac markers was observed to be dramatically reduced ($P < 0.05$) when rats were pre-treated with the extract and the findings are summarized in Table III. In the same way, the amount of TBARS was higher, and the level of antioxidants was found to be lower in the serum and heart homogenate of the diseased group of rats. Pre-treating animals with WS extract can considerably improve antioxidant levels ($P < 0.05$), reduce membrane damage, and reduce the release of TBARS which are shown in Table IV.

C. GC–MS Analysis of WS Extract

GC–MS analysis showed octadecadienoic acid methyl ester and hexadecadienoic acid ethyl ester as the primary compound. It was followed by glycerine, sucrose, and 4H, 1,2,4-Triazol-3-amine-4-propyl as the primary compound in Fig. 1. Other chemical compounds are mentioned in Table V.

Table I
Effect Of Ws Extract And Atorvastatin In Triton Wr 1339-Induced Hyperlipidemic Rats

Groups	Treatment	Cholesterol (mg/dl)	LDL (mg/dl)	TAG (mg/dl)
1	Normal rats	63.5±5.3	40.2±10.5	53.8±10.6
2	Triton WR 1339	878.1±18.2*	678.8±22.1*	675.0±43.3*
3	Atorvastatin (10 mg/kg bw)	473.5±7.5[a]	312.3±3.6[a]	525.1±12.4[ns]
4	Triton WR 1339+WS (500 mg/kg b.wt.)	754.9±28.3[ns]	580.5±32.5[ns]	562.5±23.9[ns]
5	Triton WR 1339+WS (1000 mg/kg b.wt.)	665.3±19.5[a]	479.4±19.8[a]	525.0±14.4[ns]

Values are Mean±SD. n=6. Statistical difference is calculated in one-way ANOVA (LSD) method (least significant difference). *Statistical difference between Group 1 and 2 (P<0.05). [a]Significant difference between Groups 3, 4, and 5 versus Group 2 (P<0.05). ns – No significant difference between specific groups versus Group 2. LDL and TAG: Triacylglycerol, LDL: Low-density lipoprotein

IV. Discussion

The HMG-CoA reductase activity has been reported to have decreased by root powder of WS (Nishant and Narasimhacharya, 2006) at the dose of 750 mg/kg b.wt./day/rat. To evaluate the effect of WS's 70% ethanolic extract, we have selected two different doses with 750 mg/kg/b.wt. as the middle dose. Nishant and Narasimhacharya (2006) have administered drug for 4 weeks. In our present study, we have attempted to evaluate the effect of extract for a shorter duration. Thus for our current study, we have administered extract only for 7 days and compared the same with the effect of the standard drug atorvastatin. Peer et al., 2008, have adopted the diet-induced hyperlipidemia method, whose mechanism of action increases HMG-CoA reductase activity. We have also planned to select a hyperlipidemic model related to the activity of that enzyme. Triton WR 1339 is a surfactant that can induce hyperlipidemic conditions by increasing HMG-CoA reductase activity (Badavi et al., 2020). Moreover, Triton WR 1339 is a widely accepted model for evaluating the effect of hypolipidemic herb (Ipseeta et al., 2004).

The activity of WS extract at 1000 mg/kg b.wt. in Triton WR 1339 caused hyperlipidemic rat is comparable to that of the commercially available standard medication atorvastatin. Atorvastatin treatment was observed to significantly decrease cholesterol and LDL ($P < 0.05$) without effect on TAG. Since the Triton WR 1339 increases the activity of HMG-CoA reductase, the decrement observed in atorvastatin treatment might be due to decreasing the activity of HMG-CoA reductase (Youssef et al., 2002). A comparable activity followed by WS treatment shows that the WS extract inhibits HMG-CoA reductase. It was observed a reduction in HMG-CoA reductase activity (Subasini et al., 2014). The hypolipidemic activity of WS might be due to the presence of polyunsaturated fatty acids in chromatogram GC–MS of the chemical compounds of WS extract (Minihane et al., 2005). Isoproterenol-induced cardiotoxic model is adopted

Table II
Effect Of Ws Extract On Lipid Profile In Isoproternol-Induced Cardiotoxic Rats

Groups	Treatment	Cholesterol (mg/dl)	HDL (mg/dl)	LDL (mg/dl)	TAG (mg/dl)
1	Normal	74.10±4.1	20.30±0.7	40.40±1.2	66.80±4.6
2	ISO	95.20±2.7*	14.80±0.4*	62.80±1.3*	87.80±2.3*
3	WS (50 mg/kg b.wt.)	77.30±2.4[€]	19.70±0.9[€]	44.30±2.3[€]	66.50±5.1[€]
4	ISO+WS (50 mg/kg b.wt.)	86.60±1.7[ns]	16.30±0.7[ns]	58.04±2.3[ns]	61.30±8.9[a]

Values are Mean±SD. n=6. Statistical difference is calculated in one-way ANOVA method (least significant difference). *Statistical difference between Groups 1 and 2 (P<0.05). € – No significant difference between Group 1 versus Group 3. ns – No significant difference between Group 1 versus Group 4. [a]Significant difference (P<0.05) between Group 1 versus Group 4. HDL: High-density lipoprotein, LDL: Low-density lipoprotein, TAG: Triacylglycerol

 http://dx.doi.org/10.14500/aro.10844

Table III
Effect Of Ws On Cardiac Markers In Isoproternol-Induced Cardiotoxicity

Sample	Parameter	Normal	ISO	WS	ISO+WS
Plasma	CK	4.500±0.0300	8.300±0.0300*	4.400±0.0200€	5.800±0.0900
	LDH	0.200±0.0040	0.440±0.0300*	0.240±0.0200€	0.290±0.0070[a]
	GOT	0.050±0.0003	0.080±0.0900*	0.050±0.0200€	0.062±0.0009[a]
	GPT	0.030±0.0009	0.130±0.5000*	0.040±0.0100€	0.050±0.0040[a]
Heart	CK	236.900±4.4000	174.500±3.3000*	239.000±13.0000€	228.800±5.9000[a]
	LDH	2.700±0.0400	1.400±0.0600*	2.600±0.0200€	2.700±0.0900[a]
	GOT	2.300±0.0300	1.400±0.0170*	2.400±0.0160€	2.400±0.0900[a]
	GPT	2.700±0.0600	1.500±0.0300*	2.600±0.0100€	2.900±0.0600[a]

Values are Mean±SD. n=6. Statistical difference is calculated in one-way ANOVA method (least significant difference). *Statistical difference between Groups 1 and 2 (P<0.05). € – No significant difference between Group 1 versus Group 3; [a]significant difference (P<0.05) between Group 1 versus Group 4. One micrograms of phosphorous liberated/min/mg of protein, 2 µg of pyruvate liberated/min/mg of protein. CK: "Creatine kinase," LDH: Lactate dehydrogenase," GOT: "Glutamate oxaloacetate aminotransferase," GPT: "Glutamate pyruvate transaminase"

Table IV
Effect Of Ws On Antioxidants In Isoproternol-Induced Cardiotoxicity

Sample	Parameter	Normal	ISO	WS	ISO+WS
Plasma	TBARS	0.08±0.0005	0.17±0.0002*	0.08±0.0400€	0.11±0.0100[a]
	GSH	4.60±0.0190	2.60±0.0800*	4.20±0.0250€	4.00±0.0400[a]
	GPX	3.60±0.0600	2.70±0.1000*	3.80±0.0400€	3.60±0.0500[a]
Heart	TBARS	0.62±0.0007	0.92±0.0011*	0.64±0.0600€	0.73±0.0100[a]
	GSH	124.60±6.0000	83.60±2.5000*	127.30±11.0000€	102.60±1.7000[a]
	GPX	3.40±0.0800	2.20±0.0400*	3.20±0.0200€	4.10±0.0900[a]
	Catalase	0.50±0.0070	0.20±0.0080*	0.50±0.0100€	0.50±0.0500[a]

Values are Mean±SD. n=6. Statistical difference is calculated in one-way ANOVA method (least significant difference). *Statistical difference between Groups 1 and 2 (P<0.05). € – No significant difference between Group 1 versus Group 3. [a]Significant difference (P<0.05) between Group 1 versus Group 4. One nMol of MDA/mg of protein, 2 µg of GSH/mg of protein, 3 µg of GSH used/min/mg of protein, 4 µMol of H_2O_2 used/min/mg of protein. TBARS: "Thiobarbituric acid reactive substance," GSH: "Reduced glutathione," GPX: Glutathione peroxidase

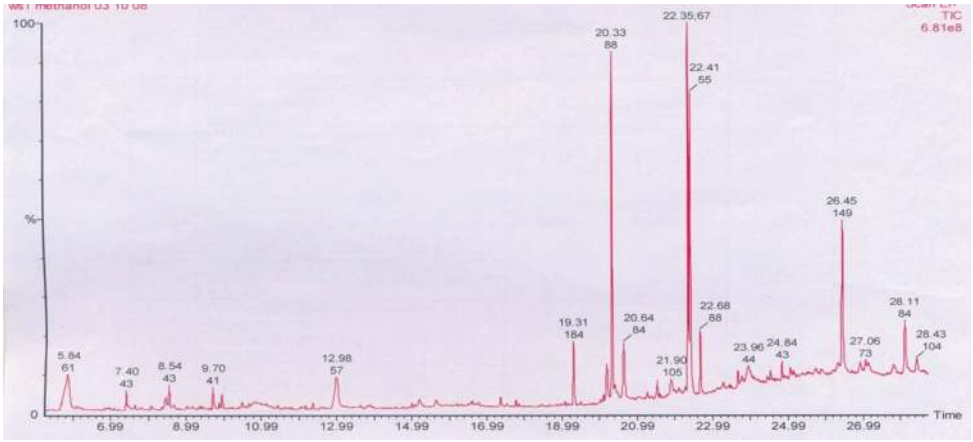

Fig. 1. Chromatogram gas chromatography–mass spectrometer of the chemical compounds of WS extract.

for the present research. The main purpose of selecting this model is to evaluate the myocardial membrane stabilizing effect through antioxidant and hypolipidemic activity of WS's 70% ethanolic extract. Minihane (Minihane et al., 2005) has also suggested that isoproterenol-induced cardiotoxicity is a widely accepted non-invasive model.

The primary purpose of selecting this model is to evaluate the myocardial membrane-stabilizing effect through antioxidant and hypolipidemic activity of WS's 70% ethanolic extract. Isoproterenol-induced cardiotoxicity has been suggested as it is a widely accepted non-invasive mode (Arnaldo et al., 2004). The modulation of oxidative stress by WS root powder has been reported earlier (Saleem et al., 2020). Isoproterenol causes ischemia or oxidative stress but also causes positive inotropic and chronotropic effects on the heart (Fontana et al., 2007). These abnormal conditions lead to the damage of the heart. The deterioration in the heart tissue results in the release of cardiac markers and lipid accumulation in the myocardium (Subasini et al., 2009a). The myocardial membrane can be protected from damage induced by isoproterenol's hazardous nature by a medication having antioxidant action.

A drug that can act as an antioxidant and as a receptor antagonist can prevent the binding of isoproterenol with its receptor and thereby protect the heart from the toxic effect of isoproterenol. Reactive oxygen species are produced

Table V
Gas Chromotography–Mass Spectrometer Peak Table Of *Withania Somnifera*

Signal no.	Peak name	Retention time	% peak area
1	Glycerine	5.84	12.9203
2	2-Pyrazolin-5-one, 1,3,4, trimethyl-	7.40	2.0233
3	Phenylethyl alcohol	8.05	0.3031
4	Tetrahydro-4H-pyran-4-ol	8.34	0.2003
5	3,4-Furandiol, tetrahydro-trans-	8.43	1.8519
6	4H-pyran-4-one, 2,3-Dihydro-3,5-	8.54	2.1537
7	2-Furancarboxaldehyde, 5-(Hydroxymethyl)-	9.70	1.8509
8	1,2,3-Propanetriol, monoacetate	9.94	0.9937
9	Phenol, 3-methyl-5-(1-methylethyl)-ethyl carbamate	10.66	0.2678
10	Sucrose	12.98	9.1228
11	1H-Pyrrole, 2,5-Dihydro-1-nitroso-	13.90	0.5008
12	3-Deoxy-d-mannoic-lactone	15.19	1.6182
13	Phenol-2,4,5-trimethyl-	17.37	0.9368
14	Benzidine, N-Vanilylidene-	19.31	5.1915
15	[1,1'-Bicyclopentyl]-2-one	20.19	3.6974
16	Hexadecanoic acid ethyl ester	20.33	24.2788
17	2-n-Hexylcyclopentanone	20.64	0.0884
18	Octadecanoic acid ethyl ester	21.53	1.4221
19	9,12-Octadecadienoinc acid-ethyl ester	22.35	23.5742
20	4H-1,2,4-Triazol-3-amine-4-Propyl-	28.11	7.0041

by a variety of mechanisms including xanthine oxidase, nicotinamide adenine dinucleotide phosphate oxidases, cytochrome P450, catecholamine auto-oxidation, and nitric oxide (NO) synthase uncoupling NO synthases. Isoproterenol (ISO), a synthetic catecholamine, undergoes oxidation and generates superoxide anion. The superoxide radical initiates the chain reactions and results in free radical intermediates and lipid peroxidation. Drugs with antioxidant qualities may supplement endogenous defense systems and lower both the initiation and propagation of the lipid peroxidation process (Thenmozhi and Subasini, 2016). The decreased TBARS and increased activity of antioxidants observed in the present study might be due to the presence of withanolides (Peer et al., 2008). According to Badavi et al., 2020, ISO causes myocardial infarction in experimental animals by acting on the sarcoplasmic membrane, stimulating adenylate cyclase, activating Na^+ and Ca^{2+} channels, and causing myocardium cell death. The elevated level of marker enzymes in serum may be due to the harm induced by these impacts (Subasini, 2009a). CK level is increased significantly ($P < 0.05$) in serum of diseased rats against normal rats. The results are in line with an earlier reference (Vimal and Devaki, 2004). The decreased level of LDH in heart tissue of diseased rats is in line with a previous referred reference (Saravanan et al., 2011). The reduced activity of LDH prevents the conversion of lactate to pyruvate. As mentioned above, ischemia increases anaerobic glycolysis.

Similarly, the GPT level considerably reduces the cardiac tissue of diseased group of rats. In experimental inflammatory circumstances, Priscilla (Priscilla and Prince, 2009) discovered that enzymatic tissue activities, particularly aminotransferases, increased. The WS extract's mechanism may work by lowering Ca^{2+} inflow and avoiding enzyme leakage by reducing myocardial damage. Still, the mechanism of the protective action of this extract should be evaluated. The decreased release of cardiac markers by WS pre-treatment might be due to various antioxidant activity exhibiting compounds like withanolides (Durg et al., 2015).

Ipseeta et al., 2004, have shown that the WS treatment can prevent the influx of calcium, negative inotropic and chronotropic activity. Moreover, Gupta (Gupta et al., 2004) has explained that ISO causes increased myocardial lipids. It raises LDL cholesterol levels in the blood, causing dangerous deposits to form in the arteries and so favoring coronary heart disease.

In addition, ISO promotes lipolysis in the myocardium (Jasemi et al., 2020, and Ipseeta et al., 2004). Lipolysis results in the release of a large amount of free fatty acids and TAG. The decrement of TAG observed in our present study reveals that WS extract is exhibiting membrane stabilizing activity (Subasini et al., 2009b). GC–MS analysis of methanol-soluble volatile compounds of WS's 70% ethanolic extract has indicated fatty acids such as octadecadienoic acid, methyl ester, and hexadecadienoic acid ethyl ester. The hexadecadienoic acid-ethyl ester with a peak area of 24.27% is present in higher concentrations. The cardioprotective activity of this compound has not been reported earlier. The observed cardioprotective activity in the present study might be due to the presence of octadecadienoic acid, methyl ester, hexadecadienoic acid ethyl ester, and hexadecadienoic acid-ethyl ester. The action might be due to the synergistic action of all the mentioned above compounds. The extract contains sucrose and sucrose administration can induce lipid peroxidation and decrease Cu-Zn SOD (Jerome et al., 2002). The observed antioxidant activity might be due to the presence of other compounds like fatty acids, which are present in higher concentrations (peak area = 23.57%) than that of sucrose (peak area = 9.12%) (Subasini et al., 2007).

V. Conclusion

In Triton WR 1339 generated hyperlipidemic rats, WS has hypolipidemic action by lowering cholesterol and LDL levels. Similarly, WS extract administration decreases cardiotoxicity in isoproterenol-induced cardiotoxic rats through boosting antioxidant levels. Increased antioxidants also reduce TBARS release and cardiac marker release from cardiac tissue. Moreover, the WS extract also reduces the level of TAG in the plasma of isoproterenol administered in rats. The presence of fatty acids detected by the GC–MS spectrum is responsible for the extract's hypolipidemic, cardioprotective, and antioxidant activities.

References

Adams, J.D., Yang, J., Mishra, L.C. and Singh, B.B., 2002. Effects of Ashwagandha in a rat model of stroke. *Alternative Therapies in Health and Medicine*, 8, pp.18-19.

Aebi, H., 1974. Catalase. In: Bergmayer, H.E., (Ed.), *Methods of Enzymatic Analysis*. 2nd ed. Verlag Chemie/Academic Press Inc., Weinheim/NewYork.

pp.673-680.

Arnaldo, P., Silvio, T., Livio, T., Sergio, B., Edgardo, B. and Roberto, A., 2004. Isoproterenol-induced myocardial infarction in rabbits protection by propranolol or labetalol: A proposed non-invasive procedure. *European Journal of Pharmaceutical Sciences*, 23(3), pp.277-285.

Badavi, M., Mard, S.A., Dianat, M. and Dashtbozorgi, N., 2020. Crocin attenuates oxidative stress and inflammation in myocardial infarction induced by isoprenaline via PPARγ activation in diabetic rats. *Journal of Diabetes and Metabolic Disorders*, 19(2), pp.1517-1525.

Boehm, E., Ventura-Clapier, R., Mateo, P., Lechene, P. and Veksler, V., 2000. Glycolysis supports calcium uptake by the sarcoplasmic reticulum in skinned ventricular fibres of mice deficient in mitochondrial and cytosolic creatine kinase. *Journal of Molecular and Cellular Cardiology*, 32, pp.891-902.

Dar, P.A., Singh, L.R., Kamal, M.A. and Dar, T.A., 2016. Unique medicinal properties of *Withania somnifera*: Phytochemical constituents and protein component. *Current Pharmaceutical Design*, 22(5), pp.535-540.

Durg, S., Dhadde, S.B., Vandal, R., Shivakumar, B.S. and Charan, C.S., 2015. *Withania somnifera* (Ashwagandha) in neurobehavioural disorders induced by brain oxidative stress in rodents: A systematic review and meta-analysis. *Journal of Pharmacy and Pharmacology*, 67(7), pp.879-899.

Fontana, M., Olschewski, H., Olschewski, A. and Schlüter, K.D., 2007. Treprostinil potentiates the positive inotropic effect of catecholamines in adult rat ventricular cardiomyocytes. *British Journal of Pharmacology*, 151, pp.779-786.

Foster, L.B. and Dunn, R.T., 1973. Standard reagents for determination of serum triglycerides by colorimetric Hantzch condensation method. *Clinical Chemistry*, 19, pp.338-340.

Friedewald, W.T., Levy, R.I. and Fredirckson, D., 1972. Estimation of the concentration of low-density lipoprotein cholesterol in plasma, without use of the preparative ultracentrifuge. *Clinical Chemistry*, 8, pp.499-502.

Gupta, S.K., Mohanty, I., Talwar, K.K., Dinda, A., Joshi, S., Bansal, P., Saxena, A. and Arya, D.S., 2004. Cardioprotection from ischemia and reperfusion injury by *Withania somnifera*: A hemodynamic, biochemical and histopathological assessment. Mol Cell Biochem., 260 (1-2), pp.39-47. doi: 10.1023/b: mcbi.0000026051.16803.03.

Ipseeta, M., Dharamvir, S.A., Amit, D., Keval, K.T., Sujata, J. and Suresh, K.G., 2004. Mechanisms of cardioprotective effect of *Withania somnifera* in experimentally induced myocardial infarction. Basic and Clinical Pharmacology and Toxicology, 94(4), pp.184-190.

Jasemi, S.V., Khazaei, H., Aneva, I.Y., Farzaei, M.H. and Echeverría, J., 2020. Medicinal plants and phytochemicals for the treatment of pulmonary hypertension. *Frontiers in Pharmacology*, 11, pp.145-166.

Jerome, B., Wioletta, Z., Edmond, R., Yves, R. and Andrzej, M., 2002. Rats fed a high sucrose diet have altered heart antioxidant enzyme activity and gene expression. *Life Science*, 71(11), pp.1303-1312.

King, J., 1959. Colorimetric determination of serum lactate dehydrogenase. *The Journal of Medical Laboratory Technology*., 16, pp.265-269.

Kumari, M., Gupta, R.P., Lather, D. and Bagri, P., 2020. Ameliorating effect of *Withania somnifera* root extract in *Escherichia coli*-infected broilers. *Poultry Science*, 99(4), pp.1875-1887.

Majithiya, J.B., Parmar, A.N. and Balaraman, R., 2004. Effect of curcumin on triton WR 1339 induced hypercholesterolemia in mice. *Indian Journal of Pharmacology*, 36(6), pp.382-383.

Minihane, A.M., Brady, L.M., Lovegrove, S.S., Lesauvage, S.V., Williams, C.M. and Lovegrove, J.A., 2005. Lack of effect of dietary n-6:n-3 PUFA ratio on plasmalipids and markers of insulin responses in Indian Asians living in the UK. *European Journal of Nutrition*, 44(1), pp.26-32.

Mohun, A.F. and Cook, I.J.Y., 1957. Simple method of measuring serum levels of glutamate oxaloacetate and glutamate pyruvate transaminases. *Journal of Clinical Pathology*, 10, pp.374-399.

Moron, M.S., Depierre, J.W. and Mannervik, B., 1979. Levels of glutathione, glutathione reductase and glutathione S-transferase activities in rat lung and liver. *Biochimica et Biophysica Acta*, 528, pp.67-78.

Nishant, P.V., Narasimhacharya, A., 2006. Hypocholesteremic and antioxidant effects of *Withania somnifera* (Dunal) in hypercholesteremic rats. *Phytomedicine*, 14(2-3), pp.136-142.

Ohkawa, H., Ohishi, N. and Yagi, K., 2004. Assay of lipid peroxide in animal tissue by thiobarbituric acid reaction. *Annals of Clinical Biochemistry*, 95(2), pp.351-358.

Paglia, D.E. and Valentine, W.N., 1967. Studies on the quantitative and qualitative characterization of erythrocyte peroxidase. *Journal of Laboratory and Clinical Medicine*, 2, pp.158.

Peer, P.A., Trivedi, P.C., Nigade, P.B., Ghaisas, M.M. and Deshpande, A.D., 2008. Cardioprotective effect of *Azadirachta indica* A. Juss. on isoprenaline induced myocardial infarction in rats. *International Journal of Cardiology*, 126(1), pp.123-126.

Priscilla, D.H. and Prince, P.S., 2009. Cardioprotective effect of gallic acid on cardiac troponin-T, cardiac marker enzymes, lipid peroxidation products and antioxidants in experimentally induced myocardial infarction in Wistar rats. *Chemico-Biological Interactions*, 179(2-3), pp.118-24.

Richmond, W., 1973. Preparation and properties of a cholesterol oxidase from *Nocardia* sp. and its application to the enzymatic assay of total cholesterol in serum. *Clinical Chemistry*, 19, pp.1350-1356.

Saggam, A., Limgaokar, K., Borse, S., Chavan-Gautam, P., Dixit, S., Tillu, G. and Patwardhan, B., 2021. *Withania somnifera* (L.) Dunal: Opportunity for clinical repurposing in COVID-19 management. *Frontiers in Pharmacology*, 12, pp.1-18.

Saleem, S., Muhammad, G., Hussain, M.A., Altaf, M. and Bukhari, S.N.A., 2020. *Withania somnifera* L.: Insights into the phytochemical profile, therapeutic potential, clinical trials, and future prospective. *The Iranian Journal of Basic Medical Sciences*, 23(12), pp.1501-1526.

Saravanan, S., Ramachandran, S., SujaRajapandian, Subasini, U., Victor R.G. and Dubey,G.P., 2011. Anti-atherogenic activity of ethanolic fraction of *Terminalia arjuna* bark on hypercholesterolemic rabbits. *Evidence-Based Complementary and Alternative Medicine*., 2, pp.1-8.

Subasini, U. and Javed, A., 2019. Phytochemical analysis of different fractions of *Terminalia arjuna* bark by GC-MS. *International Research Journal of Pharmacy*, 10(1), pp.42-48.

Subasini, U., 2019. Novel biomarkers of atherogenic diet induced dyslipidemia and metabolic syndrome suppressed by *Terminalia arjuna*. *International Journal of Pharmaceutical Sciences and Research*, 10(5), pp.2528-2536.

Subasini, U., Mohamed, M., Shabi, G.K., Dhevi, R., Ramakrishnan,N., Victor, G., Rajamanickam, G.P. and Dubey, G.P., 2009. Phytochemical evaluation with hypoglycaemic and antioxidant activity of *Tribulus terrestris* Linn. *International Journal of Biomedicine*, 29(2), pp.121-127.

Subasini, U., Rajamanickam, G.V., Dubey, G.P., Prabu, P.C., Sahayam, C.S., Mohammed, S.M., Gayathri, K., Aruna, A., 2007. Hydroalcoholic extract of *Terminalia arjuna*: A potential hepatoprotective herb. *Journal of Biological Sciences*, 2, pp.255-262.

Subasini, U., Sundaraganapathy, R., Narmadha, M.P., Victor, G., Rajamanickam, G.V. and Dubey, G.P., 2009. Cardio-protective effect of polyherbal formulation in isoproterenol induced cardio toxicity. *International Journal of Pharma Research*, 2(3), pp.75-82.

Subasini, U., Thenmozhi, S., Venkateswaran, V., Pavani, P., Sumeet, D. and Victor, R.G., 2014. Phytochemical analysis and anti hyperlipidemic activity of *Nelumbo nucifera* in male wistar rats. *International Journal of Pharmacy Teaching and Practices*, 5(1), pp.935-940.

Thenmozhi, S. and Subasini, U., 2016. Isolation, characterization and *in-vitro* cytotoxic study of vitexin from *Vitex pinnata* Linn. Leaves. *International Journal of Research in Pharmacology and Pharmacotherapeutics*, 1, pp.84-89.

Vimal, V. and Devaki, T., 2004. Linear furanocoumarin protects rat myocardium against lipid peroxidation and membrane damage during experimental myocardial injury. *Biomedicine and Pharmacotherapy*, 58, pp.393-400.

Warnick, G.R., Bederson, J. and Albers, J.J., 1992. Dextran-sulfate-Mg^{2+} precipitation procedure for quantitation of high density lipoprotein cholesterol. *Clinical Chemistry*, 28, pp.13791388.

Youssef, S., Stüve, O., Patarroyo, J.C., Ruiz, P.J., Radosevich, J.L., Hur EM, B.M., Mitchell, D.J., Sobel, R.A., Steinman, L. and Zamvil, S.S., 2002. The HMG-CoA reductase inhibitor, atorvastatin, promotes a Th2 bias and reverses paralysis in central nervous system autoimmune disease. *Nature*, 420(6911), pp.78-84.

http://dx.doi.org/10.14500/aro.10840

Identification and Characterization of Different Types of Plastics Wastes Using X-Ray Diffraction and X-Ray Fluorescence Techniques

Shawbo A. Abubaker, Faten A. Chaqmaqchee and Akram H. Taha

Department of Physics, Faculty of Science and Health, Koya University, Koya KOY45, Kurdistan Region-F.R. Iraq

***Abstract*—In this study, different types of polymers in post-consumer plastics with pure plastics have been studied. High-density polyethylene (HDPE1 and HDPE2), polyvinyl chloride (PVC3 and PVC4), polyethylene terephthalate (PET5 and PET6), and polypropylenes (PP7 and PP8) were compared using X-ray diffraction (XRD) and X-ray fluorescence (XRF) techniques. XRF has shown the spectral in K-lines of polymer materials present in plastics waste. The peak intensity and degree of crystallinity of commercial polymers are varied using XRD analysis. The intensity not attributable to the crystalline peaks may be regarded as the amorphous scattering and used as a template in analyzing the diffraction pattern of the samples. The XRD analysis helps to provide characteristic spectral lines whose intensities vary with the type of each constituent polymer. The combined usage of XRD and XRF techniques yielded very useful and effective results for a commercial plastic management.**

***Index Terms*—Commercial plastics; mass concentrations; polymers X-ray diffraction; X-ray fluorescence.**

I. Introduction

Humans in daily life have benefited from the use of polymers compared with other materials. Polymers are amongst the most important materials with relatively good mechanical and physical properties, which applied to a wide variety of applications (Andrady and Neal, 2009). Plastics are one of the most used materials in the world due to variety of applications such as furniture, clothes, building materials, and automotive components. Plastics have replaced a wide range of traditional materials including glass, steel, wood, and even concrete. According to the chemical structure and processing, plastics are varying their applicability, due to a range of desirable properties such as low density and resistance to a wide range of chemicals (Siddiqui, et al., 2008; Tadayyon, Zebarjad and Sajjadi, 2012). There are important factors contributing the rapid growth of manufacturing and usage of polymeric plastics such as low cost, weigh less, high strength, design flexibility for any shape, and good esthetic goodness. These plastics are generally produced from fossil fuels (Kwong, et al., 2004; Lobo and Bonilla, 2003), and by extending range of products with using plastics continuously, the plastic waste causing pollution. However, with these severe rises in the use of plastic materials, identical development of processes for the harmless degradation of the plastic waste has not been noticed. Recycling of plastic waste has become one of the solutions compared with other materials, due to the full identification and characterization of collected plastics can be a formidable challenge, however, the cost of recycling is high and the recycled products have lower qualities (Chaqmaqchee, Baker and Salih, 2017). Nowadays, polyethylene terephthalate (PET) is the most common plastic and has significant applications in industry such as drug and food packaging (Han, 2019). PET accounts for roughly 40% of all plastic made in the world (Andrady and Neal, 2009; Alnaimi, Elouadi, and Kamal, 2015). Among all PET types, high-density polyethylene (HDPE) contains carbon and hydrogen as fundamental elements. It also has stronger intermolecular forces with higher tensile strength than PET (Prasad, De and De, 2011). Physically, it is harder, opaquer, with a high degree of crystalline structure that can resist somewhat higher temperatures with extensive industrial applications. For example, HDPE pipes are used to carry potable water, waste water, cables, and transportation of oil and compressed gases (Tadayyon, Zebarjad and Sajjadi, 2012). In addition, polypropylene (PP) is widely used in many fields, including floor coverings, automobiles, building materials, electronics and electric materials, wall coverings (Singh, et al., 2017). However, poor thermal stability and fire resistance of PP limit the status and range of its practical application (Sajwan, Singh and Aggarwal, 2007). Among the different commodity polymers, polyvinyl chloride (PVC) is a versatile and most extensively used along with polyethylene due to its industrial applications and academic interests. PVC has many applications in construction, medicine, window, and door (Wang, Zhang and Zhou, 2017; Pan, et al., 2004).

The aim of this study is to characterize different types of plastics including HDPE (HDPE1 and HDPE2), PVC (PVC3 and PVC4), PET (PET5 and PET6), and PPs (PP7 and PP8). X-ray diffraction (XRD) and X-ray fluorescence (XRF)

ARO-The Scientific Journal of Koya University
Vol. IX, No.2 (2021), Article ID: ARO.10840, 4 pages
DOI: 10.14500/aro.10840
Received 11 July 2021; Accepted: 25 September 2021
Regular research paper: Published 28 October 2021
Corresponding author's, e-mail: shawbo.abdulsamad@koyauniversity.org

techniques were used as relative ease of use, fast sample preparation and analysis, minimal recalibration, a broad range of detectable elements, and a broad concentration range for analysis. The morphological features of semi-crystalline polymers such as crystalline level and crystal thickness are mainly decided by the nature of the polymer. Thus, XRD and XRF are two successful techniques for performing material analysis without changing structure avoid any damage, non-destructive, and exact qualitative and quantitative analysis and suited for real-world plastics recycling environments (Kubala-Kuku, et al., 2013).

II. Materials and Methods

The morphological features of semi-crystalline polymers such as crystalline level and crystal thickness are mainly decided by the nature of the polymer. XRD and XRF are two successful techniques for performing material analysis (Sabri, 2020) without changing structure, avoid any damage, non-destructive, and exact qualitative and quantitative analysis. Four pure polymer materials of around 11 g of HDPE1, PVC1, PET1, and PP1 and four commercial plastics of size 2 × 2 cm^2 of HDPE2, PVC2, PET2, and PP2 have been collected from different companies of Erbil and Sulaymaniyah in the Iraqi Kurdistan region. XRD technique was used to determine the peak position and it is operating at 45 kV and 40 mA and can perform various analyses from phase identification and quantification to determine the phases and the morphological properties of the sample and to compare of complex chemical materials structures (Song, et al., 2016).

In addition, the bonding nature of plastics can be analyzed using XRF technique, which is an effective approach to distinguish plastic sorting quantitative and the elemental concentration and their emitted energies for all plastics samples. All measurements were carried out under vacuum, using a Rigaku NEX CG with RX9, Mo, Cu, and Al targets. Chemical elements with a high and a low concentration were detected with the samples. The XRF K^{α} and K^{β} line intensities were measured for the all eight samples' elements, in which the applied voltage increased in general with the required lines energies. The X-ray measuring time was only 200 s for the Al target and 100 s for the other targets. X-rays from the X-ray tube pass through an optional filter on their way to the samples that placed in the chamber and measured by 20 mm diaphragm in vacuum. The X-rays then travel from the sample to the detector, which is cooled electrically. The signal is then processed by electronics and sent to a computer program, where the chemical compositions and intensity versus energy are measured.

III. Results and Discussion

Structural analysis of pure HDPE1, PVC1, PET1, and PP1 and commercial HDPE2, PVC2, PET2, and PP2 was carried out by XRD analytical under 45 kV/40 mA–X-ray, 2θ/θ-Scanning mode as shown in Fig. 1. Data were taken

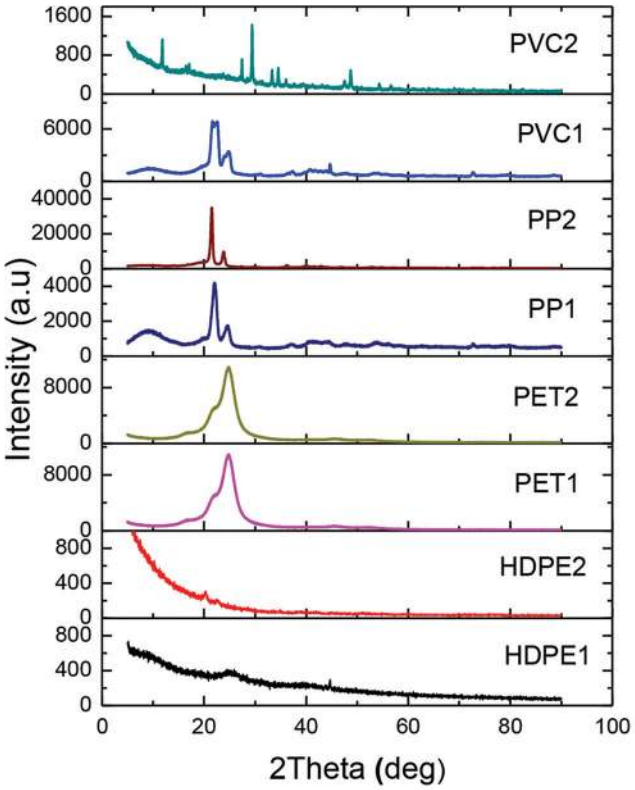

Fig. 1. A compression X-ray diffraction spectra of pure high-density polyethylene (HDPE), polyethylene terephthalate (PET), polypropylenes (PP), and polyvinyl chloride (PVC) with commercial HDPE, PET, PP, and PVC polymers.

for the 2θ range of 0–90° with a step of 0.012°. The XRD spectra of HDPE1, HDPE12 and PET1, PET 2 polymers have not shown large distinguishable differences. However, PP1, PP2 and PET1, PET2 show different characteristic, this is due to the amount of elements added during production. For each polymer, a unique spectral line of XRD is available for identification. The XRD pattern of HDPE that taken from water pipe as sample is based on the spectral line near 2θ = 25°. The analysis crystal structure indicates that the HDPE is orthorhombic structure, monoclinic and hexagonal, depending on the processing conditions. Some small peaks are also apparent at angles larger than 40° (Hasan, Banerjee and Lee, 2015). For the PET1, a broad peak at the 2θ = 24.8° was observed, which clearly shows its poor crystallinity due to the high integrated area, while the XRD patterns for PET2, have 2θ in the range of 20–25°, one strong peak operating at 24.8° and one moderately peak at 22.02°. For pure PP1, the amorphous nature has a broad peak in the region of 10–25°, whereas for PP2 has more intensive peak at around 21.49°, hence more crystalline. In addition, the maximum peak of pure PVC1 was around 22.02°. The PVC2 that taken from door as sample shows more peaks compared to the pure PVC1 due to the addition of different amount elements to it. The intensity and the width of each peak are different, depending on the samples. These peaks are due to XRD from the superimposed on a broad region of intensity which results from the amorphous component of the polymer (polymers

http://dx.doi.org/10.14500/aro.10840

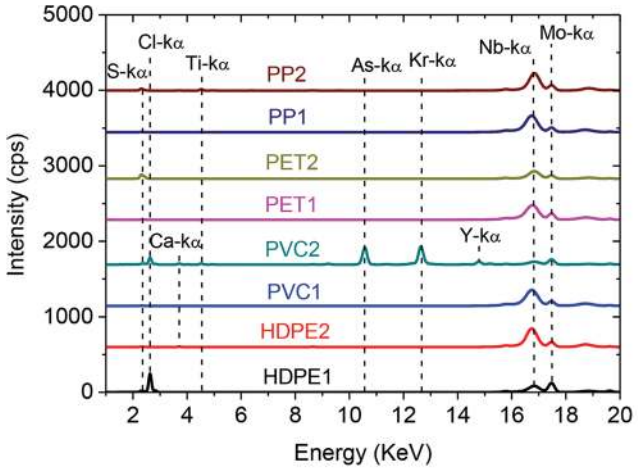

Fig. 2. Intensity versus energy for various pure polymers (high-density polyethylene [HDPE1], polyvinyl chloride [PVC1], polyethylene terephthalate [PET1], and polypropylenes [PP1]) and commercial plastics (HDPE2, PVC2, PET2, and PP2) calculated over the energy range from 1 to 20 KeV using XRF with RX9, Mo, Cu, and Al targets.

are usually not 100% crystalline) (Kwong, et al., 2004). In Table 1, the peak intensity and crystalline size for each maximum peak have been estimated using Debye-Scherrer formula (Lin, et al., 2005; Mote, Purushotham and Dole, 2012; Parvin, et al., 2013).

$$t = \frac{0.9\lambda}{\beta \cos\theta} \quad (1)$$

Where, λ, β, θ, and t are the wavelength of X-ray (1.5406 Å), the full width at half maximum, the diffraction angle, and the particle diameter size, respectively.

Rigaku NEX CG XRF spectrometer analyses were used to determine HDPE1, PVC1, PET1, and PP as well as the commercial plastics HDPE2, PVC2, PET2, and PP2. When these samples are irradiated with X-rays, the intensity as a function of energy can be calculated over the energy range of 1–40 keV at the same computing conditions. Fig. 2 shows the peaks in the ranges of 2.65, 4.51, 10.58, 12.63, 14.79, 16.83, and 17.48 keV corresponding to S-kα, Cl-kα, Ca-kβ, Ti-kα, As-kr, Nb-kα, and Mo-kα lines. It shows clearly that the highest peak intensities appear with Cl-kα line in HDPE1 of pure sample, and with As-kα and Kr-kα lines in PVC2 of door sample, and finally with Nb-kα line for almost all the eight samples.

Furthermore, the chemical compositions for four polymer samples of HDPE1, PVC1, PET1, and PP1 underwent analysis, along with four commercial plastics samples of HDPE2, PVC2, PET2, and PP2 using XRF. The raw and processed data are listed in Table 2, where the elements are distributed in the random samples. The total percentages of the eight samples were less and more than 100% due to the statistical errors during measurements. Element of Cl appears with high mass percentage at around 53.9 and 93.2 Mg/cm^2 in HDPE1 and PVC2, respectively, whereas other elements appear with low mass concentration, and has good agreement with Fig. 2. The mass concentration of propene PP appears to be high in the six samples, which is highly hazardous in daily use. PP has a good chemical and heat resistance and can be used in household and industrial applications (Chen, et al., 2020).

Table I
Intensity, Crystalline Size, and d Spacing of the Most Intense Peak of the Samples

2θo of the intense peak pure polymer	Intensity (cps)	FWHM (°)	Crystalline size (Å)
25.33 (HDPE1)	392.4926	0.614	2.5
24.688 (PET1)	10,751.261	0.80	1.90
21.949 (PP1)	3346.55	0.358	4.17
21.54 (PVC1)	5312.01	0.179	8.32

FWHM: Full width at half maximum, HDPE: High-density polyethylene, PET: Polyethylene terephthalate, PP: Polypropylenes, PVC: Polyvinyl chloride

Table II
XRF Measurements for Elements of Plastics (%), Where the Totals 100%±0.05 Statistical Errors

No.	Elements	Plastics mass concentration % Mg/cm^2							
		HDPE1	HDPE2	PVC1	PVC2	PET1	PET2	PP1	PP2
1	Cl	53.9	0.018	0.0072	93.2	0.0030	0.0012	0.0515	0.0218
2	pp	45.7	99.7	99.8	--	99.8	100.0	99.7	99.7
3	Si	0.273	--	0.0478	0.877	0.0212	0.0037	0.0275	0.0284
4	P	0.103	0.001	0.0047	0.293	0.0012	0.0015	0.0027	0.0050
5	Ca	0.0510	0.213	0.0161	2.73	0.0025	0.0023	0.0150	0.0453
6	Sn	0.0065	0.0025	0.0046	0.0021	0.0066	0.0006	0.0042	0.0012
7	Ti	0.0037	0.0215	0.0004	1.38	--	--	0.0003	0.146
8	V	0.0025	--	--	--	--	--	--	--
9	Fe	0.0024	0.0014	--	0.0057	--	0.0003	--	0.0006
10	Cu	0.0008	0.0005	0.0002	--	0.0001	0.0001	0.0002	0.0001
11	Br	0.0002	0.0001	--	--	--	--	--	--
12	S	--	0.0248	0.0152	0.439	0.0181	0.0023	0.0174	0.0031
13	Al	--	0.0107	0.0261	--	0.0098	--	0.0189	0.0477
14	Zn	--	0.0028	--	0.0073	--	--	0.0001	0.0009
15	K	--	0.0007	0.0019	--	0.0006	--	0.0018	--
16	Pb	--	0.0004	--	0.992	--	--	--	--
17	Cr	--	0.0001	0.0007	--	--	--	--	0.0001
18	Mg	--	--	0.0652	--	0.0890	--	0.122	--
19	Bi	--	--	--	0.0051	--	--	--	--
20	Y	--	--	--	0.0038	--	--	--	--
21	Sr	--	--	--	0.0013	--	--	--	--
22	Sb	--	--	--	--	0.0438	0.0050	--	--
23	Co	--	--	--	--	0.0003	0.0003	--	--
24	Mn	--	--	--	--	--	0.0001	--	--
25	Hf	--	--	--	--	--	0.0001	--	0.0001

FWHM: Full width at half maximum, HDPE: High-density polyethylene, PET: Polyethylene terephthalate, PP: Polypropylenes, PVC: Polyvinyl chloride, X-ray fluorescence

IV. Conclusion

In this study, we demonstrated the application of XRD and XRF for the identification of various types of plastics presented in the waste that is dangerous to the health and the environment. The robustness of these techniques was explained by reliable and repeatable results analyzed for different polymers. The XRD analysis indicated that both pure polymers and plastic wastes have amorphous nature. The structure of commercial plastics as examined by the XRD technique reveals different materials added to the pure polymers in which confirmed the presence by XRF

techniques. The existence of additional peaks at various diffraction angles in XRD spectra of plastic wastes is due to variation in the crystallization during the manufacturing procedure, diverse additives, and their ratio in the sample. Results show that containing different elements effectively improved the crystallization properties of PVC2, PP2, without changing the crystalline structure of them. However, in plastics production elements such as chloride, ethylene dichloride, lead, cadmium, and other toxic chemicals were observed in most of them. Commercial PVC shows the higher ratio of ~ 0.992 lead and ~ 2.73 cadmium, which is widely known as the most toxic elements that cause health problems for human and animal health and environment as a whole. It can also be concluded that the XRD and XRF studies of HDPE1, PP1, PET1, PVC1 and HDPE2, PP2, PET2, PVC2 that acquired from different manufacturer reveal their prominent forensic characterization future. The combined uses of XRD and XRF techniques have excellent potential for rapid identification and analysis of plastics as well as they are benefit for recycling and management of plastic waste.

V. Acknowledgment

The authors gratefully acknowledge the Department of Physics, Faculty of Science and Health at Koya University for enabling this study.

References

Alnaimi, S., Elouadi, B. and Kamal. I., 2015. Structural, thermal and morphology characteristics of low density polyethylene produced by QAPCO. *In Proceedings of the 8th International Symposium on Inorganic Phosphate Materials*, Agadir, Morocco.

Andrady, A.L. and Neal, M.A., 2009. Applications and societal benefits of plastics. *Philosophical Transactions of the Royal Society B: Biological Sciences*, 364(1526), pp.1977-1984.

Chaqmaqchee, F.A.I., Baker, A.G. and Salih, N.F., 2017. Comparison of various plastics wastes using X-ray fluorescence. *American Journal of Materials Synthesis and Processing*, 2(2), pp.24-27.

Chen, D.M.C., Bodirsky, B.L., Krueger, T., Mishra, A. and Popp, A., 2020. The world's growing municipal solid waste: Trends and impacts. *Environmental Research Letters*, 15, pp.1-12.

Han, M., 2019. Depolymerization of PET bottle via methanolysis and hydrolysis. In: *Recycling of Polyethylene Terephthalate Bottles*, William Andrew Publishing, Burlington, MA, pp.85-108.

Hasan, M., Banerjee, A.N. and Lee, M., 2015. Enhanced thermo-mechanical performance and strain-induced band gap reduction of TiO_2@ PVC nanocomposite films. *Bulletin of Materials Science*, 38(2), pp.283-290.

Kubala-Kukuś, A., Ludwikowska-Kędzia, M., Banaś, D., Braziewicz, J., Majewska, U., Pajek, M. and Wudarczyk-Moćko, J., 2013. Application of the X-ray fluorescence analysis and X-ray diffraction in geochemical studies of the Pleistocene tills from Holy Cross Mountains. *Radiation Physics and Chemistry*, 93, pp.92-98.

Kwong, C., Choy, W.C.H, Djurišić, A.B, Chui, P.C., Cheng, K.W. and Chan, W.K., 2004. Poly (3-hexylthiophene): TiO_2 nanocomposites for solar cell applications. *Nanotechnology*, 15(9), p.1156.

Lin, Y., Du, W., Tu, D., Zhong, W. and Du, Q., 2005. Space charge distribution and crystalline structure in low density polyethylene (LDPE) blended with high density polyethylene (HDPE). *Polymer International*, 54(2), pp.465-470.

Lobo, H. and Bonilla, J.V., 2003. General introduction to plastics analysis. *Plastics Engineering New York*, 68, pp.1-42.

Mote, V., Purushotham, Y. and Dole, B., 2012. Williamson-Hall analysis in estimation of lattice strain in nanometer-sized ZnO particles. *Journal of Theoretical and Applied Physics*, 6(1), pp.1-8.

Pan, M., Shi, X., Li, X., Hu, H., Zhang, L., 2004. Morphology and properties of PVC/clay nanocomposites via in situ emulsion polymerization. *Journal of Applied Polymer Science*, 94(1), pp.277-286.

Parvin, N., Ullah, M.S., Mina, M.F.G. and afur, M.A., 2013. Structures and mechanical properties of talc and carbon black reinforced high density polyethylene composites: Effects of organic and inorganic fillers. *Journal of Bangladesh academy of Sciences*, 37(1), pp.11-20.

Prasad, S.G., De, A. and De, U., 2011. Structural and optical investigations of radiation damage in transparent PET polymer films. *International Journal of Spectroscopy*, 2011, p.810936.

Sabri, M.M, 2020. Chemical and structural analysis of rocks using X-ray fluorescence and X-ray diffraction techniques. *ARO The Scientific Journal of Koya University*, 8(1), pp.79-87.

Sajwan, M.B., Singh, R. and Aggarwal, S., 2007. Characterization of plastic pipes by X-ray diffraction in forensic analysis. *Indian Journal of Criminology and Criminalistics*, 28, pp.76-81.

Siddiqui, M.N., Gondal, M.A. and Redhwi, H.H., 2008. Identification of different type of polymers in plastics waste. *Journal of Environmental Science and Health, Part A*, 43(11), pp.1303-1310.

Singh, N., Hui, D., Singh, R., Ahuja, I.P.S., Feo, L. and Fraternali, F., 2017. Recycling of plastic solid waste: A state of art review and future applications. *Composites Part B: Engineering*, 115, pp.409-422.

Song, W., Sun, Z., Zhang, D., Han, B., He, L., Wang, X. and Lei, Q., 2016. Synthesis and characterization of low density polyethylene with multiferroic bismuth ferrite nanocomposite. *Journal of Materials Science: Materials in Electronics*, 27(3), pp.2328-2334.

Tadayyon, G., Zebarjad, S.M. and Sajjadi, S.A., 2012. Effect of both nano-size alumina particles and severe deformation on polyethylene crystallinity index. *Journal of Thermoplastic Composite Materials*, 25(4), pp.479-490.

Wang, L., Zhang, M. and Zhou, B., 2017. Thermal stability, combustion behavior, and mechanical property in a flame-retardant polypropylene system. *Applied Sciences*, 7(1), p.55.

 http://dx.doi.org/10.14500/aro.10846

A Comparison of Top Distributed Bragg Reflector for 1300 nm Vertical Cavity Semiconductor Optical Amplifiers Based on III–V Compound

Shawbo A. Abubaker

Department of Physics, Faculty of Science and Health, Koya University, Koya KOY45, Kurdistan Region-F.R. Iraq

***Abstract*—In this work, the design of GaAs/AlGaAs distributed Bragg reflector (DBR) has been implemented for 1300 nm vertical cavity semiconductor optical amplifiers)VCSOAs(for optical fiber communication applications. The top DBR period and Al concentration are varied, the peak reflectivity of the DBR is increasing from 50% to 97.5% for 13 periods with increasing Al concentration, whereas the reflectivity bandwidth is increased to almost 190 nm. The relation between wavelength and incidence angle variation on DBR reflectivity is increasing with the incident angle (0°, 20°, 30°, and 50°), the resonant wavelength and bandwidth of the measured reflectance spectra shifts to shorter wavelength and wider bandwidth, respectively. In addition, a comparison between the linear, the graded, and the parabolic DBRs has been achieved with transfer matrix method using MATLAB software to show the influence of layer in DBRs and its effect on lasing wavelength. It is shown that using grading DBR mirror is much more beneficial compared to abrupt DBR, whereas it has lower reflectivity of almost 10% due to VCSOAs device which needs less number of top layers until prevent reaching lasing threshold.**

***Index Terms* — Vertical cavity semiconductor optical amplifiers; distributed Bragg reflector; abrupt and grading distributed Bragg reflector.**

I. Introduction

III–V compound semiconductors have played a critical role in modern electronic and optoelectronic device technologies. They have many potential applications, pervading our everyday lives in optical communication systems, computing, entertainment, lighting, and medicine (Tu and Paul, 2003; Kuech, 2016; Hasnayeen, Othman and Faidz, 2008). Recently, vertical cavity semiconductor optical amplifier (VCSOA) has been developed, for applications including optical communications and optical interconnection systems (Bjorlin et al., 2001; Chaqmaqchee, 2015). Reports and data have shown that VCSOAs at 1300 nm have focused on DBRs and multi-quantum well active regions, structures such as GaInNAs/GaAs were optically pumped through the GaAs substrate (Chaqmaqchee et al., 2012; Chaqmaqchee, Salh and Sabri, 2020). Nevertheless, incorporation antimony GaInNAsSb/GaAs to the active regions provides important advantages for developing 1300 nm vertical cavity devices, such as monolithic integration with the GaAs/AlGaAs distributed Bragg reflectors (DBR) and improved optical behavior (Chaqmaqchee, Salh and Sabri, 2020). VCSOA consists of a vertical cavity mode formed by placing an active region between two DBRs, the operation of the surface emitting semiconductor optical amplifier depends heavily on the performance and design of Bragg mirror. As its particular vertical structure, the VCSOA has a very small active region, small length of the cavity, therefore, the top and bottom DBRs should have high reflectivity, to be able to obtain a long wavelength VCSOAs (Chen, et al., 2020; Hurtado, Gonzalez-Marcos and Martin-Pereda, 2005). DBRs, which consist of a periodic quarter-wave layers with alternating high and low refractive index materials that work as a highly reflecting mirror for optical as well as electrical confinement in the active region, have an important role in optoelectronic devices. DBRs are a set of two highly reflecting mirrors of semiconductor compounds, generally III–V materials, these mirrors are named as quarter wavelength mirrors because the thickness of each layer equals to the one-quarter wavelength of the light travelling inside the mirror material (Mishkat-Ul-Masabih, et al., 2019; Choquette and Hou, 1997; Winston and Hayes, 1998). This study will report and analyze the influence of Al composition, number of layers in the DBR, effects of thickness layers, and incident angle variation due to optical properties through reflectivity.

II. Design and Simulation Modeling Method

The VCSOAs structure is modified version of vertical cavity surface emitting lasers (VCSELs) (Piprek, Bjorlin and Bowers, 2001; Chaqmaqchee, 2016) that driven below threshold current. In this paper, the VCSOA design is modified as shown in Fig. 1. The structure consists of

ARO-The Scientific Journal of Koya University
Vol. IX, No.2 (2021), Article ID: ARO.10846, 4 pages
DOI: 10.14500/aro.10846
Received: 02 August 2021; Accepted: 11 October 2021
Regular research paper; Published: 28 October 2021
Corresponding author's email: shawbo.abdulsamad@koyauniversity.org

13 pairs of top and 24.5 pairs of bottom DBR mirrors. The active region consists of three QW $Ga_{0.6}In_{0.4}N_{0.027}As_{0.9605}Sb_{0.0125}$/GaAs. The reflectance R and transmittance T are calculated according to transfer matrix method (Sanchez, Cerutti and Tournié, 2013, Karim, et al., 2000, Yu, 2003):

Eqs. 1 and 2 are used for determine the reflectivity (R) and transmittance (T) of the DBR.

$$R = \left| \frac{\mu_{0B-C}}{\mu_0 B + C} \right|^2 \quad (1)$$

$$T = \frac{4\mu_0 \bar{\mu}_m}{\left|\mu_{0B+C}\right|^2} \quad (2)$$

Where, μ_o is incident admittance, μ_m is optical admittance of the substrate, B and C are the total electric and magnetic field amplitude method (Karim, et al., 2000).

The VCSOAs with variation of DBR composition are studied with different samples studies for DBR of surface-emitting lasers. Each pair differs in refractive index and thickness, GaAs as a high refractive index layer $Al_xGa_{1-x}As$, and AlAs as a low refractive index of layer, with different x composition. Details of the parameters for each sample are shown in Table 1. In the DBRs structure, the top and the bottom DBRs are designed with 13 periods and 24.5 periods, respectively. In this work, a simulation was done to compare the reflectivity of different semiconductor materials each one of these samples reflectivity and bandwidth is varies according to the number of alternating layer pairs and refractive index contrast between layers. In performing VCSOAs DBR, refractive index and lack of GaAs lattice matched in DBR material are critical properties that need to be considered.

Table I
DBR mirror with various Al composition

Sample	Materials	Al composition (wt.%)
1	GaAs/AlAs	1
2	GaAs/$Al_{0.9}Ga_{0.1}As$	0.9
3	GaAs/$Al_{0.7}Ga_{0.3}As$	0.7
4	GaAs/$Al_{0.5}Ga_{0.5}As$	0.5
5	GaAs/$Al_{0.3}Ga_{0.7}As$	0.3
6	GaAs/$Al_{0.2}Ga_{0.8}As$	0.2

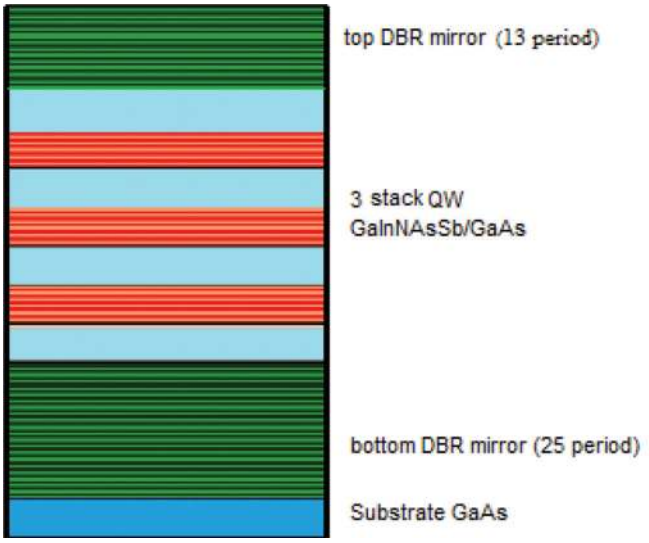

Fig. 1: The structure of vertical cavity semiconductor optical amplifiers.

In this paper, two types of DBRs were studied, the first one is called linear (abrupt) DBRs and the second is graded DBRs, as shown in Fig. 2. Table 2 shows the design of p-type for linear and graded DBRs. Table 2a shows the design of abrupt (linear) DBR with 13 periods of GaAs and $Al_{0.9}$ $Ga_{0.1}$ As p-doped layers, beryllium doped with concentration of 3×10^{18} cm^1. Abrupt (linear) DBR was used to achieve a high index contrast as well as provide good thermal conductivity, which is also one of the necessary requirements for material used to design a VCSOA structure. Table 2 shows the design of graded DBR, which made by inserting an intermediate layer $Al_{0.1}$ $Ga_{0.9}As$ between GaAs and $Al_{0.9}$ $Ga_{0.1}As$. The DBR composition ramped continuously from $Al_{0.1}$ $Ga_{0.9}As$ to $Al_{0.9}$ $Ga_{0.1}As$. In addition, the layer thickness of 10 nm doped GaAs cap is used in DBR to protect the sample and to make the electrical contact between the DBRs structure and the metal contact much easier.

III. Results and Discussion

The reflectivity spectrum of different Al composition of top DBR is shown in Fig. 3, whereas the reflectivity of GaAs/AlGaAs with different periods (10, 13, and 16) is shown in Fig. 4. The result shows that reflectivity increases when Al concentration

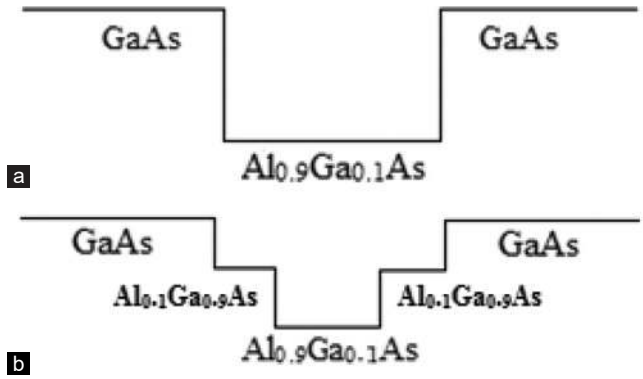

Fig. 2: GaAs/AlGaAs DBR structure : a) the basic reflector design (abrupt), and b) addition of intermediate layer (graded).

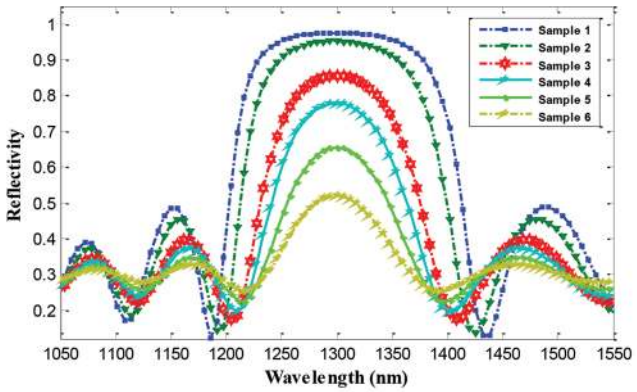

Fig. 3: Reflectivity spectrum of DBR for various Al composition of 13 top layers.

http://dx.doi.org/10.14500/aro.10846

increases. Sample 1, GaAs/AlAs exhibits the highest reflectivity and the largest stopband width which is around 200 nm due to the highest refractive index between low and high refractive index materials of DBR followed by the sample 2 to the last one sample 6 which is GaAs/$Al_{0.2}Ga_{0.8}As$. Nevertheless, reflectivity of the DBR increases with increasing number of DBR layers. These graphs show that the peak maximum increase with increasing the number of layers also with increasing refractive index contrast for 13 periods of DBR AlAs/GaAs have the higher reflectivity of 97.5% at 1300 nm, whereas reflectivity at 1300 nm for $Al_{0.9}Ga_{0.1}As$/GaAs DBR is 95.1%.

Fig. 5 shows the reflectivity spectra of DBR under various incident angles of 0°, 15°, 30°, and 50°. From the dependent angle results, we can obtain the wavelength of the stopband center of the DBRs. It can be seen that with increasing incident angle, the stopband center shifts toward the shorter wavelength. However, the reflectivity becomes high, and in Fig. 6, several interests can be seen that at angle of 0° for AlGaAs/GaAs layers, the bandwidth of the stopband is narrowed and the resonant wavelength shifts toward longer wavelength with lower reflectivity compared to AlAs/GaAs DBRs. Thus, the phase of a DBR is zero or pi response in the center wavelength of the reflection stopband. As the angle of incidence increased, the resonant wavelength decreased.

Fig. 7 displays the variation of reflectivity as a function of wavelength for abrupt and graded DBR with using different material was determined. It can be seen that the reflectivity of graded DBR for both of them GaAs/AlAs and GaAs/AlGaAs is lower compared to the abrupt DBR GaAs/$Al_{0.2}Ga_{0.8}As$/AlAs and GaAs/$Al_{0.1}Ga_{0.9}As$/$Al_{0.1}Ga_{0.9}As$ with increasing the intermediate layer forgraded DBR reduce the potential energy barriers for majority carriers, hence reducing the resistance and self-heating nevertheless influence the reflectivity of the

Table II
P-type DBRs Structures: (a) Linear DBR (b) Graded DBR

(a)	
Material	Layer thickness (nm)
GaAs cap	10
GaAs	94
$Al_{0.9}$ $Ga_{0.1}$ As	109
GaAs substrate	
Total layers thickness=2852 nm (for 13 periods)	
(B)	
Material	Layer thickness (nm)
GaAs cap	10
GaAs	94
$Al_{0.1}$ $Ga_{0.9}$ As	92
$Al_{0.9}$ $Ga_{0.1}$ As	109
$Al_{0.1}$ $Ga_{0.9}$ As	92
GaAs substrate	

Total layers thickness=5041 nm (for 13 periods)

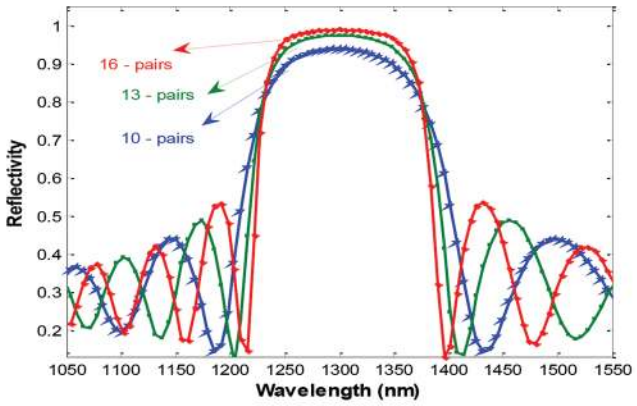

Fig. 4. Reflectivity spectrum of distributed Bragg reflector for three different layers of $Al_{0.9}Ga_{0.1}As$.

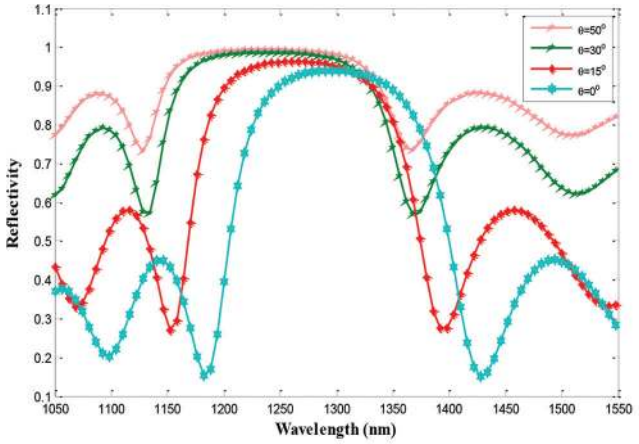

Fig. 5: Reflectivity of a distributed Bragg reflector calculated for a different incident angle.

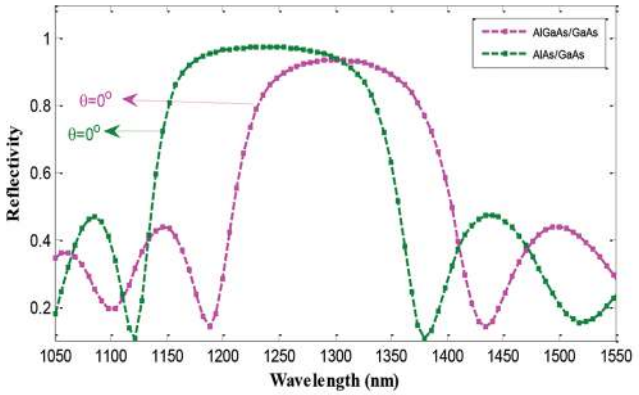

Fig. 6: Reflectivity of a DBR calculated for different materials at same angle

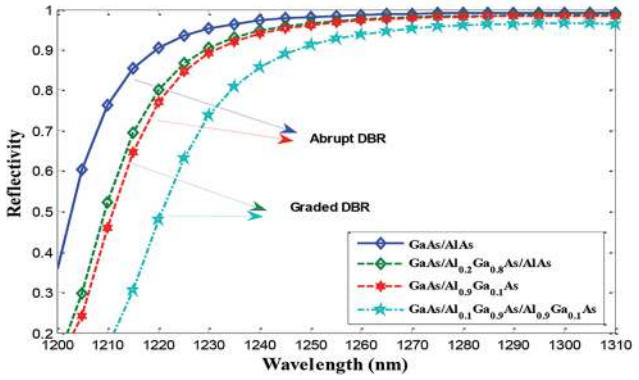

Fig. 7: Comparison of the abrupt and the graded reflectivity spectra for different materials with fixed 13 pairs top distributed Bragg reflector.

device. This variation in Al composition causes the decreasing reflectivity spectrum and bandwidth of graded DBR is more suitable for operating VCSOA devices, compared to the VCSELs which require the higher reflectivity of the top DBR until it gets to the lasing wavelength. To reach the reflectivity of more than 99%, more than 13 pairs of DBRs are required for graded DBR compared to the linear DBR. However, using AlAs in DBR mirrors the reflectivity of the device increased either in linear and graded DBR compared to the AlGaAs, this is due to decreasing the refractive index contrast between layers and the intermediate layer being more prominent with the structure which influence the relative barrier high.

IV. Conclusion

An analytical simulation method for the change of reflectivity, wavelength of DBR, and VCSOAs reflective mode operation, stopband, and incidence angle variation for DBR-based VCSOAs has been studied. High reflective mirror was obtained which are 97.5% for GaAs/AlAs, $Al_{0.9}Ga_{0.1}As$/GaAs DBR is 95.1% decreased with decreasing Al concentration to almost 50%. With increasing incident angle of light beam, the band center shifts toward shorter wavelength, also its depend on the material. It was observed that increasing intermediate layers using grading junction DBR resulting in a decreasing reflectivity due to decreasing the potential barriers which is more suitable for performance of VCSOAs. The simulation results show that the higher refractive indices contrast, incident angle and periodic number of DBR layer will cause an increase in reflectivity, and decrease the depth of cavity mode (resonant cavity).

Acknowledgment

The author would like to thank Assist. Prof Dr. Faten A Ismael for her valuable comments during data analysis.

References

Bjorlin, E.S., Riou, B., Abraham, P., Piprek, J., Chiu, Y.Y., Black, K.A., Keating, A. and Bowers, J.E., 2001. Long wavelength vertical-cavity semiconductor optical amplifiers. *IEEE Journal of Quantum Electronics*, 37(2), pp.274-281.

Chaqmaqchee, F., Mazzucato, S., Sun, Y., Balkan, N., Tiras, E., Hugues, M. and Hopkinson, M., 2012. "Electrical characterisation of p-doped distributed Bragg reflectors in electrically pumped GaInNAs VCSOAs for 1.3 μm operation. *Materials Science and Engineering: B*, 177(10), pp.739-743.

Chaqmaqchee, F.A., 2016. Optical design of dilute nitride quantum wells vertical cavity semiconductor optical amplifiers for communication systems. *ARO The Scientific Journal of Koya University*, 4(1), pp.8-12.

Chaqmaqchee, F.A.I., 2015. Optical amplification in dilute nitride hot electron light emission-VCSOAs devices. *Arabian Journal for Science and Engineering*, 40(7), pp.2111-2115.

Chaqmaqchee, F.A.I., Salh, S.A.A. and Sabri, M.F.M., 2020. Optical analysis of 1300 nm GaInNAsSb/GaAs vertical cavity semiconductor optical amplifier. *Zanco Journal of Pure and Applied Sciences*, 32(2), pp.87-92.

Chen, Y.R., Zhang, Z.W., Miao, G.Q., Jiang, H., Li, Z.M. and Song, H., 2020. AlGaN-based UV-C distributed Bragg reflector with a λ-cavity designed for an external cavity structure electron-beam-pumped VCSEL. *Journal of Alloys and Compounds*, 820, p.153415.

Choquette, K.D. and Hou, H.Q., 1997. Vertical-cavity surface emitting lasers: Moving from research to manufacturing. *Proceedings of the IEEE*, 85(11), pp.1730-1739.

Hasnayeen, M.A., Othman, M. and Faidz, A.R., 2008, Design and modeling of dilute nitride VCSEL by using DBR mirror. In: *2008 6th National Conference on Telecommunication Technologies and 2008 2nd Malaysia Conference on Photonics*, IEEE, pp.52-55.

Hurtado, A., Gonzalez-Marcos, A. and Martin-Pereda, J., 2005. Modeling reflective bistability in vertical-cavity semiconductor optical amplifiers. *IEEE Journal of Quantum Electronics*, 41(3), pp.376-383.

Karim, A., Bjorlin, S., Piprek, J. and Bowers, J.E., 2000. Long-wavelength vertical-cavity lasers and amplifiers. *IEEE Journal of Selected Topics in Quantum Electronics*, 6(6), pp.1244-1253.

Kuech, T.F., 2016. III-V compound semiconductors: Growth and structures. *Progress in Crystal Growth and Characterization of Materials*, 62(2), pp.352-370.

Mishkat-Ul-Masabih, S.M., Aragon, A.A., Monavarian, M., Luk, T.S. and Feezell, D.F., 2019. Electrically injected nonpolar GaN-based VCSELs with lattice-matched nanoporous distributed Bragg reflector mirrors. *Applied Physics Express*, 12(3), p.036504.

Piprek, J., Bjorlin, S. and Bowers, J.E., 2001. Design and analysis of vertical-cavity semiconductor optical amplifiers. *IEEE Journal of Quantum Electronics*, 37(1), pp.127-134.

Sanchez, D., Cerutti, L. and Tournié, E., 2013. GaSb VCSELs with cascaded active-region for improved output power. In: *40th International Symposium on Compound Semiconductors 2013* (*ISCS2013*).

Tu, C.W. and Paul, K., 2003. Material properties of III-V semiconductors for lasers and detectors. *MRS Bulletin*, 28(5), pp.345-349.

Winston, D.W. and Hayes, R.E., 1998. Optoelectronic device simulation of Bragg reflectors and their influence on surface-emitting laser characteristics. *IEEE Journal of Quantum Electronics*, 34(4), pp.707-715.

Yu, S.F., 2003. *Analysis and Design of Vertical Cavity Surface Emitting Lasers*, John Wiley and Sons, Hoboken, New Jersey.

 http://dx.doi.org/10.14500/aro.10857

Examining Heterogeneity Structured on a Large Data Volume with Minimal Incompleteness

Nahla Aljojo

Department of Information system and Technology, College of Computer Science and Engineering, University of Jeddah, Jeddah, Saudi Arabia

***Abstract*—*Whereas* Big Data analytics can provide a variety of benefits, processing heterogeneous data comes with its own set of limitations. A transaction pattern must be studied independently while working with Bitcoin (BTC) data. Hence, this study examines twitter data related to BTC and investigate communications pattern on BTC transactional tweet. Using the hashtags #BTC or #BTC on Twitter, a vast amount of data was gathered, which was mined to uncover a pattern that everyone either (speculators, teaches, or the stakeholders) uses on Twitter to discuss BTC transactions. This aim is to determine the direction of BTC transaction tweets based on historical data. As a result, this research proposes using Big Data analytics to track BTC transaction communications in tweets in order to discover a pattern. Hadoop platform MapReduce was used. The finding indicate that in the map step of the procedure, Hadoop's tokenize the dataset and parse them to the mapper where thirteen patterns were established and reduced to three patterns using the attributes previously stored data in the Hadoop context, one of which is the Emoji data that was left out in previous research discussions, but the text is only one piece of the puzzle on BTC transaction interaction, and the key part of it is "No certainty, only possibilities" in BTC transactions.**

***Index Terms*—Heterogenouis dataset; Bitcoin transactions; Bitcoin tweets**.

I. Introduction

Different people may have varying motivations for using Bitcoin (BTC) because it can be used for a variety of purposes, including investment, transfer (both sending and receiving) from one BTC wallet to another, and for a variety of other purposes as well. When people want to stay up to date on the newest events in the world of BTC transactions, one of the best ways to do so is to use Twitter (Grover, et al., 2019). Unfortunately, because of different caliber of people on Twitter, the information about BTC transactions that would be shared on Twitter would come from a variety of different sources, making it difficult to verify. However, some well-known people, for example, Tweets from Elon Musk about BTC, for example, have had a significant impact on the current state of BTC transactions. It is possible that other individuals who tweet about BTC will not do the same. Now, it only makes sense to figure out how important a BTC-related tweet is and how significant it is. This is associated with the transaction. The focus of this study is not associated with BTC sentiment analysis on Twitter. This study formulates this concept to focus on transactional information, which involves all the various data sources that BTC has access to. With everything pertaining to BTC transaction data, the whole system is forced into a state of heterogeneity. This means that the information contained in BTC transaction data is associated with a heterogeneous property. In the BTC market, there is a great number of speculators and tech-savvy investors on Twitter coming together in the midst of turbulent market conditions, where, they switch to a contrarian strategy when market volatility increases (Lee, Li and Zheng, 2020).

The research challenge or problem in this scope is to trace a pattern to which everyone (speculators, tech-savvy, and stakeholders) use on Twitter about BTC transactions. Whether there is an established direction of certain Tweets from information of historical investment on price depreciation, appreciation, and fluctuation. Huge dataset is expected in this situation, and if the dataset is large, the chance of it being heterogeneous increases. This has a direct relationship to a Big Data characteristic. As a result, heterogeneous dataset, from BTC transaction data associated with a tweet, can be any data that contains a high variability of data types and formats. A large amount of information can be retrieved from Twitter by using the hashtags #BTC or #BTC. Because so many people of varying calibers are responsible for posting that information, it is possible that the data will be ambiguous and of low quality, as well as containing missing value values. In fact, it should be expected to contain a high level of data redundancy as well as inaccurate and sometimes misleading information. It would be difficult to integrate all of these disparate data sources in order to achieve a comprehensive understanding of the real outcome experienced by people during a BTC transaction.

The research gaps that was established lies with the fact that whereas there are millions of people who invest in BTC, their motives for doing so are not as well understood as those for making other kinds of investments (Mattke, et al., 2021). Furthermore, because of the variety of data

ARO-The Scientific Journal of Koya University
Vol. IX, No.2 (2021), Article ID: ARO.10857, 8 pages
DOI:10.14500/aro.10857
Received: 18 August 2021; Accepted: 16 October 2021
Regular research paper: Published: 02 November 2021
Corresponding author's e-mail: nmaljojo@uj.edu.sa

acquisition techniques available, the data generated from BTC tweets is frequently of personal views (Thelwall, Buckley and Paltoglou, 2011), but there is no prevision of stashing some pattern. Similarly, those data would be on a large scale due to the fact that there would be historical data on the nature of BTC performance within a specific time frame available (Kamps and Kleinberg, 2018). When it comes to data acquisition, there would be a strong correlation between the time and space in which it was done, as well as the geographic location of each piece of information (Yue, et al., 2018). After all is said and done, the effectiveness of the data would only account for a small portion of the decision (Dwyer, 2015). Because there would be a large amount of noise data that could be collected during the acquisition, this is an important consideration in establishing pattern for better understanding.

Given that BTC can be regarded as a private currency (Dwyer, 2015), and that the data generated as a result of its transactions can multiply in an exponential manner each day (Gandomi and Haider, 2015), and that the total number of BTC owners is approximately 100 million, huge information can be generated by Twitter about its transaction. Tweeter had 199 million daily active users with 500 million tweets/day as of the first quarter of 2021, while considering that when it comes to big data, the first and, in some cases, the only dimension that comes to mind is its sheer size (Sean, 2021). This study proposes to use Big Data analytic to analyze BTC transaction tweets to establish a pattern of the direction of the BTC market investment.

II. Related Work

Big data analytic is currently a very important area of study in data science, similarly BTC dwell one of the major part of computer studies. In terms of working with both areas, it creates the possibilities to show the process by which the data were collected changed the structure of the resulting dataset to draw some conclusion.

The extreme diversity of data in the Big Data world is one of the most difficult challenges to deal with (Christophides, et al., 2020). The previous study establish that heterogeneity can be created by grouping data from different experiments together in a single analysis (Lugli, Roederer and Cossarizza, 2010). In this instance, it is assumed that an experiment designed to develop heterogeneity will be the one to bring it to light. Each experiment will be tailored to the study's specifications, which means that the data generated by these experiments is likely to have a diverse range of characteristics (Bridges, et al., 2020). On the other hand, natural heterogeneity is also established by the underlying data sources, for example, in medical data (Yue, et al., 2020), Labor market data (Kikuchi, Kitao and Mikoshiba, 2020), Landscape data (Urrutia, et al., 2020), business data (George and Kabir, 2012), all these can be attributed to "data pooling" as a well-known cause of heterogeneity in data analysis.

When performing data analysis, it is common for the data distributions attribute to be non-normal, and that is where the first problem of heterogeneity arises (Kazemi and Hassanzadeh, 2020). Variety is one of the most important characteristics of Big Data, and it is closely associated with the heterogeneous nature of data sources (Hashem, et al., 2015). Given that Big Data encompasses the various data types that make up a dataset, it includes datasets that contain structured, semi-structured, and unstructured data, among other things (Casado and Younas, 2015). The previous research identified that, the vast majority of the data is structured and extremely well organized (Schulze, et al., 2018), whereas in data science, many believe that managing unstructured data is one of the most difficult problems because of the tools and techniques that are successful with handling structured data are not as effective with unstructured data, which results in much confusion (Blumberg and Are, 2003; Malik, Burney and Ahmed, 2020). One of the shortcomings identified by previous research studies in dealing with mixed-up data is that it is not entirely within the control of the application running it (Alkatheeri, et al., 2020).

It has been highlighted that there is a chance of receiving incorrect results in any situation when working with a variety of data types (Cappa, et al., 2021). This is also associated with BTC data. Big data analytics and block chain technology has been discussed in (Krithika and Rohini, 2020). The previous studies associated with BTC and big data are mostly focusing on price prediction, typical to these studies are the work of (Lahmiri and Bekiros, 2020) who investigate a multifractal analysis of BTC's price and volume relationships involves looking at a range of time scales, from the nanosecond to the year, to illustrate various multifractal processes that are occurring at differing intervals. Similarly, Big data analytics has been found to be useful for to identifying illegal activities on BTC transactions (Kumar, et al., 2021). Prediction of price of BTC has been to more appropriate with Big data analytics (Dutta, Kumar and Basu, 2020). In same direction, Big data have been used to identify the most time-efficient and accurate model for predicting the price of BTC ((Shankhdhar, Singh, Naugraiya and Saini, 2020).

Finally, it is important to note that all of the previous research in the areas of BTC and Big data reviewed in this study is either concerned with the problems of heterogeneity in data (Christophides, et al., 2020; Alkatheeri, et al., 2020) or with the application of big data for the prediction of BTC price or some part of BTC operations (Cappa, et al., 2021; Shankhdhar, et al., 2021). Pano and Kashef, 2020, who investigated sentiment analysis of BTC Tweets, served as inspiration for this study, which identified a gap in the current state of the art by not applying analysis of BTC tweets to the general BTC operations that are associated with its transaction.

III. Methodology

In the context of this study, a more specific phrase for "research methodology" is one that is focused on problem-based methodologies. This is critical when dealing with BTC transaction data, which is dealt with one transaction pattern at a time and must be dealt with on an individual basis. The study investigates the structural heterogeneity

that is associated with the abundance of data derived from the (#BTC and #btc hashtags) to better understand how minimal presentational incompleteness can be achieved on BTC-associated tweets data. One of the biggest problems in the realm of Big Data is extreme diversity. That is why Big data analytic was adopted using Hadoop platform, to test for patterns from heterogeneity data.

In performing this kind of test with Hadoop, there is an intrinsic property of data analytics that need to be considered as the major problems to solves, such as multimodality, incompleteness, and noise, which constitute a considerable obstacle to the successful deployment of revolutionary data analytics algorithms (Vaduva, Iapaolo and Datcu, 2020). This strategy is essential because it is critical to examine applying data analytical techniques, for the input data in such a way that it can be comprehensive and well-formatted for the technique to be effective; otherwise, the technique will be rendered ineffective. Many people have had trouble sorting through all of the data in big data analytics, and that can be seen in the amount of data that has been collected (Hu, et al., 2014). That is why when faced with the challenge of analyzing a huge volume of unstructured and semi-structured data, identifying meaningful patterns can be challenging because the material has nothing in common. For this current research methodology, unreliable, partial, and imprecise data in the real world about BTC transaction will be analyzed. It's expected that the analytical technique might lead to a poor application performance under certain circumstances because the datasets are tweets.

A number of data cleaning and integration approaches are used in conjunction with data transformation to remove noise from the data. The methodology is also responsible for the data transformation of the cleaned data. This type of technique is used in the context of traditional data analytics. For the fact that BTC tweets come with numerous challenges associated with big data, new techniques for data cleaning are required to deal with the uncertainty and data quality problems that arise as a result of data noise and inconsistent data, as well as the sheer volume of data size (Dey, et al., 2019). The justification of applying the propose methodology lies with these noise-removal techniques and the quality of the data analysis from Hadoop. That is why the findings obtained from the analytic can be greatly improved as compared with the previous method that relies on sentiment analysis.

A. Dataset

The dataset used in this study was obtained from Kaggle (Kaushik, 2021), which consisted of "BTC Tweets with trending #BTC and #btc hashtags" and "BTC Tweets with trending #BTC and #btc hashtags." The dataset for tweets can be obtained using the R-package, but due to the limited number of tweets and time that can be downloaded from each account when using the package, as well as the fact that data from Kaggle are open for use by many researchers to have some comparison, the Kaggle dataset was used in this study. The dataset is analyzed since it is associated with heterogeneity in the direction of redundancy or missing values, the results of analysis is correlated with properties of BTC values.

B. Analytical Framework

The research analytical framework is presented in Fig. 1. Pattern types are used by the project to accommodate a diverse range of data types and transaction ideas. These pattern types are described in greater detail to present data types. Among other things, classes can be classified in a variety of ways, including across multiple languages and even within a single language, among other things. Note that, despite the fact that all of the data sources make reference to the same entities, each of the data sources refers to those entities using a different name to distinguish them from one another. In situations where different domain modeling models are applied to the same subject matter in a variety of ways, the term "semantic or logical mismatch" can be used to describe the differences in domain modeling approaches. The fact that this is true even when concepts are defined through the application of a variety of axioms is what gives you the confidence to believe that it is true in the first place. This is due to the fact that their conceptualizations are diametrically opposed to one another, which allows them to be easily distinguished from one another. As a result of the various ways in which the concepts have been modeled, there is a misalignment in the concepts as a result of the misalignment.

When two or more data sources describe the same geographic region at the same level of detail but from a different point of view than the first, the coverage of those two or more data sources is defined as the sum of their coverage when the two or more data sources are combined. When two datasets that describe the same geographic region, but with finer-grained detail, are compared, the datasets with different levels of detail (granularity differences) are referred to as a dataset with different levels of detail (granularity differences) in the literature (also known as a dataset with granularity differences). Data that were generated as a result of incompatible points of view or, more specifically, differences in scope between two parties are referred to as "incompatibility data," which is another term for it. Semiotic heterogeneity is defined as the phenomenon of different people interpreting the same entity in a way that is different from their own interpretation. The use of computers to detect and solve heterogeneity in a complex problem, such as this one, is required when dealing with a problem that can only be solved by humans in this situation. The fact is that this is a difficult task for computers to complete and is therefore not recommended.

C. The Analytic Experiment

Based on the analytical framework presented in the previous section, the Hadoop distributed data management and processing system was used in this study, specifically because it allows for distributed data management and processing. The direct impact of utilizing the Hadoop lies with, tokenizing formatted data and parsing the data during the map phase and preparing the data for the Hadoop map reduce cycle. The pre-

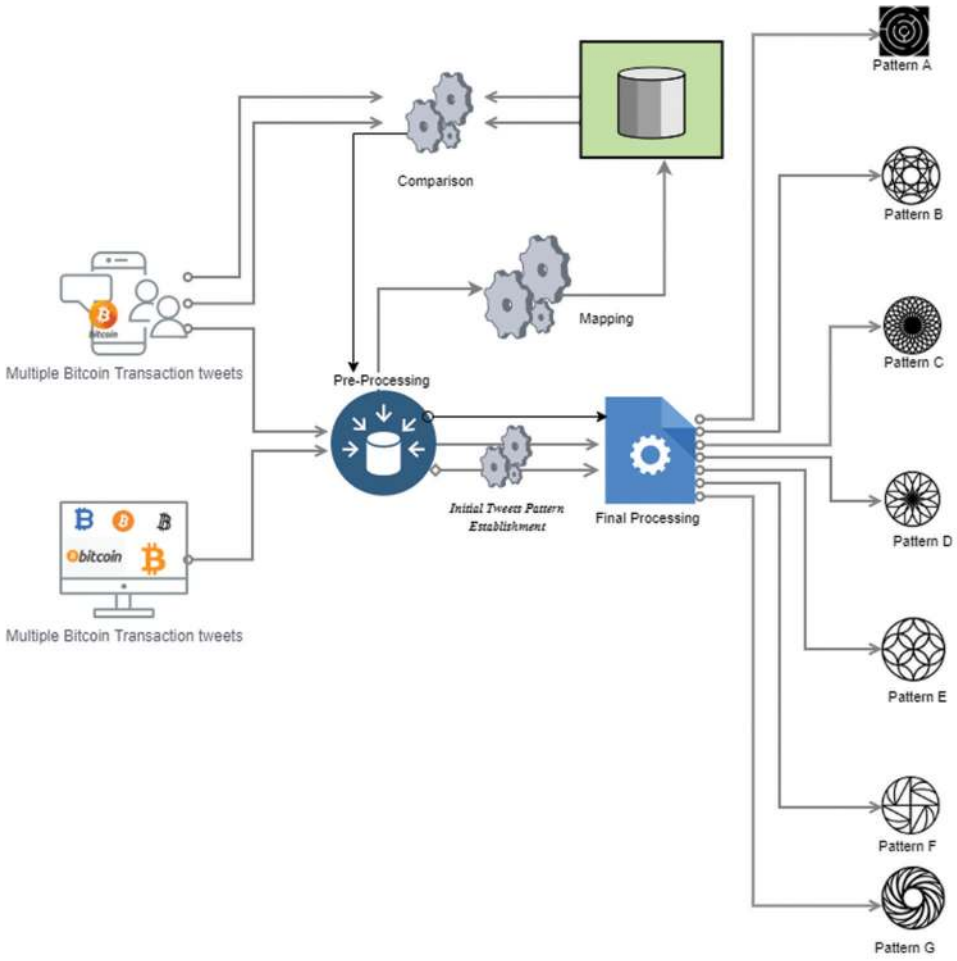

Fig. 1. The research analytical framework.

proceed data retrieved the attributes and transferred them to the Hadoop context, where they were used in the reduce step to aggregate the results for the particular data type in question. The Hadoop Distributed File System (HDFS), which was developed by Google, improved the efficiency of MapReduce processing and is well-suited analyzing BTC tweets because it is a clustered storage file system with increased bandwidth and self-healing capabilities. It is scalable with good error detection, and enhanced response handling. It was also designed with built-in redundancy, means failure is not a concern, and it is capable of achieving high availability through the use of parallel computing techniques (Abubakar, El-Gammal and Alarood, 2020).

Among other things, the cluster in Hadoop includes functionality that protects information stored on the nodes in the event of a node crash or failure, among other things. For each data node, three copies of its data are stored on the server by default, according to the default configuration. When a cluster has multiple data nodes, the HDFS manages and balances the data load among them, allowing the cluster to add or remove data nodes as needed. This study distributes our Name Nodes across multiple points to avoid having a single point of failure, so that they can continue to function even if one is lost due to a node failure.

D. MapReduce

MapReduce is used to construct the analytical framework for this study. MapReduce allows for the analysis of large datasets in a parallel manner. In this study, MapReduce was used to read each piece of BTC transaction data one at a time and record it into a hash table, with each data unit serving as the key and the value representing the number of times it occurs. When a unit of data does not fit into a predefined pattern, it is added and given a numerical value. It is also possible that a data unit exists in the hash table, in which case the value of that data unit is updated to reflect the new occurrence count. This operates in a serial fashion, with the amount of time required increasing in direct proportion to the complexity of the data and the size of the data set being processed. When dealing with a large dataset, this is, without a doubt, extremely difficult to compute. As a result, serial data possession is not feasible and takes an inordinate amount of time, and we must implement parallel data processing.

The research analysis process begins with the division of the input sequence into several files. This number has been assigned to a number in the sequence of numbers. The Mapper returns an associative key/value pair as a result of its operation. Values from different mappers that have the same key combine to form a single value. In other words, a pattern has been established and maintained. The A-G

http://dx.doi.org/10.14500/aro.10857

pattern was laid out in the manner depicted in Fig. 1. Each pattern has a value, which corresponds to the first Mapping in the MapReduce process, which is the first stage. The data elements in the input file are combined to form a set of key-value pairs. Each symbol is represented by two symbols when the mapping function is used to count. It is a mapper function, which means that it does not change the data in the input list but instead returns a new output list. Reducers, also known as reducers, are used to switch between the outputs of the mapping step. Reducer nodes each have a subset of keys that are unique to them. In order to generate patterns, this subset is the next reducing step (partitioning). A task has the ability to push key-value pairs to any partition it chooses. On every mapper/reducer, the result is the same. Reducers are capable of dealing with a wide range of keysets. Prior to the keys being placed into the next stage, sorting, they must first be reduced. Finally, reduce the size of the object. Each reducer key necessitates the inclusion of a single instance of user-provided code. The inputs are a loop with a key on top of it, and the output is a key. It is possible that the iterator values are in an unexpected order. Each reducer produces a single output file.

The Kaggle dataset was preprocess, after setting up MapReduce by using IntelliJ IDEA instance. This was followed by creating a Java Project and downloading Hadoop from its official website where it was extracted into the working directory. Finally, in order to extend and perform the MapReduce tasks, we will require a few jar files from the Hadoop files. They will be dependencies that are required for the experimentation and will be referenced by the code. Once the directory has been created, the next step is to set up an input directory within the project. In here, we will detail which data is required for analysis.

IV. Presentation of the Results

After initial mapping g of the dataset by #BTC and #btc, MapReduce examined one piece of the BTC transaction data at a time and recorded each value and key as the sum of all occurrences in a hash table. That is following the isolations of dataset generated by #BTC and #btc, thirteen patterns where mapped under various categories (Fig. 2), where 1 (String, 1), 2 (Boolean, 2), 3 (Text, 3), 4 (Datetime, 4), 5 (Timestamp, 5), 6 (Date, 6), 7 (Hyperlink, 7), 9 (Currency, 9), 10 (Emoji, 10), 11 (Tags,11), 12 (Floating- point number, 12), and 13 (Character, 13).

When the data are not part of a specified pattern categorized from Fig. 2, it is given a separate value. Data units can exist in the hash table, in which case the value is updated to reflect the new occurrence count. The more complex the data, the more time it takes to process it, but evaluating A hash map is used to keep track of a list of records. It is likely that several highly active processing operations are going on simultaneously, because, it is difficult to compute when the dataset is large and many operations are going through the processing pipeline at the same time. For this particular reason, the serial data processing time-consuming that is the time needed to process a certain amount of data in dataset was measured (Fig. 3).

Whereas, it requires parallel data processing to be implemented. The mapper specifically mapped [map(π,μ)→list(λ,β)] where π is the in-key and μ is the in-value for which λ represent intermediate key, β represent the intermediate value. This application makes it possible to store data in a distributed manner. It also contributes to the reduction of a significant amount of data. In MapReduce, the terms reducing and mapping are used interchangeably. This research is currently in a position where it must complete the current mapped task before moving on to the next. As a result, the complete mapping was given by [{π, 1}, {μ, 1}, {λ, 1}, {β, 1}]…, [{π, n}, {μ, n}, {λ, n}, {β, n}] where the reducer modules consolidate the intermediate map data, thereby alleviating the processing load on the underlying framework. Among the 13 patterns mapped using attributes previously stored in the Hadoop context, the three out of them that were formed after the reduced operation, includes many used of “Emoji” “no certainty, only possibilities” and “patience” which were mostly associated with web link. However, the text is only one piece of the puzzle in terms of BTC transaction interaction. Whereas analyzing the “text,” it was reveals that many texts that are associated with hyperlink and uniform resource locator (URL) were connected to a secured connection. That is apart from the term “BTC” and “Crypto” web link dominated a connection with all other

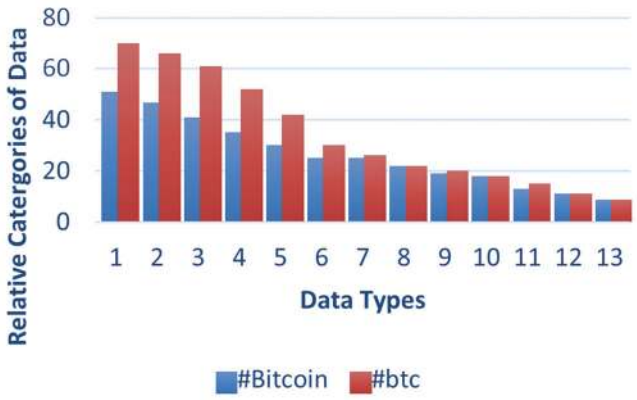

Fig. 2. The relative mapped data.

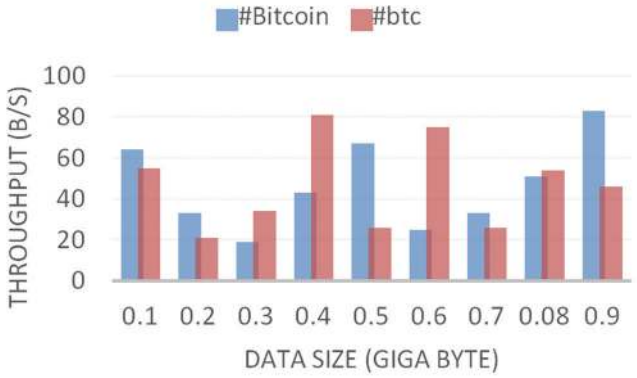

Fig. 3. The time required to process the Mapped #Bitcoin and #btc amount of data.

data types in the interaction of Bitcon transaction in BTC tweets (Fig. 4). The data-network map highlighted t.co at high frequencies and while following down the link. One of the most significant data types discovered is the Twitter automatic shorten URLs data, which is represented by the t.co. Twitter shorten URLs are displayed on any post that shares a URL on Twitter. There is no weblink in a tweet that can be used to opt out of link shortening. In tweets, you can combine URLs that are no longer than a maximum number of characters and tweet out only the shortened link, without jeopardizing the character count for the rest of the message.

It turns out there was unknown "emoji data" and other known emoji. No sure thing, just a lot of possibilities, followed by patience Even so, the text is only one of many aspects to take into consideration when considering BTC transaction interactions. Those emoji interactions were created in order to compensate for the lack of presentation of a more comprehendible data format. Typically, the finding of this study reveals that when emoji were used, the recipient was able to understand the based on emotions of the sender. Tweets that use emoji appear to be friendlier and more extroverted than those who do not. This suggests that it is possible to achieve an increase in approachability and competence in BTC transactional tweets with emoji. Many tweet rely heavily on emoji because they're vital for conveying emotions through visual expression.

Even though it has been revealed that the text is only one piece of the puzzle when it comes to BTC transaction interaction, and that one of the most important pieces is the statement, it is important to note that "no certainty, only possibilities" in BTC transactions and "patience" are the reduced form of the text outcome of the Hadoop. Hence, the cloud-tags of the text data type were with keyword clouds, also known as keyword cloud visualization are drawn (Fig. 5). The term "price" has the highest frequency a part from the term "BTC," "Cryto," and "BTC" Lots of tweets lies with BTC's price and its volume, and the data types associated with this interaction are mostly "Datetime," "Timestamp," and "Date."

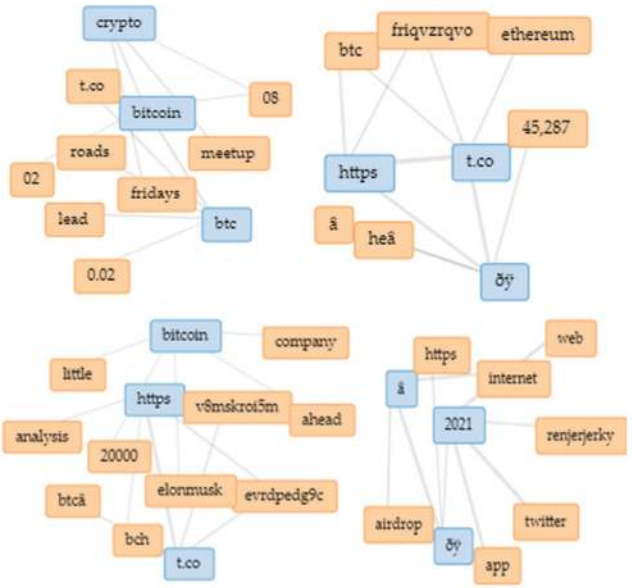

Fig. 4. Networked pattern of the Bitcoin transaction tweet.

Fig. 5. The keyword cloud visualization of the Bitcoin tweet.

V. Discussion

Whereas many study deals with text analysis concerning characters or strings, this study found it important to include other data types in analyzing the communication between people in regards to BTC transactions. MapReduce has been used, and it mapped out thirteen key attributes of other data types used with the inclusion of string and text. These data were used for interaction about The BTCs transaction. One of the key terms that comes out about the data is the word "Patience." This has been used when the transaction was in turbulent case. Other data types that are mostly not been considered by previous research is emoji. It was found that emojis are attached to messages. The senders' motivations for sending a message may be different.

In light of the massive amounts of data that are being collected as a result of real-time transactions that occur around the clock, this study first supports the perceptions of the technical community about the massive amount of new data that are being generated every day, and it is referred to as possessing the characteristics of Big Data in the scientific community. Big Data analytics has made a significant contribution to the success of data science, especially when taking into consideration the ability to have an analytical technique that can deal with massive amounts of information. To draw some reasonable conclusions from BTC transactions, Big data can be used to handle the data from the transactions. Whereas Big Data analytics can provide a variety of benefits in general, as well as to the decision-making process for BTC transactions in particular, there are some limitations to the way heterogeneous data is handled when the technique is employed. This means that when working with BTC data, there will be a plethora of different sources that will be required to be examined with each transaction based on how it appears in the pattern of transactions. The data associated with BTC tweets is examined in this study, in contrast to the previous research, to determine the amount of minimal presentation incompleteness that can be achieved using the

data. When the hashtags for BTC and BTC volume were used on Twitter, large amounts of information could be retrieved, which was then mined to uncover a pattern that was used by everyone.

It is critical to use Twitter to communicate BTC transaction information in order to ensure a successful transaction. As a result, BTC transaction tweets are influenced by data and information from the previous day. It is proposed to use Big Data analytics to identify a pattern in Twitter message transactions to track down BTC communications in order to track down BTC communications. The workflow that resulted in the development of the map reduce system was created with the goal of handling the tokenization and parsing of structured data during the map phase of the process. As a result, only 13 patterns were discovered, one of which was the Emoji data, which had previously been overlooked in previous Hadoop-related research efforts. Although the text is significant, only one piece of the BTC transaction puzzle, namely, the statement "There is no certainty, only possibilities," appears in the transaction details, regardless of its significance.

VI. Conclusion

The volume of Big Data is increasing every day. Big Data analytics has progressed substantially as a result of data science. Big Data analytics may be incredibly useful when dealing with massive amounts of data. Before a transaction can be finalized, it must be thoroughly examined. The usage of the majority of those who have invested in BTC and used Twitter to acquire information are still confused what tweets are correct or incorrect. The data storage technique used by BTC is incapable of maintaining any of the patterns that provide additional information. Previous research did not include several data types required for understanding people's views on BTC transactions, thus it's possible that information concerning BTC's history will be used in the future. When working with BTC data, a transaction pattern must be evaluated independently. This investigates how the pattern that was developed was established using Twitter data connected to BTC transactions. To find a pattern, Big Data analytics was utilized to follow BTC transaction communications in tweets. Hadoop's map reduce workflow was designed in the map step of the procedure, and the mapper components mapped thirteen sets of patterns, which were reduced by the reducer into three patterns using the attributes previously stored data in the Hadoop context, one of which is the Emoji data, which was left out in previous research discussions but is critical to unlock the BTC transaction key communication. Along with web links, the phrase "No certainty, only possibilities" and the word "patience" were prominently featured. In BTC transactional tweets, URLs and linked text were commonly used. The majority of BTC-related tweets include a link to another website. The impact of BTC tweets produced patterns that centered on continuing to wait or exercising patience in regards to BTC price and volume.

References

Abubakar, A., El-Gammal M.T. and Alarood, A.A., 2020. End-to-end fully-informed network nodes associated with 433 MHz outdoor propagation environment. *International Journal of Computing and Digital Systems*, 10, pp.1-19.

Alkatheeri, Y., Ameen, A., Isaac, O., Nusari, M., Duraisamy, B. and Khalifa, G.S., 2020. The effect of big data on the quality of decision-making in Abu Dhabi Government organisations. In: *Data Management, Analytics and Innovation*, Springer, Singapore, pp.231-248.

Blumberg, R. and Atre, S., 2003. The problem with unstructured data. *Dm Review*, 13(42-49), p.62.

Bridges, D., Pitiot, A., MacAskill, M.R. and Peirce, J.W., 2020. The timing mega-study: Comparing a range of experiment generators, both lab-based and online. *PeerJ*, 8, p.e9414.

Cappa, F., Oriani, R., Peruffo, E. and McCarthy, I., 2021. Big data for creating and capturing value in the digitalized environment: unpacking the effects of volume, variety, and veracity on firm performance. *Journal of Product Innovation Management*, 38(1), pp.49-67.

Casado, R. and Younas, M., 2015. Emerging trends and technologies in big data processing. *Concurrency and Computation: Practice and Experience*, 27(8), pp.2078-2091.

Christophides, V., Efthymiou, V., Palpanas, T., Papadakis, G. and Stefanidis, K., 2020. An overview of end-to-end entity resolution for big data. *ACM Computing Surveys*, 53(6), pp.1-42.

Dey, N., Das, H., Naik, B. and Behera, H.S., 2019. *Big Data Analytics for Intelligent Healthcare Management*, Academic Press, Cambridge, Massachusetts.

Dutta, A., Kumar, S. and Basu, M., 2020. A gated recurrent unit approach to bitcoin price prediction. *Journal of Risk and Financial Management*, 13(2), p.23.

Dwyer, G.P., 2015. The economics of Bitcoin and similar private digital currencies. *Journal of Financial Stability*, 17, p.81-91.

Gandomi, A. and Haider, M., 2015. Beyond the hype: Big data concepts, methods, and analytics. *International Journal of Information Management*, 35, pp.137-144.

George, R. and Kabir, R., 2012. Heterogeneity in business groups and the corporate diversification firm performance relationship. *Journal of Business Research*, 65()3, pp.412-420.

Grover, P., Kar, A.K., Janssen, M. and Ilavarasan, P.V., 2019. Perceived usefulness, ease of use and user acceptance of blockchain technology for digital transactions insights from user-generated content on Twitter. *Enterprise Information Systems*, 13(6), pp.771-800.

Hashem, I.A.T., Yaqoob, I., Anuar, N.B., Mokhtar, S., Gani, A. and Khan, S.U., 2015. The rise of "big data" on cloud computing: Review and open research issues. Information Systems, 47, pp.98-115.

Hu, H., Wen, Y., Chua, T.S. and Li, X., 2014. Toward scalable systems for big data analytics: A technology tutorial. *IEEE Access*, 2, pp.652-687.

Kamps, J. and Kleinberg, B., 2018. To the moon: defining and detecting cryptocurrency pump-and-dumps. *Crime Science*, 7(1), pp.1-18.

Kaushik, S., 2021. *Bitcoin Tweets, Tweets with trending #Bitcoin and #btc hashtag.* Available from: https://www.kaggle.com/kaushiksuresh147/bitcoin-tweets [Last accessed on 2021 May].

Kazemi, I. and Hassanzadeh, F., 2020. Modelling multivariate, overdispersed count data with correlated and non-normal heterogeneity effects. *Statistics and Operations Research Transactions*, 1, pp.335-356.

Kikuchi, S., Kitao, S. and Mikoshiba, M., 2020. Who suffers from the COVID-19 shocks? Labor market heterogeneity and welfare consequences in Japan. *Covid Economics*, 40, pp.76-114.

Krithika, D.R. and Rohini, K., 2020. Blockchain with bigdata analytics. In: *Intelligent Computing and Innovation on Data Science*, Springer, Singapore, pp.403-409.

Kumar, A., Abhishek, K., Nerurkar, P., Khosravi, M.R., Ghalib, M.R. and Shankar, A., 2021. Big data analytics to identify illegal activities on bitcoin blockchain for IoMT. *Personal and Ubiquitous Computing*, 1, pp.1-12.

Lahmiri, S. and Bekiros, S., 2020. Big data analytics using multi-fractal wavelet leaders in high-frequency Bitcoin markets. *Chaos, Solitons and Fractals*, 131, p.109472.

Lee, A.D., Li, M. and Zheng, H., 2020. Bitcoin: Speculative asset or innovative technology? *Journal of International Financial Markets*, 67, p.101209.

Lugli, E., Roederer, M. and Cossarizza, A., 2010. Data analysis in flow cytometry: The future just started. *Cytometry Part A*, 77(7), pp.705-713.

Malik, A., Burney, A. and Ahmed, F., 2020. A comparative study of unstructured data with SQL and NO-SQL database management systems. *Journal of Computer and Communications*, 8(4), pp.59-71.

Mattke, J., Maier, C., Reis, L. and Weitzel, T., 2021. Bitcoin investment: A mixed methods study of investment motivations. *European Journal of Information Systems*, 30(3), pp.261-285.

Pano, T. and Kashef, R., 2020. A complete VADER-based sentiment analysis of bitcoin (BTC) tweets during the era of COVID-19. *Big Data and Cognitive Computing*, 4(4), p.33.

Schulze, P., Unger, B., Beattie, C. and Gugercin, S., 2018. Data-driven structured realization. *Linear Algebra and its Applications*, 537, pp.250-286.

Sean, B., 2021. *Twitter Hits 199 Million Users, Reports "Solid" Q1 Revenue.* Available from: https://www.thewrap.com/twitter-hits-199-million-users-reports-solid-q1-revenue [Last accessed on 2021 May].

Shankhdhar, A., Singh, A.K., Naugraiya, S. and Saini, P.K., 2021. Bitcoin price alert and prediction system using various models. In: *IOP Conference Series: Materials Science and Engineering*. Vol. 1131. IOP Publishing, p.012009.

Thelwall, M., Buckley, K. and Paltoglou, G., 2011. Sentiment in twitter events. *Journal of the American Society for Information Science and Technology*, 62(2), pp.406-418.

Urrutia, A.L., González-González, C., Van Cauwelaert, E.M., Rosell, J.A., Barrios, L.G. and Benítez, M., 2020. Landscape heterogeneity of peasant-managed agricultural matrices. *Agriculture, Ecosystems and Environment*, 292, p.106797.

Vaduva, C., Iapaolo, M. and Datcu, M., 2020. A Scientific Perspective on Big Data in Earth Observation. In: *Principles of Data Science*, Springer, Cham, pp.155-188.

Yue, L., Tian, D., Chen, W., Han, X. and Yin, M., 2020. Deep learning for heterogeneous medical data analysis. *World Wide Web*, 23(5), pp.2715-2737.

Yue, X., Shu, X., Zhu, X., Du, X., Yu, Z., Papadopoulos, D. and Liu, S., 2018. Bitextract: Interactive visualization for extracting bitcoin exchange intelligence. *IEEE Transactions on Visualization and Computer Graphics*, 25(1), pp.162-171.

Spontaneous Emission Enhancement of CdSe Quantum Dots Embedded in a Two-dimensional Photonic Crystal L3 Nanocavity

Khalid N. Sediq

Department of Physics, Koya University, Faculty of Science and Health, Koya University, University Park, Danielle Mitterrand Boulevard, Koya KOY45, Kurdistan Region – F.R. Iraq

***Abstract*—Two-dimensional photonic crystal nanocavities were designed to tailor cavity quantum electrodynamics. Enhancing the spontaneous emission of low-quality factor nanocavity with embedded CdSe quantum dots (QDs) emitters is the aim of this study. Low concentration layer of CdSe QDs was sandwiched between two layers of Si_2N_3 membrane using plasma-enhanced chemical vapor deposition. The modification rate in spontaneous emission of L3 nanocavity up to 2.3-fold has been observed at 629.5 nm in compare to bare cavities. High field confinement in the sub-wavelength regime became an interest field for quantum electrodynamics applications and good platform to study light matter interactions.**

***Index Terms*—Quantum dots; L3 cavity; Photonic crystal; Purcell factor.**

1. Introduction

The ability to confine light into small volumes is important for enhancing the light and matter interaction in the emerging field of nanophotonics. Optical confinement in the sub-wavelength regime is of high interest for quantum electrodynamics applications (Chang, et al., 2006; Gong and Vučković, 2007). They are bounding the electromagnetic excitations between semiconductors and a dielectric, leading to a strong interaction between quantum emitters and photon fields (Chang, et al., 2006). This interaction can further be enhanced through an appropriate feedback mechanism that provided by nanocavity structures. The enhancement of cavity spontaneous emission (Purcell effect) is essential for a variety of applications, such as, single-photon sources (Wie, 2019), integrated quantum optics (Mahmoodian, et al., 2016; Daveau, et al., 2017), nanoscale lasers (Oulton, et al., 2009), active meta-materials (Schulz, et al., 2016), biotechnological devices for enhanced fluorescence intensity (Lakowicz, et al., 2003), and ultra-fast modulated LEDs (Shambat, et al., 2011). Nanolaser performances are also highly affected by light emitters that introduced within the resonator. The gain properties of semiconductor quantum dots (QDs) have a lot of advantageous due to their temperature stability, small line width enhancement factor, and the ability to suppress the non-radiative recombination (Arakawa, et al., 1982). In addition, QDs are suitable for studying cavity QED, because of their atom like quantum emission (Yoshie, et al., 2004; Reithmaier, et al., 2004; Arakawa, et al., 2012). Recently, a study has been carried on field improvement at communication wavelength using InGaAs QDs embedded in a GaAs nanowire having groove like cavity, which manifested high enhancement by 617-fold (Wie, 2019). Recently, some studies were carried out on field improvement at communication wavelength, for example, InGaAs QDs was embedded in a GaAs nanowire having groove like cavity, which manifested high enhancement by 617-fold (Wie, 2019); while using Ge/Si QDs within Si two-dimensional photonic crystal (2D PC) field enhanced by about 25 times at $\lambda = 1.2$ μm and by 34 times $\lambda = 1.6$ μm (Yakimov, 2021).

In this study, field enhancement toward visible wavelength using CdSe QDs embedded in Si_2N_3 2D PC was proposed. A remarkable field enhancement was observed using even low-quality factor L3 nanocavity. Such result can be promising to study light mater interaction at visible wavelength.

II. Materials and methods

In this work, the realization and characterization of a hybrid photonic crystal (PC) cavity that combines the benefits of both QDs and photonic elements has been presented. Here, an 8 nm of CdSe QDs (provided by Sigma-Aldrich) is used as an active emitter layer.

A. 2D PC Fabrication

First, a suspended layer of Si_2N_3 with a thickness of 100 nm was coated with a thin layer of 8 nm of CdSe QDs which diluted to a concentration of 0.01 mg/ml in toluene solution. Second, another layer with 100 nm of Si_2N_3 is deposited by plasma-enhanced chemical vapor deposition. The whole

ARO-The Scientific Journal of Koya University
Vol. IX, No.2 (2021), Article ID: ARO.10810, 4 pages
DOI: 10.14500/aro.10810
Received: 21 April 2021; Accepted: 07 October 2021
Regular research paper: Published: 02 November 2021
Corresponding author's email: khalid.sediq@koyauniversity.org

http://dx.doi.org/10.14500/aro.10810

structure thickness becomes 200 nm with a sandwiched layer of CdSe QDs. A 200 nm polymethyl-methacrylate (PMMA) electron beam resist layer was spin coated on the Si_2N_3 surface then backed on a hot plate for 1 min at 100°C to harden it and remove any residual solution. Subsequently, a 30 kV electron beam lithography was used to define the required PC pattern in PMMA. Then, exposed PC pattern in resist by electron beam is removed by methyl isobutyl ketone: isopropyl alcohol 1:3 developer. Finally, the PC pattern is transferred from PMMA into the Si_2N_3 layer using reactive ion etching to obtain air holes through the Si_2N_3 layer. The used recipe of the RIE dry etching device was based on a mixture gas of CHF_3 and O_2, with flow rates 30 and 5 sccm, respectively.

B. Photolumens (PL) Measurements

The fabricated PC is optically pumped using a CW diode pumped solid state laser at 532 nm. The beam focused through a 100× long working distance objective lens (6 mm) having a 0.77 numerical aperture (NA) to a 2.5 μm diameter spot on the cavity surface. The laser spot was controlling using a three-dimensional piezo motor stage (Piezosystem Jena Tritor 100, Micro XYZ Positioner stage NV 40/3s controller). The emission spectra were collected using the same objective lens and analyzed by nitrogen cooled CCD detector. Long-pass filter with a cutoff wavelength at 532 nm was used to block the excitation light from reaching the detector.

III. Results and Discussion

The QDs solution diluted to a concentration of 0.01 mg/ml in toluene and spun into the structures at 1.5 krpm (to reduce unwanted aggregation) on 100 nm Si_2N_3 layer, resulting up to ~ 10^2 emitters dots per 2 μm^2. The coating was not uniform due to the small chip size of the membrane (0.25 mm^2) as it is shown in Fig. 1.

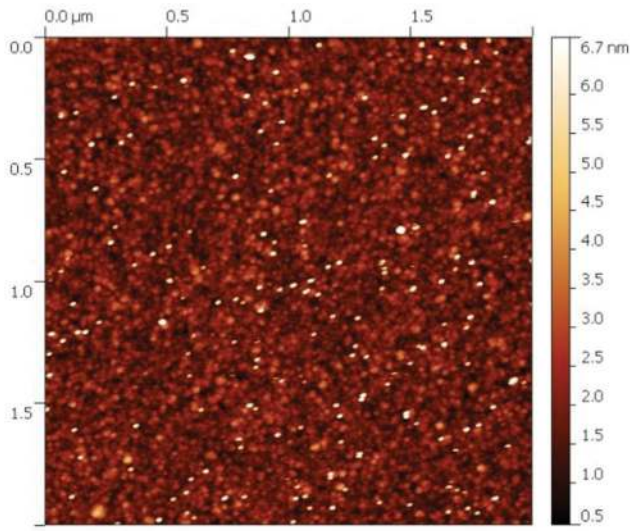

Fig. 1. Atomic force microscopy image of thin layer of 0.01 mg/mL of CdSe quantum dots coated on a thin layer of Si_2N_3 membrane. Acceptable distribution and low aggregation are observed.

PL has been taken for embedded layer of QDs as shown in Fig. 2. The emission spectrum shows a peak position at 640 nm with full width at half maximum (FWHM) 50 nm. The wide width of emission spectrum line is due to the effect of the dots aggregation which leads to red shift, besides the influence Si_2N_3 layer PL emission.

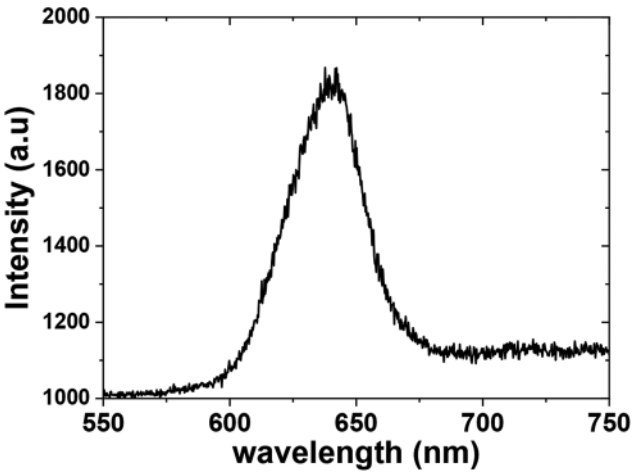

Fig. 2. Photo lumens emission of 0.01 mg/mL of CdSe quantum dots sandwiched within 200 nm layer of Si_2N_3 layer.

The fabricated PC dimension is 10 μm × 10 μm with three missed holes in the center act as nanocavity. Such structure is known as PC with L3 cavity. The produced PC L3 cavity has a lattice constant a = 260 nm (distance between two adjacent holes), hole radius r = 0.288a, and total cavity length 0.78 μm approximately, as shown in Fig. 3.

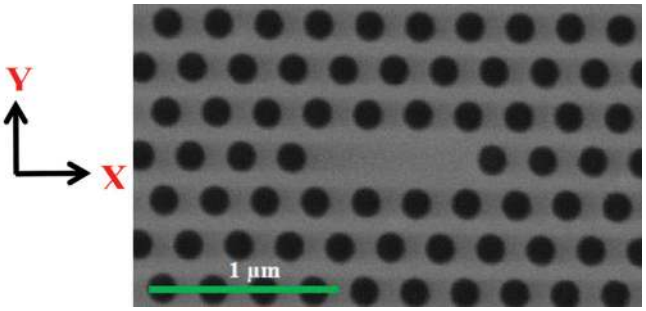

Fig. 3. Scanning electron microscope image of two-dimensional photonic crystal L3 cavity printed on Si_2N_3 membrane.

In general, PC as an optical system can enhance or suppress the rates of spontaneous emission for any quantum emitters. The coupling between cavity modes and the QDs as two-level system is a type of energy exchanging between them. In such system (QDs – nanocavity), photons are supplied with a certain probability that depends on their environment and density of states. The coupling between quantum emitters and cavity mode leads to a remarkable enhancement of the spontaneous emission of the output modes which is known as Purcell effect (Purcell, 1946) and the Purcell factor is totally depend on Q/V ratio (Ryu and Notomi, 2003):

$$F = \frac{3}{4\pi^2}\frac{Q}{V_{mode}}\left(\frac{\lambda_0}{n}\right)^3 \quad (1)$$

Where: Q quality factor, V_{mode} mode volume, and n is medium refractive index.

The enhancement of spontaneous emission rate γ is strongly ruled by the emitter alignment with the dipole moment $\vec{\mu_i}$ at a point on the cavity, which can be derived from Fermi's Golden rule (Boroditsky, et al., 1999; Englund, et al., 2005).

$$\gamma = \frac{\gamma_{cav}}{\gamma_{free}} = F \times \left(\frac{\overrightarrow{E}.\vec{\mu}}{\left|\vec{E}\right|_{max}\left|\vec{\mu}\right|} \right)^2 \times \frac{\Delta\lambda_{cav}^2}{4\left(\lambda - \lambda_{cav}\right)^2 + \Delta\lambda_{cav}^2} \quad (2)$$

To measure the enhancement of the confined field through Purcell factor inside nanocavity before and after introducing QDs emitters, number of parameters should be estimated, such as quality factor Q and mode volume V_{mode}.

Physically, the effective cavity mode volume is known as a spatial distribution of electromagnetic energy (Balanis, 2013).

$$V_{mode} = \frac{\int \in E^2 dV}{\max(\in E^2)} \quad (3)$$

In purely dielectric cavities, the ratio of the volume of the active region (V_a) to mode volume (V_{mode}) is known as confinement factor (Chang and Chuang, 2009):

$$\tilde{A} = \frac{V_a}{V_{mode}} \quad (4)$$

Therefore, to obtain high confined cavities, the mode volume should be smaller than the active region volume, that is, Γ > 1. In general, the 3D nanocavity effective mode volume calculation needs to use numerical methods due to the geometric and material complexity of the cavities. Experimentally, the modes are considered completely confined to the active region volume; V_{mode} approaches the geometrical active medium volume V_a and Equation 4 becomes Γ≈1 (Li, 2018).

In this experiment, cavities without QDs show no output mode enhancement (Fig. 4). However, PC L3 designed cavity supports one mode on X-axis direction (long cavity axis), λ= 625 nm FWHM Δλ= 2.08 nm (Fig. 5 red curve). Mode quality factor Q inside nanocavity which known as the ratio of stored energy to dissipated one can be calculated by $Q = \lambda/\Delta\lambda$. Hence, mode cavity shows low-quality factor Q=303 (Fig. 5 red curve) whereas the field enhancement calculated from Purcell factor from Eq. 1 is F_{bare}=30.29 using the mode volume normalized to the mode wavelength $V_{mode} = 0.76\left(\frac{\lambda}{n}\right)^3$.

Introducing a thin layer of CdSe QDs which sandwiched in the PC membrane, two modes were observed λ_1 = 624.5 nm and λ_2 = 629.5 nm with both Δλ ≈ 0.9 nm as shown in Fig. 5 (black curve). Consequently, both modes' Q-factor increased significantly to Q_1 = 690 and Q_2 = 699, respectively. Using the same mode volume normalized to the mode wavelength in the Purcell factor formula for the highest Q_2, factor mode

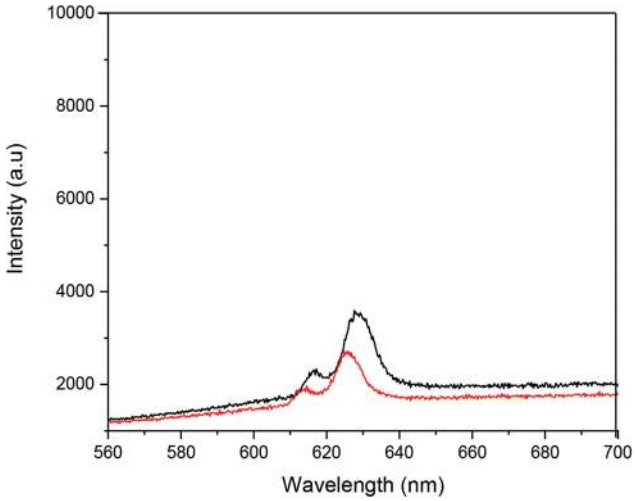

Fig. 4. Photo lumens spectrum for L3 cavity modes before introducing CdSe quantum dots (QDs) (red curve) and after introducing a thin layer of CdSe QDs (black curve).

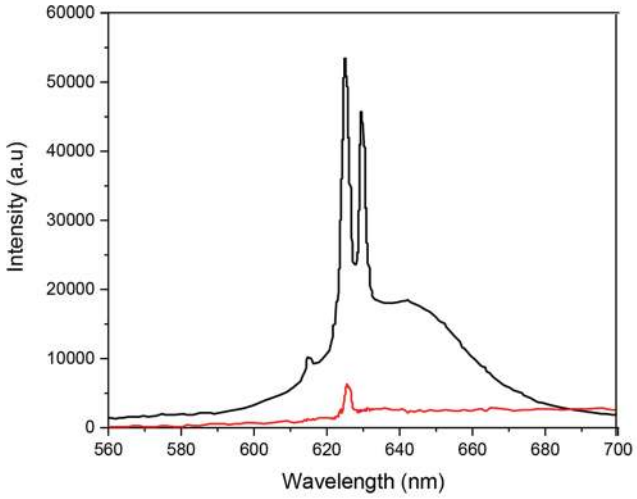

Fig. 5. Photo lumens (PL) spectrum for L3 cavity modes before introducing CdSe quantum dots (QDs) (red curve) and after introducing a thin layer of CdSe QDs (black curve). Here, QDs emission modes are highly aligned with cavity modes shows remarkable enhancement of PL.

is F_{QD} = 71.29 so that the cavity field shows enhancement by 2.36-fold (F= F_{QD}/F_{bare}).

In addition, Eq. 2 indicates that the location of quantum emitters inside nanocavities plays an essential role to either enhance or suppress the output emission. Thus, the PC cavity modes-QD exciton system on resonance should be located at the maxima electric cavity field (Vuckovic and Yamamoto, 2003). Enhancements in both λ1 and λ2 modes (Fig. 5) can be referred to the increase of coupling parameter to the decay rates ratio through strong coupling system (Vuckovic and Yamamoto, 2003; Yoshie, et al., 2001).

On the other hand, cavities that contain slightly misaligned QDs position show PL enhancement but low quality factor mode Q=233 as illustrated in Fig. 6 (red curve before and black curve after introducing QDs layer).

http://dx.doi.org/10.14500/aro.10810

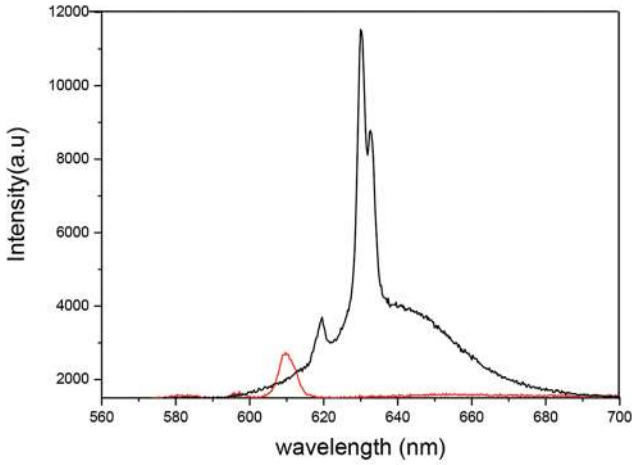

Fig. 6. Photo lumens (PL) spectrum for L3 cavity modes before introducing CdSe quantum dots (QDs) (red curve) and after introducing a thin layer of CdSe QDs (black curve). Here, QDs emission modes are slightly misaligned with cavity modes. PL emission shows enhancement but low Q factor 233.

VI. Summery

PC cavity-QD emitters system is a good platform to study light matter interaction. Mode field enhancement was observed in the order of 2.3-fold at 629.5 nm which occurs when the QD and the cavity are in resonant and the QD is spatially aligned to the cavity mode. The advantages of the used technique are the low cost and limitation of using chemicals, however, it is difficult to locate QDs at a desirable position due to random distribution of the QDs during the coating process. Using semiconductor, QDs as a gain material can improve the effective light matter interactions through nanolasers performance.

References

Arakawa, Y. and Sakaki, H., 1982. Multidimensional quantum well laser and temperature dependence of its threshold current. *Applied Physics Letters*, 40(11), pp.939-941.

Arakawa, Y., Iwamoto, S., Nomura, M., Tandaechanurat, A. and Ota, Y., 2012. Cavity quantum electrodynamics and lasing oscillation in single quantum dot-photonic crystal nanocavity coupled systems. *IEEE Journal of Selected Topics in Quantum Electronics*, 18(6), pp.1818-1829.

Balanis, C.A., 2012. *Advanced Engineering Electromagnetics*, 2nd ed. John Wiley and Sons Comp., Hoboken, NJ, USA.

Boroditsky, M., Vrijen, R., Krauss, T., Coccioli, R., Bhat, R. and Yablonovitch, E., 1999. Spontaneous emission extraction and purcell enhancement from thin-film 2-D photonic crystals. *Journal of Light Wave Technolegy*, 17(11), p.6424901.

Chang, E., Sorensen, S., Hemmer, R. and Lukin, D., 2006. Quantum optics with surface plasmons. Physical Review Letters, 97, p.053002.

Chang, S. and Chuang, S.L., 2009. Fundamental formulation for plasmonic nanolasers. *IEEE Journal of Quantum Electronics*, 45(11), pp.1014-1023.

Daveau, R., Balram, K., Pregnolato, T., Liu, J., Lee, E., Song, J., Verma, V., Mirin, R., Nam, S., Midolo, L., Stobbe, S., Srinivasan, K. and Lodahl, P., 2017. Efficient fiber-coupled single-photon source based on quantum dots in a photonic-crystal waveguide. *Optica*, 4(2), pp.178-184.

Englund, D., Fattal, D., Waks, E., Solomon, G., Zhang, B., Nakaoka, T., Arakawa, Y., Yammamoto, Y. and Vučković, J., 2005. Controlling the spontaneous emission rate of single quantam dots in two dimentional photonic crystal. *Physical Review Letters*, 95(1), pp.013904-013908.

Gong, Y. and Vučković, J., 2007. Design of plasmon cavities for solid-state cavity quantum electrodynamics applications. Applied Physics Letters, 90, p. 033113.

Lakowicz, J., Malicka, J., Gryczynski, I., Gryczynski, Z. and Geddes, C., 2003. Radiative decay engineering: The role of photonic mode density in biotechnology. *Journal of Physics D*, 36(14), p.R240-R249.

Li, X., Smalley, J., Li, Z. and Gu, Q., 2018. Effective modal volume in nanoscale photonic and plasmonic near-infrared resonant cavities. *Applied Sciences*, 8, p.1464.

Mahmoodian, S., Lodahl, P., and Sørensen, A., 2016. Quantum networks with chiral-light-matter interaction in waveguides. *Physical Review Letters*, 117, p.240501.

Oulton, R., Sorger, V., Zentgraf, T., Ma, R., Gladden, C., Dai, L., Bartal, G. and Zhang, X., 2009. Plasmon lasers at deep sub-wavelength scale. *Nature*, 461, pp. 629-632.

Purcell, E., 1948. Spontaneous emission probabilities at radio frequencies. *Physical Review*, 69, p.681.

Reithmaier, J., Sek¸ J., Loffler, A., Hofmann, C., Kuhn, S., Reitzenstein, S., Keldysh, L., Kulakovskii, V., Reinecke, T. and Forchel, A., 2004. Strong coupling in a single quantum dot-semiconductor microcavity system. *Nature*, 432(7014), pp.197-200.

Ryu, Y. and Notomi, M., 2003. Enhancement of spontaneous emission from the resonant modes of a photonic crystal slab single-defect cavity. *Optics Express*, 28(23), pp.2390-2392.

Schulz, K., Vu, H., Schwaiger, S., Rottler, A., Korn, T., Sonnenberg, T., Kipp, T. and Mendach, S., 2016. Controlling the spontaneous emission rate of quantum wells in rolled-up hyperbolic metamaterials. *Physical Review Letters*, 117, p.085503.

Shambat, G., Ellis, B., Majumdar, A., Petykiewicz, J., Mayer, M., Sarmiento, T., Harris, J., Haller, E. and Vučković, J., 2011. Ultrafast direct modulation of a single-mode photonic crystal nanocavity light-emitting diode. *Nature Communions*, 2, p.539.

Vuckovic, J. and Yamamoto, Y., 2003. Photonic crystal microcavities for cavity quantum electrodynamics with a single quantum dot. *Applied Physics Letters*, 82(15), p.2374.

Wei, W., Yan, X., Liu, J., Shen, B., Luo, W., Ma, X. and Zhang, X., 2019. Enhancement of single-photon emission rate from InGaAs/GaAs quantum-dot/nanowire heterostructure by Wire-Groove nanocavity. *Nanomaterials* (Basel, Switzerland), 9(5), p.671.

Yakimov, I., Kirienko, V., Bloshkin A., Utkin, E. and Dvurechenskii, V., 2021. Near-infrared photoresponse in Ge/Si quantum dots enhanced by photon-trapping hole arrays. *Nanomaterials*, 11(9), p.2302.

Yoshie, T., Scherer, A., Hendrickson, J., Khitrova, G., Gibbs, H., Rupper, G., Ell, C., Shchekin, O. and Deppe, D., 2004. Vacuum Rabi splitting with a single quantum dot in a photonic crystal nanocavity. *Nature*, 432, pp.200-203.

Yoshie, T., Vuc˘kovic, J. and Scherer, A., 2001. High quality two-dimensional photonic crystal slab cavities. *Applied Physics Letters*, 79(26), p.4289.

 http://dx.doi.org/10.14500/aro.10870

Comparative Quality Analysis between Tap Water and Bottled Water: A Case Study of Koya City in Iraq

Hanaa A. Muhammad[1], Khalid N. Sediq[2], and Kwestan H. Sdiq[3]

[1]Department of Biology, Faculty of Science and Health, Koya University, Koya KOY45, Kurdistan Region – F.R. Iraq

[2]Department of Physics, Faculty of Science and Health, Koya University, Koya KOY45, Kurdistan Region – F.R. Iraq

[3]Department of Medical Microbiology, College of Health Science, Hawler Medical University, Erbil, Kurdistan Region – F.R. Iraq

***Abstract*—Recently, bottled water consumption has been increasing significantly, even when the quality of tap water is considered excellent, which contribute for plastic pollution. Besides, reducing the use of plastic generally is recommended world widely, as its consumption is in an alarming rate. Therefore, this study aims to compare between the tap and bottled water and manifest the reasons behind choosing the bottled water which is less comfortable and often more expensive over the tap water. In this study, samples have been taken from both bottled and tap water in Koya city from November 2020 to May 2021 to test their quality using potential hydrogen, dissolved oxygen (DO), electrical conductivity, and total dissolved solids (TDS) meter, hardness was determined by complexometric titration method at 21°C, and X-ray fluorescence spectrometers. According to the quality standards, most of the variables were in a permissible range, except for DO and aluminum content in both types of water and TDS for two types of bottled water. However, the quality of tap water was much safer to be used, as compared with the bottled water.**

***Index Terms*—Dissolved oxygen; Total dissolved solid; Electrical conductivity; Potential hydrogen; Total alkalinity**

1. Introduction

Water is vital for human survival and existence of life on earth, therefore using it is imperative; 70% of humans' body is water, urine and sweat are the main cause of losing much of this water, hence hydration is crucial at all times. Besides, flushing bacteria out of a bladder, carrying oxygen and nutrient to the cells, aiding digestion, preventing constipation, maintaining the electrolyte balance, etc., are all carried out by water, thus it helps improve health (Qian, 2017). The aim of providing potable water was successful by the majority of the governments in the world, nonetheless, bottled water consumption has risen globally, for example, Asia which was the largest regional market in 2001 (Ferrier, 2001).

ARO-The Scientific Journal of Koya University
Vol. IX, No.2 (2021), Article ID: ARO.10870, 4 pages
DOI: 10.14500/aro.10870
Received: 05 September 2021; Accepted: 16 October 2021
Regular research paper; Published: 08 November 2021
Corresponding author's email: hanaa.muhammad@koyauniversity.org

As stated by Qian in 2017, there are two main reasons behind concerning about bottled water consumption, which are: Production and distribution energy requirements; and plastic pollution, therefore it is better to be replaced by filtered or tap water. In this study, drinking water choices of Koya city has been explored and examined the factors that determine their choices. Empirical study has been carried out in four different places throughout the city for tap water, and four samples from different companies of making bottled water. Despite the fact that the quality of the municipal tap water is potable, yet the choice as major drinking water source was personal to choose between tap and bottled water. Hence, this comparative study was conducted to address the current behaviors of drinking water choices in Koya city; factors that determine the drinking water choices of people; and motivating people to consume less bottled water and concern about the environment by manifesting the quality test of the water samples from both types.

II. Materials and Methods

Four samples from Tap water have been collected from different stations throughout the city (General Hospital, Iskan, Hamamok, and Koya University campus); in addition, samples from four different companies of making bottled water which were frequently consumed by the citizen of Koya city were taken from November 2020 to May 2021.

Laboratory tube has been used during collecting the samples and kept under a temperature of 4°C, then these samples directly were taken to the laboratory to quantify the following variables at 21°C: Potential hydrogen (pH), total alkalinity (TA), electrical conductivity (EC), total dissolved solids (TDS), total hardness (TH), and dissolved oxygen (DO). Besides, X-ray fluorescence (XRF) has been used to indicate the existence of some other minerals in the samples.

III. Results and Discussion

A. pH

pH takes the lead in clarification process and disinfection of clean water. PH of the tap water samples was ranged from

6.4 to 7.7; however, it was from 6.1 to 6.6 for the bottled water samples as it is shown in Table 1. Therefore, most of the water samples were found to be in the permissible range of pH value that recommended by the World Health Organization and Environmental Protection Agency in 2006 which is from 6.5 to 8.5 except for the one type of bottle water samples which was just under 6.5.

B. TA

Alkalinity of water is a measure of how much acid it can neutralize (EPA, 2006). For this test, phenolphthalein and methyl red have been used as an indicator. In general, all the samples from both bottled and tap water as it has been demonstrated in Table 2, were in a permissible range which is from 84 to 110 mg/l of CaCO3. Based on Trick et al.'s research in 2018, the alkalinity of water is due to only bicarbonate (HCO_3^-) when the presence of hydroxyl (OH^-) is zero, which is the case here for all the samples of both Tap and Bottled water.

C. TH

TH is the existence of minerals that dissolved in water. Besides, the levels of Ca^+_2, Mg^+_2, and HCO_3^- ions increase if the water passes over or through deposits, for instance, Limestone or Gypsum which consequently turns the water into hard water (WHO, 2011). For this test, ammonium purpuras have been used as indicator. Depend on WHO standard in 2006 all the samples were considered to be soft (from 40 to 65 mg/l) except for the University area which was fluctuating from 70 to 77 mg/l (Table 3). They are all in a suitable range for a good quality of water though.

D. EC

Water pollution can be detected when the value of EC is high (Xianhong, et al., 2021). EC of the tap water was fluctuated between 297 to 570 uS/cm, whereas it ranged from 136 to 340 uS/cm for the bottled water (Table 4). Therefore, the conductivity value is considered to be safe as for both types of water except for the University as the range should not exceed 400 µS/cm based on the WHO slandered in 2006.

E. TDS

It shows the sum of dissolved solids and minerals which is entered to the water naturally or artificially (Hayashi, 2004). In spite of the water of Hamamok and Iskan (which starts from 190 to 198 mg/l respectively), University and Hospital water contain higher amount of TDS (ranges from 202 to 365 mg/l respectively). Besides, the same difference has been noticed among the bottled water samples. B4 contains the most amount of TDS (about 217.1 mg/l), whereas the rest were fluctuated from 88 to 102 mg/l (Table 5).

Depend on the WHO in 1996, the rate of TDS should be <1000 mg/l, yet a very low rate (<100 mg/L) gives a flat, insipid taste to the water. High concentration of TDS may

Table I
Illustrates pH for the Samples of Both Tap and Bottled Water

Samples	November	December	January	February	March	April
Bottled water						
B1	6.2	6.31	6.32	6.30	6.1	6.0
B2	6.5	6.54	6.6	6.55	6.5	6.43
B3	6.51	6.52	6.52	6.5	6.5	6.4
B4	6.45	6.46	6.5	6.44	6.48	6.5
Tap water						
General Hospital	6.6	6.67	6.7	6.61	6.6	6.5
Iskan	7.6	7.7	7.7	7.47	7.45	7.4
Hamamok	6.43	6.45	6.5	6.5	6.5	6.4
Koya University	6.5	6.5	6.55	6.5	6.5	6.45

Table II
Shows Total Alkalinity in Mg/L for the Samples of Both Tap and Bottled Water

Samples	November	December	January	February	March	April
Bottled water						
B1	90	90	91	92	92	93
B2	85	84	86	87	86	86
B3	88	89	90	90	90	90
B4	88	88	89	89	90	90
Tap water						
General Hospital	92	91	95	96	98	98
Iskan	108	108	101	109	109	110
Hamamok	98	90	91	99	99	100
Koya University	100	100	101	100	102	101

Table III
Demonstrate The Total Hardness In Mg/L, for the Samples of Both Tap and Bottled Water

Samples	November	December	January	February	March	April
Bottled water						
B1	55	55	50	56	56	56
B2	40	41	41	41	41	41
B3	41	40	40	42	43	43
B4	42	42	44	45	45	45
Tap water						
General Hospital	48	48	48	50	50	49
Iskan	60	60	61	65	64	65
Hamamok	60	62	60	60	60	64
Koya University	70	71	71	72	76	77

Table IV
Represents EC in us/cm for the Samples of Both Tap and Bottled Water

Sample	November	December	January	February	March	April
Bottled water						
B1	160	158.5	158	159	159	160
B2	140	138.1	138	139.7	140	140.5
B3	140	136	135.6	137.9	138	138
B4	341	336	335	338	338	340
Tap water						
General Hospital	320	316	316	317	320	322
Iskan	310	305	305	308	308	309
Hamamok	300	298.1	297	299	301	301
Koya University	568	568.1	567	569	569	570

http://dx.doi.org/10.14500/aro.10870

Table V
Demonstrates TDS in mg/l for the Samples of Both Tap and Bottled Water

Samples	November	December	January	February	March	April
Bottled water						
B1	102.4	101.4	101.12	101.76	101.7	102
B2	89.9	88.38	88.3	89.4	89.5	89.5
B3	89.6	87.1	86.8	87.68	87.8	90
B4	218.2	215.1	214.4	216.32	217	217.1
Tap water						
General Hospital	204.8	202.2	202.3	202.88	203.45	203.67
Iskan	198.4	195.2	195.2	197.2	198.3	198.5
Hamamok	192	190.8	190.1	191.36	190.6	192.3
Koya University	363.5	363.6	362.8	364.16	364.3	364.8

Table VI
Shows Do in mg/l for the Samples of Both Tap and Bottled Water

Samples	November	December	January	February	March	April
Bottled water						
B1	2.5	2.6	2.5	2.48	2.3	2.29
B2	0.6	0.65	0.7	0.61	0.5	0.5
B3	2.4	2.4	2.5	2.23	2.2	2.2
B4	2.4	2.5	2.4	2.35	2.35	2.33
Tap water						
General Hospital	5.3	5.4	5.5	5.45	5.4	5.2
Iskan	5.5	5.5	5.6	5.56	5.56	5.3
Hamamok	6.5	6.6	6.6	6.56	6.55	6.44
Koya University	5.7	5.8	5.7	5.60	5.55	5.53

cause problems whom suffer from kidney and heart diseases, (Meride and Ayenew, 2016). Thus, it is considered to be lower than the permissible range for both B2 and B3

F. DO

The high concentrations of oxygen in water indicate good quality. DO is temperature and somewhat on atmospheric pressure dependence, similarly, EC, TDS, Salinity, and oil and grease decreases the rate of DO exponentially (Sen Gupta and McNeil, 2012). Based on the measurements, DO from the tap water samples were fluctuated from 5.2 to 6.6 mg/l whereas its range for the bottled water was from 0.6 to 2.6mg/l as it represented in Table 6. Despite of the tap water, bottled water considered being under the standard limit of EPA (Chapman, 1986) (5–9 mg/L) this might be due to the Biochemical oxygen demand (BOD) that occurs from the beginning of preserving water inside the bottle. Whereas, aeration helps the rivers reoxygenate that mostly tap water comes from.

G. Element Contents

The WHO in 2006 declared that the concentration of some minerals is crucial to life, for instance, the high concentration of Arsenic, Fluoride, and aluminum leads to many different type of disease, such as, cancer, teeth mottling, and Alzheimer. For this test, XRF has been used to determine the amount of the minerals that exist in the water (Fig. 1). Samples from both B1 and B2 as the bottled water, and General Hospital (Tap 1) and the university area (Tap2) as

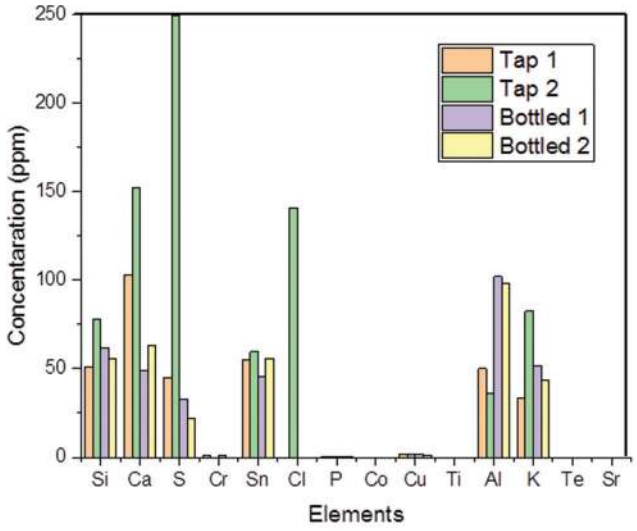

Fig. 1: X-ray fluorescence for the element concentration in ppm for the samples of both tap and bottled water.

the Tap water have been taken as they were found to contain higher amount of TH, EC, and TDS compare to the rest of the samples. In this test, Al was found to be present in a high concentration in both bottled and tap water; however, its concentration is much higher in a bottle water. This might be due to the use of the aluminum salt as coagulants for reducing the level of organic matter, color, turbidity, and microorganism (WHO, 2006)

IV. Conclusion

Since scientists developed water quality criteria to provide basic scientific information about the effects of pollutants in water, and to describe the requirements to protect and maintain an individual use (Enderlein, Enderlein and Williams, 1997). Therefore, testing the water that uses by the consumers or residents is essential.

Recently, plastic pollution in both land and water is a colossal concern world widely, which contributed by bottled water. To tackle this problem, this study has been done which could enhance raise awareness to reduce the usage of bottled water and return back the trust of tap water.

Based on the results from tests that were required for this comparative study between four different stations for the tap water and four different companies of making bottled water samples throughout Koya city, the quality of tap water is much higher compare to the bottled water. For instance, the amount of Al and TDS were too high for the bottled water which could cause a real damage to health, beside the low amount of DO existed in them.

Hence, the tap water is of a higher quality, environmentally friendly choice, and cheaper option, why would people still use the bottled water? Is it because of the taste and/or Personal and Family Habits, easy to get mostly everywhere? Or is it due to the quality that they have been objected to it through the media? To deal with these questions and answer them properly, it's crucial for

the government to educate our nation by schooling them about the water quality which mainly depends on these variables: pH, total alkalinity, T.H, TDS, EC, DO, and mineral content, and the damage they may cause to the environment through the plastic pollution.

References

Chapman, G., 1986. *Ambient Water Quality Criteria for Dissolved Oxygen, EPA-440/5-86-003*. U. S. Environmental Protection Agency, Washington, D.C. Available from: https://www.who.int/water_sanitation_health/resourcesquality/wpcchap2.pdf. [Last accessed on 10 Aug 2021].

Enderlein, U., Enderlein, R. and Williams, W., 1997. In: World Health Organization, editor. *Water Pollution Control: A Guide to the Use of Water Quality Management Principles*. E & FN Spon, London, pp.9-47. Available from: https://www.apps.who.int/iris/handle/10665/41967. [Last accessed on 10 Aug 2021].

Environmental Protection Agency (EPA) on pH and Alkalinity, 2006. *Volunteer Estuary Monitoring a Methods Manual*. 2nd ed. Environmental Protection Agency, Washington, DC, United States, pp.185-196. Available from: https://www.epa.gov/sites/default/files/2015-09/documents/2007_04_09_estuaries_monitoruments_manual.pdf. [Last accessed on 10 Aug 2021].

Ferrier, C., 2001. Bottled water: Understanding a social phenomenon. *AMBIO: A Journal of the Human Environment*, 30(2), pp.118-119.

Hayashi, M., 2004. Temperature-electrical conductivity relation of water for environmental monitoring and geophysical data inversion. *Environmental Monitoring and Assessment*, 96, pp.119-128. Available from: https://www.link.springer.com/article. [Last accessed on 10 Aug 2021].

Meride, Y. and Ayenew, B., 2016. Drinking water quality assessment and its effects on resident's health in Wondo genet campus, Ethiopia. *Environmental Systems Research*, 5(1), p.35.

Qian, N., 2017. Bottled water or tap water? A comparative study of drinking water choices on University Campuses. *Water*, 10(1), p.59.

Sen Gupta, A. and McNeil, B., 2012. Variability and change in the ocean. In: Henderson-Sellers, A. and McGuffie, K., editors. *The Future of the World's Climate*. 2nd ed., Ch. 6. Elsevier, Boston, pp.141-165.

World Health Organization and International Programme on Chemical Safety, 1996. *Guidelines for Drinking-Water Quality*. 2nd ed., Vol. 2. World Health Organization, Geneva. Available from: https://www.file:///c:/users/high%20tech/downloads/9241544805.pdf. [Last accessed on 10 Aug 2021].

World Health Organization and International Programme on Chemical Safety, 2006. *Guidelines for Drinking-Water Quality* [*Electronic Resource*]: *Incorporating First Addendum*. 3rd ed., Vol. 1. World Health Organization, Geneva. Available from: https://www.who.int/water_sanitation_health/dwq/gdwq0506.pdf. [Last accessed on 10 Aug 2021].

World Health Organization and International Programme on Hardness in Drinking-Water, 2011. *Guidelines for Drinking-Water Quality*. World Health Organization Press, Geneva. Available from: https://www.who.int/water_sanitation_health/dwq/chemicals/hardness.pdf. [Last accessed on 10 Aug 2021].

Xianhong, Y., Shijun, L., Jian, H. and Jie, X., 2021. Application analysis of conductivity in drinking water quality analysis. *IOP Conference Series: Earth and Environmental Science*, 784(1), p.012028.

http://dx.doi.org/10.14500/aro.10852

The Study of Optical and Electrical Properties of Nanostructured Silicon Carbide Thin Films Grown by Pulsed-Laser Deposition

Muhanad A. Ahmed[1], Mohammed M. Sabri[2], Wathiq R. Abed[1]

[1]Department of Electrical Techniques, Institute of Technology, Middle Technical University, Baghdad, Iraq

[2]Department of Physics, Faculty of Science and Health, Koya University Koya KOY45, Kurdistan Region - F.R. Iraq

***Abstract*—In this paper, nanostructured silicon carbide (SiC) thin films are deposited onto glass substrate using pulsed laser deposition technique. Electrical and optical characterizations such as conductivity, resistivity, transmission, Seeback effect, absorption, absorption coefficient, energy band gap, and extinction coefficient as a function of photon energy, and the effect of thin films thickness on transmission are carried out to characterize the prepared samples. Results showed that the prepared SiC thin film is an n-type semiconductor with an indirect bandgap of ~3 eV, 448 nm cutoff wavelength, 3.4395 × 10^4 cm^{-1} absorption coefficient and 0.154 extinction coefficient. The surface morphology of the SiC thin films is studied using scanning electron microscope at a substrate temperature of 400°C and it is found that the grain size of the prepared SiC thin film is about 30 nm. As such, the nano thin films optical and structural characteristics enable the films to be used as gases sensors in many optoelectronic devices such as the environment and ultraviolet photodiode.**

***Index Terms*—Nanostructure, Pulsed laser deposition, Silicon carbide, Thin film.**

I. Introduction

Due to their potential application in many forms of optoelectronic devices such as photodiodes, image sensors and solar cells, crystalline silicon carbide (SiC) thin films have attracted a considerable attention in recent years (Jha and Agarwal, 2015; Phan, et al., 2015 and Xu, et al., 2020). Pulsed-laser deposition (PLD) (Ahmed, Sabri and Mohammad, 2020) is now an established technique for the production of a wide range of thin films (Zakaria, et al., 2020 and Wang, et al., 2021). High quality ceramic films can be produced by PLD technique at much lower temperatures compared to that produced by other techniques. Nowadays, Radio Frequency (RF) sputtering technique and Neodymium-Doped Yttrium Aluminum Garnet (Nd-YAQ) laser typically perform films screened by PLD (Gupta, Sauer and Tsui, 2013). The energy from the photons depends on the type of the gas mixture used to create the Nd-YAG. For instance, when Nd-YAG is used, photons of energy 4-eV are released. PLD technique is performed in a high-vacuum atmosphere and the synthesized film and target material have the similar stoichiometric ratio, which can realize the growth of multilayer film and superlattice on the atomic level clean interface in the similar cavity, with a huge application range, easy control, quick growth rate, and adjustable deposition parameter (Chen, et al., 2009). Recently, PLD has been widely used for the fabrication of various technological devices photovoltaic cells and light emitting diodes (Ogugua, Ntwaeaborwa and Swart, 2020). In addition, PLD films have applied as protective barriers in corrosive atmosphere. All these applications made PLD a unique technique for growing complex and multi-component ceramic thin films.

SiC is an IV-IV compound material with unique physical and chemical properties. The strong chemical bonding between Si and C atoms gives this material high hardness, chemical inertness, and high thermal conductivity (Kimoto and Cooper, 2014). As a semiconductor, SiC exhibits a wide band gap (2.2 eV–3.2 eV), high breakdown field (>20 × 10^5 V cm^{-1}), good thermal conductivity (5 W cm^{-1} K^{-1}–7 W cm^{-1} K^{-1}), and high mobility (10^3 cm^2/Vs). Among the various types of SiC, cubic SiC (3C-SiC) has a crystal structure of great interest for piezoresistive applications such as pressure sensors (Dao, et al., 2016), advanced bioelectronic devices (Saddow et al., 2014), electrochemical applications (Yang and Jiang, 2019), and photovoltaic applications (Rasheed, et al., 2020). SiC provides a variety of optical and electronic applications (Majidi, et al., 2018 and Abderrazak and Hmida, 2011). All the above-mentioned properties and applications make SiC a promising material for manufacturing of high temperature, high frequency, and high-power devices (Liu, Tuttlr and Dhar, 2015 and Ho, et al., 2012). The electrical engineering sector

ARO-The Scientific Journal of Koya University
Vol. IX, No.2 (2021), Article ID: ARO.10852, 5 pages
DOI: 10.14500/aro.10852
Received: 09 August 2021; Accepted: 18 October 2021
Regular research paper; Published: 10 November 2021
Corresponding author's email: muhanad.adil@mtu.edu.iq

including high voltage requirements could therefore be able to replace Si power transistors, thermistors, and rectifiers with SiC devices in the future (Rabkowski, Peftitsis and Nee, 2012). SiC crystal growth has then been undergone several progresses to contribute in industrial wafers and epitaxial structures (Kimoto, 2016). Furthermore, the optimum performance of microwave systems is related to ohmic contact accuracy, low contact strength, and a high temperature stability (Phan, et al., 2017). In addition, the interest of SiC and its various types have rapidly increased including various applications in optoelectronic devices and electronic such as semiconductors lasers, solar cells, modulators, and detectors, which mainly operates under high frequency, high temperature conditions, high power, and intensive radiation. Simple α-SiC is an endogenous semiconductor with an energy band gap of 2.2 eV to render it an extremely poor electrical conductor (~ 10 $\Omega^{-1}.cm^{-1}$–13 $\Omega^{-1}.cm^{-1}$). These together with its chemical and mechanical stability accounts for its extensive use during the heating elements of electricity. Furthermore, a high temperature semiconductor such as pure β-SiC (band gap = 3.3 eV) has different applications in electro-luminescent diodes, diode rectifiers, transistors, and also in the future nuclear systems (Li, et al., 2018 and Aristov, 2001).

The main objective of this work is synthesizing SiC thin film by the usage of PLD technique and then studying the important properties of this material.

II. Experimental Details

It has been demonstrated that the PLD technique reproduces the target's stoichiometry. Herein, a 100 μm sieve was sieved 5 g of β-SiC material. The high purity (99.999%) SiC powder was pressed under 5 tons to obtain the targeted shape with a diameter of 2.5 cm and a thickness of 0.4 cm. The aim should be as dense and homogeneous as possible to ensure a good deposit quality and be used to deposit a thin SiC film on a glass slide. The glass slides that used as substrates have the area of 3 × 2 cm^2. To remove impurities and residuals from their surfaces, the glass slides were cleaned using alcohol with ultrasonic waves generated by Cerry PUL for 15 min. The Nd-YAG laser wavelength was at 532 nm and with pulse width of 7 ns and operates at up to 10 Hz.

The laser beam at a fluence of 1.5 J/cm^2 was centered on a high purity SiC target. The substrates were located 6 cm away from the SiC target. A diffusion pump was used, and the chamber was held at a vacuum pressure of 10^{-6} torr. To achieve single layer thin films, the SiC target was ablated from 10 to 100 pulses in 10 min – 20 min. The substrate temperatures (Ts) were preserved at 400°C during the deposition process. The following measurements were then included transmission and absorption spectrum, type of conductivity (σ) and resistivity (ρ) as functions of temperature, absorption coefficient (α) as function of photon energy (*hv*). In addition, the value and the nature of the energy band gap (E_g) of the formed SiC structure, the extinction coefficient (k_{ex}) at cutoff wavelength and the transmittance at different points at the inclined surface were also determined. Finally, the thickness and the morphology of the film were estimated from the cross-sectional scanning electron microscopy (SEM) of type SEM JEOL 7000.

III. Results and Discussion

Fig. 1 shows the transmission spectrum of the SiC thin film in the range of 300–900 nm wavelengths. Three distinguished regions are observed from this figure. First, in the ultraviolet (UV) range, the transmittance increases rapidly from 53.1% to about 80% within the range of 300 - 400 nm wavelengths, indicating that SiC thin film absorbs the UV wavelength well and the maximum absorption is included. In the second region, within the visible range (400 nm–700 nm), the transmittance is increasing slowly from 80% to 92.5% and the cutoff wavelength is included in this range. Hence, the absorption is mainly determined by the thickness of the SiC film according to Beer-Lambert law (Axelevitch, Gorenstein and Golan, 2012). Finally, and beyond 700 nm, the absorption is at the minimum and the SiC film is approximately transparent to the infrared (IR) wavelengths and this gives such films to be used as optical windows.

Fig. 2 shows the results of Seeback measurements, which confirm that the SiC film is n-type semiconductor. As can be seen from this figure, Seebeck voltage develops continuously with increasing the temperature until reaching a certain value at which this voltage remains constant (this is noticed at about −18 V in Fig. 2) due to the stability of electrical properties related to the density of carriers and the dimensions of the sample. Few research works have also been published reporting the Seebeck coefficient-temperature relationship of silicon carbide such as in (Wang, et al., 2003 and Ohba, Shimozaki and Era, et al., 2008). Moreover, full details about Seebeck effect, Seebeck coefficient, and Seebeck voltage can be found in Molki, 2010, Iwanaga, et al., 2011 and Babaei, et al., 2017.

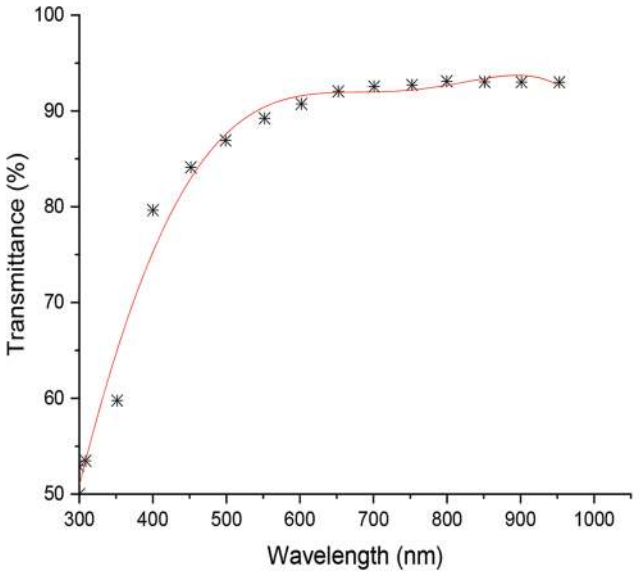

Fig. 1. Variation of silicon carbide thin film transmittance with the incident wavelength. The red line represents the fitting line.

http://dx.doi.org/10.14500/aro.10852

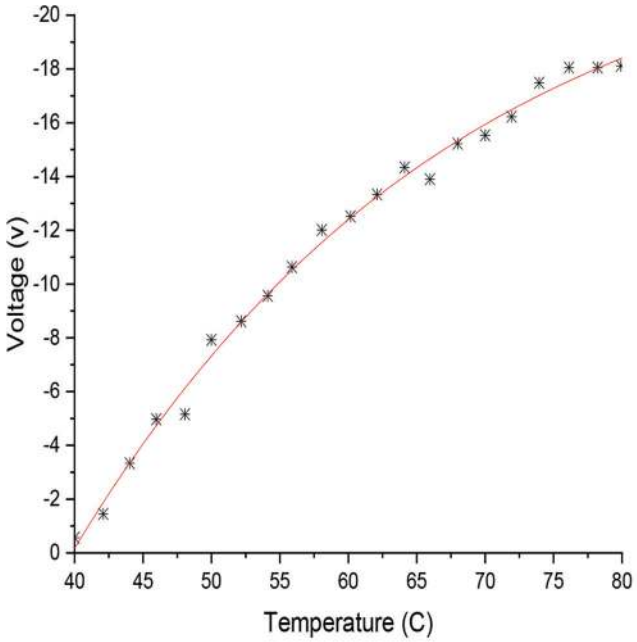

Fig. 2. Variation of Seebeck voltage with temperature. The red line represents the fitting line.

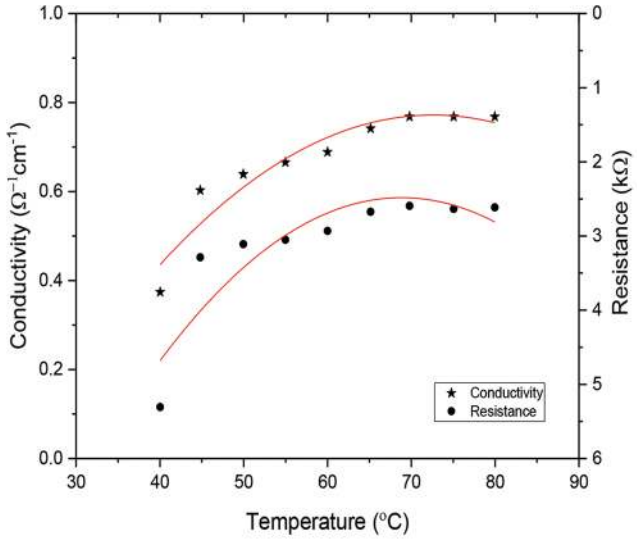

Fig. 3. Variation of the conductivity and resistance of silicon carbide thin film with temperature. The red line represents the fitting line.

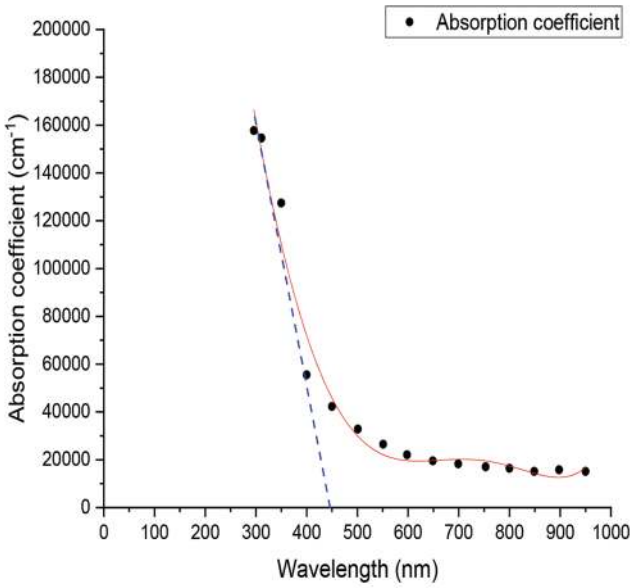

Fig. 4. Variation of absorption coefficient with the wavelength of the incident photon of silicon carbide thin film. The cutoff wavelength is 448 nm. The red line represents the fitting line.

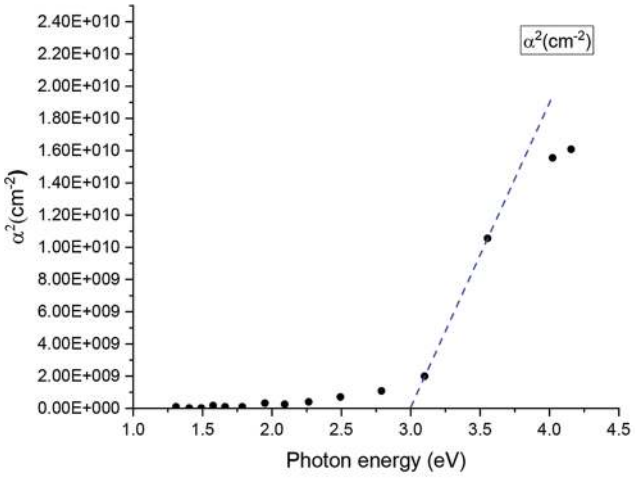

Fig. 5. Variation of α^2 with the incident photon energy of the silicon carbide thin film. The energy gap is about 3 eV.

Fig. 3 explains the variation of conductivity and resistance of the SiC thin film with temperature. Both properties are constant over the temperature of 70°C. This is due to the fact that the prepared thin film is characterized by the steady properties at the elevated temperatures.

Fig. 4 represents the relation of absorption coefficient (α) with photon wavelength (λ). The absorption coefficient drops rapidly within the range of 300 nm–600 nm assigning the minimum at about 448 nm which represents the cutoff wavelength (λ_{cutoff}).

Fig. 5, on the other hand, shows the value of the energy bandgap (E_g) of the SiC thin film, which is about 3 eV. Absorption processes (α^2) was graphed versus photon energy ($h\nu$). Consequently, the SiC thin film that prepared in this work has an indirect band-gap and the allowed fundamental absorption processes are the dominant.

Furthermore, the extinction coefficient (k_{ex}) is represented in Fig. 6 as a function of photon energy.

The typical value of k_{ex} at minimum absorption (448 nm) is around 0.154 (the black arrow in Fig. 6). Due to the inclination of the thin film deposition, the transmittance is supposed to change with the film thickness (The deposited film had a thickness of approximately 50 nm) on the inclined surface. Since we did not measure the film thickness at each point on the inclined surface, we measured the transmittance as the function of the incident wavelength then determine the relative transmittance at four different points on the inclined surface. Fig. 7 shows the decrease in transmittance as the

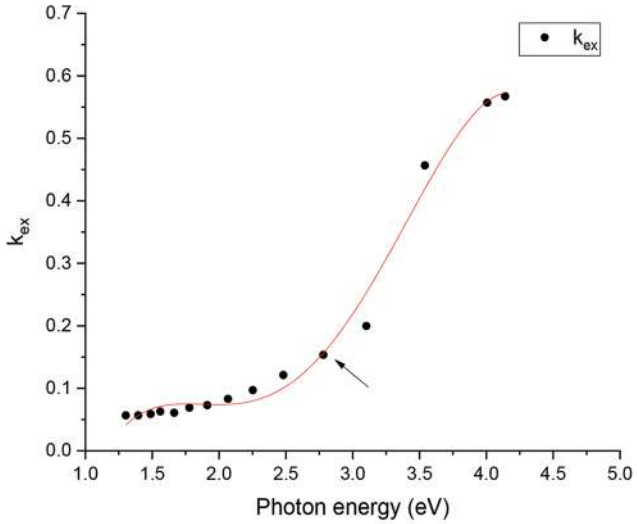

Fig. 6. Variation of the extinction coefficient (k_{ex}) with the incident photon energy. The red line represents the fitting line.

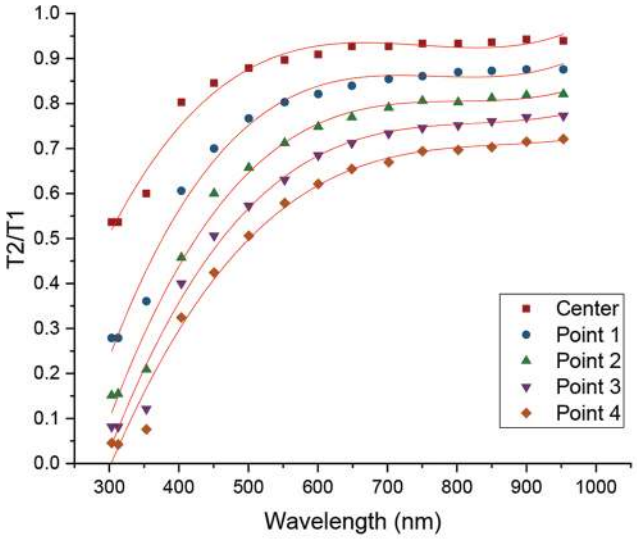

Fig. 7. Variation of the transmittance at center and different points on the inclined deposited thin films. The red lines represent the fitting lines.

thickness is increasing on the inclined surface. The first top line in Fig. 7 represents the center point followed by the other four points.

The thickness at each point at a certain wavelength can roughly be determined as follows:

$$I_1 = I_0 \exp(-ad_1) - - - -(1a)\, at\ thickness\ d_1$$

$$I_1 = I_0 \exp(-ad_P) - - - -\left(1b\right) at\ thickness\ d_P = ud_1$$

where u is the multiple of thickness at different point (p) than the center (d_1 = 50 nm). Then:

$$U = \frac{\ln T_P}{\ln T} \qquad (2)$$

where Tp and T are the transmittance at point p and the transmittance at the minimum thickness (50 nm), respectively. Hence, as transmittance decrease to about 4% at the last point (point 4), then we predict that the thickness at this point is 5 times thicker than that at the center.

Fig. 8. Scanning electron microscopy micrograph of silicon carbide nanostructure thin film at substrate temperature of 400°C.

Fig. 8 shows the SEM image of the SiC thin films prepared at a substrate temperature of 400°C. This image shows that the SiC nanoparticle was obtained in an agglomerated state and also the voids were occurred between the grains of the SiC thin films, which have a quite uniform and hole-free surface. The film has homogeneous surface morphology, with a grain size of about 30 nm and most particles are polyhedron-shaped with some facets.

IV. Conclusions

Nanostructured deposits of SiC were prepared in vacuum on glass substrates by nanosecond PLD at operating wavelength of 532 nm. Based on the obtained results, the deposited SiC films are of a high-transparent at visible and IR wavelengths, the electrical conductivity is of n-type and being constant at temperatures over 70°C, the experimental measured values included cut-off wavelength of 448 nm, the energy band-gap is indirect and of about 3 eV, the absorption coefficient of about 3.4395 × 10^4 cm^{-1} and the extinction coefficient of 0.154. The transmittance of such structure could be controlled by the thickness along the inclined surface, which is, in turn, a function of the substrate inclination angle. The surface morphology of the deposits SiC thin films has been studied using SEM and it was found that the film has homogeneous surface morphology with a grain size of about 30 nm at the Ts of 400°C. Such films are of a considerable impact in high-temperatures, high-power, and high-frequency applications. Therefore, this attempt may encourage to construct devices such as TFTs, detectors, solar cells, and optoelectronics.

V. Acknowledgment

Muhanad A. Ahmad expresses thanks and acknowledges to Oday Ata and Khalid Zakariya for their help during the experimental work.

References

Abderrazak, H. and Hmida E.S.B., 2011. Silicon carbide: Synthesis and properties. In: Gerhardt, R., (Ed.), *Properties and Applications of Silicon Carbide*. IntechOpen, London, United Kingdom. pp.361-388.

Ahmed, M.A., Sabri, M.M. and Mohammad, H.Q., 2020. Study of structural and optical properties of Cu2O thin film prepared by rapid thermal annealing using Nd-YAG laser. *NeuroQuantology*, 18, pp.15-22.

Aristov, V.Y., 2001. β-SiC (100) surface: Atomic structures and electronic properties. *Physics Uspekhi*, 44, pp.761.

Axelevitch, A., Gorenstein, B. and Golan, G., 2012. Investigation of optical transmission in thin metal films. *Physics Procedia*, 32, pp.1-13.

Babaei, F.H., Faramarz, Masoumi, S. and Noori, A., 2017. Seebeck voltage measurement in undoped metal oxide semiconductors. *Measurement Science and Technology*, 28, p.115002.

Chen, B., Yang, D., Charpentier, P.A. and Zeman, M., 2009. Al^{3+}-doped vanadium dioxide thin films deposited by PLD. *Solar Energy Materials and Solar Cells*, 93, pp.1550-1554.

Dao, D.V., Phan, H.P., Qamar, A. and Dinh, T., 2016. Piezoresistive effect of p-type single crystalline 3C-SiC on (111) plane. *Royal Society of Chemistry (RSC) Advances*, 6, pp.21302-21307.

Gupta, M., Sauer, V. and Tsui, Y.Y., 2013. Pulsed laser deposition of uniform semiconductor nanodot arrays. *Applied Physics A*, 110, pp.817-821.

Ho, C.N.M., Breuninger, H., Pettersson, S., Excobar, G., Serpa, L.A. and Coccia, A., 2012. Practical design and implementation procedure of an interleaved boost convertor using SiC diodes for PV applications. *IEEE Transactions on Power Electronics*, 27, pp.2835-2845.

Iwanaga, S., Toberer, E.S., LaLonde, A. and Snyder, G.J., 2011. A high temperature apparatus for measurement of the Seebeck coefficient. *Review of Scientific Instruments*, 82, pp.063905-063906.

Jha, H.S. and Agarwal, P., 2015. Highly crystalline silicon carbide thin films grown at low substrate temperature by HWCVD technique. *Journal of Materials Science: Materials in Electronics*, 26, pp.1381-1388.

Kimoto, T. and Cooper, J.A., 2014. *Fundamentals of Silicon Carbide Technology: Growth, Characterization, Devices and Applications*. John Wiley and Sons, New York, United States. pp.1-544.

Kimoto, T., 2016. Bulk and epitaxial growth of silicon carbide. *Progress in Crystal Growth and Characterization of Materials*, 62, pp.329-351.

Li, M., Zhou, X., Yang, H., Du, S. and Huang, Q., 2018. The critical issues of SiC materials for future nuclear systems. *Scripta Materialia*, 143, pp.149-153.

Liu, G., Tuttlr, B.R. and Dhar, S., 2015. Silicon carbide: A unique platform for metal-oxide-semiconductor physics. *Applied Physics Reviews*, 2, p.021307.

Majidi, S., Nezafat, N.B., Rai, D.P., Achour, A., Ghaziasadi, H., Sheykhian, A. and Solaymani, S., 2018. Optical and electronic properties of pure and fully hydrogenated SiC and GeC nanosheets: First-principles study. *Optical and Quantum Electronics*, 50, p.292.

Molki, A., 2010. Simple demonstration of the Seebeck effect. *Science Education Review*, 9, pp.103-107.

Ogugua, S.N., Ntwaeaborwa, O.M. and Swart, H.C., 2020. Latest development on pulsed laser deposited thin films for advanced luminescence applications. *Coatings*, 10, pp.1078-1100.

Ohba, Y., Shimozaki, T. and Era, H., 2008. Thermoelectric properties of silicon carbide sintered with addition of boron carbide, carbon, and alumina. *Materials Transactions*, 49, pp.1235-1241.

Phan, H.P., Cheng, H.H., Dinh, T., Wood, B., Nguyen, T.K., Mu, F., Kamble, H., Vadivelu, R., Walker, G., Hold, L., Iacopi, A., Haylock, B., Dao, D.V., Lobino, M., Suga, T. and Nguyen, N-T., 2017. Single-crystalline 3C-SiC anodically bonded onto glass: An excellent platform for high-temperature electronics and bioapplications. *American Chemical Society (ACS) Applied Materials and Interfaces*, 9, pp.27365-27371.

Phan, H.P., Dao, D.V., Wang, L., Dinh, T., Nguyen, N.T., Qamar, A., Tanner, P., Dimitrijev, S. and Zhu, Y., 2015. Strain effect on electrical conductance of P-type nanocrystalline silicon carbide thin film. *Journal of Materials Chemistry C*, 3, pp.1172-1176.

Rabkowski, J., Peftitsis, D. and Nee, H.P., 2012. Silicon carbide power transistors: A new era in power electronics is initiated. *IEEE Industrial Electronics Magazine*, 6, pp.17-26.

Rasheed, M.N., Maryam, A., Fatima, K., Iqbal, F., Afzal, M., Syvajarvi, M., Murtaza, H., Zhu, B. and Asghar, M., 2020. Enhanced electrical properties on nonstructural cubic silicon carbide with graphene contact for photovoltaic applications. *Digest Journal of Nanomaterials and Biostructures*, 15, pp.963-972.

Saddowa, S.E., Frewina, C.L., Reyesa, M., Registera, J., Nezafatia, M. and Thomasa, S., 2014. 3C-SiC on Si: A biocompatible material for advanced bioelectronic devices. *ECS Transactions*, 61, pp.101-111.

Wang, D., Yang, Y., Guo, T., Xiong, X., Xie, Y., Li, K., Li, B. and Ghali, M., 2021. Effect of pulse bias voltages on performance of CdTe thin film solar cells prepared by pulsed laser deposition. *Solar Energy*, 213, pp.118-125.

Wang, X.H., Yamamoto, A., Eguchi, K., Obara, H. and Yoshida, T., 2003. Thermoelectric properties of SiC thick films deposited by thermal plasma physical vapor deposition. *Science and Technology of Advanced Materials*, 4, pp.167-172.

Xu, Z., Tao, K., Jiang, S., Jia, R., Li, W., Zhou, Y., Jin, Z. and Liu, X., 2020. Application of polycrystalline silicon carbide thin films as the passivating contacts for silicon solar cells. *Solar Energy Materials and Solar Cells*, 206, p.110329.

Yang, N. and Jiang, X., 2019. Cubic silicon carbide: Growth, properties, and electrochemical applications. In: *Novel Carbon Materials and Composites*. Wiely, Hoboken, New Jersey, pp.1-33.

Zakaria, M.A., Menazea, A.A., Mostafa, A.M. and Al-Ashkar, E.A., 2020. Ultra-thin silver nanoparticles film prepared via pulsed laser deposition: Synthesis, characterization, and its catalytic activity on reduction of 4-nitrophenol. Surfaces and Interfaces, 19, p.100438.

Seroprevalence of Severe Acute Respiratory Syndrome-Coronavirus-2 Immunoglobulin M and Immunoglobulin G Antibodies among the Population of Koya University

Safia S. I. Blbas[1], Hiwa A. Ahmad[1], Dawan J. Hawezy[2], Hemn Shawgery[2], Hersh N. Bahadin[2]

[1]Department of Medical Microbiology, Faculty of Science and Health, Koya University, Koya KOY45, Kurdistan Region - F.R. Iraq

[2]School of Medicine, Koya University, Koya KOY45, Kurdistan Region - F.R. Iraq

***Abstract*–Coronavirus is a pandemic disease. In most cases, the exact infection rate cannot be determined as not everybody can be tested for the virus, even though some of them carry the virus silently. Therefore, detection of antibodies of this virus is more practical to give us a better clue about the rate of infection because the asymptomatic people can be tested too. The serological detection of anti-Severe Acute Respiratory Syndrome-Coronavirus (SARS-COV-2) antibodies among asymptomatic and moderate symptomatic individuals gives us the vital point to understanding the prevalence rate of COVID-19 among the population. Total of (436) volunteers were participated, (96) from teaching staff, (172) employee, and (168) students. Anti-SARS-COV-2 immunoglobulin G (IgG) and Immunoglobulin M (IgM) were detected in the serum by ELISA technique, and complete blood count was performed for all participants. The number of seropositive of anti-SARS-COV-2/ IgG was (159), whereas IgM was (66). The highest prevalence rate of IgG detected among participants with family member infected with coronavirus (42.7%). Total WBCs count significantly increased among IgM positive participants. Many asymptomatic people were infected with coronavirus, which lead to more spreading of the virus among the population. Therefore, mass screening of the population for specific antibody against coronavirus is important to reduce the infection rate.**

***Index Terms* — Anti-severe acute respiratory syndrome-coronavirus-2 Antibody, Coronavirus, Coronavirus disease-19, Immunoglobulin G, Immunoglobulin M.**

ARO-The Scientific Journal of Koya University
Vol. IX, No.2 (2021), Article ID: ARO.10831, 07 pages
DOI: 10.14500/aro.10831
Received: 19 June 2021; Accepted: 17 October 2021
Regular research paper: Published: 22 November 2021
Corresponding author's email: safia.ibrahim@koyauniversity.org

I. Introduction

As a zoonosis that has spread to several million human beings and probably to domestic and wild animals, the world has witnessed waves of coronavirus infection threatening the global catastrophe of Severe Acute Respiratory Syndrome (SARS) in 2002–2003 and Middle East Respiratory Syndrome in 2011 (MERS). In both cases, newly described coronaviruses of the genus Beta-coronavirus with zoonotic origins were causative agents. In Wuhan, Hubei, China, an outbreak of another coronavirus that causes pulmonary disease has been announced in late of 2019.

The disease officially called Coronavirus Disease 2019 (COVID-19), SARS-COV-2 (etiological agent of COVID-19) genome sequences analysis demonstrated close to the genomic structure of both MERS and SARS-COV (Wu, et al., 2020; Azkur, et al., 2020). The recent study done by Dimonte et al. (2020) illustrated that the phylogenic tree analysis by sequencing the amino acids associated with the structural proteins of the novel coronavirus (nCOV) almost indistinguishable from the SARS-COV, which founded among the different area (Dimonte, et al., 2020).

COVID-19 is transmissible between humans through nasal particles or close contact in both clinical and subclinical persons (Lauer, et al., 2020). The first case of COVID-19 recorded in Iraq, on February 24, 2020, was registered in Najaf province for a student who had travelled from Iran, followed by four cases of one family members in the Kirkuk zone on February 25, all of whom had travelled to Iran, by April 16, 2020, the number of reported cases rose to 1415, with 78 deaths (Sarhan, et al., 2020).

The serological analysis is available to be applied commercially based on Enzyme-linked immunosorbent assay (ELISA) and other techniques, mainly designed to examine anti-spike (S) and anti-nuclear (N) antibody in the blood that synthesized by B-lymphocytes after induced by viral particles (S and N) because of their high antigenic properties (Li et

al., 2005). Anti-S immunoglobulin M (IgM) antibodies can be detected in proximity about 5–12 days after the symptoms appear among individuals who suffered from COVID-19, whereas immunoglobulin G (IgG) and IgA capable of detected in the sera of patients after a fortnight (Wölfel, et al., 2020). Immunoglobulin detection against SARS-COV-2 in the serum samples of individuals shows they had been infected at a particular stage during the outbreak. As a result, serologic analyses could be used to achieve people-based assessments of infection, including individuals who also had asymptomatic or moderate illnesses or who were not ever examined although having symptoms. Mainly the reported cases focused on symptomatic persons and those who have been in contact with the confirmed COVID-19 individuals and came back from an epidemic area. In general, used reverse transcription-polymerase chain reaction (RT–PCR) method for detecting the genome of the virus is a highly sensitive technique. Sadly, a vast population of asymptomatic and subclinical infected persons cannot be diagnosed based on molecular biology strategy (Huang, et al., 2020). The existence of anti-SARS-CoV-2 antibodies in a community may provide a better realistic prediction of the cumulative prevalence of SARS-CoV-2 infection than the viral examination because immunoglobulin against the virus, predominantly IgG, can persist for a prolonged period after the viral infection is eliminated (Xu, et al., 2020).

The benefits of seroprevalence investigation focus on their efficiency in evaluating the degree of asymptomatic exposure among patients and identifying high-risk classes. The study aimed to establish the prevalence of SARS-CoV-2 (IgG and IgM) antibodies in Koya University among academic staff, employers, and students.

II. Materials And Methods

A. Study design and Participants

This study was performed at Science and Health Research center/Koya University/Erbil/Iraq from January 5 to March 10, 2021. It is a cross-sectional study which involved a random selection of (436) participants, (96) from teaching staff, (172) employee, and (168) students. Bodyweight was one of the parameters represented by body mass index (BMI) (BMI=kg/m2 where kg is a person's weight in kilograms and m2 is their height in meters squared). The participants classified as smokers according to the WHO's Smoking and Tobacco Use Policy; a smoker is someone who smokes any tobacco product, either daily or occasionally.

B. Sample Collection and Examination

We collected 5 ml venous blood, 2 ml were put in a lavender tube (Biozek-BE320030) for complete blood count, and 3 ml were put in a gel bottom tube (Biozek-BVG419020) to obtain serum. The blood in the gel bottom tube was centrifuged at (5000 RPM) for 5 min. The obtained serum was divided into two-part and stored in a 1.5 ml Eppendorf test tube, then preserved at -80 °C in (GLF-6483) and defrosted upon testing. Complete Blood Count (CBC) was performed using (Mythic 18). COVID-19 IgM and IgG were evaluated using (SARS-Cov-2 IgM Capture ELISA kit 96t Cat. No: 7424-96) and (SARS-Cov-2 IgG Capture ELISA kit 96t Cat. No: 7324-96), respectively, according to manufacturer's instruction. The test performed using (BIOTEK-ELX800) reader. The result of anti-SARS-COV-2/IgM and IgG was calculated using the cutoff index (COI) method. The result was marked positive if COI > 1.1 and negative if COI < 0.9.

C. Questionnaire and Statistical Analysis

To determine the seroprevalence of COVID-19 at Koya University, a questionnaire was designed. The questionnaire was involved asking some categorical (Yes and No) response. Analysis of data was performed using Statistical Package for the Social Science (SPSS) Version 25.0. Quantitative data, the test of significance used for comparing differences in means, were made by t-test, whereas for qualitative data, the difference in proportions was tested by using Chi-square (X2) test. P-value ≤ 0.05 was considered statistically significant.

III. Results

The study was carried out among (436) participants who compromised academic staff (22%), employed (39.5%), and (38.5) students, and the highest (44.7%) were at the age range of (24≤) years. The mean age of the participant was (30.61 ± 10.95) years. More than half (64%) were male. 16.3 had a smoker, and only (4.4%) person consume alcohol. The residence was predominantly home (67%), compare to accommodation which was (33%), with approximately half of them wearing masks regularly (50.5%). Mostly the blood group of volunteers was O positive (34.4%) and followed by blood group B plus (27.3%). The BMI of 211 participants out of the total were normal, whereas (12.8) members of participants were obese, shown in Table I.

The highest cases of IgG anti-SARS-COV-2 were detected in obese individuals (42.9%), and IgM type antibody found among normal body weight (16.6%). The Chi-square analysis shows no significant differences ($P > 0.05$). Table II illustrated that the prevalence of IgG antibody significantly higher among people who had blood B+ types (50.4%) ($P < 0.05$). Simultaneously, there was a non-significant difference in IgM anti-SARS-COV-2 antibody among blood groups ($P > 0.05$). The risk of Coronavirus (COVs) infection increased highly significantly among participant's that had a family history infected by SARS-COV-2 (42.7%) in comparison to those who did not their family members suffered by COVID-19 ($P < 0.01$).

Furthermore, regularly wearing a face mask reduces the rate of transmission of viral infection. The data revealed seropositivity of anti-SARS-COV-2 IgG significantly declined among individuals who wear a face mask daily (30%), ($P < 0.01$), in comparison to other classes that did not wear it on a daily basis was 43.1%. Recent infection of COVs, which capable determined by anti-SARS-COV-2 IgM antibody significantly lower in participants was (3.1%) who have a chronic disease ($P < 0.05$). There is no significant difference in seropositivity prevalence rate in terms of alcohol genders, consumption, smoking, and occupations, as shown in Table II.

Table I
Socio-demographic Attributes among study Samples

Variables	Frequency	%
Age Group		
24≤	195	44.7
25–34	104	23.9
35≥	137	31.4
Gender		
Female	157	36
Male	279	64
Total	436	100
Residency		
Home	292	67
Accommodation	144	33
Occupation		
Teacher	96	22
Employed	172	39.5
Student	168	38.5
BMI Categories		
Underweight	9	2.1
Normal	211	48.4
Overweight	160	36.7
Obesity	56	12.8
Smoking		
No	365	83.7
Yes	71	16.3
Alcohol consumption		
No	417	95.6
Yes	19	4.4
Wearing mask		
No	216	49.5
Yes	220	50.5
Blood types		
A+	105	24.1
B+	119	27.3
O+	150	34.4
AB+	28	6.4
A-	14	3.2
B-	7	1.6
O-	12	2.8
AB-	1	0.2
Total	436	100

t-test explains that, total white blood cells (WBCs) count significantly decreased ($P < 0.05$) in the blood sample of seropositive for IgG participants (6.29 ± 1.44*103/µl) compare to seronegative individuals (6.67 ± 1.61*103/µl), in contrast, IgM positive blood sample, total WBCs counts dramatically increased (7.01 ±1.74 *103/µl) in compare to non-detected IgM blood samples, which was 6.45 ± 1.51*103/µl. Absolute granulocyte counts significantly decreased among seropositive IgG individuals whereas increased among IgM seropositive samples ($P < 0.05$), vice versa, monocyte and lymphocyte percentage significantly reduced during IgG positive and elevated among IgM positive blood specimens ($P < 0.05$). Other blood parameters such as total erythrocyte count, hemoglobin concentration, platelet count, and indexes show no significant differences among blood samples, as shown in Table III.

Among all the samples, the overall of frequency of IgM positivity was (15.1%), whereas the IgG was (36.5%), whereas only 20 participants (4.6%) were positive for both SARS-Cov-2 immunoglobulins, IgG and IgM depending on the Cutoff Index (COI) as shown in Table IV.

IV. Discussion

Coronavirus disease 2019 (COVID-19) is a pandemic disease which has a significant effect on global economy and other sectors of life. Educational institutes form schools to universities were obligated by the governments to close their doors at the beginning of the pandemic in fear of spreading the virus within the community. In Kurdistan, Iraq, Kurdistan Regional Government (KRG) put tight restrictions for travelers coming to the region and announce safety measures and raising awareness for its residence. One of the restriction measures was closing all states and private schools and universities in the region from February 26 until May 2, 2020 (Merza, et al., 2020). Koya University was one of the state Universities that closed due to the Coronavirus pandemic. However, Koya University was the first university to open its door on October 4, 2020, after releasing the restrictions by the government and brought students to the university accommodation and campus.

Since the beginning of COVID-19 outbreaks, many questions were asked about controlling the spread of the virus; one of the classical ways of controlling any infection in the community is by gaining herd immunity, how long does it take for the herd immunity to reach the protection level this depends on different regions (Britton, Ball and Trapman, 2020). These results represent the first seroprevalence data to be conducted within Kurdistan regional government universities in Iraq. However, a larger scale community-based seroprevalence study will give a better representative picture in this area.

In the present study, the overall seroprevalence of anti-SARS-COV-2 antibodies, IgG and IgM was (36.6%) and (15.2%), respectively. Therefore, measuring the amount of seropositivity, as recommended by the WHO, will notify the proportion of people positive for anti-SARS-CoV-2 antibodies in the community and thereby show the transmission rate over time (WHO, 2020b). Furthermore, the degree of infection in a society depends primarily on communication encounters and population size; it is crucial to assess the proportion of potentially healthy and protected persons in communities with different exposure levels (Shakiba, et al., 2020).

Over 14 day duration, 30-40% among all infected persons by SARS-COV-2 are thought to be asymptomatic (Oran and Topol, 2020). According to the Centers for Disease Control and Prevention, 35% of COVID-19 patients are asymptomatic, and 40% of infection happens before symptoms appear (CDC and Prevention, 2020). Therefore, mass screening aims to determine and isolate victims and tracing their associations, which are essential to minimizing the spread of coronavirus (Hellewell, et al., 2020).

During this asymptomatic stage of infection specific antibody will form against the virus and the first IgM antibodies can be detected as early as 3 days after infection, which serve as a first line of defense. Then its

http://dx.doi.org/10.14500/aro.10831

Table II
Association between Socio-demographic Attributes with Anti-SARS-COVID-2 Antibodies

Variables	IgG				*P* value	IgM				*P* value
	Negative		Positive			Negative		Positive		
	No.	%	No.	%		No.	%	No.	%	
Gender										
Female	97	61.8	60	38.2	0.569	134	85.4	23	14.6	0.83
Male	180	64.5	99	35.5		236	85.6	43	15.4	
Age group										
24≤	130	66.7	65	33.3	0.221	161	82.6	34	17.4	0.35
25–34	68	64.5	36	34.6		88	84.6	16	15.4	
35≥	79	57.7	58	42.3		121	88.3	16	11.7	
BMI										
Underweight	9	100	0	0.0	0.08	8	88.9	1	11.1	0.538
Normal	131	62.1	80	37.9		176	83.4	35	16.6	
Overweight	105	65.6	55	34.4		135	84.4	25	15.6	
Obesity	32	57.1	24	42.9		51	91.1	5	8.9	
Occupation										
Teacher	57	59.4	39	40.6	0.446	82	85.4	14	14.6	0.159
Employed	115	66.9	57	33.1		152	88.4	20	11.6	
Student	105	62.5	63	37.5		136	81	32	19	
Blood groups										
A+	70	66.7	35	33.3	0.029*	91	86.7	14	13.3	0.69
B+	59	49.6	60	50.4		105	88.2	14	11.8	
O+	105	70	45	30		122	81.3	28	18.7	
AB+	19	67.9	9	32.1		22	78.6	6	21.4	
A-	11	78.6	3	21.4		13	92.9	1	7.1	
B-	4	57.1	3	42.9		6	85.7	1	14.3	
O-	8	66.7	4	33.3		10	83.3	2	16.7	
AB-	1	100	0	0.0		1	100	0	0.0	
Residency										
Home	184	63	108	37	0.749	235	86.6	39	13.4	0.139
Accommodation	93	64.6	51	35.4		117	81.3	27	18.8	
Family member infected by COVID-19										
No	152	69.7	66	30.3	0.007*	187	85.8	31	14.2	0.593
Yes	125	57.3	93	42.7		183	83.9	35	16.1	
Chronic diseases										
No	257	63.8	146	36.2	0.619	338	83.9	65	16.1	0.03*
Yes	19	59.4	13	40.6		31	96.9	1	3.1	
Wearing Mask										
No	123	56.9	93	43.1	0.003*	182	84.3	34	15.7	0.72
Yes	154	70	66	30		188	85.5	32	14.5	
Smoking										
No	225	61.6	140	38.4	0.063	309	84.7	56	15.3	0.78
Yes	52	73.2	19	26.8		61	85.9	10	14.1	
Alcoholism										
No	264	63.3	153	36.7	0.425	325	84.4	65	15.6	0.18
Yes	13	68.4	6	31.6		18	94.7	1	5.3	
Total	277	63.4	159	36.6		369	84.4	66	15.2	

* Indicate significant levels ($P \leq 0.05$)

level will decline, and IgG antibody will form. This will make a long-term memory and fight against the virus in the future (Racine and Winslow, 2009). Therefore, in our data both SARS-COV-2 IgG and IgM antibody detection in 20 participants (4.6%) are normal as any other viral infection. The presence of both antibodies at the same time represents the overlap production of both antibodies during microbial infection throughout the course of the disease. A study conducted by Nakano et al. in 2021 showed that anti- SARS-COV-2 IgM titer would increase until day 18 after the symptoms appeared, after that it will decline and, IgG remains stable above 400AU/ml after day 13, it increases afterwards (Nakano, et al., 2021).

The seropositive IgM was significantly higher among participants with chronic diseases such as hypertension and diabetes (3.1%) (George, et al., 2019) and (42.7%) of participants were IgG positive had family members infected with COVID-19, which agrees with other research done in India (George, et al., 2021) one of the first protective strategies against SARS-COV-2 was wearing the mask, the governments were asking, or in some order to wear masks, since then many researches and public reports showed the significance

Table III
Comparison of Blood Cell Parameters in Seroprevalence of Anti-SARS-COV-2

Blood parameters	IgG (Mean±SD)		*P* value	IgM (Mean±SD)		*P* value
	Positive *n* (159)	Negative *n* (277)		Positive *n* (66)	Negative *n* (369)	
WBC (10^3/µl)	6.29±1.44	6.67±1.61	0.014*	7.01±1.74	6.45±1.51	0.007*
LYM (10^3/µl)	1.9±0.47	1.89±0.55	0.865	1.95±0.43	1.88±0.54	0.368
MON (10^3/µl)	0.397±0.18	0.4±0.18	0.66	0.38±0.15	0.4±0.19	0.465
GRA (10^3/µl)	3.99±1.21	4.37±1.41	0.004*	4.67±1.59	4.15±1.29	0.004*
LYM%	30.98±7.31	29.05±7.5	0.009*	28.77±6.96	29.93±7.56	0.264
MON%	6.38±2.76	6.2±2.79	0.517	5.64±2.24	6.38±2.85	0.021*
GRA%	62.81±7.31	64.77±8.05	0.012*	65.58±7.37	63.79±7.89	0.087
RBC (10^6/µl)	5.33±2.89	5.18±0.612	0.434	5.3±0.736	5.22±1.94	0.744
HGB (g/dl)	14.8±1.99	15±1.94	0.175	15.08±1.8	14.95±1.99	0.618
HCT (%)	44.4±4.57	44.95±5.21	0.268	45.48±4.2	44.61±5.11	0.195
MCV	87.47±7.47	87.08±8.16	0.628	86.68±8.73	87.32±7.76	0.542
HCH (pg)	29.27±3.36	29.32±3.53	0.897	28.79±4.0	29.39±3.36	0.195
MCHC (g/dl)	33.47±2.4	33.52±2.63	0.847	33.15±2.46	33.57±2.56	0.225
RDW	12.81±1.25	12.86±2.32	0.810	12.7±1.34	12.85±2.1	0.765
PLT	245.13±74.4	245.87±54.4	0.904	246.61±54.54	245.42±63.76	0.887
PDW	15.05±1.32	15.13±1.414	0.544	14.92±1.182	15.13±1.41	0.259

* indicate significant levels ($P \leq 0.05$)

Table IV
Frequency anti-SARS-CoV-2 Immunoglobulins among participants

Anti-SARSCoV-2	Positive	Negative
IgM	66 (15.1%)	370 (84.9%)
IgG	159 (36.5%)	277 (63.5%)
IgM and IgG	20 (4.6%)	416 (95.4%)

of wearing the mask in decreasing the transmission of the virus as this may help in reducing the direct contact with the droplets of an infected person (Howard, et al., 2020). In our finding, the seropositive IgG of SARS-COV-2 was significantly lower among participants wearing mask daily (30%) ($P < 0.01$) in comparison to those not wearing a mask on a daily basis (43.1%), which mean good protection against virus transmission, this result is compatible with many other researches done regarding the efficiency of wearing a mask in reducing virus transmission. A study by Leffler et al. (2020) comparing the effect of wearing a mask in different countries, they found that the transmission of the virus was 7.5% higher in countries wearing a mask was not compulsory.

The relationship between blood group and microbial infection has been documented previously (Leffler, et al., 2020). This relation was connected to the difference in antigens found in erythrocytes that react differently with different bacteria, parasites and viruses (Acik and Bankir, 2021); this can be true for SARS-COV-2 infection as well. The results of our study showed that the highest seropositive IgG was found among B+ blood group participants (50.4%) who disagree with (Pourali, et al., 2020). Our result, similar to other researches, showed that the blood group O+ was more resistant to SARS-COV-2 infection (30%) (Wu, et al., 2020; Zhao, et al., 2020; Acik and Bankir, 2021).

Since the onset of COVID-19, many factors were connected to the severity and mortality rate among infected people, for example, chronic disease cardiovascular diseases and diabetes, age and gender (Guzik, et al., 2020; Teng, et al., 2020). Moreover, WBC count is one of the factors that have been linked to COVID-19 infection severity and mortality. Possibility of death will be higher in COVID-19 patients with elevated WBC count (Zhu, et al., 2021). Increase total WBC count and neutrophils, decreased lymphocyte count has reported in many studies about COVID-19. However, other studies in the same field reported different and variable results regarding the WBC profile of COVID-19 patients (Sun, Zhou and Ye, 2021). These inconsistence in the results of WBC in Coronavirus infected people make it difficult to connect it to the severity of the disease or use it as a prognosis tool, since this difference or changes in the WBC counts are strongly related to the immune system and variability in immune response within people (Siedlinski, et al., 2020; Sun, Zhou and Ye, 2021).

As a result of the importance of the WBCs in establishing the immune response and inflammation, it is used as a parameter in determining the severity of COVID-19 infection and increased risk of mortality (Wang, et al., 2021). Coronavirus infection, as any other infection, is companied by immune response and inflammation, which indicated by many inflammatory markers in the body, including inflammatory cytokines and WBCs. The results of our study showed increased total WBC in IgM positive or recent infection ($P > 0.01$), which agree with the meta-analysis review study done by Feng, et al., 2020. However, there was no significant difference between infected and non-infected participants regarding total lymphocytes and monocytes.

On the other hand, our data showed significant reduction in total WBC among seropositive IgG participants compared with seronegative individuals ($P > 0.05$) which agree with a study contacted by Liu et al. (2020), demonstrating that approximately 80% of the patients suffered from COVID-19 had a normal or reduced WBC counts. Lymphocytes levels were low in 72.3 percent (Liu, et al., 2020). By studying the relation between coronaviruses infection and the innate immune response, the possibility of persisting and developing of chronic inflammation among these population will be more clear (Zhu, et al., 2021).

In most COVID-19 seroprevalence assessments up to date, the cumulative rate of infection was identified primarily by age group, race, ethnicity, and nationality. Antiviral IgG screening of people in high-risk jobs to COVs due to repeated or high social activities could be needed for public health decisions on immediate lockdowns or return to work policies (WHO, 2020a; Bendavid, et al., 2021; Rosenberg, et al., 2020).

V. Conclusion

Many people in the community are infected with coronavirus without any symptoms, which has a bigger threat on spreading the virus to a non-infected person. The previous infected asymptomatic individuals can be detected just by antibody testing, giving a clear picture of the rate of COVID-19 infection among the population. This figure could be used to assist the health sectors in confirming better identify infection, death rates and make policy decisions. Based on the studied samples from people at Koya University, we recommend that the analyses with a vast sample size yield more reliable estimation of the proportion that has historically been infected with SARS-COV-2 and, as a result, provide more detailed information on herd immunity.

References

Acik, D.Y. and Bankir, M., 2021. Relationship of SARS-CoV-2 pandemic with blood groups. *Transfusion Medicine Hemotherapy*, 382, pp.1-7.

Azkur, A.K., Akdis, M., Azkur, D., Sokolowska, M., van de Veen, W., Brüggen, M.C., O'Mahony, L., Gao, Y., Nadeau, K. and Akdis, C.A., 2020. Immune response to SARS-CoV-2 and mechanisms of immunopathological changes in COVID-19. *Allergy*, 75, pp.1564-1581.

Bendavid, E., Mulaney, B., Sood, N., Shah, S., Bromley-Dulfano, R., Lai, C., Weissberg, Z., Saavedra-Walker, R., Tedrow, J. and Bogan, A., 2021. COVID-19 antibody seroprevalence in santa clara county, california. *International Journal of Epidemiology*, 50, pp.410-419.

Britton, T., Ball, F. and Trapman, P.J.A., 2020. *The Disease-Induced Herd Immunity Level for COVID-19 is Substantially Lower than the Classical Herd Immunity Level*.

CDC and PREVENTION, 2020. *COVID-19 Pandemic Planning Scenarios*. United States Centers for Disease Control, United States.

Dimonte, S., Jalal, P.J., Ahmad, H.A., Karim, S.B., Soor, T.A.H., Ali, S.I., Babakir-Mina, M. and Greco, F., 2020. Is the SARS-CoV2 evolved in human being: A prospective genetic analysis. *Kurdistan Journal of Applied Research*, 5, pp.169-177.

Feng, X., Li, S., Sun, Q., Zhu, J., Chen, B., Xiong, M. and Cao, G., 2020. Immune-inflammatory parameters in COVID-19 cases: A systematic review and meta-analysis. *Frontiers in Medicine*, 7, p.301.

George, C.E., Inbaraj, L.R., Chandrasingh, S. and Witte, D., 2021. High seroprevalence of COVID-19 infection in a large slum in South India; what does it tell us about managing a pandemic and beyond? *Epidemiology Infection*, 149, pp.e39.

George, C.E., Norman, G., Wadugodapitya, A., Rao, S.V., Nalige, S., Radhakrishnan, V., Behar, S. and de Witte, L., 2019. Health issues in a Bangalore slum: Findings from a household survey using a mobile screening toolkit in Devarajeevanahalli. *BMC Public Health*, 19, pp.1-12.

Guzik, T.J., Mohiddin, S.A., Dimarco, A., Patel, V., Savvatis, K., Marelli-Berg, F.M., Madhur, M.S., Tomaszewski, M., Maffia, P. and D'Acquisto, F., 2020. COVID-19 and the cardiovascular system: Implications for risk assessment, diagnosis, and treatment options. *Cardiovascular Research*, 116, pp.1666-1687.

Hellewell, J., Abbott, S., Gimma, A., Bosse, N.I., Jarvis, C.I., Russell, T.W., Munday, J.D., Kucharski, A.J., Edmunds, W.J. and Sun, F., 2020. Feasibility of controlling COVID-19 outbreaks by isolation of cases and contacts. *The Lancet Global Health*, 8, pp.e488-e496.

Howard, J., Huang, A., Li, Z., Tufekci, Z., Zdimal, V., van der Westhuizen, H.M., von Delft, A., Price, A., Fridman, L. and Tang, L.H., 2020. *Face Masks Against COVID-19: An Evidence Review*. Available form: https://www. preprints.org. [Last accessed on 2021 Jun 01].

Huang, C., Wang, Y., Li, X., Ren, L., Zhao, J., Hu, Y., Zhang, L., Fan, G., Xu, J. and Gu, X., 2020. Clinical features of patients infected with 2019 novel Coronavirus in Wuhan, China. *The Lancet*, 395, pp.497-506.

Lauer, S.A., Grantz, K.H., Bi, Q., Jones, F.K., Zheng, Q., Meredith, H.R., Azman, A.S., Reich, N.G. and Lessler, J., 2020. The incubation period of Coronavirus disease 2019 (COVID-19) from publicly reported confirmed cases: Estimation and application. *Annals of Internal Medicine*, 172, pp.577-582.

Leffler, C.T., Ing, E., Lykins, J.D., Hogan, M.C., Mckeown, C.A. and Grzybowski, A., 2020. Association of country-wide Coronavirus mortality with demographics, testing, lockdowns, and public wearing of masks. *American Society of Tropical Medicine and Hygiene*, 103, pp.2400-2411.

Li, F., Li, W., Farzan, M. and Harrison, S.C., 2005. Structure of SARS coronavirus spike receptor-binding domain complexed with receptor. *Science*, 309, pp.1864-1868.

Liu, K., Fang, Y.Y., Deng, Y., Liu, W., Wang, M.F., Ma, J.P., Xiao, W., Wang, Y.N., Zhong, M.H. and Li, C.H., 2020. Clinical characteristics of novel coronavirus cases in tertiary hospitals in Hubei Province. *Chinese medical Journal*, 133, p.1025.

Merza, M.A., Al Mezori, A.A.H., Mohammed, H.M. and Abdulah, D.M., 2020. COVID-19 outbreak in Iraqi Kurdistan: The first report characterizing epidemiological, clinical, laboratory, and radiological findings of the disease. *Diabetes and Metabolic Syndrome: Clinical Research and Reviews,* 14, pp.547-554.

Nakano, Y., Kurano, M., Morita, Y., Shimura, T., Yokoyama, R., Qian, C., Xia, F., He, F., Kishi, Y. and Okada, J., 2021. Time course of the sensitivity and specificity of anti-SARS-CoV-2 IgM and IgG antibodies for symptomatic COVID-19 in Japan. *Scientific Reports,* 11, pp.1-10.

Oran, D.P. and Topol, E., 2020. Prevalence of asymptomatic SARS-CoV-2 infection: A narrative review. *Annals of Internal Medicine*, 173, pp.362-367.

Pourali, F., Afshari, M., Alizadeh-Navaei, R., Javidnia, J., Moosazadeh, M. and Hessami, A., 2020. Relationship between blood group and risk of infection and death in COVID-19: A live meta-analysis. *New Microbes New Infections*, 37, pp.100743.

Racine, R. and Winslow, G.M., 2009. IgM in microbial infections: Taken for granted? *Immunology Letters,* 125, pp.79-85.

Rosenberg, E.S., Tesoriero, J.M., Rosenthal, E.M., Chung, R., Barranco, M.A., Styer, L.M., Parker, M.M., Leung, S.Y.J., Morne, J.E. and Greene, D., 2020. Cumulative incidence and diagnosis of SARS-CoV-2 infection in New York. *Annals of Epidemiology*, 48, pp.23-29.e4.

Sarhan, A.R., Flaih, M.H., Hussein, T.A.and Hussein, K.R., 2020. *Novel Coronavirus (COVID-19) Outbreak in Iraq: The First Wave and Future Scenario, medRxiv*.

Shakiba, M., Nazari, S.S.H., mehrabian, F., Rezvani, S.M., Ghasempour, Z. and Heidarzadeh, A., 2020. *Seroprevalence of COVID-19 Virus Infection in Guilan Province, Iran, MedRxiv*.

Siedlinski, M., Jozefczuk, E., Xu, X., Teumer, A., Evangelou, E., Schnabel, R.B., Welsh, P., Maffia, P., Erdmann, J. and Tomaszewski, M., 2020. White blood cells and blood pressure: A mendelian randomization study. *Circulation*, 141, pp.1307-1317.

Sun, Y., Zhou, J. and Ye, K., 2021. White blood cells and severe COVID-19: A mendelian randomization study. *Journal of Personalized Medicine*, 11**,** p.195.

Teng, Y., Xu, J., Zhang, Y., Liu, Z. and Zhang, S., 2020. Mendelian randomization in COVID-19: Applications for cardiovascular comorbidities and beyond. *EBioMedicine*, 57, p.102847.

Wang, S., Fu, L., Huang, K., Han, J., Zhang, R. and Fu, Z., 2021. Neutrophil-to-lymphocyte ratio on admission is an independent risk factor for the severity and mortality in patients with Coronavirus disease 2019. *Journal of Infection*, 82**,** pp.e16-e18.

WHO, 2020a. *Considerations for Implementing and Adjusting Public Health and Social Measures in the Context of COVID-19: Interim Guidance, 14 June 2021*. World Health Organization, Geneva.

WHO, 2020b. *Population-Based Age-Stratified Seroepidemiological Investigation Protocol for COVID-19 Virus Infection, 17 March 2020*. World Health Organization, Geneva.

Wölfel, R., Corman, V.M., Guggemos, W., Seilmaier, M., Zange, S., Müller, M.A., Niemeyer, D., Jones, T.C., Vollmar, P. and Rothe, C., 2020. Virological assessment of hospitalized patients with COVID-2019. *Nature*, 581**,** pp.465-469.

Wu, Y., Feng, Z., Li, P. and Yu, Q., 2020. Relationship between ABO blood group distribution and clinical characteristics in patients with COVID-19. *Clinica Chimica Acta*, 509**,** pp.220-223.

Xu, X., Sun, J., Nie, S., Li, H., Kong, Y., Liang, M., Hou, J., Huang, X., Li, D. and Ma, T. 2020. Seroprevalence of immunoglobulin M and G antibodies against SARS-CoV-2 in China. *Nature Medicine*, 26**,** pp.1193-1195.

Zhao, J., Yang, Y., Huang, H., Li, D., Gu, D., Lu, X., Zhang, Z., Liu, L., Liu, T. and Liu, Y. 2020. Relationship between the ABO blood group and the Coronavirus Disease 2019 (COVID-19) Susceptibility. *Clinical Infectious Diseases*, 73(2), pp.328-331.

Zhu, B., Feng, X., Jiang, C., Mi, S., Yang, L., Zhao, Z., Zhang, Y. and Zhang, L., 2021. Correlation between white blood cell count at admission and mortality in COVID-19 patients: A retrospective study. *BMC Infectious Diseases*, 21**,** pp.1-5.

http://dx.doi.org/10.14500/aro.10843

Preparation and Characterization of Green Fe_3O_4 Nanoparticle Using the Aqueous Plant Extract of *Gundelia tournefortii* L.

Aveen F. Jalal, Nabil A. Fakhre

Department of Chemistry, College of Education, Salahaddin University-Erbil,
Erbil, Kurdistan Region - F.R. Iraq

***Abstract*—In this work, the magnetite nanoparticles (Fe_3O_4-NPs) synthesized using a simple, fast, and environmentally acceptable green approach. *Gundelia tournefortii* L. extract, an aqueous plant extract, was used for the 1st time in green synthesis to prepare nanoparticles as reducing, capping, and stabilizing agents. Such biomolecules as flavonoids, alkaloids, and antioxidants are found in the aqueous leaf extract, and their presence has been determined to have an important role in the synthesis of Fe_3O_4-NPs. The techniques used in this analysis include Fourier Transform Infrared, Scanning Electron Microscopy, Energy-Dispersive X-ray spectroscopy, X-ray Diffraction, Transmission Electron Microscopy, and Vibrating Sample Magnetometer. The Vibrating Sample Magnetometer demonstrated that the samples were superparamagnetic, with a magnetization value of 48.6 emu/g. The prepared nanoparticle was applied to remove chrystal violet, malachite green, and safranin dyes from prepared aqueous solutions with the adsorption capacity of 13.9, 15.6, and 14.4 mg/g, respectively.**

***Index Terms*—Green synthesis; *Gundelia tournefortii* L. leaf extract; Fe_3O_4 nanocomposite; Characterization.**

I. Introduction

Iron nanoparticles have generated a lot of interest in ecological research due to their great surface sensitivity and huge surface area; moreover, pathogenic microorganisms, organic pollutants, and inorganic toxins are all eliminated in ecological studies. There are plethoras of physical, chemical, biological, and hybrid techniques available for synthesizing various kinds of nanoparticles, and the nanoparticles generated by each process have certain characteristics. However, there is currently the development of metal nanoparticles production by plants. Green nanotechnology has been drawn by a broad variety of procedures to decrease or remove toxic substances for environmental restoration. A modern approach for their production is to synthesize metal nanoparticles by utilizing inactivated tissues, plant extracts, exudates, and other components (Kanagasubbulakshmi and Kadirvelu, 2017). To avoid the toxic and flammable sodium borohydride, which is used as a reducing agent, scientists are working at green preparations of iron nanoparticles. Furthermore, because no harmful chemicals are employed during the preparation of plant extracts as a reducing agent, they are suitable for biomedical and pharmaceutical applications. Recently, a significant amount of research on iron nanoparticles have been published that use plant extracts for producing green iron nanoparticles (Da'na, Taha and Afkar, 2018). *Gundelia tournefortii* L. (GT), an edible spiky, thistle-like plant native to Iran, Iraq, Turkey, Azerbaijan, Egypt, Cyprus, Jordan, and other parts of Western Asia, is locally known as "Kangar" in Iran and the Kurdistan region of Iraq. Galgal, Tumbleweed, Tumble Thistle, Akkub, and Akoub are among the most common names for GT For a long time, the plant's stem has been used as a hepatoprotective purifier and as a possible cure for diabetes, chest discomfort, and heart attacks in traditional medicine in the Middle East (Hajizadeh-Sharafabad, et al., 2016). Phytochemical analysis of GT leaves revealed the presence of phenolic compounds, particularly flavonoids, including caffeoylquinic acid derivatives, quercetin, gallic acid, and other phytoconstituents, namely, total alkaloids, ascorbic acid, reducing power, total antioxidant activity, and metal chelating activity (Ibrahim, Jalal and Ibrahim, 2013). An aqueous extract of white tea (*Camellia sinensis*) was used as a reducing and capping agent to prepare iron oxide magnetic nanoparticles (Shojaee and Shahri, 2016). For the first time, the influence of *Glycosmis mauritiana* leaf extract on the synthesis of iron oxide nanoparticles (Fe_2O_3 NPs) was investigated, as well as the efficacy of *G. mauritiana* leaves as a biomaterial as a reducing agent (Amutha and Sridhar, 2018). Iron Fe_2O_3 NPs were synthesized in a green way by extracting pomegranate (*Punica granatum*) seeds (Bibi, et al., 2019). Mango peel extracts were used to effectively manufacture GMP-nZVI (Desalegn, et al., 2019). The treatment of ferrous and ferric salt aqueous solutions in an alkaline medium with *Myrtus communis* L. leaf extract resulted in the rapid production of Fe_3O_4-NPs (Saleh, 2020). As far as we know, this is the first study used in the biosynthesis of Fe_3O_4-NPs of inexpensive GT raw extract for probable hyperthermia. X-ray powder diffraction

ARO-The Scientific Journal of Koya University
Vol. IX, No.2 (2021), Article ID: ARO.10843, 6 pages
DOI: 10.14500/aro.10843
Received: 26 July 2021; Accepted: 13 November 2021
Regular research paper: Published: 01 December 2021
Corresponding author's e-mail: aveen.jalal@su.edu.krd

(XRD), transmission electron microscopy (TEM), scanning electron microscope (SEM), energy-dispersive X-ray spectroscopy, vibrating sample magnetometer (VSM), and Fourier-transform infrared (IR) spectroscopy are used in the analysis of the present research. The prepared nanoparticle was applied to remove chrystal violet (CV), malachite green (MG), and Safranin (S) dyes from prepared aqueous solutions.

II. Material and Methods

A. Reagents

All chemicals used in the present work are in reagent grade, namely, Iron(III) Chloride Hexahydrate ($FeCl_3.6H_2O$) (Sigma-Aldrich), Iron(II) Sulfate-heptahydrate ($FeSO_4 \cdot 7H_2O$) (Sigma-Aldrich), Sodium hydroxide (NaOH) (Scharlau), and Ethanol (Sigma-Aldrich). Deionized distilled water and distilled water were obtained from our analytical laboratory.

B. Preparation of Plant Extract

Fig. 1 shows a photo of GT (Family name, Asteraceae and Local name, Kangir) from the mountains of Kurdistan region, Iraq. After collecting, the specimens were thoroughly cleaned to remove particles of dust so that any remaining moisture could be removed. The plant was left to dry in a shady, well-ventilated area; it was sliced into small parts and then transferred into a thin powder, depending on how the plant is harvested with some modifications (Ramesh, et al., 2018, Sravanthi, Ayodhya and Swamy, 2019). To prepare the solution, 5 g of the powdered plant was put into a conical flask containing 100 ml of deionized H_2O. After 15 min of heating at 60°C, the extract was filtered on Whatman's No.1 filter paper. The pale brown filtrate was kept at a 4°C temperature.

C. Synthesis of Fe_3O_4 NPs

Iron Fe_2O_3 NPs were prepared, firstly, 20 ml of 2.0 M of $FeCl_3.6H_2O$ solution and 20 ml of 1.0 M of $FeSO_4.7H_2O$ solution (2:1 molar ratios), then it was added into a 100 ml of plant extract solution. The solution was then added dropwise to 1.0 M NaOH while stirring continuously. The solution's pH was adjusted to 11. It was agitated for 1.0 h to ensure homogeneity and to complete the reaction. The Fe_3O_4-NPs were separated using magnet, as shown in Fig. 2. Fe_3O_4-NPs were cleaned several times by ethanol, and deionized distilled water. The nanoparticles were dried for 24 h at a 70°C temperature.

Fig. 1. Image of *Gundelia tournefortii* L.

D. Characterization of Fe_3O_4 NPs

PANalytical X'Pert X-ray diffractometer was utilized to examine the crystal structure and purity of the produced adsorbents. To prepare the sample for testing, it was scanned using Cu Kα radiation (λ = 1.54 Å) at 2θ angle configuration scanning from 20° to 80°, with an applied current of 40 mA and a voltage of 45 kV. Fourier transform IR (FT-IR) spectroscopy was recorded on SHIMADZU IR AFFINITY-I FTIR spectrophotometer to study the presence of the biomolecules, which are responsible for the synthesis of Fe_3ONPs. Dried samples were grinded with potassium bromide to produce a pellet, which was examined in a wavelength range of 400–4000 cm^{-1}. Surface shape, morphology, and elemental composition of materials were obtained using SEM (SEM Compact 6073) and energy dispersive X-ray analysis (EDX) (Merlin Compact 6073) (Carl Zeiss, Germany). The size and morphology of the synthesized Fe_3O_4 NPs were observed using the FEI TECNAI G2 F20 TEM. Measurement of the magnetic properties of the nanoparticles was done in a VSM produced by Daghigh Kavir Corporation at room temperature.

III. Results and Discussion

A. FTIR

FT-IR spectra of synthesized magnetic nanoparticles were carried out to identify the possible biomolecules responsible for the capping and stabilization of nanoparticles. As shown in Fig. 3, the stretching vibrations are at 3409 cm^{-1}, 1587 cm^{-1}, 1097 cm^{-1} and 615 cm^{-1} within the region of 400–4000 cm^{-1}. These peaks represent the following bonding in the sample that confirms the reducing agent role in the formation of Fe_3O_4 -NPs. The peak at 3409 cm^{-1} corresponds to the O-H stretching vibration in OH-groups,

Fig. 2. Magnetite nanoparticles separated by using an external magnetic field.

http://dx.doi.org/10.14500/aro.10843

which indicates the aqueous phase as well as the reduction of the Iron salts. The peaks at 1587 cm^{-1} and 1097 cm^{-1} attributed to the asymmetric and symmetric stretching vibration to the C=O, and C-O bond stretching denotes the existing phytochemicals in the plant extract which stabilize as well as act as capping agents (Awwad and Salem, 2012). Fe-O stretching vibration is attributed to the band below 700 cm^{-1}. The Fe-O stretching band of Fe_3O_4 nanoparticles can be detected at 615 cm^{-1} (Sobh, Nasr and Mohamed, 2020, Sari and Yulizar, 2017, Kanagasubbulakshmi and Kadirvelu, 2017).

B. SEM

Visual inspection of the surface using SEM analysis was carried out to discern morphological features, shape, and distribution of the nanoparticles' size, as illustrated in Fig. 4. As shown, GT extraction reveals the spherical with some hexagonal-shaped crystalline structure of Fe_3O_4 in the SEM micrograph of magnetic iron Fe_2O_3 NPs; it can be found that, given of high surface energy and adherence, most particles are approximately spherical with some hexagonal-shaped (Ardelean, et al., 2017) (Alzaidi, Alzahrani and El-Mouhty, 2016).

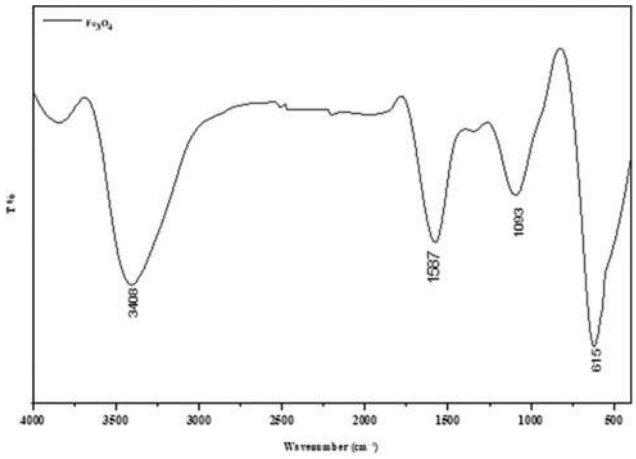

Fig. 3. Fourier transform infrared spectra Fe_3O_4 nanoparticles.

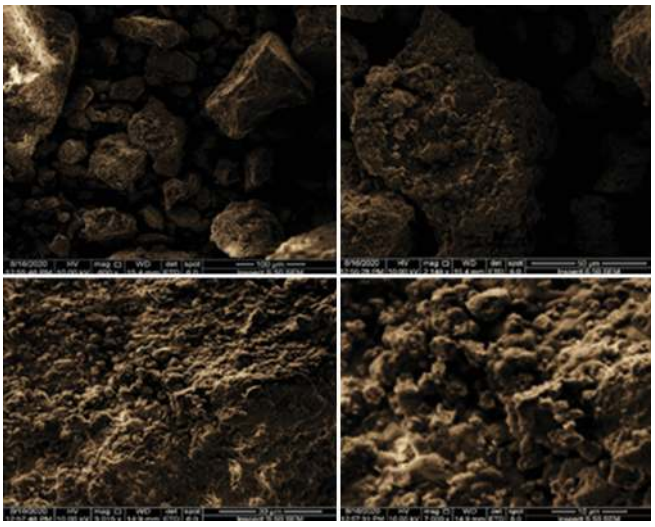

Fig. 4. Scanning electron microscope images of the biosynthesized iron oxide nanoparticles.

C. EDX

EDX analysis was used to perform qualitative analysis of prepared nanoparticles (Fig. 5), which indicates the presence oxygen and Iron elements in the composition of magnetite nanoparticles (Fe3O4-NPs) prepared from an aqueous plant extract of GT The iron and oxygen atoms in Fe3O4-NPs are stoichiometric to each other, the theoretical and experimental values are in agreement. The presence of a significant amount of iron ions inside these nanoparticles highlights the effective production of Fe3O4-NPs using the plant (Saleh, 2017) (Ahmadi, et al., 2020).

D. TEM

The size and morphology of the synthesized Fe_3O_4 nanoparticles were measured using TEM imaging. The Fe_3O_4 nanoparticles are nanocrystalline, as seen in Fig. 6, though their shape is mostly spherical with some hexagonal-shaped nanoparticles (Nejati-Koshki, et al., 2014, Yew, et al., 2016). The average particle size of the spherical nanoparticles is 29.9 nm. Moreover, Fe_3O_4 nanoparticles are agglomerations in some areas. The presence of agglomeration might be due to van der Waals forces that bind particles together, as well as nanoscale shear forces. Furthermore, the presence of

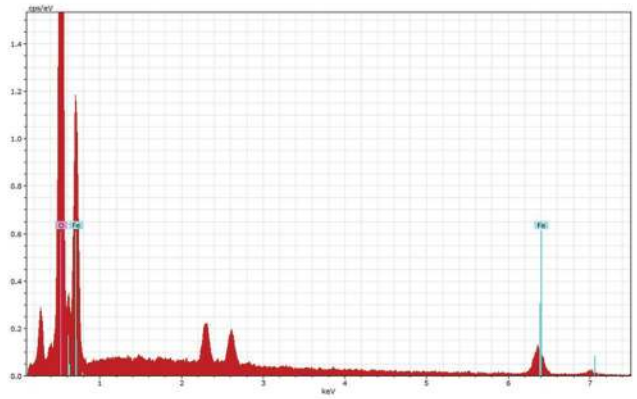

Fig. 5. Energy dispersive X-ray analysis spectrum of iron oxide nanoparticles.

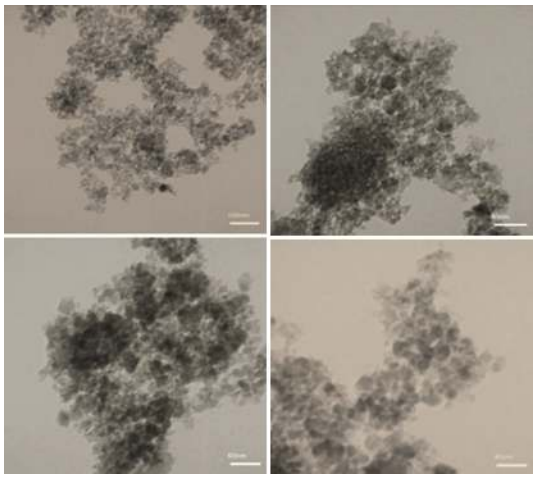

Fig. 6. Transmission electron microscopy images of the synthesized magnetite nanoparticles by *Gundelia tournefortii* L extraction.

hydroxyl groups in plant extracts may cause agglomeration (Yusefi, et al., 2021).

Table I
Removal Percent of Dyes

Fe_3O_4-NPs	
Dyes	Removal %
MG	78
CV	69.5
S	72

CV: Chrystal violet, MG: Malachite green, S: Safranin

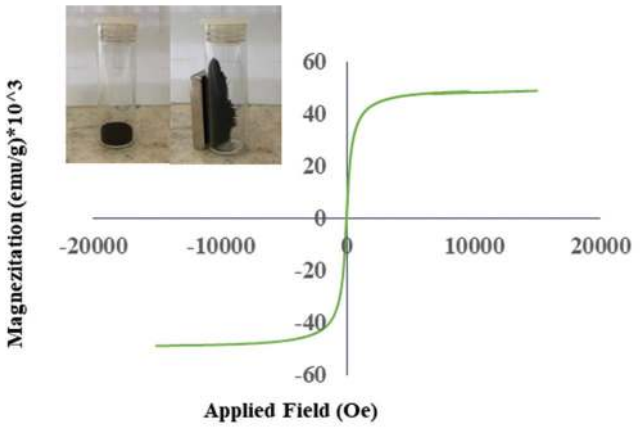

Fig. 7. Vibrating-sample magnetometry diagrams for magnetite nanoparticles.

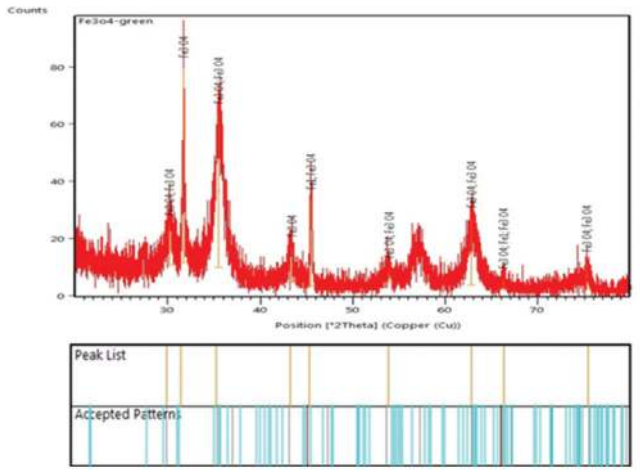

Fig. 8. X-ray powder diffraction patterns of iron oxide nanoparticles.

E. VSM

One of the expected features of the synthesized nanoparticles in this study is magnetic properties. Magnetometry technique was used to measure the magneto-resistance impact of nanoparticle-generated magnetic characteristics in the field of 20,000–20,000 at room temperature. Fig. 7 shows that the iron Fe_2O_3 NPs prepared using GT extraction are superparamagnetic, with saturation magnetization value of 48.6 emu/g being established by measuring magnetic hysteresis curves. Saturation magnetization values for Fe_3O_4 nanoparticles prepared by this plant were higher than those Fe_3O_4 nanoparticles prepared by other researches in literature (Zhen, et al., 2011, Deshmukh, Gupta and Kim, 2019).

F. XRD

Fig. 8 shows the XRD pattern of Fe_3O_4-NPs prepared using extraction of GT These peaks reflect the amorphous structure (220), (311), (400), (442), (511), (440) of iron oxide. Moreover, the rhombohedral structure of iron oxide may be indexed to all of the reflection peaks (JCPDS NO. 89-8104). Similar to iron Fe_2O_3 NPs, these studies describe a crystalline form (Amutha and Sridhar, 2018; Ahmadi, et al., 2021). The typical crystalline size of Fe_3O_4 nanoparticles, according to the dominant peak (311) diffraction peak, is 15.17 nm as expected by Scherrer's equation: $D311 = \frac{0.94\lambda}{\beta Cos\theta(311)}$, where D311 is the usual crystallographic dimension normal to the (311) crystal plane, λ is the X-ray wavelength (1.5406 Å), and β is the full width at half maximum of the (311) plane (Barzinjy, et al., 2020). The crystalline size was 29.6 nm, according to the results. The crystallite size of the Fe3O4-NPs formed varied between 11.7 mn and 69.3 nm, according to the XRD study (Yew, et al., 2016).

IV. Applications

Fe_3O_4 nanoparticles have been applied to remove CV, MG, and S dyes from syntheses solution, as can be seen in Fig. 9. The optimum conditions for removal of 10 µg/mL dyes were 50 mg of nanoparticles with natural pH 5.5 at room temperature, and one hour shaking in thermostat shaker water bath after separating adsorbent to adsorbate using an external magnet and the residue measured with a ultraviolet-visible spectrophotometer. Results had been illustrated in Table 1 and Fig. 10. Table 2 shows that the adsorption capacity of MG, S, and CV is comparable to various adsorbents reported in the literature.

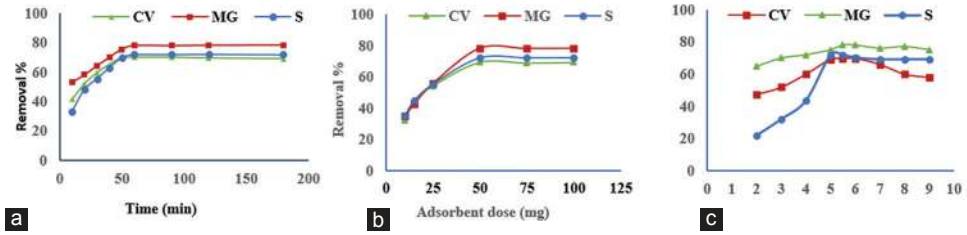

Fig. 9. (a) Adsorption time impact of chrystal violet, malachite green, and safranin removal, (b) Adsorbent dose effect on percent removal of chrystal violet, malachite green, and safranin, and (c) pH Effect on removal percentage.

http://dx.doi.org/10.14500/aro.10843

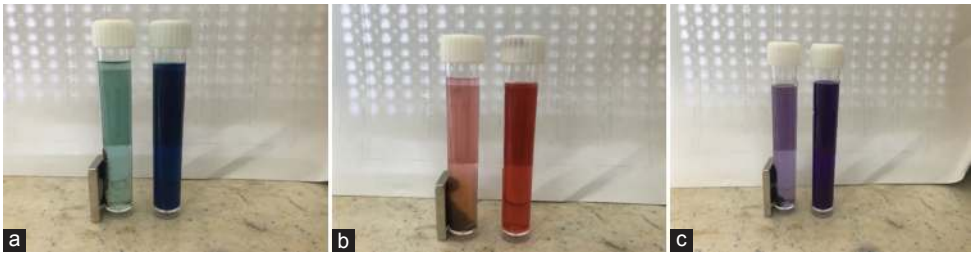

Fig. 10. Magnetite nanoparticles applied of Dyes (a) malachite green, (b) safranin and (c) chrystal violet.

Table II
Comparison of CV, MG and S Adsorbent in Different Adsorbent Materials

Adsorbents	Dyes	Adsorption capacity (mg/g)	References
Sagaun sawdust		3.5	(Khattri and Singh, 2012)
(PNIPAm) nanocomposite (CPN) hydrogels		1.2	(Zhang, et al., 2014)
$CaFe_2O_4$ magnetic nanoparticles (MNPs)		10.68	(An, et al., 2015)
Clay/poly (N-isopropyl acrylamide)			
Magnetite Alginate		37.5	(Elwakeel, et al., 2017)
BC-PKS		24.45	(Kyi, et al., 2020)
Fe_3O_4-NPs		13.9	This study
Fly ash		0.219-0.644	(Khan, et al., 2009)
Neem sawdust (Azadirachta indica)		4.354	(Khattri and Singh, 2009)
Orange peel		1.744	(Abdurrahman, et al., 2013)
Activated Carbon (AC)		28.8	(Lam, et al., 2017)
Fe_3O_4-NPs		15.6	This study
Natural Raw Kaolinite (NRK) clay		15.6	(Adebowale, et al., 2014)
Pineapple peels		21.7	(Mohammed, et al., 2014)
Iron oxide/sepiolite magnetite composite		18.48	(Fayazi, et al., 2015)
Tea waste powder		14.814	(Nehaba, et al., 2019)
Activated Carbon		20.04	(Nehaba, et al., 2019)
Fe_3O_4-NPs		14.4	This study

CV: Chrystal violet, MG: Malachite green, S: Safranin, Fe_3O_4-NPs: Magnetite nanoparticles

V. Conclusion

Fe_3O_4 nanoparticles were successfully synthesized through the green method of utilizing aqueous plant extracts of GT, as characterized by FT-IR, XRD, EDX, SEM, TEM, and VSM techniques. The photochemical present in aqueous leaf extract of GT can act as a reducing, stabilizing, and capping agent for the preparation of megnatied Fe_3O_4-NPs. The average particle size of the particles was measured at 29.9 nm. The magnetic Fe_3O_4 nanoparticles in magnetization curve illustrates their superparamagnetic characteristics at room temperature, with a magnetization value of 48.6 emu/g. The prepared nanoparticle was successfully applied to remove CV, MG, and S dyes from prepared aqueous solutions with the adsorption capacity of 13.9, 15.6, and 14.4 mg/g, respectively.

References

Abdurrahman, F.B., Akter, M. and Abedin, M.Z., 2013. Dyes removal from textile wastewater using orange peels. *International Journal of Scientific and Technology Research*, 2, pp.47-50.

Adebowale, K.O., Olu-Owolabi, B.I. and Chigbundu, E.C., 2014. Removal of safranin-O from aqueous solution by adsorption onto kaolinite clay. *Journal of Encapsulation and Adsorption Sciences*, 4, p.89.

Ahmadi, S., Fazilati, M., Mousavi, S.M. and Nazem, H., 2020. Anti-bacterial/fungal and anti-cancer performance of green synthesized Ag nanoparticles using summer savory extract. *Journal of Experimental Nanoscience*, 15, pp.363-380.

Ahmadi, S., Fazilati, M., Nazem, H. and Mousavi, S.M., 2021. Green synthesis of magnetic nanoparticles using Satureja hortensis essential oil toward superior antibacterial/fungal and anticancer performance. *BioMed Research International,* 2021, p.8822645.

Alzaidi, J., Alzahrani, E. and El-Mouhty, N., 2016. Chemical studies on the preparation of magnetic nanoparticles coated with glycine and its application for removal of heavy metals. *Oriental Journal of Chemistry*, 32, pp.1503-1513.

Amutha, S. and Sridhar, S., 2018. Green synthesis of magnetic iron oxide nanoparticle using leaves of *Glycosmis mauritiana* and their antibacterial activity against human pathogens. *Journal of Innovations in Pharmaceutical and Biological Sciences*, 5, pp.22-26.

An, S., Liu, X., Yang, L. and Zhang, L., 2015. Enhancement removal of crystal violet dye using magnetic calcium ferrite nanoparticle: Study in single-and binary-solute systems. *Chemical Engineering Research and Design*, 94, pp.726-735.

Ardelean, I.L., Stoencea, L.B.N., Ficai, D., Ficai, A., Trusca, R., Vasile, B.S., Nechifor, G. and Andronescu, E., 2017. Development of stabilized magnetite nanoparticles for medical applications. *Journal of Nanomaterials*, 2017, p.6514659.

Awwad, A.M. and Salem, N.M., 2012. A green and facile approach for synthesis of magnetite nanoparticles. *Nanoscience and Nanotechnology*, 2, pp.208-213.

Barzinjy, A.A., Abdul, D.A., Hussain, F.H. and Hamad, S.M., 2020. Green synthesis of the magnetite (Fe3O4) nanoparticle using Rhus coriaria extract: A reusable catalyst for efficient synthesis of some new 2-naphthol bis-Betti bases. *Inorganic and Nanometal Chemistry*, 50, pp.620-629.

Bibi, I., Nazar, N., Ata, S., Sultan, M., Ali, A., Abbas, A., Jilani, K., Kamal, S., Sarim, F.M. and Khan, M.I., 2019. Green synthesis of iron oxide nanoparticles

using pomegranate seeds extract and photocatalytic activity evaluation for the degradation of textile dye. *Journal of Materials Research and Technology*, 8, pp.6115-6124.

Da'na, E., Taha, A. and Afkar, E., 2018. Green synthesis of iron nanoparticles by *Acacia nilotica* pods extract and its catalytic, adsorption, and antibacterial activities. *Applied Sciences*, 8, p.1922.

Desalegn, B., Megharaj, M., Chen, Z. and Naidu, R., 2019. Green synthesis of zero valent iron nanoparticle using mango peel extract and surface characterization using XPS and GC-MS. *Heliyon*, 5, p.e01750.

Deshmukh, A.R., Gupta, A. and Kim, B.S., 2019. Ultrasound assisted green synthesis of silver and iron oxide nanoparticles using fenugreek seed extract and their enhanced antibacterial and antioxidant activities. *BioMed Research International*, 2019, p.1714358.

Elwakeel, K.Z., El-Bindary, A., El-Sonbati, A. and Hawas, A.R., 2017. Magnetic alginate beads with high basic dye removal potential and excellent regeneration ability. *Canadian Journal of Chemistry*, 95, p.807-815.

Fayazi, M., Afzali, D., Taher, M., Mostafavi, A. and Gupta, V., 2015. Removal of Safranin dye from aqueous solution using magnetic mesoporous clay: Optimization study. *Journal of Molecular Liquids*, 212, pp.675-685.

Hajizadeh-Sharafabad, F., Alizadeh, M., Mohammadzadeh, M.H.S., Alizadeh-Salteh, S. and Kheirouri, S., 2016. Effect of *Gundelia tournefortii* L. extract on lipid profile and TAC in patients with coronary artery disease: A double-blind randomized placebo controlled clinical trial. Journal of Herbal Medicine, 6, pp.59-66.

Ibrahim, G.I., Jalal, A.F. and Ibrahim, B.M., 2013. Evaluation of antioxidant activity, phenolic, flavonoid and ascorbic acid. *Tikrit Journal of Pure Science*, 18, p.3.

Kanagasubbulakshmi, S. and Kadirvelu, K., 2017. Green synthesis of iron oxide nanoparticles using Lagenaria siceraria and evaluation of its antimicrobial activity. *Defence Life Science Journal*, 2, pp.422-427.

Khan, T.A., Ali, I., Singh, V.V. and Sharma, S., 2009. Utilization of fly ash as low-cost adsorbent for the removal of methylene blue, malachite green and rhodamine B dyes from textile wastewater. *Journal of Environmental Protection Science*, 3, p.11-22.

Khattri, S. and Singh, M., 2009. Removal of malachite green from dye wastewater using neem sawdust by adsorption. *Journal of Hazardous Materials*, 167, p.1089-1094.

Khattri, S. and Singh, M., 2012. Use of Sagaun sawdust as an adsorbent for the removal of crystal violet dye from simulated wastewater. *Environmental Progress and Sustainable Energy,* 31, pp.435-442.

Kyi, P.P., Quansah, J.O., Lee, C.G., Moon, J.K. and Park, S.J., 2020. The removal of crystal violet from textile wastewater using palm kernel shell-derived biochar. *Applied Sciences*, 10, p.2251.

Lam, S.S., Liew, R.K., Wong, Y.M., Yek, P.N.Y., Ma, N.L., Lee, C.L. and Chase, H.A., 2017. Microwave-assisted pyrolysis with chemical activation, an innovative method to convert orange peel into activated carbon with improved properties as dye adsorbent. *Journal of Cleaner Production*, 162, pp.1376-1387.

Mohammed, M., Ibrahim, A. and Shitu, A., 2014. Batch removal of hazardous safranin-O in wastewater using pineapple peels as an agricultural waste based adsorbent. *International Journal of Environmental Monitoring and Analysis,* 2, pp.128-133.

Nehaba, S.S., Abdullah, R.H., Oda, A.M., Omran, A.R. Mottaleb, A.S., 2019. Evaluation of the efficiency of tea waste powder to remove the Safranin O dye compared to the activated carbon as adsorbent. *Oriental Journal of Chemistry*, 35, p.1201.

Nejati-Koshki, K., Mesgari, M., Ebrahimi, E., Abbasalizadeh, F., Fekri Aval, S., Khandaghi, A.A., Abasi, M. and Akbarzadeh, A., 2014. Synthesis and *in vitro* study of cisplatin-loaded Fe3O4 nanoparticles modified with PLGA-PEG6000 copolymers in treatment of lung cancer. *Journal of Microencapsulation*, 31, pp.815-823.

Ramesh, A., Rama Devi, D., Mohan Botsa, S. and Basavaiah, K., 2018. Facile green synthesis of Fe3O4 nanoparticles using aqueous leaf extract of *Zanthoxylum armatum* DC. for efficient adsorption of methylene blue. Journal of Asian Ceramic Societies, 6, pp.145-155.

Saleh, H.I., 2017. *Green Synthesis of Magnetite Nanoparticles using Myrtus communis* L. Grown in Egypt, Egypt.

Saleh, H.I., 2020. Green Synthesis of Magnetite Nanoparticles using *Myrtus communis* L. Grown in Egypt, Egypt.

Sari, I. and Yulizar, Y., 2017. *Green Synthesis of Magnetite (Fe3O4) Nanoparticles using Graptophyllum pictum Leaf Aqueous Extract*. IOP Conference Series: Materials Science and Engineering, IOP Publishing, United Kingdom, p.012014.

Shojaee, S. and Shahri, M.M., 2016. Green synthesis and characterization of iron oxide magnetic nanoparticles using Shanghai white tea (Camelia sinensis) aqueous extract. *Journal of Chemical and Pharmaceutical Research*, 8, pp.138-143.

Sobh, R.A., Nasr, H. and Mohamed, W.S., 2020. Synthesis and characterization of magnetic sponge nanocomposite for cleaning archeological lime stones. *Egyptian Journal of Chemistry*, 63, pp.507-514.

Sravanthi, K., Ayodhya, D. and Swamy, P.Y., 2019. Green synthesis, characterization and catalytic activity of 4-nitrophenol reduction and formation of benzimidazoles using bentonite supported zero valent iron nanoparticles. *Materials Science for Energy Technologies*, 2, pp.298-307.

Yew, Y.P., Shameli, K., Miyake, M., Kuwano, N., Khairudin, N.B.B., Mohamad, S.E.B. and Lee, K.X., 2016. Green synthesis of magnetite (Fe 3 O 4) nanoparticles using seaweed (*Kappaphycus alvarezii*) extract. *Nanoscale Research Letters*, 11, pp.1-7.

Yusefi, M., Shameli, K., Yee, O.S., Teow, S.Y., Hedayatnasab, Z., Jahangirian, H., Webster, T.J. and Kuča, K., 2021. Green synthesis of Fe3O4 nanoparticles stabilized by a Garcinia mangostana fruit peel extract for hyperthermia and anticancer activities. *International Journal of Nanomedicine*, 16, p.2515.

Zhang, Q., Zhang, T., He, T. and Chen, L., 2014. Removal of crystal violet by clay/PNIPAm nanocomposite hydrogels with various clay contents. *Applied Clay Science*, 90, pp.1-5.

Zhen, G., Muir, B.W., Moffat, B.A., Harbour, P., Murray, K.S., Moubaraki, B., Suzuki, K., Madsen, I., Agron-Olshina, N. and Waddington, L., 2011. Comparative study of the magnetic behavior of spherical and cubic superparamagnetic iron oxide nanoparticles. *The Journal of Physical Chemistry C*, 115, pp.327-334.

http://dx.doi.org/10.14500/aro.10864

Categorization of Bacterial Pathogens Present in Infected Wounds and their Antibiotic Resistance Profile Recovered from Patients Attending Rizgary Hospital-Erbil

Ahmed A. Al-Naqshbandi[1], Hedy A. Hassan[2], Mahmoud A. Chawsheen[3] and Haval H. Abdul Qader[4]

[1]Department of Laboratory, Rizgary Teaching Hospital,
Erbil, Kurdistan Region – F.R. Iraq
[2]Department of Clinical Biochemistry, College of Health Sciences, Hawler Medical University,
Erbil, Kurdistan Region – F.R. Iraq
[3]Department of General Sciences, Faculty of Education, Soran University,
Erbil, Kurdistan Region – F.R. Iraq
[4]Nanakali Hospital for Blood Diseases and Cancer,
Erbil, Kurdistan Region – F.R. Iraq

***Abstract*—Wound infection with antibiotic-resistant bacteria can extend a patients' debility and increase the expense of treatment in the long term; therefore, careful management of patients with wound infections is necessary to avoid complications. The usage of antimicrobial agent is a major factor in resistance development. This study aims to understand the causes of wound infections, as well as the criteria for diagnosing them for more sensible antibiotic prescribing. Samples from 269 wound patients were collected, and cultured for bacterial growth. Gram stain technique, bacterial identification through VITEK 2 compact system was investigated in this study. Gram-negative bacteria (GNB) accounted for 59.15% of the total isolates, whereas pathogenic Gram-positive bacteria (GPB) accounted for 40.85% of total isolates. *Escherichia coli* and *Pseudomonas aeruginosa* are the dominant pathogenic GNB in wounds, whereas *Staphylococcus aureus* and *Staphylococcus epidermidis* are the dominant pathogenic GPB. *P. aeruginosa* showed 100% resistance to the majority of antibiotic tested, including Ampicillin, Amoxicillin/Clavulanic Acid, Aztreona, Ceftriaxone, and others. *S. aureus* and *S. epidermidis* are 100% resistant to Ampicillin, Ceftriaxone, and Cefotaxime. For more efficient antibiotic prescriptions, the causative microorganisms, and their current susceptibility patterns need to be mandated for testing before prescribing any antibiotics to patients. Prescriptions are frequently based solely on general information about the antibiotic's function, rather than on individual response variation to the pathogen and the antibiotic. Particularly, when the common pathogens in this study show multidrug resistance in wounds.**

***Index Terms*—Antibiotic resistance, Healing, Infection, Multi drug resistant, Pathogenic bacteria, Wound.**

ARO-The Scientific Journal of Koya University
Vol. IX, No.2 (2021), Article ID: ARO.10864, 7 pages
DOI: 10.14500/aro.10864
Received: 16 August 2021; Accepted: 13 November 2021;
Regular research paper: Published: 01 December 2021
Corresponding author's email: mahmoud.hassan@soran.edu.iq

I. Introduction

Globally, infection with multidrug-resistance bacteria is the main contributing agent to nearly 700,000 deaths. This estimate is expected to rise to up to 10 million deaths by the year 2050 (Reale, et al., 2017). The main route of bacteria entry to the body is through open wounds. Among the four wound cleanliness classifications established by the US Centers for Disease Control and Prevention, clean, clean-contaminated, contaminated, and dirty-infected, the fourth class shows harm to skin, mucous membranes, and organs and can demonstrate microorganism infection and inflammation (Herman and Bordoni, 2021). Wound healing processes involve repair of the damaged tissue with the help of platelets, immune cells, fibroblasts, microvascular cells, and keratinocytes. The healing process is divided into four phases that coinciding with each other; coagulation, inflammation, proliferative (formation of granulation tissue), and formation (remodeling) phases (Chadwick and Ousey, 2019). Chronic non-healing wounds begin as minor damage, including those caused by insect bites, skin scratches, or deep skin penetration. Minor injuries usually heal in a few days or weeks, but in abnormal health conditions such as diabetes, the healing process takes much longer (Demidova-Rice, et al., 2012). Chronic wounds have been classified into diabetic ulcers, pressure ulcers, and vascular ulcers. These types of chronic wounds are characterized by a longer inflammatory phase, infections, presence of biofilms, and unresponsiveness to skin healing stimuli (Frykberg and Banks, 2015). Infections with more than 105 live bacteria (or A-hemolytic streptococci) can cause harmful damage to the body. Viable bacteria or their toxins cause an inflammatory response, which can result in abscess, cellulites, and osteomyelitis. In addition to an increase in the production of Matrix metalloproteinases (MMPs) with the aid of the host's immune cells. The MMP breaks down extracellular matrix and growth factors needed for tissue recovery in wounded regions. Bacteria are colonized in wounds form a biofilm. They are often associated with delayed wound healing (Demidova-Rice, et al., 2012). The bacterial capability

to endure antimicrobial agents has two components; antibiotic tolerance and antibiotic resistance. Tolerance is the bacterial ability to maintain their physical state in the presence of the antibiotic. These biofilms have a high tolerance to antimicrobial agents, but when the biofilm is disrupted the microbes become susceptible to antibiotic treatment (Chadwick and Ousey, 2019; Cooper, et al., 2014). Antibiotic resistance emerges as a result of the response to antibiotic exposure. It has developed naturally over billions of years as a microorganism's successful survival strategy. However, bacteria have evolved antibiotic resistance mechanisms in <80 years since their introduction due to the overuse of antibiotics in human and animal health. Antibiotic resistance is one of the most serious risks to human health today. As a result, antimicrobial wound management remains a significant challenge that necessitates new approaches to combat microbes and their biofilms (Bowler, 2018; Daeschlein, 2013).

Gram-positive bacteria (GPB) are typically the first to penetrate the wound space; coagulase-negative staphylococci are the most common group obtained as commensals from the physiological milieu of unbroken skin in the wound's vicinity. Days to weeks later, Gram-negative bacteria (GNB), primarily rods, penetrate the field and compete with surviving species, depending on the patient's specific immunological habitat control. These germs usually come from sanitary barrier failures in everyday hospital hygiene, nutritional supply, and water. Other important microbial players in acute wounds are *Pseudomonas aeruginosa* and *E. coli*. Gram-negative rods (*Enterobacteriaceae*) and *P. aeruginosa* are the most common species found in chronic wound biofilms, followed by Gram-positive cocci such as fecal streptococci (*Enterococcus faecalis* and *Enterococcus faecium*) and *Staphylococcus aureus* (Bowler, 2018; Negut, et al., 2018).

Because of the essential functional and esthetic role of this tissue, the treatment of wounds is a key research domain. When the skin's barrier function is compromised, bacteria may quickly invade the underlying tissues, resulting in life-threatening infections. As a result, successful therapies for such pathological conditions are needed (Bjarnsholt, 2013). This study aims to describe the antibiotic resistance profile for bacterial pathogens present in infected wounds and make an assessment of the most suitable antibiotic with the best impact on wound healing.

II. Materials and Methods

A. Specimen Collection and Transport

Wound swaps were collected directly from patients attended Rizagary Teaching Hospital in Erbil city for the period between: January, 2014 and December, 2016. After the collection, 269 specimens were transported to laboratories of the microbiology department for analysis.

B. Bacterial Culture and Identification

After collection specimens were inoculated separately on: Blood, chocolate, and MacConkey agar. The inoculum was first smeared thoroughly over the surface of the solidified medium by sterilized loop. The loop was sterilized again and drawn-out from the first site of inoculation into three parallel lines on fresh surfaces of the medium. Series of strokes were made in succession, with the inoculum derived from the most distal part of the immediately preceding strokes at each step. The plates were incubated overnight at 37°C. Number of colonies was counted and bacterial numbers were calculated per ml of specimen. For aerobic bacterial growth, colony characteristics and Gram's staining were considered for their identification (Kumar, 2016). Classification of GPB and GNB was performed by following the VITEK® 2 compact system (bioMérieux S.A., France) using the following kits: VITEK®2 GN Reference 21341, VITEK®2 GP Reference 21342, and VITEK®2 AST-GN 82 Reference 413439.

C. Antibiotics

Antimicrobial sensitivity tests were performed using the VITEK® 2 compact system (bioMérieux S.A., France) with the following kits: VITEK®2 AST-P580 Reference 22233, and VITEK®2 AST-ST01 Reference 410028. The following antibiotics were covered in this study: AM-Ampicillin, AMC-Amoxicillin/Clavulanic Acid, AN-Amikacin, ATM-Aztreonam, CAZ-Ceftazidime, CIP-Ciprofloxacin, CM-Clindamycin, CRO-Ceftriaxone, CTX-Cefotaxime, CZ-Cefazolin, E-Erythromycin, ETP-Ertapenem, FA-Fusidic acid, FEP-Cefepime, FOS-Fosfomycin, FT-Nitrofurantoin, GM-Gentamicin, IPM-Imipenem, LEV-Levofloxacin, LNZ-Linezolid, MEM-Meropenem, MNO-Minocycline, MUP-Mupirocin, MXF-Moxifloxacin, OX1-Oxacillin, P-Benzylpenicillin, PEF-Pefloxacin, PIP-Piperacillin, RA-Rifampicin, SAM-Ampicillin/Sulbactam, SXT-Trimethoprim/Sulfamethoxazole, TEC-Teicoplanin, TE-Tetracycline, TGC-Tigecycline, TIC-Ticarcillin, TM-Tobramycin, TZP-Piperacillin/Tazobactam, and VA-Vancomycin.

D. Data Analysis

Abundance, distribution, and drug sensitivity of all bacterial isolates were presented in percentile (%). When the percentile of sensitivity of a certain isolate was <30%, that isolate was considered to be resistant. For the collective antibiotic resistance in GPB and GNB, drugs were presented in a descending manner and only with a value ≥90% were considered to be highly resistant. For these calculations Microsoft Excel 2010 was used.

III. Results

A. Pathogenic Bacteria were Isolated in One Fourth of the Collected Samples

Pathogenic bacteria were recovered in 71 of the 269 wound samples grown, accounting for 26.39% of the total samples. Non-pathogenic bacteria were found in 124 (46.1%) of the samples. Meanwhile, no bacterial growth was found in 74 (27.51%) of the samples, (Table 1).

B. Gram-Negative Bacterial is the Dominant Type of Bacteria in Wounds

In wound isolates from 71 human individuals, pathogenic GNB were shown to be more prevalent than pathogenic GNB. GNB accounted for 42 (59.15%) of the total, while pathogenic GNB accounted for 29 (40.85%) of total isolates, (Table 2).

http://dx.doi.org/10.14500/aro.10864

C. E. coli and P. aeruginosa are the Dominant Pathogenic GNB in Wounds

E. coli and *P. aeruginosa* showed the higher growth in isolated bacteria representing 13 (30.95%) and 9 (21.43%) of total GNB identified, respectively, followed by *Klebsiella pneumonia* 5 (11.9%), *Enterobacter cloacae* 3 (7.14%), and *Proteus mirabilis* 3 (7.14%). *Citrobacter koseri* is the bacteria with the least dominance, accounting for only 1 (2.38%) of the total, (Table 3).

D. S. aureus is the Dominant Pathogenic GPB in Wounds

More than half of the isolated pathogenic GPB were *S. aureus*, followed by *Staphylococcus epidermidis,* which constituted one fourth of the total isolates. *Staphylococcus haemolyticus* and *E. faecalis* were found in only two colony isolates, as *Streptococcus pneumoniae* was the rarest. It was found only in one colony isolate, (Table 3).

E. Gram-Negative P. aeruginosa is 100% Resistant to Most of the Tested Antibiotics

E. coli showed 100% resistance to Pefloxacin and Piperacillin. As well as 92.31% resistance to Monocyline, 84.62% resistance to Ampicillin, Amoxicillin/Clavulanic Acid, Aztreonam, and Ampicillin/Sulbactam, (Table 4).

Table I
Distribution of Bacterial Growth of Wound Swab Culture

Bacterial growth	Number of growth (%)
No growth of bacteria	74 (27.51%)
No bacterial pathogen isolates	124 (46.1%)
Pathogenic bacteria isolates	71 (26.39%)

Table II
Distribution of Pathogenic Bacteria Isolated from Wound Swab Culture

Bacterial growth	Number of growth (%)
GPB isolates	29 (40.85%)
GNB isolates	42 (59.15%)

Table III
Distribution of GNB and GPB Isolated from Wound Swab Culture

GNB isolates	Number of isolates (%)	GPB isolates	Number of isolates (%)
Escherichia coli	13 (30.95%)	*Staphylococcus aureus*	17 (58.62%)
Pseudomonas aeruginosa	9 (21.43%)	*Staphylococcus epidermidis*	7 (24.13%)
Klebsiella pneumonia	5 (11.9%)	*Staphylococcus haemolyticus*	2 (6.9%)
Enterobacter cloacae	3 (7.14%)	*Enterococcus faecalis*	2 (6.9%)
Proteus mirabilis	3 (7.14%)	*Streptococcus pneumoniae*	1 (3.45%)
Acinetobacter baumannii	2 (4.76%)	-	-
Enterobacter aerogenes	2 (4.76%)	-	-
Klebsiella oxytoca	2 (4.76%)	-	-
Morganella morganii	2 (4.76%)	-	-
Citrobacter koseri	1 (2.38%)	-	-

Whereas, the second dominant Gram-negative pathogen is *P. aeruginosa* showed 100% resistance to the majority of antibiotics tested, including Ampicillin, Amoxicillin/Clavulanic Acid, Aztreona, Ceftriaxone, Cefazolin, Ertapenem, Nitrofurantoin, Minocycline, Pefloxacin, Piperacillin, Ampicillin/Sulbactam, Tigecycline, Ticarcillin, and Piperacillin/Tazobactam, (Table 5).

F. The Wound Dominant GPB are 100% resistant to Ampicillin, Ceftriaxone, and Cefotaxime

Antibiotic sensitivity test showed that *S. aureus* is 100% resistant to Ampicillin, Ceftriaxone, and Cefotaxime, and 64.71% resistant to Ciprofloxacin. *S. epidermidis* is 100% resistant to Ampicillin, Ceftriaxone, and Cefotaxime. It also shows 85% resistance to Ciprofloxacin, Fusidic acid, and Quinupristin/Dalfopristin. Moreover, *S. epidermidis* is 71.43% resistant to Erythromycin, and Teicoplanin, (Table 6).

G. Both GPB and GNB in Wounds are Resistant to Ampicillin

Collectively GPB were resistant to Ampicillin, Ceftriaxone, and Cefotaxime by 96.55%, followed by Ciprofloxacin and Quinupristin/Dalfopristin by 72.41% and 68.97%, respectively. Whereas, the bacteria were least resistant to Linezolid by 3.45%, and Fosfomycin, Moxifloxacin, Tigecycline, Benzylpenicillin by 6.89%. Collectively, GNB were resistant to Ampicillin by 92.86% and Minocycline by 90.48%. Whereas, the least resistance was seen when using Amikacin by 33.33% and Cefepime by 40.48, (Table 7).

IV. Discussion

The over usage of antibiotics is a crucial factor in the development of resistance toward these drugs. Knowing the signs and symptoms of wound infections, as well as the causative organisms, and their current susceptibility trends are essential for pragmatic antibiotic prescribing (Filius and Gyssens, 2002). This study aimed to identify types of bacteria in wounds and their antibiotic susceptibility. Our results indicate that the dominant types of pathogenic bacteria in wounds are GNB *E. coli* and *P. aeruginosa*, accounting for 30.95% and 21.43% of total GNB, respectively. In wounds, *K. pneumoniae* 11.9%, *E. cloacae* 7.14%, and *P. mirabilis* 7.14% were found. The GNB with the least amount of dominance is *C. koseri* with only 2.38%.

Our result is similar to the finding of other research regarding predominance of GNB in wounds. Park, et al. (2017) reported that the majority (52%) of wound associated pathogens are of GNB. However, the commonalty of the species might show some differences for example in a research by Azzopardi, et al. (2014) found that the most prevalent Gram-negative-burn wound-pathogens were *P. aeruginosa, K. pneumoniae, Acinetobacter baumannii, Enterobacter spp., Proteus spp., and E. coli* (Azzopardi, et al., 2014; Azzopardi, et al., 2011; Park, et al., 2017).

S. aureus accounted for more than half of the pathogenic GPB identified, followed by *S. epidermidis*, which accounted

Table IV
Antimicrobial Agent's Responses to the Isolated GNB

Agent	*Acinetobacter baumannii* (2)	*Citrobacter koseri* (1)	*Enterobacter aerogenes (2)*	*Enterobacter cloacae* (3)	*Escherichia coli* (13)
AM-Ampicillin	R2 (100%)	R1 (100%)	R2 (100%)	R3 (100%)	S2 (15.38%) R11 (84.62%)
AMC-Amoxicillin/ Clavulanic Acid	R2 (100%)	R1 (100%)	R2 (100%)	S2 (66.67%) R1 (33.33%)	S2 (15.38%) R11 (84.62%)
AN-Amikacin	R2 (100%)	S1 (100%)	S2 (100%)	S2 (66.67%) R1 (33.33%)	S7 (53.85%) R6 (46.15%)
ATM-Aztreonam	R2 (100%)	S1 (100%)	S2 (100%)	S1 (33.33%) R2 (66.67%)	S2 (15.38%) R11 (84.62%)
CAZ-Ceftazidime	R2 (100%)	S1 (100%)	S2 (100%)	S2 (66.67%) R1 (33.33%)	S5 (38.46%) R8 (61.54%)
CIP-Ciprofloxacin	R2 (100%)	S1 (100%)	S2 (100%)	S3 (100%)	S3 (23.08%) R10 (76.92%)
CRO-Ceftriaxone	R2 (100%)	S1 (100%)	R2 (100%)	S1 (33.33%) R2 (66.67%)	S3 (23.08%) R10 (76.92%)
CZ-Cefazolin	R2 (100%)	S1 (100%)	R2 (100%)	R3 (100%)	S3 (23.08%) R10 (76.92%)
ETP-Ertapenem	R2 (100%)	S1 (100%)	R2 (100%)	S2 (66.67%) R1 (33.33%)	S9 (69.23%) R4 (30.77%)
FEP-Cefepime	R2 (100%)	S1 (100%)	S2 (100%)	S3 (100%)	S5 (38.46%) R8 (61.54%)
FT-Nitrofurantoin	R2 (100%)	R1 (100%)	R2 (100%)	S1 (33.33%) R2 (66.67%)	S5 (38.46%) R8 (61.54%)
GM-Gentamicin	R2 (100%)	S1 (100%)	S2 (100%)	S1 (33.33%) R2 (66.67%)	S9 (69.23%) R4 (30.77%)
IPM-Imipenem	R2 (100%)	S1 (100%)	S2 (100%)	S3 (100%)	S12 (92.31%) R1 (7.69%)
LEV-Levofloxacin	R2 (100%)	S1 (100%)	R2 (100%)	S2 (66.67%) R1 (33.33%)	S3 (23.08%) R10 (76.92%)
MEM-Meropenem	R2 (100%)	R1 (100%)	S2 (100%)	S2 (66.67%) R1 (33.33%)	S7 (53.85%) R6 (46.15%)
MNO-Minocycline	R2 (100%)	R1 (100%)	S2 (100%)	S1 (33.33%) R2 (66.67%)	S1 (7.69%) R12 (92.31%)
PEF-Pefloxacin	R2 (100%)	R1 (100%)	S2 (100%)	S1 (33.33%) R2 (66.67%)	R13 (100%)
PIP-Piperacillin	R2 (100%)	R1 (100%)	S2 (100%)	R3 (100%)	R13 (100%)
SAM-Ampicillin/ Sulbactam	S2 (100%)	R1 (100%)	R2 (100%)	R3 (100%)	S2 (15.38%) R11 (84.62%)
SXT-Trimethoprim/ Sulfamethoxazole	S2 (100%)	S1 (100%)	S2 (100%)	S1 (33.33%) R2 (66.67%)	S7 (53.85%) R6 (46.15%)
TGC-Tigecycline	R2 (100%)	S1 (100%)	R2 (100%)	S1 (33.33%) R2 (66.67%)	S4 (30.77%) R9 (69.23%)
TIC-Ticarcillin	R2 (100%)	R1 (100%)	S2 (100%)	R3 (100%)	R13 (100%)
TM-Tobramycin	S1 (50%)	R2 (50%) S1 (100%)	S2 (100%)	R3 (100%)	S6 (46.15%) R7 (53.85%)
TZP-Piperacillin/ Tazobactam	R2 (100%)	S1 (100%)	S2 (100%)	S3 (100%)	S6 (46.15%) R7 (53.85%)

S: Sensitive, R: Resistant

Table V
Antimicrobial Agent's Responses To The Isolated GNB

Agent	*Klebsiella oxytoca* (2)	*Klebsiella pneumonia* (5)	*Morganella morganii* (2)	*Proteus mirabilis* (3)	*Pseudomonas aeruginosa* (9)
AM-Ampicillin	R2 (100%)	R5 (100%)	R2 (100%)	S1 (33.33%) R2 (66.67%)	R9 (100%)
AMC-Amoxicillin/Clavulanic Acid	R2 (100%)	S1 (20%) R4 (80%)	R2 (100%)	S1 (33.33%) R2 (66.67%)	R9 (100%)
AN-Amikacin	S2 (100%)	S3 (60%) R2 (40%)	S2 (100%)	S1 (33.33%) R2 (66.67%)	S8 (88.89%) R1 (11.11%)
ATM-Aztreonam	S2 (100%)	R5 (100%)	S2 (100%)	S1 (33.33%) R2 (66.67%)	R9 (100%)
CAZ-Ceftazidime	S2 (100%)	R5 (100%)	S2 (100%)	S2 (66.67%) R1 (33.33%)	S5 (55.56%) R4 (44.44%)
CIP-Ciprofloxacin	S2 (100%)	S1 (20%) R4 (80%)	S2 (100%)	S2 (66.67%) R1 (33.33%)	S4 (44.44%) R5 (55.56%)
CRO-Ceftriaxone	S2 (100%)	R5 (100%)	R2 (100%)	S1 (33.33%) R2 (66.67%)	R9 (100%)
CZ-Cefazolin	S2 (100%)	R5 (100%)	R2 (100%)	S1 (33.33%) R2 (66.67%)	R9 (100%)
ETP-Ertapenem	S2 (100%)	S3 (60%) R2 (40%)	R2 (100%)	S1 (33.33%) R2 (66.67%)	R9 (100%)
FEP-Cefepime	S2 (100%)	R5 (100%)	S2 (100%)	S2 (66.67%) R1 (33.33%)	S8 (88.89%) R1 (11.11%)
FT-Nitrofurantoin	R2 (100%)	S1 (20%) R4 (80%)	R2 (100%)	R3 (100%)	R9 (100%)
GM-Gentamicin	S2 (100%)	S1 (20%) R4 (80%)	S (50%) R1 (50%)	S1 (33.33%) R2 (66.67%)	S6 (66.67%) R3 (33.33%
IPM-Imipenem	S2 (100%)	S3 (60%) R2 (40%)	R2 (100%)	R3 (100%)	S8 (88.89%) R1 (11.11%)
LEV-Levofloxacin	S2 (100%)	R5 (100%)	R2 (100%)	S1 (33.33%) R2 (66.67%)	S4 (44.44%) R5 (55.56%)
MEM-Meropenem	S2 (100%)	S2 (40%) R3 (60%)	S2 (100%)	S1 (33.33%) R2 (66.67%)	S8 (88.89%) R1 (11.11%)
MNO-Minocycline	R2 (100%)	R5 (100%)	R2 (100%)	R3 (100%)	R9 (100%)
PEF-Pefloxacin	R2 (100%)	S1 (20%) R4 (80%)	S2 (100%)	S1 (33.33%) R2 (66.67%)	R9 (100%)
PIP-Piperacillin	R2 (100%)	R5 (100%)	S2 (100%)	S1 (33.33%) R2 (66.67%)	R9 (100%)
SAM-Ampicillin/Sulbactam	S2 (100%)	R5 (100%)	R2 (100%)	S1 (33.33%) R2 (66.67%)	R9 (100%)
SXT-Trimethoprim/Sulfamethoxazole	S2 (100%)	S1 (20%) R4 (80%)	S1 (50%) R1 (50%)	R3 (100%)	S6 (66.67%) R3 (33.33%
TGC-Tigecycline	S2 (100%)	S2 (40%) R3 (60%)	R2 (100%)	R3 (100%)	R9 (100%)
TIC-Ticarcillin	S2 (100%)	R5 (100%)	S2 (100%)	S1 (33.33%) R2 (66.67%)	R9 (100%)
TM-Tobramycin	S2 (100%)	R5 (100%)	S2 (100%)	S2 (66.67%) R1 (33.33%)	S8 (88.89%) R1 (11.11%)
TZP-Piperacillin/Tazobactam	S2 (100%)	R5 (100%)	S2 (100%)	S2 (66.67%) R1 (33.33%)	R9 (100%)

S: Sensitive, R: Resistant

 http://dx.doi.org/10.14500/aro.10864

Table VI
Antimicrobial Agent's Responses To The Isolated GPB

Agent	*Enterococcus faecalis* (2)	*Staphylococcus aureus* (17)	*Staphylococcus epidermidis* (7)	*Staphylococcus haemolyticus* (2)	*Streptococcus pneumoniae* (1)
AM-Ampicillin	R2 (100%)	R17 (100%)	R7 (100%)	R2 (100%)	S1 (100%)
CIP-Ciprofloxacin	R2 (100%)	S6 (35.29%) R11 (64.71%)	S1 (14.29%) R6 (85.71%)	R2 (100%)	S1 (100%)
CM-Clindamycin	R2 (100%)	S12 (70.59%) R5 (29.41%)	S4 (57.14%) R3 (42.86%)	R2 (100%)	R1 (100%)
CRO-Ceftriaxone	R2 (100%)	R17 (100%)	R7 (100%)	R2 (100%)	S1 (100%)
CTX-Cefotaxime	R2 (100%)	R17 (100%)	R7 (100%)	R2 (100%)	S1 (100%)
E-Erythromycin	R2 (100%)	S12 (70.59%) R5 (29.41%)	S2 (28.57%) R5 (71.43%)	R2 (100%)	S1 (100%)
FA-Fusidic acid	R2 (100%)	S10 (58.82%) R7 (41.18%)	S1 (14.29%) R6 (85.71%)	R2 (100%)	S1 (100%)
FOS-Fosfomycin	R2 (100%)	S17 (100%)	S7 (100%)	S2 (100%)	S1 (100%)
FT-Nitrofurantoin	S2 (100%)	S17 (100%)	S7 (100%)	S2 (100%)	S1 (100%)
GM-Gentamicin	R2 (100%)	S16 (94.12%) R1 (5.88%)	S7 (100%)	S1 (50%) R1 (50%)	S1 (100%)
LEV-Levofloxacin	R2 (100%)	S16 (94.12%) R1 (5.88%)	S7 (100%)	S1 (50%) R1 (50%)	S1 (100%)
LNZ-Linezolid	S1 (50%) R1 (50%)	S17 (100%)	S7 (100%)	S2 (100%)	S1 (100%)
MUP-Mupirocin	R2 (100%)	S9 (52.94%) R8 (47.06%)	S5 (71.43%) R2 (28.57%)	R2 (100%)	R1 (100%)
MXF-Moxifloxacin	R2 (100%)	S17 (100%)	S7 (100%)	S2 (100%)	S1 (100%)
OX1-Oxacillin	R2 (100%)	S11 (64.71%) R6 (35.29%)	S7 (100%)	S1 (50%) R1 (50%)	R1 (100%)
P-Benzylpenicillin	R2 (100%)	S17 (100%)	S7 (100%)	S2 (100%)	S1 (100%)
QDA-Quinupristin/Dalfopristin	R2 (100%)	S7 (41.18%) R10 (58.82%)	S1 (14.29%) R6 (85.71%)	S1 (50%) R1 (50%)	R1 (100%)
RA-Rifampicin	R2 (100%)	S16 (94.12%) R1 (5.88%)	S3 (42.86%) R4 (157.14%)	R2 (100%)	R1 (100%)
SXT-Trimethoprim/Sulfamethoxazole	R2 (100%)	S16 (94.12%) R1 (5.88%)	S5 (71.43%) R2 (28.57%)	S2 (100%)	R1 (100%)
TE-Tetracycline	R2 (100%)	S9 (52.94%) R8 (47.06%)	S3 (42.86%) R4 (157.14%)	S1 (50%) R1 (50%)	S1 (100%)
TEC-Teicoplanin	S2 (100%)	S10 (58.82%) R7 (41.18%)	S2 (28.57%) R5 (71.43%)	R2 (100%)	R1 (100%)
TGC-Tigecycline	S2 (100%)	S15 (88.24%) R2 (11.76%)	S7 (100%)	S2 (100%)	S1 (100%)
TM-Tobramycin	R2 (100%)	S9 (52.94%) R8 (47.06%)	S6 (85.71%) R1 (14.29%)	S1 (50%) R1 (50%)	R1 (100%)
VA-Vancomycin	S2 (100%)	S15 (88.24%) R2 (11.76%)	S3 (42.86%) R4 (57.14%)	S1 (50%) R1 (50%)	S1 (100%)

S: Sensitive, R: Resistant

Table VII
Pattern Of Antimicrobial Resistance Among Detected Bacteria

S. No.	GPB		GNB	
	Antibiotics	% Resistance	Antibiotics	% Resistance
1.	AM-Ampicillin	96.55	AM-Ampicillin	92.86
2.	CRO-Ceftriaxone	96.55	MNO-Minocycline	90.48
3.	CTX-Cefotaxime	96.55	PIP-Piperacillin	88.1
4.	CIP-Ciprofloxacin	72.41	AMC-Amoxicillin/Clavulanic Acid	85.71
5.	QDA-Quinupristin/Dalfopristin	68.97	CZ-Cefazolin	83.33
6.	FA-Fusidic acid	58.62	FT-Nitrofurantoin	83.33
7.	MUP-Mupirocin	51.72	PEF-Pefloxacin	83.33
8.	TE-Tetracycline	51.72	SAM-Ampicillin/Sulbactam	83.33
9.	TEC-Teicoplanin	51.72	TIC-Ticarcillin	83.33
10	E-Erythromycin	48.28	CRO-Ceftriaxone	80.95
11.	CM-Clindamycin	44.83	TGC-Tigecycline	76.19
12.	TM-Tobramycin	44.83	TZP-Piperacillin/Tazobactam	71.43
13.	OX1-Oxacillin	34.48	LEV-Levofloxacin	69.05
14.	RA-Rifampicin	34.48	ATM-Aztreona	64.29
15.	VA-Vancomycin	24.14	ETP-Ertapenem	57.14
16.	SXT-Trimethoprim/Sulfamethoxazole	20.69	CIP-Ciprofloxacin	52.38
17.	GM-Gentamicin	13.79	CAZ-Ceftazidime	50
18.	LEV-Levofloxacin	13.79	SXT-Trimethoprim/Sulfamethoxazole	45.24
19.	FOS-Fosfomycin	6.89	TM-Tobramycin	45.24
20.	MXF-Moxifloxacin	6.89	GM-Gentamicin	42.86
21.	P-Benzylpenicillin	6.89	FEP-Cefepime	40.48
22.	TGC-Tigecycline	6.89	MEM-Meropenem	38.1
23.	LNZ-Linezolid	3.45	AN-Amikacin	33.33
24.	-	-	IPM-Imipenem	26.19

for one-fourth of the total isolates. Only two colony isolates contained *S. haemolyticus* and *E. faecalis*, with *S. pneumoniae* being the least common. This finding is supported by other studies since *S. aureus* is reported to be the common GPB in wound patients (Mahat, et al., 2017; Guan, et al., 2021).

There seems to be variability in the diversity of bacterial culture in wounds. A study done by Bessa, et al. (2015) showed that the most common bacterial species detected was

S. aureus (37%), followed by *P. aeruginosa* (17%), *P. mirabilis* (10%), *E. coli* (6%), and *Corynebacterium spp*. Our results came in agreement with theirs regarding antibiotic sensitivity tests as they also reported that Vancomycin and Linezolid were effective against all GPB, and GNB revealed a significant level of resistance to the majority of antibiotics with Amikacin being the most effective against them (Bessa, et al., 2015).

In general, speaking, GPB were highly resistant toward each of Ampicillin, Ceftriaxone, and Cefotaxime. Meanwhile, they were highly sensitive to Fosfomycin, Moxifloxacin, P-Benzylpenicillin, Tigecycline, and Linezolid specifically. For being resistant by 100% to 19 (out of 24) drugs, *E. faecalis* was the most resistant recovered GPB. Since *S. pneumoniae* was sensitive by 100% toward 16 (out of 24) drugs it was the most sensitive recovered GPB (Tables 6 and 7).

These results indicate that multidrug-resistant (MDR) bacteria were associated with the identified pathogens and may play a negative role in chronic wound infection. These findings come in agreement with previous studies of ours that confirmed the existence of MDR bacteria among patients identified with urinary tract and lower respiratory tract infections (Al-Naqshbandi, et al., 2019; Chawsheen, et al., 2020; Abbas and Owaid, 2021).

IV. Conclusion

It is concluded from this research the importance of learning more about the causes of wound infections and the criteria for detecting them so that more appropriate antibiotics may be prescribed. GNB made up to two third of total bacterial isolates cultured from wounds. The most dominant pathogenic GNB were *E. coli* and *P. aeruginosa*. The most dominant pathogenic GNB isolated from wounds were *S. aureus* and *S. epidermidis*. The majority of antibiotics tested, including ampicillin, amoxicillin/clavulanic acid, Aztreona, Ceftriaxone, and others, exhibited 100% resistance. Ampicillin, Ceftriaxone, and Cefotaxime are completely ineffective against *S. aureus* and *S. epidermidis*. The pathogenic bacteria and their current susceptibility patterns must be enforced for testing before administering any antibiotics to patients for more efficient antibiotic prescriptions.

V. Recommendations

A significant number of MDR bacteria were recognized as the causal agents of wound infection in this study. Mandatory investigation of wound specimens, as well as antibiotic susceptibility testing, is recommended to guide physicians in pragmatic wound infection therapy, thereby reducing the propagation of resistant bacteria.

VI. Author Contributions

The 1st and 4th authors contributed to this study by collecting data and conducting laboratory techniques. The 2nd and 3rd authors contributed in writing this manuscript. Data analysis was conducted by the 1st and 3rd authors.

VII. Acknowledgments

We would like to acknowledge the instrumental support of Rizgary Teaching Hospital to complete this study.

VIII. Conflict of Interest

The authors declare no conflict of interest.

IX. References

Abbas, Z.K. and Owaid, M.N., 2021. Prevalence of antibiotics resistance in the isolated bacteria from bronchial washing fluids in Ramadi Teaching Hospital, Iraq. *Gazi Medical Journal*, 32(3), pp.359-363.

Al-Naqshbandi, A.A., Chawsheen, M.A. and Abdulqader, H.H., 2019. Prevalence and antimicrobial susceptibility of bacterial pathogens isolated from urine specimens received in Rizgary hospital-Erbil. *Journal of Infection and Public Health*, 12, pp.330-336.

Azzopardi, E.A., Azzopardi, S.M., Boyce, D.E. and Dickson, W.A., 2011. Emerging gram-negative infections in burn wounds. *Journal of Burn Care and Research*, 32, pp.570-576.

Bessa, L.J., Fazii, P., Di Giulio, M. and Cellini, L., 2015. Bacterial isolates from infected wounds and their antibiotic susceptibility pattern: Some remarks about wound infection. *International Wound Journal*, 12, 47-52.

Bjarnsholt, T., 2013. The role of bacterial biofilms in chronic infections. *Apmis*, 121, pp.1-58.

Bowler, P.G., 2018. Antibiotic resistance and biofilm tolerance: A combined threat in the treatment of chronic infections. *Journal of Wound Care*, 27, pp.273-277.

Chadwick, P. and Ousey, K., 2019. Bacterial-binding dressings in the management of wound healing and infection prevention: A narrative review. *Journal of Wound Care*, 28, pp.370-382.

Chawsheen, M.A., Al-Naqshbandi, A.A. and Abdulqader, H.H., 2020. Bacterial profile and antimicrobial susceptibility of isolates recovered from lower respiratory tract infection for patients in Rizgary Hospital, Erbil. *Aro-the Scientific Journal of Koya University*, 8, pp.64-70.

Cooper, R.A., Bjarnsholt, T. and Alhede, M., 2014. Biofilms in wounds: A review of present knowledge. *Journal of Wound Care*, 23, pp.570-582.

Daeschlein, G., 2013. Antimicrobial and antiseptic strategies in wound management. *International Wound Journal*, 10, pp.9-14.

Demidova-Rice, T.N., Hamblin, M.R. and Herman, I.M., 2012. Acute and impaired wound healing. *Advances in Skin and Wound Care*, 25, pp.304-314.

Filius, P.M. and Gyssens, I.C., 2002. Impact of increasing antimicrobial resistance on wound management. *American Journal of Clinical Dermatology*, 3, pp.1-7.

Frykberg, R.G. and Banks, J., 2015. Challenges in the treatment of chronic wounds. *Advances in Wound Care*, 4, pp.560-582.

Guan, H., Dong, W., Lu, Y., Jiang, M., Zhang, D., Aobuliaximu, Y., Dong, J., Niu, Y., Liu, Y., Guan, B., Tang, J. and Lu, S., 2021. Distribution and antibiotic resistance patterns of pathogenic bacteria in patients with chronic cutaneous wounds in China. *Frontiers in Medicine*, 8, pp.609584.

Herman, T.F. and Bordoni, B., 2021. Wound classification. In: *StatPearls*. StatPearls Publishing, Treasure Island, FL.

Kumar, S., 2016. *Essentials of Microbiology*. Jaypee Group, Noida.

Mcdowell, A., Azzopardi, E.A., Azzopardi, E., Camilleri, L., Villapalos, J., Boyce, D.E., Dziewulski, P., Dickson, W.A. and Whitaker, I.S., 2014. Gram negative wound infection in hospitalised adult burn patients-systematic review and metanalysis. *PLoS One*, 9, p.e95042.

Negut, I., Grumezescu, V. and Grumezescu, A., 2018. Treatment strategies for infected wounds. *Molecules*, 23, p.2392.

Park, H.S., Pham, C., Paul, E., Padiglione, A., Lo, C. and Cleland, H., 2017. Early pathogenic colonisers of acute burn wounds: A retrospective review. *Burns*, 43, pp.1757-1765.

Pushpa, M., 2017. Bacteriological profile of wound infection and antibiotic susceptibility pattern of the isolates. *Journal of Microbiology and Experimentation*, 4, pp.119-122.

Reale, M., Strazzulla, A., Quirino, A., Rizzo, C., Marano, V., Postorino, M.C., Mazzitelli, M., Greco, G., Pisani, V., Costa, C., Cesana, B.M., Liberto, M.C., Torti, C. and Foca, A., 2017. Patterns of multi-drug resistant bacteria at first culture from patients admitted to a third level University hospital in Calabria from 2011 to 2014: Implications for empirical therapy and infection control. *Infezioni in Medicina*, 25, pp.98-107.

First Principle Calculations for Silver Halides AgBr, AgCl, and AgF

Akram H. Taha

Department of Physics, Faculty of Science and Health, Koya University, Koya KOY45, Kurdistan Region - F.R. Iraq

***Abstract*—Density functional theory (DFT) coupled with Generalized Gradient Approximation (GGA) method are carried out to calculate the electronic structures of AgX (X; Br, Cl, and F). The effect of hybridizing between 4d orbital of Ag element and the p orbitals of the X in the valence band plays a very important role in the total density of states configuration. The electronic structure has been studied and all results were compared with the experimental and theoretical values. The importance of this work is that there are insufficient studies of silver halides corresponding the great importance of these compounds. Almost all the results were consistent with the previous studies mentioned here. We found the band gap of AgX to be 2.343 eV, 2.553 eV, and 1.677 eV for AgBr, AgCl, and AgF, respectively, which are in good agreement with the experimental results.**

***Index Terms*—Density functional theory; Generalized gradient approximation; Silver halides; Density of states**

1. Introduction

Density functional theory (DFT) is one of the most important theories that can be used to simulate the chemical and some of the physical properties. Many codes with some specific methods of approximations has been used this theory (such as Gaussian 09, WIEN2K, Quanta, SUESTA, …etc) because of its flexibility in writing codes and programming. Some of these codes are free and others are commercial. ab-initio calculations success is due to the fact that they don't require a lot of inputs rather than they are parameter free. In addition, the improvements in algorithms and computer facilities which can be more applicable with the increasing physical and chemical phenomena (Jonathan et al., 2019).

One of the most important compounds used in photographic process are silver halides (James, 1977). Photo- catalytically, silver chloride layer AgCl plays a key role in the oxidation of water to O_2 (Lanz, Schürch and Calzaferri, 1999; Calzaferri et al., 2001). Due to Silver halide's excellent photocatalysts performance, it received huge attention from researchers (Changhua et al., 2016). (Masahiro et al., 2021) developed an *in situ* diffracted X-ray flash to observe high-resolution diffraction patterns from the single crystal grains with a time resolution of 50 ms. The diffraction spots of single grains of silver and silver halides moved in two directions during the photochemical reaction. The motions of the spots represent tilting and rotational motions.

The augmented plane wave (APW) method was used to calculate both valance and conduction bands of silver bromide and silver chloride. For both crystals, the calculated bands were adjusted so that the experimental value of the direct band gap at Γ was duplicated (E_g=5.13 eV in AgCl, E_g=4.29 eV in AgBr). The calculated indirect band gaps were 3.28 and 2.89 eV for AgCl and 2.67 eV for AgBr, respectively (Peter 1965). Self-consistent local density calculations of the electronic structures of AgF, AgCl and AgBr are carried out by the tight binding linearized muffin-tin orbital-atomic sphere approximation (TB LMTO-ASA) method (Onwuagba, 1996). The silver halides rock salt structure has competing minimum in the conduction band at X and Γ points (Gordienko, Zhuravlev and Poplavnoi, 1991). The full-potential linear augmented-Slater-type-orbital implementation of the local-density approximation is employed to stimulate the electronic structure of five of silver halides. The calculated band gaps and bandwidths were in good agreement with the experimental results (Victora, 1997). Silver bromide, silver chloride, and silver fluoride have been subjected of many different quantum investigations. The electronic properties described in the early calculation work done by Scop (Scop, 1965; Bassani, Knox and Fowler, 1965).

The present work depends on the first principle, *i.e.*, the only inputs are the positions of the nuclei. SIESTA code (Spanish Initiative for Electronic Simulations with Thousands of Atoms) under LINUX can provide total energies, stress, and forces using the atomic orbitals with finite-support basis orbitals are the key for calculating the Hamiltonian and overlap matrices in O (N) operation. The used basis set in running the code play key role for more accurate calculations. The electron-ion interaction is represented using pseudopotentials which all plane wave codes do. The used basis set was the double zeta basis plus polarization (DZP) to give minimal angular momentum *l*. where zeta is given in the following wave function (Milton and Stegun, 1964):

$$\Psi_{nlm}(\boldsymbol{r}) = r^{n-1}e^{-\xi r}Y_{lm}(\theta,\phi) \quad (1)$$

The DFT coupled with generalized gradient approximation (GGA) (Perdew, Burke and Ernzerhof, 1996) is used in this

ARO-The Scientific Journal of Koya University
Vol. IX, No.2 (2021), Article ID: ARO.10874, 5 pages
DOI: 10.14500/aro.10874
Received: 09 September 2021; Accepted: 02 November 2021
Regular research paper: Published: 03 December 2021
Corresponding author's email: akram.hashim@koyauniversity.org

http://dx.doi.org/10.14500/aro.10874

work to simulate the electronic structure for silver halides using SIESTA free code.

II. Theory

As we mentioned that the DFT is one of the promising theories that can be used to predict behavior of the atoms and molecular moreover, so a brief theory will be discussed here. This theory is concerned with ground state of the system and the basic variables that deals with is the density of the electron $\rho(\vec{r})$ instead of the wave function $\psi(r_1, r_2,\ldots\ldots,r_N)$.

For an insulated N-electron system in the Schrödinger equation is:

$$\hat{H}\psi(\mathrm{r}_1,\mathrm{r}_2,\cdots,\mathrm{r}_N)=E\psi(\mathrm{r}_1,\mathrm{r}_2,\cdots,\mathrm{r}_N) \tag{2}$$

Where the Hamiltonian is

$$\hat{H}=\underbrace{-\sum_i \frac{\hbar^2}{2m_e}\nabla^2_{\mathbf{r}_i}}_{(K.E)_e}\underbrace{-\sum_i \frac{\hbar^2}{2M_i}\nabla^2_{\mathbf{R}_i}}_{(K.E)_n}+\underbrace{\frac{1}{2}\sum_{i\neq j}\frac{1}{4\pi\varepsilon_o}\frac{e^2}{|\mathbf{r}_j-\mathbf{r}_i|}}_{V_{e-e}}$$
$$\underbrace{-\sum_i\sum_j\frac{1}{4\pi\varepsilon_o}\frac{e^2 Z_j}{|\mathbf{R}_j-\mathbf{r}_i|}}_{V_{e-n}}+\underbrace{\frac{1}{2}\sum_{i\neq j}\frac{1}{4\pi\varepsilon_o}\frac{e^2 Z_i Z_j}{|\mathbf{R}_j-\mathbf{R}_i|}}_{V_{n-n}} \tag{3}$$

Born-Oppenheimer makes use of the large difference between the heavy nucleus mass and the mass of electron ($M_i >> m_e$), so the Schrödinger equation (3) can be written in the form (Harrison, 2011):

$$\hat{H}_{elec}=-\sum_i\frac{\hbar^2}{2m_e}\nabla^2_{\mathbf{r}_i}+\frac{1}{2}\sum_{i\neq j}\frac{1}{4\pi\varepsilon_o}\frac{e^2}{|\mathrm{r}_j-\mathrm{r}_i|}$$
$$-\sum_i\sum_j\frac{1}{4\pi\varepsilon_o}\frac{e^2 Z_j}{|\mathrm{R}_j-\mathbf{r}_i|} \tag{4}$$

After solving this equation one can get the electronic wave functions (eq. 1) and the energies of the electrons as a function as position. By using the DFT, the dependency can be changed from the coordinates of the electrons to the electron density $\rho(\mathbf{r})$. This theory deal with total electron density instead of many-body Schrödinger wave functions and all calculations were done assuming the ground state of the system. For an *N*-particle system by integrating the *N*-particle distribution probability density function $\rho(\mathbf{r}_1, \mathbf{r}_2, \mathbf{r}_N)$ over $N-1$ variables, as (Carlos, Nogueira and Marques, 2003)

$$\rho(\mathbf{r}_1)=N\int\cdots\int P(\mathbf{r}_1,\mathbf{r}_2,...,\mathbf{r}_N)\ d^3r_2\, d^3r_3\cdots\cdots d^3r_N \tag{5}$$

The Basis set that is used in DFT is the Kohn-Sham (KS) theorem, which is represented by (Hohenberg and Kohn, 1964; Kohn and Sham, 1965):

$$E_{V_{ext}}[\rho(\mathrm{r})]=\underbrace{T_e[\rho(\mathrm{r})]+V_{e-e}[\rho(\mathrm{r})]}_{F_{\mathrm{HK}}[\rho(\mathrm{r})]}+\underbrace{V_{e-n}[\rho(\mathrm{r})]}_{V_{ext}[\rho(\mathrm{r})]}$$
$$=F_{\mathrm{HK}}[\rho(\mathbf{r})]+\int\rho(\mathbf{r})\,V_{ext}(\mathbf{r})\,d^3r \tag{6}$$

This equation represents the first KS theorem which states that "For any system of interacting particles in an external potential V_{ext}, the external potential V_{ext} is uniquely determined, apart from an additive constant, by knowledge of the ground-state electron density $\rho_o(r)$."

Where T[ρ(r)] is the kinetic energy, the potential energy is $V_{ext}[\rho(\mathbf{r})]$ and $F_{\mathrm{HK}}[\rho(\mathbf{r})]$ is the *Hohenberg-Kohn* universal constant and all are *functionals* of the density $\rho(\mathbf{r})$.

The second KS theorem "*For a trial electron density $\rho_t(\mathbf{r})$, with properties $\rho_t(\mathbf{r})\geq 0$ and $\int\rho_t(\mathbf{r})\,d^3r=N$ (number of electrons), will give an energy higher than {or equal to, if it were exactly the true electron density $\rho_o(\mathbf{r})$ }the true ground-state energy* $E_{V_{ext}}[\rho_o(\mathrm{r})]$ „ $\left(i.e.\ E_{V_{ext}}[\rho_t(\mathrm{r})]\geq E_{V_{ext}}[\rho_o(\mathrm{r})]\right)$

The GGA exchange-correlation energy can be written as follows (Becke, 1988):

$$\left[E_{xc}^{\mathrm{GGA}}[\rho_\uparrow(\mathrm{r}),\rho_\downarrow(\mathrm{r})]=\int\rho(\mathbf{r})\epsilon_{xc}^{\mathrm{GGA}}\right.$$
$$\left.[\rho_\uparrow(\mathrm{r}),\rho_\downarrow(\mathrm{r}),\nabla\rho_\uparrow,\nabla\rho_\downarrow]\,d^3r\right] \tag{7}$$

III. Results and discussion

The band structure of the three silver halides is shown in Fig. 1. The kgrid is chosen to be 15 Angstroms. The kgrid is chosen to be 15 Angstroms, which represents the kgrid cutoff that determines the fineness of the k-grid used for Brillion zone sampling. We can estimate the differences in the gap energies some times by expecting a smaller band gap when decreasing the unit cell constant

We can estimate the differences in the gap energies some times by expecting a smaller band gap when decreasing the unit cell constant. A stronger interaction between atom to atom distance and hence a stronger splitting the smaller sizes of these halides, the radii of ions, can compensate this effect. To make the comparison we can use the equation (Glaus and Calzaferri, 2003):

$$\Delta_E = 2\{r(X^-) + r(Ag^+)\}/a(AgX) \tag{8}$$

Where Δ_E represents the estimation energy, $r(X^-)$ is the radius of the halide, $r(Ag^+)$ is the ionic radius of a silver ion and the a(AgX) is the unit cell constant.

The value of the indirect Γ- L transition of AgF (1.677 eV) differs little bit smaller than AgBr and AgCl (2.343 eV and 2.553 eV). However, the nature of this transition is the same (Wolan and Hoflund, 1998).

Figs. 1 and 2 shows the relationship between the calculated band structure and the density of states of AgBr, AgCl, and AgF. A comparison between Figs. 1 and 2 shows a good agreement with the experimental data for all cases in the first electronic transition of indirect Γ – L type and the direct Γ transition see Table 1. It is known that he indirect transition energy of AgF is a bit smaller than AgCl because of small energy difference is

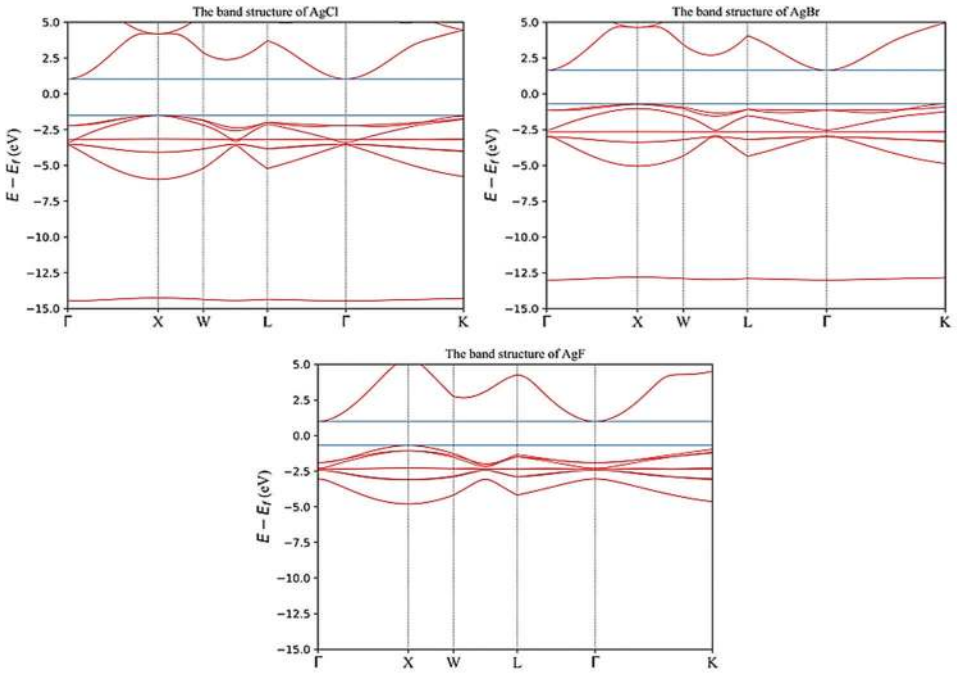

Fig. 1. Band structure of AgCl, AgBr, and AgF (FCC).

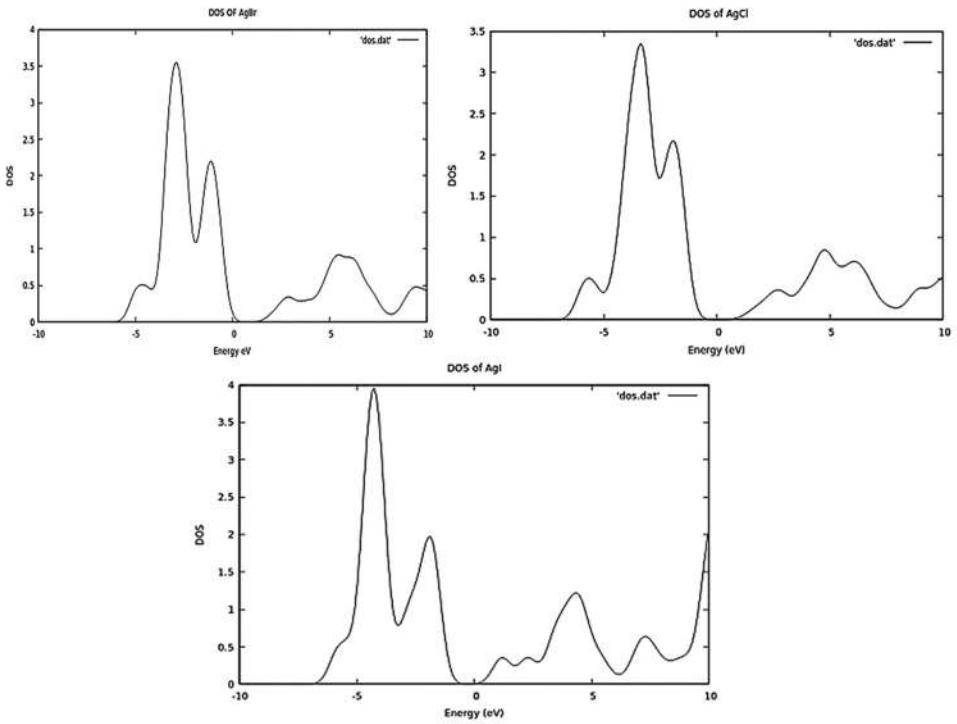

Fig. 2. The density of states and the contribution of the 4-d (Ag) of the three silver halides.

due to the difference in the bounding energy due the interaction between the atoms (Glaus and Galzaferri, 1999). The broad bandgap is due to the strong surface plasmon resonance of the silver halides photosensitivity (Prachi et al., 2020).

Self-consistent local density calculations of the electronic structures of AgF, AgCl and AgBr are carried out by the tight binding linearized muffin-tin orbital-atomic sphere approximation (TB LMTO-ASA) method. The silver 4d orbital strongly hybridizes with the halogen p orbitals in the valence band and this plays a key role in the configuration of the total density of states (Gordienko, Zhuravlev and Poplavnoi, 1991). The relative position of the sharp peaks in the Ag d level and F, Cl, Br p level as well as the band gap values obtained in the total density of states of these silver halides are compared with the previous theoretical and experimental values. The silver halide AgX is used in

 http://dx.doi.org/10.14500/aro.10874

Table I
Experimental and Theoretical Values of AgCl, AgBr, and AgF.

	Unit cell (A)	Ind. Transmission (eV)	Direct transmission (eV)	Unit cell (A)	Ind. Trans. Ev	Direct Trans. eV	Estimation ΔE	Unit cell (A)	Ind. Trans. (eV)	Direct Trans. (eV)	Estimation ΔE
	Experimental Data			Theoretical (Stephan and Calzaferri, 2003)				This work			
AgCl	5.54	2.8	5.15	5.46[a]	3.28	5.28	1.06	5.65	2.553	5.23	1.06
AgBr	5.77	3.25	4.29	5.63[a]	2.67	4.20	1.07	5.95	2.343	3.98	1.08
AgF	4.936	2.69	4.63	4.936	2.85	3.61	1.00	5.20	1.667	3.51	0.98

F. (Kirchhoff, Honender and Gilan, 1994)[a]

Table II
The Band Energies at Symmetric Points

Γ	Γ_1	Γ_{12}		Γ'_{25}			Γ_{15}			Γ_1
	−14.4	−3.55	−3.55	−3.53	−3.53	−3.53	−2.22	−2.21	−2.21	1.23
L	−14.36	−5.22	−3.84	−3.84	−3.18	−3.18	−2.12	−1.98	−1.98	3.71
X	−14.26	−5.97	−4.08	−4.08	−3.16	−3.16	−1.53	−1.53	−1.51	4.19
W	−14.36	−5.21	−3.85	−3.84	−3.18	−3.18	−2.18	−1.87	−1.83	2.85
K	−14.29	−5.78	−4.03	−3.98	−3.19	−3.16	−1.78	−1.73	−1.56	4.43

photography because they are photosensitive to light and hyposolution because these halides decompose in to silver positive ion and negative halide ion (eq. 8). Silver is black in color, therefore it is sensitive to react with the light to form the halides. The hybridation comes from the transition of the exceeded electron from the 2, 3, and 4 p state halides to the positive silver halide to form the silver halides. Table 2 shows the band energies of AgCl in eV at symmetry points. For the zone center (Gamma), the wave function correspond each energy transforms according to the indicated irreducible representation.

Table 2 shows the band energies at symmetry points. For Γ as zone center, the 4d silver electron exhibits a threefold degenerate wave functions Γ'_{25} with defined energies of −3.53 eV and a twofold Γ_{12} wave functions with energies of −3.55 eV. The experimental binding energy (~3 eV) (Tejada et al., 1975) is little bit smaller than the theoretical one. There is some matching with the experimental value in the narrowest energy gap occurred in the Γ-L transition of the indirect energy gap.

The substantial degeneracies especially at Gamma point are due to the symmetry operations done by the point symmetry group. The size and morphologies of silver halides must be controlled when synthesizing these halides (Sasithac, Kowsalya and Yugang, 2017).

IV. Conclusions

This work gives some options to get information about these halides which can be applicable in several physical models. The simulated band gap of silver halides are in good agreement with most of the experimental and other theoretical result because of the flexibility of the code used here beside the well-chosen basis set to complete the simulation. Due to principle of used DFT theory, here we firstly tried to get a minimum energy ground state because this theory is based on the ground state energy which needs to find the minimum energy of AgX for different values of lattice constant, so finding the lattice constant for the three silver halides were carried out by a series of test to choose the optimal lattice constant values. This study can be extended to simulate other physical properties such as optical, electrical, and mechanical properties.

V. Acknowledgment

Our deep thanks to Dr. Watheq Z. Alias for his useful discussions about the program and his continuous efforts. Furthermore, our thanks are extended to Dr. Faten I. Chaqmaqchee.

References

Bassani, F., Knox, R.S. and Fowler, W.B., 1965. Band structure and electronic properties of AgCl and AgBr, *Physical Review Journals Archive*, 137, pp.1217-1224.

Becke, A.D., 1988. Density-functional exchange-energy approximation with correct asymptotic behavior. *Physical Review A*, 38, p.3098.

Calzaferri, G., Brühwiler, D., Glaus, S., Schürch, D., Currao, A. and Leiggener, C., 2001. Quantum-sized silver, silver chloride and silver sulfide clusters. Quantum-sized silver, silver chloride and silver sulfide clusters, *Journal of Imaging Science and Technology*, 45, pp.331-339.

Carlos, F., Nogueira, F. and Marques, M.A.L., 2003. A Primer in Density Functional Theory, Springer, Heidelberg.

Changhua, A., Shutao, W., Yugang, S., Qinhui, Z., Jun, Z., Chenyu, W., and Jiye, F., 2016. Plasmonic silver incorporated silver halides for efficient photochatalysts. *Journal of Materials Chemistry A*, 4(12), pp.4336-4352.

Glaus, S. and Calzaferri, G., 2003. The band structures of the silver halides AgF, AgCl, and AgBr: A comparative study. *Photochemical and Photobiological Sciences*, 2, pp.398-401.

Glaus, S. and Galzaferri. G., 1999. Silver chloride clusters and surface states. *The Journal of Physical Chemistry B*, 103, pp.5622-5630.

Gordienko, A.B., Zhuravlev, Y.N. and Poplavnoi, A.S., 1991. Electronic structure of AgCl, AgBr, and AgI. *Physica Status Solidi* (*b*), 168, pp.149-156.

Hohenberg, P. and Kohn, W., 1964, Inhomogeneous electron gas. *Physical Review Journals Archive*, 136, p.B864.

James, T.H., 1977. *The Theory of Photographic Process*, 4th ed. Macmillan, New York.

Jonathan, S., Mario, R. Marques, S.B. and Marques, A.A.L., 2019. Recent advances and applications of machine learning in solid state materials science. *Computational Materials*, 5, p.83.

Kirchhoff, F., Honender, J.M. and Gilan, M.J., 1994. Energetic and electronic structure of silver chloride. Physical Review B, 49, p.17420.

Kohn, W. and Sham, L.J., 1965. Self-consistent equations including exchange and correlation effects. Physical Review, 140, A1133.

Lanz, M., Schürch, D. and Calzaferri, G. 1999. Photocatalytic oxidation of water to O_2 on AgCl-coated electrodes. *Journal of Photochemistry and Photobiology A: Chemistry*, 120, pp.105-117.

Masahiro, K., Omata, H., Ishihara, M., Hanslin, S.O., Mizumaki, M., Kawamura, N., Osawa, H., Suzuki, M., Mio, K., Sekiguchi, H. and Sasaki, Y.C., 2021. Tilting and rotational motion of silver halide crystal with diffracted x-ray blinking. *Scientific Reports*, 11, p.4097.

Milton, A. and Stegun, I.A., 1964, *Handbook of Mathematical Functions with Formulas, Graphs, and Mathematical Tables*, National Bureau of Standards, Washington, DC.

Onwuagba, B.N., 1996. The electronics structure of AgF, AgCl, and AgBr. *Solid State Communications*, 97(4), pp.267-271.

Harrison, P., 2011, *Quantum Wells, Wires and Dots: Theoretical and Computational Physics of Semiconductor Nanostructures*, third edition, John wiley & sons, LTD.

Perdew, J.P., Burke, K. and Ernzerhof, M., 1996. Generalized gradient approximation made simple. *Physical Review Letters*, 77, p.3805.

Prachi, T., Pankaj, R., Paradeep, S., Abhinandan, K., Aftab, A., Abdullah, M., 2020. Exploring recent advances in silver halides and graphitic carbon nitride-based photocatalyst for energy and environmental applications. *The Arabian Journal of Chemistry*, 13(11), pp.8271-8300.

Sasithac, A., Kowsalya, D., and Yugang, S., 2017. Ternary silver halides nanocrystals. *Accounts of Chemical Research*, 50(7), pp.1754-1761.

Scop, P.M., 1965. Band structure of silver chloride and silver bromide. *Physical Review Journals Archive*, 139, pp.934-940.

Stephan, G. and Calzaferri, G., 2003. The band structures of the silver halides AgF, AgCl, and AgBr, A comparative study. *Photochemical and Photobiological Sciences*, 2, pp.398-401.

Tejada, J., Shevchik, N.J., Braun, W., Goldmann, A. and Cardona, M., 1975. Valence bands of AgCl and AgBr: UV photoemission and theor. *Physical Review B*, 12, p.1557.

Victora, R.H., 1997. Calculated electronic structure of silver halide crystals. *Physical Review B*, 56(8), 4417.

Wolan, J.T. and Hoflund, G.B., 1998. Surface characterization study of AgF and AgF2 powder using XPS and ISS. *Applied Surface Science*, 125, pp.251-258.

http://dx.doi.org/10.14500/aro.10871

Reducing Environment Pollution by Reusing of Alum Sludge Waste in Stone Mastic Asphalt Mixtures

Omar T. Mahmood

Department of Civil Engineering, Faculty of Engineering, Koya University, Daniel Mitterrand Boulevard, Koya KOY45, Kurdistan Region – F.R. Iraq

***Abstract*—Globally, a huge quantity of alum sludge waste is produced as a by-product material from drinking water treatment plants that utilize aluminum salts as an essential coagulate and is the most generally produced water treatment remaining sludge around the world, which causes a serious environmental problem. Direct discarding of this substance has ecological effects. Hence, it is important to reuse this alum sludge waste material in such a manner to diminish its detrimental impacts on the environment. This research investigates the possibility of reusing alum sludge waste as a partial replacement of cement filler in stone mastic asphalt (SMA) paving mixtures. For this investigation, the alum sludge was used as a filler material in SMA mixtures in two modes; dried alum sludge at 110°C and burned alum sludge at 700°C. Different percentages of alum sludge were used as a replacement by the total weight of mineral filler at 0, 20, 40, 60, 80, and 100%. The results showed that using alum sludge as a substitution of filler in SMA mixtures reduces the performance of the mixtures in terms of Marshall properties and tensile strength for both dried and burned alum sludge compared with a standard mix. However, the performance of the mixtures containing burned alum sludge gave a better performance than the mixtures containing dried alum sludge.**

***Index Terms*—Alum sludge; Alum sludge reuse; Burned alum sludge; Dried alum sludge; Environment pollution; Stone mastic asphalt.**

I. Introduction

The growth in population and urban expansion has resulted in a significant consumption of drinking water worldwide. Hence, the production of the residuals from water treatment plants is likely to increase with the growing population. From a technical perspective, nevertheless, the production of trustworthy and secure drinking water is often followed by producing water treatment residues and is called water treatment sludge (Zhao, et al., 2020). Since the water treatment plants include coagulation, flocculation, sedimentation, filtration and sterilization processes, during the "flocculation/coagulation" procedures known as water treatment residuals, a massive amount of residues as a by-product were created (Xu, et al., 2020). Alum sludge is the by-product material produced from drinking water treatment plants where aluminum salts are essential coagulating-flocculating chemicals (Yang, et al., 2006). Because of their performance and low expenses, aluminum salts are the main coagulating agents most widely used by water industries worldwide for water treatment processes (Gebbie, 2001). The environmental effects of alum sludge resulting from the water treatment process can also result in harm to human health. A part of these effects may appear instantly and others may require a longer time to affect, thusly, health impacts usually connected with natural contamination or environmental pollution that involves the utilization of chemicals or synthetic substances should be tested for the expected environmental pollution (Department of Environment, 2005). Therefore, water treatment sludge removal and the related expense besides the ecological effects are still global issues. Hence, the simple and unstudied removal techniques of water treatment sludge, such as discard in the sewer; discard in the common water body; discard in the lagoons and waste landfill; lead to unfavorable environmental effects (Turner, et al., 2019). As environmental and economic constraints restrict disposal choices, seeking appropriate alum sludge reuse options would also become imperative (Keeley, et al., 2014). Appropriate management of residual sludge is an environmentally and economically sustainable approach that remains a very serious concern. Recovery, recycle and reuse are a suitable solution for the disposal of water treatment sludge (Ahmad, et al., 2016).

To conform the disposal of waste requirements which have been stipulated by the authorities, researchers have been looking for alternative building materials as a replacement for conventional materials such as cement, bricks, ceramics, tiles, and aggregates so as to minimize the environmental effects of these wastes. In an attempt to close the distance between immense volumes of alum sludge and alleviate contamination, a series of studies aimed at beneficial reuse (Khalid, et al., 2014). Therefore, a study including the use of alum sludge in building and concrete work participates to reduce the potential pollution. Not only for being hard to get rid of growing volumes of alum sludge waste, but it also poses significant health risks. Therefore, efforts should be made to control the pollution resulting from the disposal of

ARO-The Scientific Journal of Koya University
Vol. IX, No.2 (2021), Article ID: ARO.10871, 7 pages
DOI: 10.14500/aro.10871
Received: 06 September 2021; Accepted: 20 November 2021
Regular research paper: Published: 07 December 2021
Corresponding author's e-mail: omar.taha@koyauniversity.org

alum sludge by turning these undesirable wastes into usable raw materials for use in the construction field (Ahmad, et al., 2016). One of the opportunities to dispose of the alum sludge is to recycle it in the construction field. Every year, the construction sector consumes tremendous amounts of materials; accordingly, it can be considered an opportunity to reuse alum sludge in the manufacture of construction purposes and concrete production. Subsequently, to determine the highest percentage that could be used as a replacement for raw materials, further laboratory tests are needed. The growing issue of alum discharge into the environment will thus be mitigated if new solutions for disposal apart from landfill can be discovered (Khalid, et al., 2014).

Ghazawi, et al. (2015) experimentally investigated the possibility of alum sludge being consumed in asphalt paving mixtures. Alum sludge was utilized as a replacement with different percentages by the total weight of mineral filler in the hot mix asphalt (HMA). It has been observed that with increasing amounts of sludge waste in the asphalt mixture, stability, flow, and air voids are increased, then decreased.

Sahar, et al. (2019) experimentally examined the influence of alum sludge on the performance of HMA concrete mixtures. Alum sludge was utilized as a fine aggregate substitute in HMA at various percentages by weight of fine aggregate. The results indicated that using alum sludge up to 50% as a partial replacement for fine aggregate in a HMA resulted in acceptable values complying with nearly all the standard specification requirements. The main objective of this paper is to investigate the possibility of reusing alum sludge as a replacement of cement filler in stone mastic asphalt (SMA) mixtures.

II. Materials Characterization

All materials used in this study are locally available and currently used in road construction in northern Iraq.

A. Aggregates

In this study, it was used an asphalt concrete mixture in which 19 mm maximum aggregate size has been selected according to the American Association of State Highway and Transportation Officials (AASHTO) Specifications (AASHTO, 2009). The coarse and fine aggregate used in this investigation was brought from Tanjero HMA plant, and these were originally brought from a quarry near Sulaymaniyah city and crushed at the asphalt plant by mechanical crusher. The aggregate gradation is shown in Table I according to AASHTO specification M 325-08. An ordinary Portland cement was used as a mineral filler.

B. Filler

An ordinary Portland cement was used as a mineral filler in the asphalt mixture, brought from the Al-Mas cement factory. It constitutes from 8% to 11% by the total weight of the asphalt mixture. In this study, 10% of mineral filler was used by the total weight of the asphalt mixture. The physical properties of the mineral filler are presented in Table II.

C. Asphalt Cement

In this study, one type of asphalt cement was used with penetration grade of 40-50 obtained from Baiji refinery, Iraq. The characteristics of asphalt cement are according to the American Society for Testing and Materials (ASTM). The physical properties of the asphalt samples are given in Table III.

D. Additive-sisal Fiber

Sisal fiber is one of the most commonly used natural fibers, it can be obtained from the sisal plant, and it is extremely easy to cultivate (Omar, et al., 2020). In this study, the sisal fibers were used as an additive stabilizer in the SMA mixes at a dosage of 0.3% by the total weight of the mixture as recommended by AASHTO M 325-08, (2009).

E. Alum Sludge

The alum sludge was collected from the Kanibe water treatment plant, located at the Kanibe area near Dukan, in northern Iraq. For the purpose of this study, the alum sludge was used as a filler material in SMA mixtures in two methods; the first one, was by drying the alum sludge at 110°C for 24 h, and the second method, was by burning the alum sludge at a high temperature of 700°C for 6 h then it was left to cool at room temperature before it was pulverized by Los Angeles abrasion machine, finally, a powder alum sludge passing through sieve No. 200 (75 μm) will be used

TABLE I
Selected Combined Gradation Of Aggreate And Filler According To Aashto Specifications

Sieve size (mm)	Specification range	Selected gradation
19	100	100
12.5	90-100	95
9.5	50-80	65
4.75	20-35	27
2.36	16-24	20
0.075	8-11	10

TABLE II
Physical Properties Of Portland Cement Filler

Properties	Unit	Value
Specific gravity	-	3.15
Passing Sieve No. 200	%	99

TABLE III
Physical Properties Of Asphalt Cement

Properties	Unit	Specifications	Test results	Specifications limits
Penetration at (25°C, 100 g, 5 s)	0.1 mm	ASTM D5	44	40–50
Specific gravity at 25°C	-	ASTM D70	1.03	-
Softening point (Ring and Ball)	°C	ASTM D36	54	-
Ductility (25°C, 5 cm/min)	cm	ASTM D113	112	> 100
Flash point	°C	ASTM D92	288	> 232
Fire point	°C	ASTM D92	319	-

http://dx.doi.org/10.14500/aro.10871

as a filler in the stone matrix asphalt mixture for both phases. Fig. 1 shows alum sludge after treatment.

III. Laboratory Specimen Preparation and Test Methods

A. Optimum Asphalt Content

Marshall specimens were prepared in accordance with the Marshall procedure specified in the ASTM D6926-10 with different percentages of asphalt cement varying from 4.5 to 7% at an increment of 0.5% mixed with aggregate, 0.3% sisal fibers, and 10% Portland cement filler according to the adopted gradation. The Marshall samples were left to cool at room temperature and thereafter extracted from the mold to conduct the test on the samples in accordance with the ASTM D6927-15 procedure. According to the Marshall test, the results showed that the optimum asphalt content is equal to 6.1%. The test results were represented in Figs. 2-5 which showed the Marshall properties of the SMA mixtures.

B. Effect of Alum Sludge Content

The influence of alum sludge on the performance of SMA was assessed by comparing the behavior of specimens having various percentages of alum sludge added to the asphalt mixture as a substitution of mineral filler at 0% as a reference, 20%, 40%, 60%, 80%, and 100% by total weight of filler. As compared with the conventional mixture, the results showed that when the alum sludge content in SMA increased, the Marshall stability values decreased, but they remained acceptable. Likewise, the Marshall flow were decreased when alum sludge content increased, but the accepted Marshall flow value can be obtained by replacing up to 40% of filler by alum sludge, whereas the air voids are increased when alum sludge amount increased. The results of the Marshall test for SMA mixtures are shown in Figs. 6-9.

The properties of SMA in terms of tensile strength per each alum sludge content can be examined by loading the Marshall specimen along a diametric plane with a compressive load at a constant rate acting parallel to and along the vertical diametrical plane of the specimen through two opposite loading strips. This loading method generates a relatively uniform tensile stress perpendicular to the direction of the applied load and along the vertical diametrical plane, ultimately causing the tested specimen to fail by splitting along the vertical diameter. The indirect tensile strength of a specimen is determined using the procedure stipulated

Fig. 1. Alum sludge waste materials. (a) Alum sludge oven-dried at 110°C. (b) Alum sludge furnace-burned at 700°C.

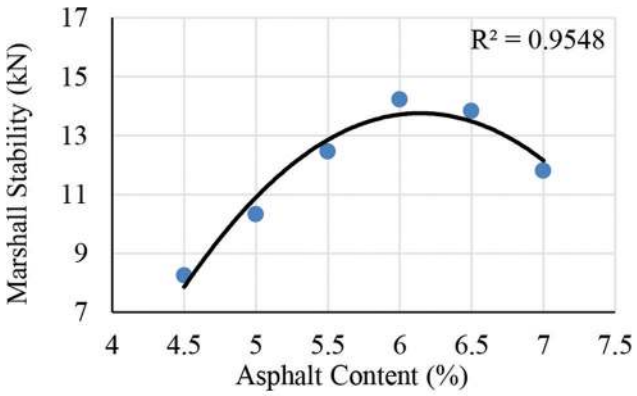

Fig. 2. Effect of asphalt content on Marshall stability of the mixtures.

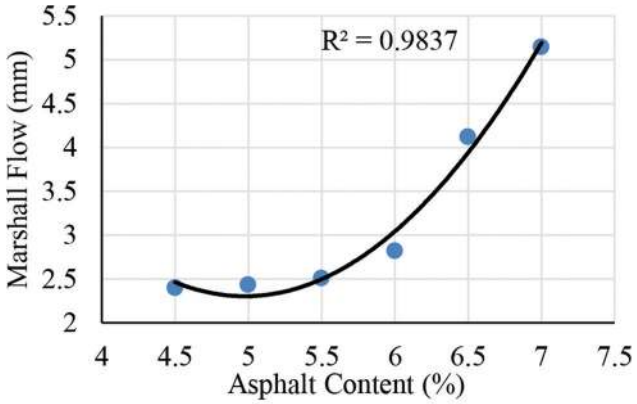

Fig. 3. Effect of asphalt content on Marshall Flow of the mixtures.

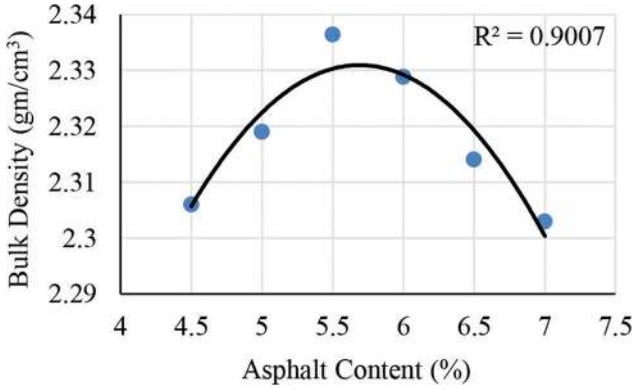

Fig. 4. Effect of asphalt content on bulk density of the mixtures.

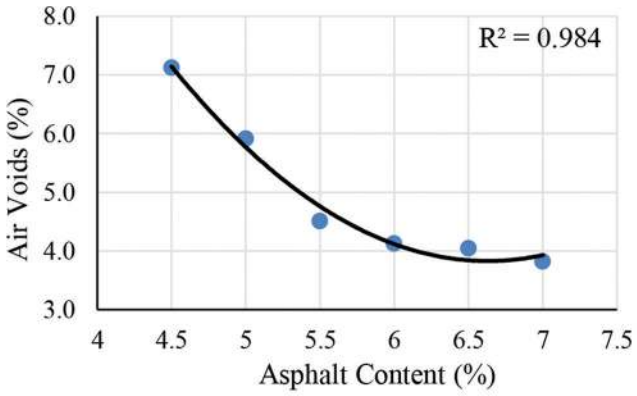

Fig. 5. Effect of asphalt content on air voids of the mixtures.

in ASTM D 6931. The tensile strength ratio depending on the result of indirect tensile strength in two scenarios; conditioned and unconditioned, and represented in Figs. 10 and 11. The results showed that when the percentage of replaced cement filler by alum sludge increased, the indirect tensile strength decreased; similarly, the tensile strength ratios were decreased as the percentage of replaced cement filler by alum sludge increased and indicated that the mixtures are more sensitive to moisture damage as a result of the presence of water in the mixture. However, the tensile strength ratios are still acceptable according to the moisture susceptibility requirement by AASHTO T 283/ASTM D4867 standard specifications.

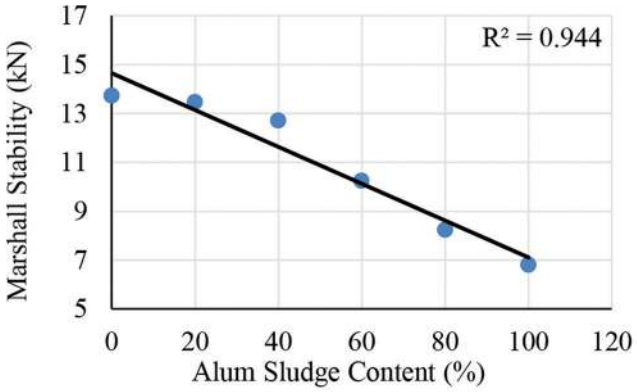

Fig. 6. Effect of alum sludge content on Marshall stability of the mixtures.

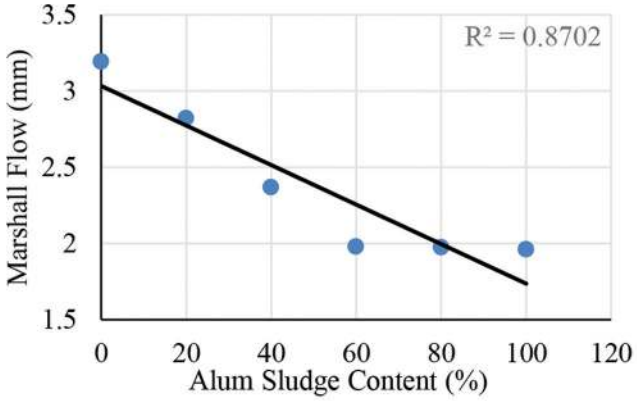

Fig. 7. Effect of alum sludge content on Marshall flow of the mixtures.

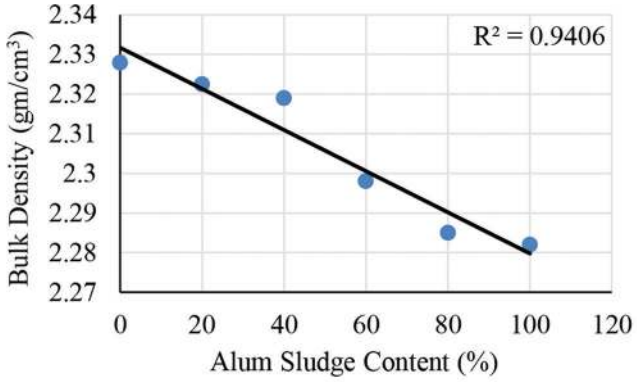

Fig. 8. Effect of alum sludge content on bulk density of the mixtures.

C. Effect of Alum Sludge burning

To investigate the effect of burning alum sludge on the performance of SMA mixtures, the material was subjected to a high temperature of 700°C for 6 h then cooled at room

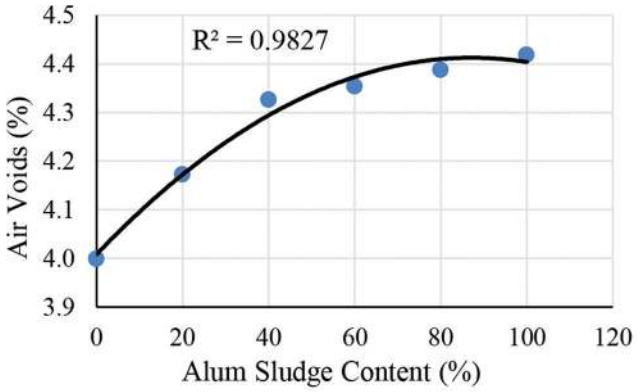

Fig. 9. Effect of alum sludge content on air voids of the mixtures.

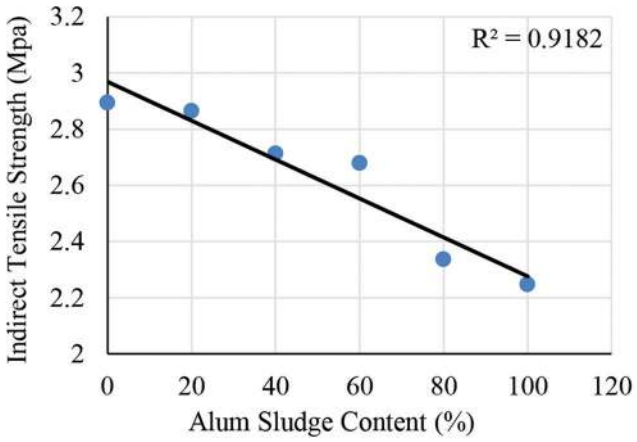

Fig. 10. Effect of alum sludge content on indirect tensile strength (unconditioned).

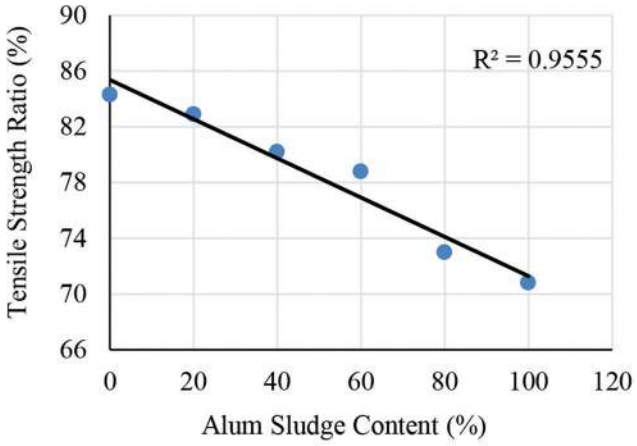

Fig. 11. Effect of alum sludge content on index of retained strength.

http://dx.doi.org/10.14500/aro.10871

temperature before being pulverized by a rotary steel ball mill and sieved on a sieve No.200 (75 μm) to be utilized as a filler in SMA mixtures. The performance of SMA was evaluated by comparing the behavior of specimens containing different percentages of burned alum sludge added to the asphalt mixture as a replacement of mineral filler at 20%, 40%, 60%, 80%, and 100% by total weight of filler. The results showed that as the replacement percentage of burned alum sludge in SMA mixtures increased, the Marshall stability, bulk density and the Marshall flow are slightly increased as compared with the mixtures containing the same percentage of dried alum sludge, whereas the air voids are decreased when the burned alum sludge amount increased in the SMA mixtures. The results of the Marshall test for the SMA mixtures are shown in Figs. 12-15.

To evaluate the effect of the burned alum sludge on the moisture susceptibility of the SMA mixtures, the tensile strength test was conducted on two sets of specimens conditioned and unconditioned in accordance to ASTM D 4867. The results indicated that when the percentage of replaced cement filler by burned alum sludge increased, the indirect tensile strength decreased as compared with the standard mix. Likewise, the tensile strength ratios were decreased when the percentage of replaced cement filler by burned alum sludge increased. However, the mixture with the replacement of burned alum sludge have showed a slight better performance as compared with those mixtures containing dried alum sludge at the same percentage. This can be attributed to the burning of organic matter content in alum sludge, which caused an increase in the bulk density, and eventually improved the performance of the mixture. Fig. 16 shows the failure mode of the indirect tensile test.

The results of the indirect tensile test and tensile strength ratio for the SMA mixtures are shown in Figs. 17 and 18.

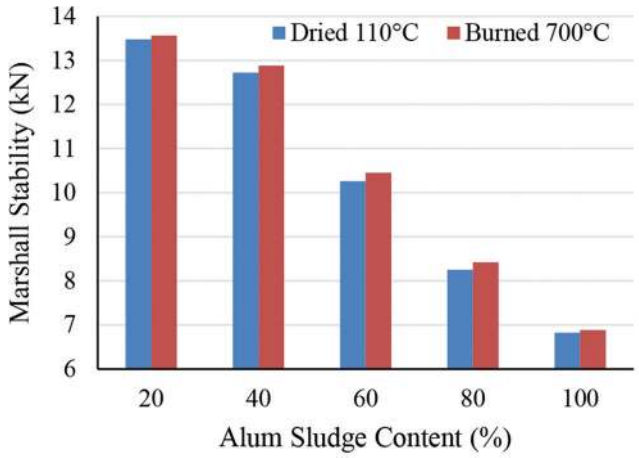

Fig. 12. Effect of alum sludge burning on Marshall stability of the mixtures.

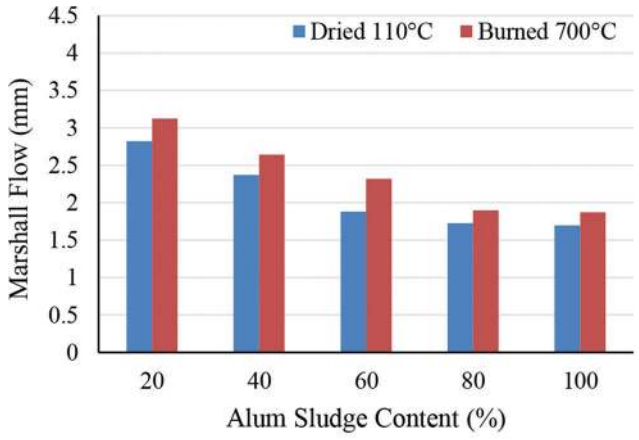

Fig. 13. Effect of alum sludge burning on Marshall flow of the mixtures.

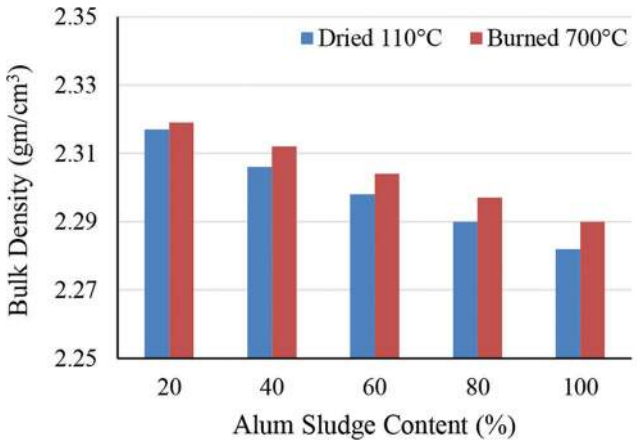

Fig. 14. Effect of alum sludge burning on bulk density of the mixtures.

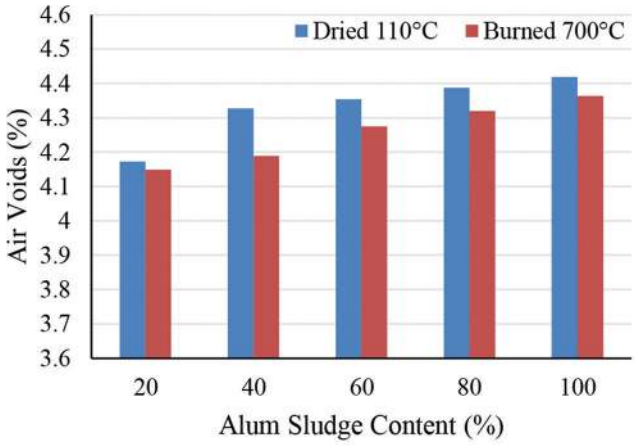

Fig. 15. Effect of alum sludge burning on air voids of the mixtures.

Fig. 16. Failure mode of indirect tensile test.

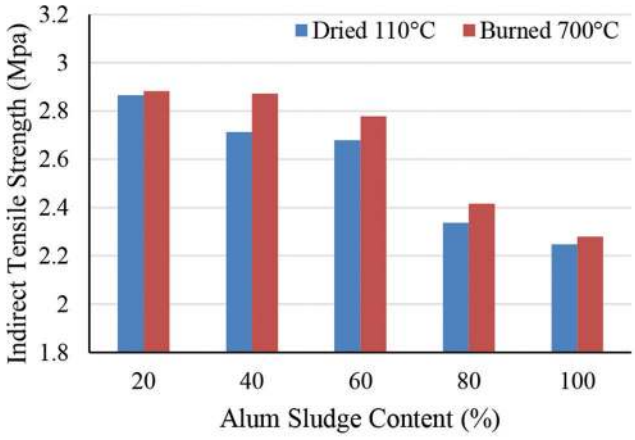

Fig. 17. Effect of alum sludge burning on indirect tensile strength (unconditioned).

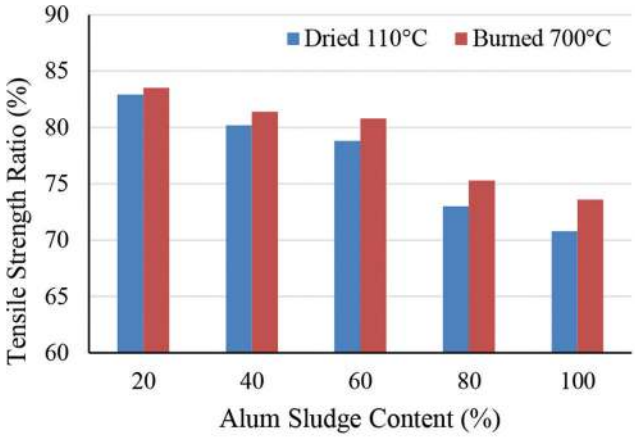

Fig. 18. Effect of alum sludge burning on index of retained strength.

IV. Conclusion

From the laboratory investigation, it can be seen that the replacing of the cement filler with alum sludge in the SMA mixtures reduces the performance of both Marshall properties and tensile strength as compared with the standard mixture of SMA. The main conclusions are drawn as the following:

1. The Marshall stability and Marshall flow values decreased when the cement filler was replaced with dried alum sludge in the SMA mixes, nevertheless, up to 40% of replacement, the results were acceptable in accordance with the standard specifications
2. The mixtures containing the burned alum sludge as a substitution of cement filler up to 60 % have satisfied all the properties required for asphalt mixtures for the Marshall properties in accordance with the standard specification
3. In SMA mixtures, when the percentage of replaced cement filler by alum sludge increased, the indirect tensile strength and tensile strength ratio decreased as compared with the standard mix by 22% and 16%, respectively, for dried alum sludge, while for the burned alum sludge decreased by 21% and 12.7%, respectively. However, the results are still acceptable in accordance with the standard specifications.

Finally, despite alum sludge decreasing the performance of asphalt mixtures in terms of Marshall properties and tensile strength, it can be used up to 40% as a partial replacement of Portland cement filler in the SMA mixtures, and because there was a slight difference in results for dried and burned alum sludge; it is recommended to reuse the alum sludge in a dried state to be more economic by saving the energy. Eventually, that will help in the safe and environmentally adequate disposal of alum sludge, besides that can contribute to keeping resources of construction materials.

References

Ahmad, T., Ahmad, K. and Alam, M., 2016. Sustainable management of water treatment sludge through 3 'R' concept. *Journal of Cleaner Production*, 124, pp.1-13.

American Association of State Highway and Transportation Officials (AASHTO), 2009. *Standard Specification for Stone Matrix Asphalt* (*SMA*), *No. M325-08*, American Association of State Highway and Transportation Officials, Washington, DC.

American Association of State Highway and Transportation Officials, 2021. *Standard Method of Test for Resistance of Compacted Asphalt Mixtures to Moisture-Induced Damage*, American Association of State Highway and Transportation Officials, No. 283, Washington, DC.

ASTM D4867-04. *Standard Practice for Effect of Moistureon Asphalt Concrete Paving Mixtures*.

ASTM D6926-10. *Standard Practice for Preparation of Bituminous Specimens Using Marshall Apparatus.*

ASTM D6927-15. *Standard Test Method for Marshall Stability and Flow of Asphalt Mixtures.*

ASTM D6931-12. *Standard Test Method for Indirect Tensile (IDT) Strength of Bituminous Mixtures*.

Department of Environment, 2005. *Guidelines for the Application of Special Management of Scheduled Waste*. Environmental Quality Act (Scheduled Waste) Regulation, Department of Environment, Ministry of Natural Resources and Environment, Malaysia.

Gebbie, P., 2001. Using Polyaluminium Coagulants in Water Treatment. In: *64th Annual Water Industry Engineers and Operators' Conference All Seasons International Hotel, Bendigo*, 5 and 6 September, 2001.

Ghazawi, Z., Khedaywi, T. and Gouneem, A., 2015. Pollution Reduction and Reuse of Sludge Waste in Asphalt Paving Mixtures. In: *Proceedings of the 4th International Conference on Energy Systems, Environment, Entrepreneurship and Innovation* (ICESEEI' 15) Dubai, United Arab Emirates February 22-24, pp.395-400.

Keeley, J., Jarvis, P. and Judd, S.J., 2014. Coagulant recovery from water treatment residuals: A review of applicable technologies. *Critical Reviews in Environmental Science and Technology*, 44(24), pp.12-25.

Khalid, M.B., Faris, G.F. and Isam, M.A., 2014. Reuse of alum sludge in construction materials and concrete works: a general overview. *Infrastructure University Kuala Lumpur Research Journal*, 2(1), pp.20-30.

Mahmood, O.T. and Ahmed, S.A., 2020. Influence of natural fibers on the performance of hot mix asphalt for the wearing course of pavement. *ARO The Scientific Journal of Koya University*, 8(2), p.10710.

Sahar A.A., Hayder A.O., Tameem M.H. and Kareem, H., 2019. Influence of Using Alum Sludge as an Aggregate on Hot Mix Asphalt. In: *International Conference on Civil and Environmental Engineering Technologies*. *IOP Conference Series Materials Science and Engineering*, Vol. 584.

Turner, T., Wheeler, R., Stone, A. and Oliver, I., 2019. Potential alternative

reuse pathways for water treatment residuals: Remaining barriers and questions a review. *Water Air Soil Pollution*, 230, p.227.

Xu, D., Lee, L.Y., Lim, F.Y., Lyu, Z., Zhu, H., Ong, S.L. and Hu, J., 2020. Water treatment residual: A critical review of its applications on pollutant removal from storm water runoff and future perspectives. *The Journal of Environmental Management*, 259, p.109649.

Yang, Y., Tomlinson, D., Kennedy, S. and Zhao, Y.Q., 2006a. Dewatered alum sludge: A potential adsorbent for phosphorus removal. *Water Science and Technology*, 54(5), pp.207-213.

Zhao, Y.Q., Liu, R.B., Awe, O.W., Yang, Y. and Shen, C., 2018. Acceptability of land application of alum-based water treatment residuals an explicit and comprehensive review. *The Chemical Engineering Journal*, 353, pp.717-726.

Design and Analysis of a Wide Stopband Microstrip Dual-band Bandpass Filter

Salah I. Yahya[1,2], Abbas Rezaei[3], Yazen A. Khaleel[2]

[1]Department of Communication and Computer Engineering, Cihan University-Erbil, Erbil, Kurdistan Region – F.R. Iraq

[2]Department of Software Engineering, Faculty of Engineering, Koya University, Koya KOY45, Kurdistan Region – F.R. Iraq

[3]Department of Electrical Engineering, Kermanshah University of Technology, Kermanshah, Iran

***Abstract*–A novel configuration of a dual-band bandpass filter (DB-BPF) working as a harmonic attenuator is introduced and fabricated. The proposed filter operates at 3 GHz, for ultra-high-frequency and super high-frequency applications, and 6.3 GHz, for wireless applications. The presented layout has a symmetric structure, which consists of coupled resonators. The designing of the proposed resonator is performed by introducing a new *LC* equivalent model of coupled lines. To verify the *LC* model of the coupled lines, the lumped elements are calculated. The introduced filter has a wide stopband up to 85 GHz with 28th harmonic suppression, for the first channel, and 13th harmonic suppression, for the second channel. The harmonics are attenuated using a novel structure. Furthermore, the proposed BPF has a compact size of 0.056 λ_g^2. Having several transmission zeros that improve the performance of the presented BPF are another feature. The proposed DB-BPF is fabricated and measured to verify the design method, where the measurement results confirm the simulations.**

***Index Terms*—Microstrip; bandpass filter; dual band; harmonic attenuator; ultra-high frequency; super high frequency.**

I. Introduction

Recently, microstrip devices such as microstrip bandpass filters (BPFs) and diplexers have been widely used in many applications (Rezaei and Yahya, 2019; Yahya, Rezaei and Nouri, 2020a; 2020b; 2020c; Rezaei, Yahya and Jamaluddin, 2020; Rezaei, et al., 2020;). High-performance microstrip dual-band BPFs (DB-BPFs) with planar structures have been used widely in multiband microwave/RF transceivers. Several kinds of DB-BPFs are reported in Hayati and Noori (2011; 2012); Liu, Li and Ren (2013); Sun, et al. (2013); Chen, et al. (2014); Huang and Huang (2014); Pan, et al. (2015); Wu, et al. (2015); Ogbodo, Wang and Yeo (2016); Malherbe (2016); Zhu and Abbosh (2016); Xu and Zhu (2017); Rezaei and Noori (2017); Rezaei, et al. (2019); Rezaei and Yahya (2019); Challal, Hocine and Mermoul (2019); Moitra, Dey and Bhowmik (2019); Borjlu and Khadem (2019); Khani, Danaie and Rezaei (2019); Karimi, et al. (2019); Oudaya and Tamilselvan (2020); Li, Kang and Liu (2020); and Rezaei, et al. (2020). A quad-mode resonator with stub-to-stub coupling structure in Sun, et al. (2013), multimode stepped-impedance resonators in Chen, et al. (2014), radial stubs and lumped capacitors in Xu and Zhu (2017), complex spiral resonators in Wu, et al. (2015), E-shape resonator in Liu, Li and Ren (2013), and coupled open loops in Hayati and Noori (2011; 2012); Rezaei and Noori (2017) are all adopted to obtain DB-BPFs. However, these DB-BPFs could not improve the return loss, where the best-achieved return loss is −21 dB. Since the harmonic attenuation is a significant factor, a well-designed filter must suppress harmonics. Nevertheless, only the designers in Sun, et al. (2013) were able to suppress the 8th harmonic. The DB-BPFs in Chen, et al. (2014); Xu and Zhu (2017); Wu, et al. (2015); and Liu, Li and Ren (2013) could suppress just the first harmonic, which is a weakness of their works. Meanwhile, Hayati and Noori (2011; 2012) could attenuate the fourth and second harmonics, respectively. In Rezaei and Noori (2017), the second harmonic is attenuated below −20 dB. In Ogbodo, Wang and Yeo (2016), several coupled U-shape resonators are connected together to create two close passbands at 1.74 GHz and 1.87 GHz. Meanwhile, it has large insertion losses without harmonic attenuation. In Zhu and Abbosh (2016), embedded coupled lines have been used to provide a high selectivity DB-BPF with two passbands from 2.28 GHz to 2.67 GHz and 3.35 GHz to 3.63 GHz for WLAN and WiMAX applications, respectively. However, it could only suppress 2nd harmonic. The dual-band frequency response in Malherbe (2016) has been created by employing cascaded shunt open and short steps. In Pan, et al. (2015), a tri-mode resonator with varactors has been used to obtain a dual-band frequency response whereas it needs a discriminated coupling to suppress the unwanted mode. In Huang and Huang (2014), a large size dual-mode defected stub-loaded resonator provides a high selectivity passband. In

ARO-The Scientific Journal of Koya University
Vol. IX, No.2 (2021), Article ID: ARO.10908, 8 pages
DOI: 10.14500/aro.10908
Received: 21 November 2021; Accepted: 04 December 2021
Regular research paper: Published: 15 December 2021
Corresponding author's email: salah.ismaeel@koyauniversity.org

Oudaya and Tamilselvan (2020), a conductor-backed CPW-based DB-BPF with a compact size has been presented for satellite applications. An adjustable high-selectivity DB-BPF is designed in Li, Kang and Liu (2020) using a quantic-mode resonator. In Challal, Hocine and Mermoul (2019), a novel DB-BPFs for wireless communication systems has been presented. In Moitra, Dey and Bhowmik (2019), the design and analysis of a DB-BPFs using coupled line structures, DGS, and series inductive metallic vias have been presented. A quad-section DB-BPF has been designed in Borjlu and Khadem (2019) using a radial stub for wireless applications. In Khani, Danaie and Rezaei (2019), a microstrip DB-BPF with compact size and wide bandwidth has been introduced. A compact DB-BPF with an ultra-narrow band has been proposed in Karimi, et al. (2019) for WiMAX applications. For providing an alternative method to miniaturize a microstrip DB-BPF, a symmetrical fractal structure has been utilized in Lu, et al. (2017). Two DB-BPFs operated at 2.4/5.7 GHz and 0.9/1.575 GHz have been proposed in Yang, et al. (2010) for WLANs and GPS, respectively. In Wu, et al. (2008), a microstrip DB-BPF with low selectivity has been introduced based on quarter-wavelength resonators for WLAN and GPS applications. A microstrip DB-BPF using tri-section stepped impedance and short stub-loaded stepped impedance resonators has been designed in Li, et al. (2015) for WLAN and WiMAX applications. In Hammed (2015), an E-shape microstrip structure has been used to design a DB-BPF for multiband wireless communication systems. To achieve a microstrip DB-BPF for WLAN applications in Zong, et al. (2012), a microstrip embedded scheme resonator has been utilized. Similar to the other DB-BPFs mentioned above, the works in Malherbe (2016); Pan, et al. (2015); Huang and Huang (2014); Lu, et al. (2017); Yang, et al. (2010); Wu, et al. (2008); Li, et al. (2015); Hammed (2015); and Zong, et al. (2012) could not improve stopband properties. In Hayati and Noori (2011), a microstrip DB-BPF has been reported which could attenuate 4th harmonic. It does not have a novel structure because of using two stub-loaded open-loop resonators. Two single-band BPFs with high losses and large dimensions are designed in Feng, Gao and Che (2015); Salleh, et al. (2008) using similar basic structures. The proposed filter in Salleh, et al. (2008) consists of two meandered closed loops but Feng, Gao and Che (2015) used only a simple loop. They used closed loops consisting of coupled lines but they could not suppress the harmonics well. Using SIRs (interlocked stepped-impedance resonators), a DB-BPFs with small size is presented in Hsu, Lyu and Chang (2020) to work at 900–1000 MHz and 1427–1518 MHz bands. In Badiaa, et al. (2020), a novel multiband filter has been presented using open ring and stubs resonators.

This paper presents a novel compact DB-BPF with remarkable features such as 13th harmonic attenuation, high selectivity at both passbands, high isolation between two channels, and good return losses better than 35 dB. The designing process is prepared as follows: At the first, a novel dual-mode resonator using coupled lines is introduced. Then, an approximated equivalent *LC* model for coupled lines is proposed. Next, an equivalent *LC* circuit of the introduced resonator is presented by utilizing the *LC* model of coupled lines. To verify the proposed *LC* circuit, the lumped inductors are calculated.

Moreover, the ranges of coupling and open-end capacitors are estimated and optimized. The simulation results of the *LC* model and EM simulator are compared with each other to verify the proposed model. After that, a theoretical method is presented to attenuate the harmonics. Finally, a DB-BPF is introduced using the proposed resonator.

II. Design of a Novel Resonator

The layout configuration of the basic resonator used in this study is shown in Fig. 1a. It has a symmetrical structure consisting of two L-shape coupled lines combined by a transmission line with the physical length l_{S1}. The vertical and horizontal coupled lines, which form the L-shaped coupled lines, have the exact physical dimensions. To obtain an equivalent *LC* circuit, first, we proposed an *LC* model of coupled lines as indicated in Fig. 1b. The proposed *LC* model is not the exact model because the number of inductors and capacitors in the exact model will be increased significantly. Therefore, we represented the equivalent model of a transmission line only by an inductance. Four inductors (presented by L_c in Fig. 1b) model the coupled lines, where each L_c is related to a half of a line.

Moreover, three capacitors of C_c show the coupling between lines. Fig. 1c demonstrates the *LC* equivalent model of Fig. 1a. The vertical and horizontal coupled lines are replaced by the proposed *LC* circuit of the coupled lines (Rezaei and Noori, 2017). The inductor L_{S2} is related to the stubs with the physical lengths l_{S2}. The capacitors C_o present the effect of open ends.

Fig. 1c shows the approximate equivalent circuit. Since the bents effects are significant at above 10 GHz, we ignored them in the *LC* equivalent circuit. Meanwhile, the *LC* equivalent model of coupled lines is an approximated circuit. To calculate the lumped inductors' values, we assume l_{S1} = 1 mm, $l_{S2} = l_c$ = 8 mm, S = 0.2 mm, and w = 0.8 mm.

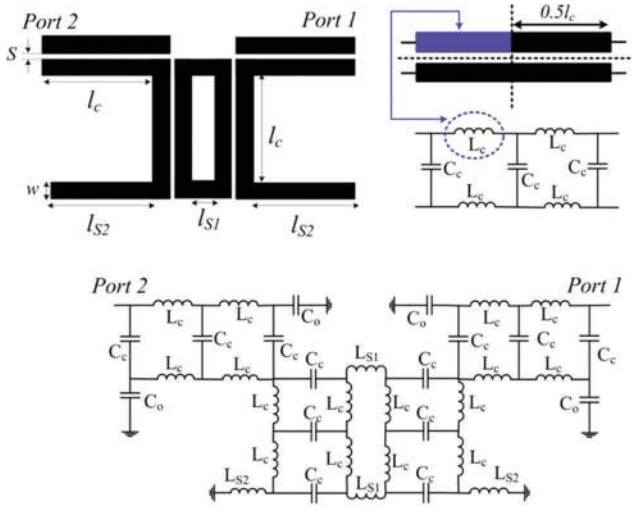

Fig. 1. (a) Proposed resonator, (b) proposed LC circuit of coupled lines, and (c) LC equivalent model of Fig. 1a.

The width value of the line with length l_{S1} is 0.8 mm. This resonator is simulated for a substrate with ε_r =2.2 and h=0.7874 mm. The EM simulation results show that it operates at 4.43 GHz. For w/h>1, the characteristic impedance of lumped inductors (Z_{in}) can be obtained (Hong and Lancaster, 2001). The characteristic impedance and effective dielectric constant are calculated as Z_c = 94.14 Ω and ε_{re} = 1.76 for all units of the proposed resonator with the width 0.8 mm. The values of lumped inductors are calculated, according to Hong and Lancaster (2001), as L_c = 0.85 nH, L_{S1} = 1.82 nH, and L_{S2} = 0.21 nH. Due to the features of coupling, the coupling capacitor (C_c) is chosen as a small value. We know that a capacitor can be created between two coupled lines which its value is proportional to the thickness of metal and length of lines. On the other hand, the coupling capacitor value has inverse coordination with the distance between lines. Since the thickness of metal is very small, and due to having small dielectric constant, the coupling capacitor value is in fF. On the other hand, the open-end capacitor can be increased by increasing the ratio $\Delta L\sqrt{\varepsilon_{re}} / Z_c$ where ΔL is an equivalent length of the transmission line (Hong and Lancaster, 2001). Due to computational complexity, we prefer to use an optimization method. As mentioned above, the values of inductors are already calculated and the range of capacitors values can be estimated in accordance with their equations. Therefore, we can change these capacitors values until the simulation results of the *LC* model approach the EM simulations results. As shown in Fig. 2, three cases of capacitors values are used to show our optimization process. Figs. 2a-c show the comparison between the EM and *LC* model results for (C_c=345 fF, C_o=2.8 pF), (C_c=280 fF, C_o=2.8pF), and (C_c=150 fF, C_o=0.3 pF), respectively. These capacitors are obtained using an optimization method (the coupling capacitors values are assumed to be small). Figs. 2a-c verify both the proposed *LC* model and calculated values. Due to the mentioned approximations, the EM and *LC* simulated results are not completely overlapped. As explained above, some approximations are used due to the complexity of the *LC* circuit, because our aim, in general, is to detect the effects of various parameters on the frequency response. Then, we can use the obtained results to optimize the main frequency response of our filter. On the other hand, the values of capacitors are obtained using an optimization method. Therefore, the values of capacitors are not exact. Fig. 2 shows the optimization process, which includes appropriate and inappropriate values. However, the dual-mode features can be seen clearly.

III. Harmonic Attenuation Method

Our harmonic attenuation technique is based on calculating resonance frequencies. Since our aim is to obtain a DB-BPF, the first and second calculated resonance frequencies are desired. If there is another resonance frequency, in addition to the main frequencies, it is an undesired harmonic. For removing this harmonic, first, we have to calculate the

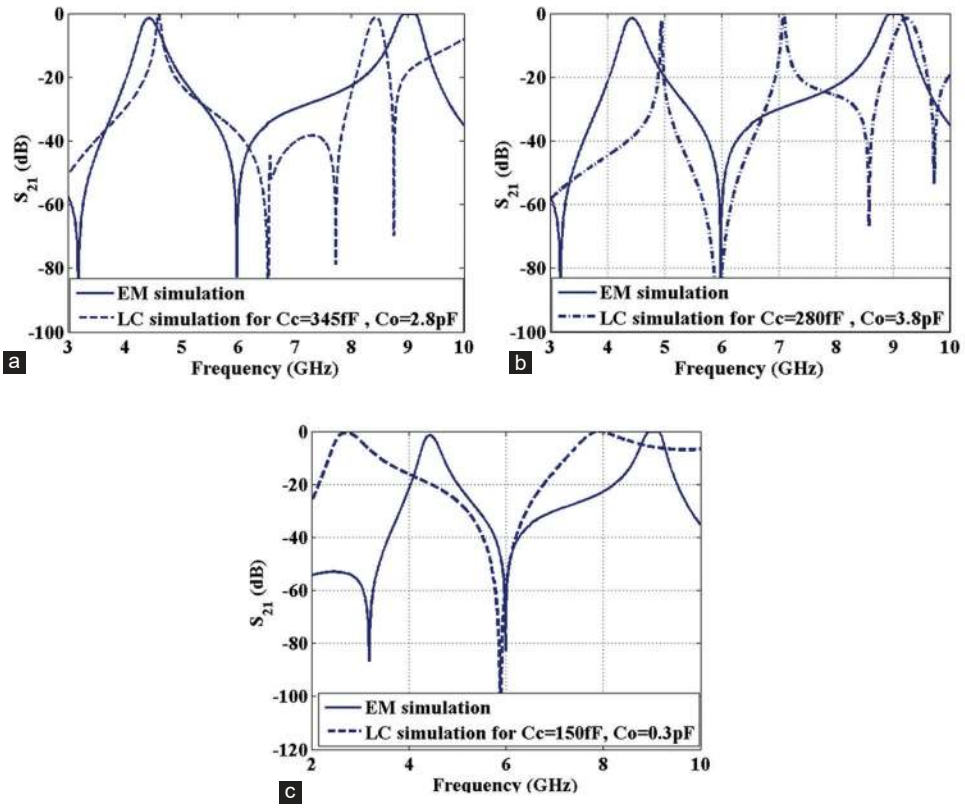

Fig. 2. Comparison between the EM and *LC* simulations results for (a) C_c=345 fF and C_o=2.8 pF (b) C_c=280 fF and C_o=3.8 pF (c) C_c=150 fF and C_o=0.3 pF.

http://dx.doi.org/10.14500/aro.10908

resonance frequencies. The resonance frequencies can be found when input admittance or input impedance is equal to zero. To calculate the input impedance, an equivalent model of the *LC* circuit can be used. Therefore, an equivalent model of the proposed resonator is demonstrated in Fig. 3a, where Z_c is the characteristic impedance of coupled lines with the physical length l_c. Fig. 3b shows a simplified model of Fig. 3a, which is obtained by star-delta transformation for:

$$Za = \frac{j\omega Ls1(2ZjZk + Z_k^2)}{j\omega Ls1Zj(2ZjZk + Z_k^2)}$$

$$Zb = Zc + j\omega L_{s2}(2L_{s2} + L_{s1})$$

Where:

$$Zj = \frac{j\omega L_{s2}^2}{2L_{s2} + L_{s1}} \text{ and } Zk = Zc + \frac{j\omega L_{s2}L_{s1}}{2L_{s2} + L_{s1}} \quad (1)$$

Where, ω is the angular frequency. For obtaining the resonance frequencies, the input impedance (or input admittance) of the equivalent circuit should be zero. Therefore, in the resonance modes, an open circuit and a short circuit for the even and odd modes should be created, respectively. The input impedance can be calculated from the equivalent circuit presented in Fig. 3b. The impedance Z_a acts as an open circuit due to its position in the equivalent circuit. After calculating the input admittance and setting it to zero, another condition of resonance modes can be obtained as $Z_b + Z_c = 0$. For simplifying in a symmetrical model, we can connect the same potential nodes. Equality of $Z_b + Z_c = 0$ presents the odd mode resonance condition obtained by calculating the input impedance and applying the short circuit condition. Therefore, the even and odd resonance modes for ω_e and ω_o (angular resonance frequencies) can be written as:

$$\text{even mode: } j\omega_e L_{s1} Z_j + 2Z_j Z_k + Z_k^2 \quad (2a)$$

$$\text{Odd mode: } 2Z_c + j\omega_o L_{s2}(2L_{s2} + L_{s1}) = 0 \quad (2.b)$$

Equations (2.a) and (2.b) are obtained from the input impedance of the equivalent model presented in Fig. 3b. When we set the input impedance $Z_{in} = 0$, the odd mode condition is obtained as shown in Equation (2.b). Furthermore, for $1/Z_{in} = 0$, ω_e (even mode resonance frequency) is achieved. In Equation (2.a), Z_j and Z_k should be calculated at $\omega=\omega_e$. It can be seen that there are several ω_e, which satisfy Equations (2.a) and (2.b). Two achieved angular resonance frequencies are fundamentals and the others are harmonics, which should be removed. To attenuate the harmonics, we assume that ω_o is the main resonance frequency. Since we have a dual-band response, an obtained ω_e from Equation (2.a) is another main angular resonance frequency. By substituting Z_c in Equation (2.a) and solving Equation (2.a):

$$\omega e = jZc \frac{Ls2^2 + Ls2Ls1 \pm \sqrt{(Ls2^2 + Ls2Ls1)^2 + 1}}{2Ls2^2 Ls1} \quad (3)$$

Where, ω_e is a positive value thus according to the above discussion, there are not any harmonics.

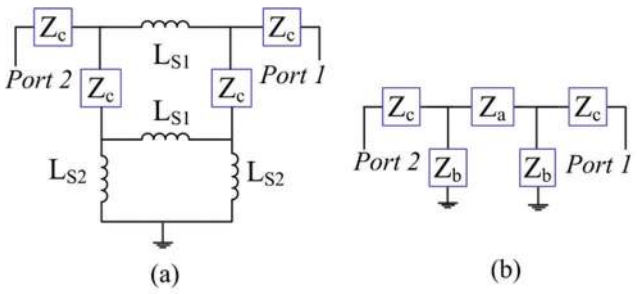

Fig. 3. (a) An equivalent model of our resonator and (b) a simplified model of Fig. 3a.

IV. The Configuration of the Proposed DB-BPF

Fig. 4 depicts the proposed DB-BPF layout (all dimensions are in mm). It includes the introduced resonator loaded by the additional stubs, which are embedded to optimize the filter performance and miniaturize the circuit size. Each stub consists of two coupled closed rings. These rings shift the resonance frequencies to the left whereas they can save the normalized size (in λ_g^2). Moreover, increasing the number of these closed rings can improve the insertion and return losses. On the other hand, by removing these rings, the frequency selectivity will be decreased. Fig. 5 demonstrates the current

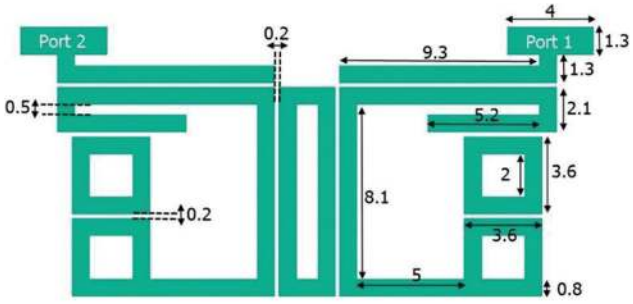

Fig. 4. Layout configuration of the presented dual-band bandpass filter.

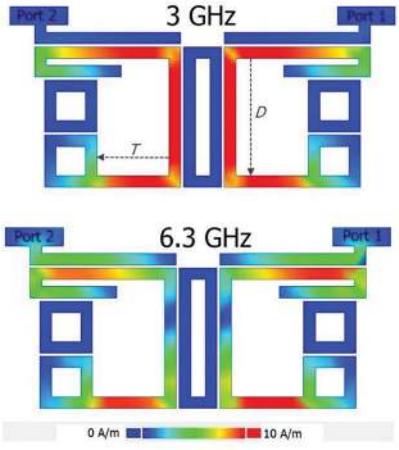

Fig. 5. Current density distributions at 3 GHz and 6.3 GHz.

density distributions over the proposed structure at 3 GHz and 6.3 GHz. As shown in Fig. 5, the minimum current densities are in the coupled closed loops. As mentioned before, the coupled closed loops are added for optimization whereas they do not have a significant effect on creating the resonance frequencies. The maximum current densities are in the designed resonator. Fig. 6 shows the frequency responses as functions of the highlighted physical lengths. These lengths have the same effects on the quality of the frequency response. Hence, by tuning them, the best values are selected. The simulations are performed on a Rogers RT/duroid5880 substrate with loss tangent=0.0009, ε_r = 2.22, and h = 31 mil.

V. Simulation and Measurement Results

We used Advanced Design System software for simulating the proposed DB-BPF. We fabricated the proposed DB-BPF on a Rogers RT/duroid5880 substrate with loss tangent=0.0009, ε_r=2.22, and h=31 mil. A N5230A network analyzer is used to measure the fabricated filter. Fig. 7a illustrates the simulation and measurement results. The simulated narrowband frequency response in the range of 2.5 GHz–7 GHz is shown in Fig. 7b. At the first and second passbands, the −3 dB cutoff frequencies are (2.9 GHz, 3.15 GHz) and (6.26 GHz, 6.38 GHz), respectively, so that it operates at 3 GHz and 6.3 GHz. Since the frequency of

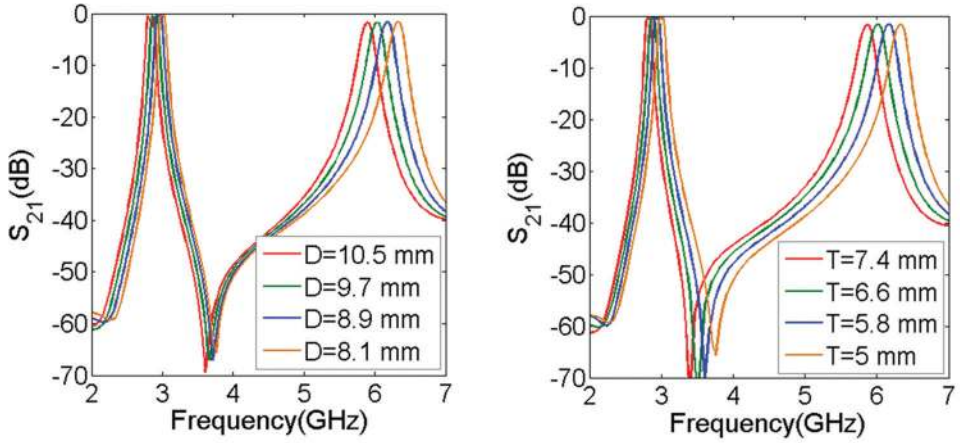

Fig. 6. Frequency responses as functions of D and T (shown in Fig. 5).

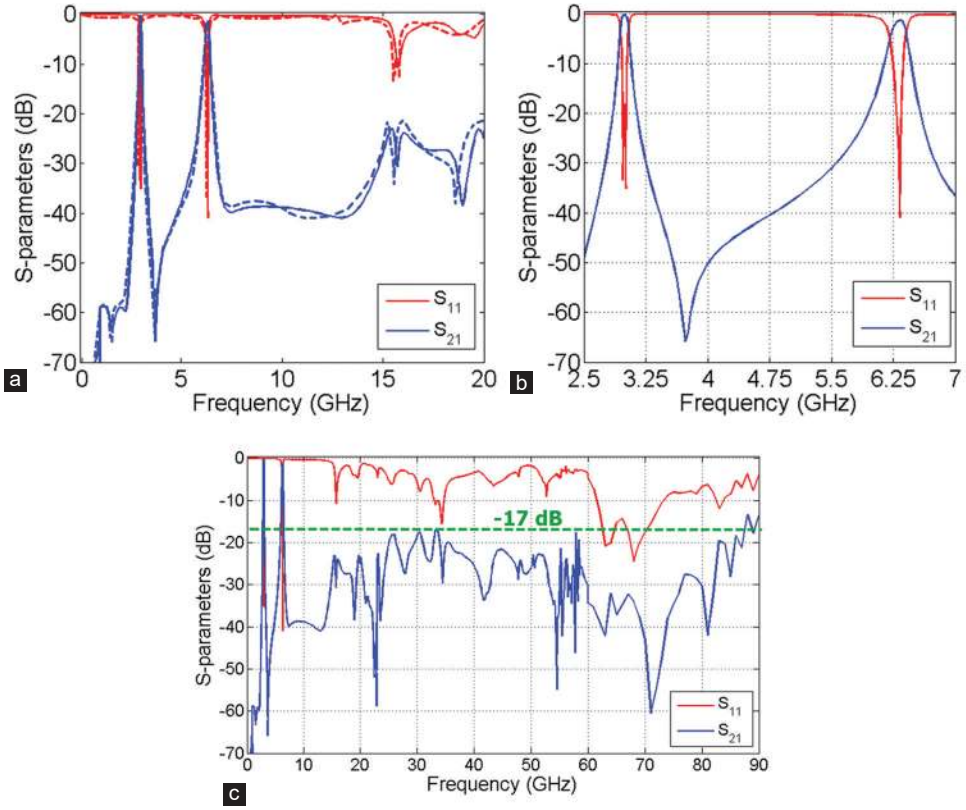

Fig. 7. Proposed dual-band bandpass filter results: (a) Measured (dashed line) and simulated (solid line) frequency responses, (b) simulated narrowband frequency response, and (c) simulated wideband frequency response.

http://dx.doi.org/10.14500/aro.10908

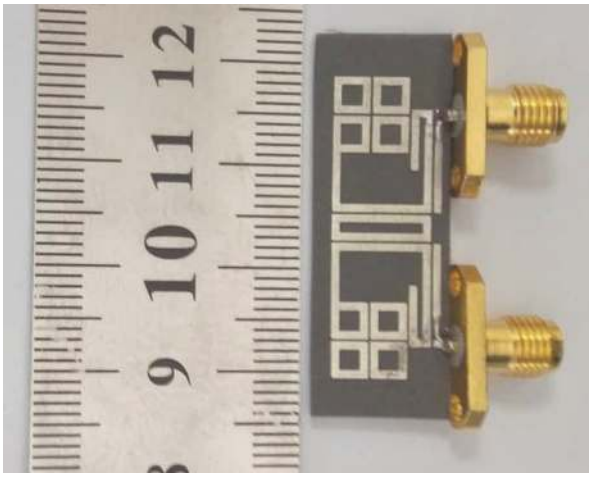

Fig. 8. Fabricated dual-band bandpass filter.

3 GHz is common between ultra-high-frequency and super high-frequency bands, it can be used in these applications. Fig. 7c shows the simulated wideband frequency response in the range of 0.1 GHz–90 GHz. From Fig. 7c, it can be seen that the harmonic levels are <−17 dB up to 85 GHz. Both return losses are better than 35 dB, where the insertion losses are 0.3 dB and 1.3 dB at 3 GHz and 6.3 GHz, respectively. The size of the proposed DB-BPF is 26.5 mm × 12.5 mm (0.35 λ_g × 0.16 λ_g). Fig. 8 shows the fabricated DB-BPF.

According to the frequency response, it has several transmission zeros (TZs) which improved the frequency response. Due to the TZ of −65 dB at 3.7 GHz, a good isolation between two passbands is obtained. Several TZs are created at 7.3, 13, 15.7, 19, and 23 GHz with the attenuation levels of −40, −40, −30, −38, and −58 dB, respectively. Below the first channel, a TZ of −82 dB is achieved at 1

Table I
Comparison with the Previous Works.

Refs	fo_1/fo_2 (GHz)	Harmonic suppression N^{th} attenuated harmonic	RL1/RL2 (dB)
Rezaei and Yahya, 2019	0.85/1.85	−20 dB–3.5 GHz 5th	21.7/20
Sun, et al., 2013	1.5/2.4	−30 dB–20 GHz 8th	---
Chen, et al., 2014	0.9/1.75	−20 dB–2.7 GHz No	18/18
Xu and Zhu, 2017	0.8/2.3	−20 dB–4.5 GHz No	15/15
Wu, et al., 2015	2.45/5.7	−20 dB–7 GHz No	21/20
Liu, Li and Ren, 2013	1.8/2.4	−20 dB–4 GHz No	15/15
Hayati and Noori, 2011	2.71/5	−20 dB–20 GHz 4th	---
Hayati and Noori, 2012	2.4/5.2	−15 dB–13GHz 2nd	10/13
Rezaei and Noori, 2017	2.39/5.7	−20 dB–13.3 GHz 2nd	13/16.6
Ogbodo, Wang and Yeo, 2016	1.7/1.9	No No	20/20
Sedighi, et al., 2019	1.57/1.85	−30 dB–3 GHz 2nd	18/15
Karimi, et al., 2019	4.3/8.6	−30 dB–14.1 GHz 3rd	12/15
Oudaya and Tamilselvan, 2020	3.8/5.9	−25 dB–9 GHz 3rd	15/35
Li, Kang and Liu, 2020	2.3/3.2	−20 dB–4 GHz 2nd	40/12
Challal, Hocine and Mermoul, 2019	2.1/5.05	−30 dB–8 GHz 4th	50.1/33
Moitra, Dey and Bhowmik, 2019	4.5/5.1	−20 dB–7 GHz 2nd	38/28
Borjlu and Khadem, 2019	1.84/3.5	−20 dB–8.5 GHz 8th	40/50
Khani, Danaie and Rezaei, 2019	3.6/5.7	−20 dB–11 GHz 3rd	25/24.7
Karimi, et al., 2019	3.5/5.8	−20 dB–16 GHz 5th	24/24
This work	3/6.3	−20 dB–25 GHz and −17 dB–85 GHz 13th	35/42

GHz. Meanwhile, we can see good selectivity at both channels. The comparison results with the previous DB-BPFs with various structures are shown in Table 1. The return losses at the first and second bands are presented by RL1 and RL2, respectively. According to the comparison table, the best harmonic attenuation and good return losses are obtained in this work.

VI. Conclusion

We fabricated and measured a DB-BPF for ultra-wide stopband and multiservice applications. The proposed structure consists of closed loops and coupled lines. The designing method is based on analyzing the *LC* approximated model of the proposed resonator, where a novel *LC* model of coupled lines is presented. Moreover, a theoretical method is presented to attenuate the harmonics. The presented DB-BPF has high selectivity and a wide stopband. The levels of harmonics are <−17 dB up to 85 GHz. Moreover, it has other advantages in terms of high isolation between two channels, compact size and good return losses compared to the previous DB-BPFs.

References

Badiaa, A.A., Otman, A., Azzeddin, N.R. and Ana Vazquez, A., 2020. Miniaturized multi-band stopband filter using circular split ring resonator and null gap separations between all parallel lines. *Progress in Electromagnetics Research C*, 106, pp.137-150.

Borjlu, S.R. and Khadem, M.S., 2019. Novel microstrip dual-band quad-section bandpass filter using radial stub for wireless communication. *Journal of Electrical Engineering and Technology*, 14, pp.1327-1333.

Challal, M., Hocine, K. and Mermoul, A., 2019. A novel design of compact dual-band bandpass filter for wireless communication systems. *Wireless Personal Communications,* 109, pp.1713-1726.

Chen, C.F., Chang, S.F., Tseng, B.H. and Weng, J.H., 2014. Compact dual-band stepped-impedance resonator filter with separate coupling paths. *Electronics Letters,* 50(21), pp.1551-1552.

Feng, W., Gao, X. and Che, W., 2015. Bandpass filters with improved selectivity based on dual-mode ring resonators. *Progress in Electromagnetics Research Letters*, 56, pp.1-7.

Hammed, R.T., 2015. Miniaturized dual-band bandpass filter using E-shape microstrip structure. *AEU-International Journal of Electronics and Communications*, 69, pp.1667-1672.

Hayati, M. and Noori, L., 2011. Compact dual band bandpass filter using open loop resonator loaded by in-line beeline for wideband applications. *IEICE Electronics Express*, 8(21), pp.1789-1794.

Hayati, M. and Noori, L., 2011. Compact dual-band band-pass filter with ultra-wide stopband using open-loop resonator loaded by T-shape and open stubs. *IEICE ELEX*, 8(14), pp.1168-1173.

Hayati, M. and Noori, L., 2012. Compact dual-band band-pass filter using open loop resonator for multimode WLANs. *Electronics Letters,* 48(10), pp.573-574.

Hong, J.S. and Lancaster, M.J., 2001. *Microwave Filter for RF/Microwave Application*, John Wiley & Sons, New York, USA.

Hsu, W., Lyu, P. and Chang, S., 2020. Design of a miniature dual-band band-pass filter with interlocked stepped-impedance resonators for 5G new radio access technology. *International Journal of Microwave and Wireless Technologies*, 12(8), pp.733-737.

Huang, D. and Huang, Z., 2014. Design of dual-band band-pass filter using dual-mode defected stub loaded resonator. *Journal of Electrical and Computer Engineering*, 2014, p.176560.

Karimi, G., Amirian, M., Lalbakhsh, A. and Ranjbar, M., 2019. A new microstrip coupling system for realization of a differential dual-band band-pass filter. *AEU-International Journal of Electronics and Communications*, 99, pp.186-192.

Karimi, G., Pourasad, Y., Lalbakhsh, A., Siahkamari, H. and Mohamadzade, B., 2019. Design of a compact ultra-narrow band dual band filter for WiMAX application. *AEU-International Journal of Electronics and Communications*, 110, p.152827.

Khani, S., Danaie, M. and Rezaei, P., 2019. Miniaturized microstrip dual-band bandpass filter with wide upper stop-band bandwidth. *Analog Integrated Circuits and Signal Processing,* 98, pp.367-376.

Li, D., Zhang, Y., Feng, X., Song, K. and Fan, Y., 2015. Dual-band band-pass filter with controllable center frequency and bandwidth using short stub-loaded SIR and tri-section SIR. *AEU-International Journal of Electronics and Communications*, 69, pp.1004-1009.

Li, K., Kang, G. and Liu, H., 2020. High-selectivity adjustable dual-band band-pass filter using a quantic-mode resonator. *Microsystem Technologies*, 26, pp.913-916.

Liu, H.W., Li, S. and Ren, B.P., 2013. Microstrip dual-band band-pass filter with E-shaped multimode resonator. *Electronics Letters*, 49(14), pp.887-888.

Lu, H., Wu, W., Huang, J., Zhang, X. and Yuan, N., 2017. Compact dual-mode microstrip bandpass filter based on greek-cross fractal resonator. *Radioengineering*, 26(1), pp.275-284.

Malherbe, J.A.G., 2016. An asymmetrical dual band band-pass filter. *Microwave and Optical Technology Letters,* 59(1), pp.163-168.

Moitra, S., Dey, R. and Bhowmik, P.S., 2019. Design and band coalition of dual band microstrip filter using DGS, coupled line structures and series inductive metallic vias. *Analog Integrated Circuits and Signal Processing*, 101, pp.77-88.

Ogbodo, E.A., Wang, Y. and Yeo, K.S.K., 2016. Microstrip dual-band band-pass filter using U-Shaped resonators. *Progress in Electromagnetics Research Letters*, 59, pp.1-6.

Oudaya, C.S. and Tamilselvan, S., 2020. A compact conductor-backed CPW-based dual band-pass filter for satellite S-band and C-band. *Journal of Electrical Systems and Information Technology,* 7(5), pp.2-11.

Pan, W.Q., Zhao, X.L., Zhang, Y. and Xu, J.X., 2015. High selectivity dual-band band-pass filter with tunable lower pass-band. *International Journal of Antennas and Propagation*, 2015, p.762504.

Rezaei, A. and Noori, L., 2017. Design of microstrip wide stopband quad-band bandpass filters for multi-service communication systems. *AEU-International Journal of Electronics and Communications*, 81, pp.1388-1393.

Rezaei, A. and Noori, L., 2017. Tunable microstrip dual-band band-pass filter for WLAN applications. *Turkish Journal of Electrical Engineering and Computer Sciences*, 25, pp.1388-1393.

Rezaei, A. and Yahya, S.I., 2019. High-performance ultra-compact dual-band band-pass filter for global system for mobile communication-850/global system for mobile communication-1900 applications. *ARO-The Scientific Journal of Koya University,* 7(2), pp.34-37.

Rezaei, A., Yahya, S.I. and Jamaluddin, M.H., 2020. A novel microstrip diplexer with compact size and high isolation for GSM applications. *AEU-International Journal of Electronics and Communications,* 114, p.153018.

Rezaei, A., Yahya, S.I., Noori, L. and Jamaluddin, M.H., 2019. Design and fabrication of a novel compact low-loss microstrip diplexer for WCDMA and WiMAX applications. *Journal of Microwaves, Optoelectronics and Electromagnetic Applications*, 18(4), pp.482-491.

Rezaei, A., Yahya, S.I., Nouri, L. and Jamaluddin, M.H., 2020. Design of a low-loss microstrip diplexer with a compact size based on coupled meandrous

open-loop resonators. *Analog Integrated Circuits and Signal Processing*, 102, pp.579-584.

Salleh, M.K.M., Prigent, G., Pigaglio, O. and Crampagne, R., 2008. Quarter-wavelength side-coupled ring resonator for band-pass filters. *IEEE Transactions on Microwave Theory and Techniques*, 56(1), pp.156-162.

Sedighi, M.S., Dousti, M., Dolatshahi, M. and Ghalamkari, B., 2019. Tunable dual-band bandpass filter for multi-standard applications. *AEU-International Journal of Electronics and Communications*, 111, p.152885.

Sun, S.J., Su, T., Deng, K., Wu, B. and Liang, C.H., 2013. Compact microstrip dual-band band-pass filter using a novel stub-loaded quad-mode resonator. *IEEE Microwave and Wireless Components Letters,* 23(9), pp.465-467.

Wu, G.C., Wang, G., Liang, J.G., Gao, X.J. and Zhu, L., 2015. Miniaturized microstrip dual-band band-pass filter using novel symmetric double-spiral resonators for WLAN application. *Electronics Letters,* 51(15), pp.1177-1178.

Wu, H.W., Su, Y.K., Weng, M.H. and Yang, R.Y., 2008. Design of dual-band band-pass filter using diverse quarter wavelength resonator for GPS/WLAN Applications. *Microwave and Optical Technology Letters*, 50(10), pp.2694-2696.

Xu, J. and Zhu, Y., 2017. Compact semi-lumped dual-and tri-wideband band-pass filters. *IET Microwaves Antennas and Propagation*, 11(1), pp.53-58.

Yahya, S.I., Rezaei, A. and Nouri, L., 2020a. Design and performance of microstrip diplexers: A review. *ARO-The Scientific Journal of Koya University*, 8(1), pp.38-49.

Yahya, S.I., Rezaei, A. and Nouri, L., 2020b. Design and fabrication of a high-performance microstrip multiplexer using computational intelligence for multi-band RF wireless communications systems. *AEU-International Journal of Electronics and Communications,* 120, p.153190.

Yahya, S.I., Rezaei, A. and Nouri, L., 2020c. A novel miniaturized microstrip lowpass-band-pass diplexer using patch and interdigital cells for wireless networks. *AEU-International Journal of Electronics and Communications,* 126(153404), pp.1-7.

Yang, R.Y., Hon, K., Hung, C.Y. and Ye, C.S., 2010. Design of dual-band band-pass filters using a dual feeding structure and embedded uniform impedance resonators. *Progress in Electromagnetics Research*, 105, pp.93-102.

Zhu, H. and Abbosh, A.M., 2016. Single-and dual-band band-pass filters using coupled stepped-impedance resonators with embedded coupled-lines. *IEEE Microwave and Wireless Components Letters*, 26(9), pp.675-677.

Zong, B.F., Wang, G.M., Zeng, H.Y. and Wang, Y.W., 2012. Compact and high performance dual-band band-pass filter using resonator-embedded scheme for WLANs. *Radioengineering*, 21(4), pp.1050-1053

Chemical Composition and Cytotoxic Activity of *Pistacia atlantica var. kurdica* Fruits

Raad A. Kaskoos[1], Javed Ahamad[2], Subasini Uthirapathy[3]

[1]Department of Pharmacy, Al-Manara College for Medical Science, Amarah, Iraq
[2]Department of Pharmacognosy, Faculty of Pharmacy, Tishk International University, Erbil, Kurdistan Region, Iraq
[3]Department of Pharmacology, Faculty of Pharmacy, Tishk International University, Erbil, Kurdistan Region, Iraq

Abstract*–*Pistacia atlantica var. kurdica* (Anacardiaceae) is a major subspecies found in the Kurdistan region of Iraq and has several beneficial bioactivities such as antioxidant, antibacterial, and antiviral. *P. atlantica* growing in the Kurdistan region is not yet studied phytochemically and pharmacologically. Hence, the goal of the present study is to characterize chemical compounds present in ethanolic extract of *P. atlantica* fruits by gas chromatography–mass spectroscopy (GC–MS) and to evaluate cytotoxic activity using A549 (human lung cancer) cell lines by (3-4,5 dimethylthiazol-2yl-2,5-diphenyl tetrazolium bromide) assay. The GC–MS analysis shows the presence of 33 chemical compounds which constitute about 99.95% of total compounds, and isospathulenol (14.63%), spathulenol (13.45%), α-terpineol (13.28%), limonene (10.92%), terpinolene (10.89%), β-myrcene (6.92%), ethyl pentadecanoate (6.15%), β-pinene (4.98%), and caryophyllene oxide (4.01%) were found as major chemical compounds. *P. atlantica* inhibits cell proliferation in A549 cell lines in a time (24 h) and dose-dependent manner (0.5–500 μg/mL). After 24 h of treatment with *P. atlantica,* the cell viability of A549 cell lines ranged from 93.01 ± 5.24 to 57.69 ± 4.15% for concentrations of 0.5–500 μg/mL, respectively. This study expands the knowledge of the chemical composition of *P. atlantica* fruits and provides scientific evidence for its possible use as an anticancer medicine. The substantial anticancer activity of *P. atlantica* fruits may be due to the presence of isospathulenol, spathulenol, α-terpineol, limonene, terpinolene, β-myrcene, ethyl pentadecanoate, β-pinene, and caryophyllene oxide.

***Index Terms*–*Pistacia atlantica var. kurdica*; Anacardiaceae; Cancer; Gas chromatography–mass spectroscopy; A549 cell lines; (3-4,5 dimethylthiazol-2yl-2,5-diphenyl tetrazolium bromide) assay.**

I. Introduction

Pistacia atlantica Desf. (Family: Anacardiaceae) is the most common species of this genus and is abundantly found in Iraq, Syria, Iran, and Turkey (Sharifi, 2014). *P. atlantica* Desf. contains four prominent varieties or subspecies, and it includes *P. atlantica var. kurdica, P. atlantica var. cabulica, P. atlantica var. mutica,* and *P. atlantica var. atlantica* (Ahmed, et al., 2021). *P. atlantica var. kurdica* is native to Kurdistan Region of Iraq and mostly found wildly in Shaqlawa and Ranya districts of Kurdistan Region. *P. atlantica subsp. kurdica* is commonly known as *Dar qezwan* or *Dareben* in Kurdish and Atlas in English (Ahmed, 2017). *P. atlantica var. kurdica* is known as a potent antioxidant plant (Ben Ahmed, et al., 2016; Gourine, et al., 2010). It also has several bioactivities such as antimicrobial (Benhammou, Bekkara and Panovska, 2008; Sharifi and Hazell, 2012), antihyperglycemic (Kasabri, Afifi and Hamdan, 2011), cytotoxic (Hamelian, et al., 2018), and antiviral (Karimi, Moradi and Gafourian, 2020). Lung cancer has emerged as a major cause of cancer-related deaths worldwide, and smoking is considered as the primary cause. Adenocarcinoma, squamous cell carcinoma, and large cell carcinoma are the three types of lung cancer (Collins, et al., 2007). Lung cancer treatment varies based on the nature and stage of the tumor and can range from surgical resection to chemotherapy. Chemotherapy and surgical resection have both been linked to serious side effects. That's why the treatment of lung cancer needs palliative therapy along with chemotherapy (Jones and Baldwin, 2018). Medicinal plants are known to have anticancer activity in *in vitro, in vivo,* and clinical studies (Gezici and Şekeroğlu, 2019; Ahamad, et al., 2019). The present study is aimed to determine the chemical composition of ethanolic extract of *P. atlantica var. kurdica* fruits by gas chromatography–mass spectrometry method and also to evaluate its cytotoxic activity in A549 (human lung cancer) cell lines.

II. Materials and Methods

A. Plant Materials and Chemicals

The fresh fruits of *P. atlantica var. kurdica* (1 kg) were collected in March 2021 from Shaqlawa, Kurdistan Region, Iraq. The authenticity of all the accession was ascertained by Dr. Raad A Kaskoos, Department of Pharmacy, Al-Manara College for

ARO-The Scientific Journal of Koya University
Vol. IX, No.2 (2021), Article ID: ARO.10868, 5 pages
DOI: 10.14500/aro.10868
Received: 05 September 2021; Accepted: 06 December 2021
Regular research paper: Published: 15 December 2021
Corresponding author's e-mail: javed.ahamad@tiu.edu.iq

Medical Science, Amarah, Iraq. The plant sample was archived for future reference in the Faculty of Pharmacy, Tishk International University, Erbil, Iraq (voucher number: PRL/2021/05).

A549 (human lung cancer) cell lines were procured from National Centre for Cell Sciences, Pune, India. Dulbecco's Modified Eagle Medium (DMEM), fetal bovine serum (FBS), and antibiotic solution were procured from Gibco (USA), whereas dimethyl sulfoxide (DMSO) and (3-4,5-dimethylthiazol-2yl-2,5-diphenyl tetrazolium bromide) (MTT) were from Sigma-Aldrich (USA), and HiMedia provided 1× phosphate-buffered saline (PBS) (India). Tarson provided a 96-well tissue culture plate and a wash beaker (India). All of the other chemicals and solvents were of analytical grade.

B. Preparation of Ethanolic Extract of P. atlantica

The fresh fruits of *P. atlantica* were pulverized in a mixed grinder and then extracted in an ultrasonicator (Elma, Germany). The pulverized fruits of *P. atlantica* were placed in a stoppered conical flask and extracted for 30 min with ethanol (250 mL) in an ultrasonicator at 30°C temperature. After filtering, the extract was treated with 5 g of activated charcoal and filtered again. The filtrate is concentrated in a rotary evaporator (Buchi, Switzerland) at 35°C. The concentrated ethanolic extract was then air-dried, and the dried ethanolic extract was kept in the refrigerator at 2–4°C until needed.

C. GC–MS Analysis and Identification of Chemical Constituents

The GC–MS method was used to analyze the chemical composition of an ethanolic extract of *P. atlantica* fruits. The test sample was analyzed on Agilent Bench Top GC–MS (Agilent Technologies, Wilmington, DE, USA) equipment using a DB-5 glass capillary column with specification of 30 m × 0.25 mm i.d.; film thickness of 0.25 µm. Helium was used as a carrier gas, and the flow rate was fixed at 1 mL/min. The oven temperature was set to 50°C for 1 min and then isothermally maintained at 320°C for 2 min, whereas the injector port temperature was kept at 280°C. The split ratio was kept at 1:5, and the 0.1 µL of *P. atlantica* ethanolic extract in DMSO was injected. Data were collected at 70 eV with 1.5 s scanning durations in the mass range of 50–1000 amu and a run time of 37 min. ChemStation software was used to handle the chromatography and mass spectra.

The individual chemical constituents were identified by comparing their Kovats index (K.I.) to those found in the literature and the mass fragmentation pattern of spectra obtained by GC–MS, and they were compared to those stored in the spectrometer database of NIST, NBS 54 K.L, WILEY8 libraries, and published literature for further identification of chemical constituents (Adams, 2007; Ali, 2001; Gourine, et al., 2010; Delazar, Reid and Sarker, 2004; Farhoosh, Tavakoli and Khodaparast, 2008). The area of the individual peaks was used to calculate the percent composition of each component.

D. Cytotoxic activity of P. atlantica var. kurdica

The potential cytotoxic activity of *P. atlantica* ethanolic extract (for concentration range 0.5–500 µg/mL) against A549 cell lines (human lung cancer) was assessed using the MTT assay. The assay was performed by the method described by Marquez, et al. (2020). A549 cell lines were cultured in liquid medium (DMEM) supplemented with 10% FBS, 100 µg/mL penicillin, and 100 µg/mL streptomycin, and kept at 37°C in a 5% CO_2 atmosphere. Trypsinization was used to extract the cultured A549 cells, which were then pooled in a 15 mL tube. The cells were then plated at a density of 1×10^5 cells/mL/well (200 µL) in a 96-well plate in DMEM medium containing 10% FBS and 1% antibiotic solution for 24–48 h at 37°C. In a serum-free DMEM medium, the cells were rinsed with sterile PBS and treated with *P. atlantica* ethanolic extract. Each sample was replicated 3 times, and the cells were cultured for 24 h at 37°C in a humidified 5% CO_2 incubator. MTT (20 µL at conc. of 5 mg/mL) was added to each well after the incubation period, and the cells were incubated for another 2–4 h until purple precipitates were visible under an inverted microscope. Finally, the medium was aspirated out of the wells together with MTT and rinsed with 1× PBS. DMSO (100 µL) was also added to dissolve formazan crystals, and the plate was agitated for 5 minutes. Using a microplate reader (Thermo Fisher Scientific, USA), the absorbance of each well was measured at 570 nm. The percent cell viability was calculated using the following formula:

$$\text{Cell viability (\%)} = \frac{\text{OD test}}{\text{OD control}} \times 100$$

III. Results and Discussion

A. GC–MS Analysis of P. atlantica var. kurdica

The GS–MS analysis was performed to identify different chemical constituents present in ethanolic extract of *P. atlantica var. kurdica* found in Iraqi Kurdistan. The GC–MS analysis of ethanolic extract of *P. atlantica* yielded 33 chemical compounds which constitute about 99.95% of total chemical compounds (Table 1 and Fig. 1). The major chemical compounds of *P. atlantica var. kurdica* were identified as isospathulenol (14.63%), spathulenol (13.45%), *α*-terpineol (13.28%), limonene (10.92%), terpinolene (10.89%), *β*-myrcene (6.92%), ethyl pentadecanoate (6.15%), *β*-pinene (4.98%), and caryophyllene oxide (4.01%). The other chemical compounds present in *P. atlantica var. kurdica* were *cis*-limonene oxide (2.18%), isobutyl hexanoate (2.19%), epiglobulol (2.02%), phytol (1.90%), and globulol (1.29%). The minor chemical compounds which are less than 1% also listed in Table 1. As *P. atlantica* is found in different parts of the world, its chemical composition has been analyzed by several researchers. Delazar, et al. (2004), studied the chemical composition of oleoresin from *P. atlantica var. mutica* by GC–MS method growing in Iran, and the results show the presence of *α*-pinene (70%) limonene oxide (9%), citral (5.72%), and myrtenol (5.31%) as major constituents. Gourine, et al. (2010), studied 34 samples of *P. atlantica* Desf. from different locations of Algeria by GC–MS and found *α*-pinene (5.54–66.61%), camphene (0.75–20.85%),

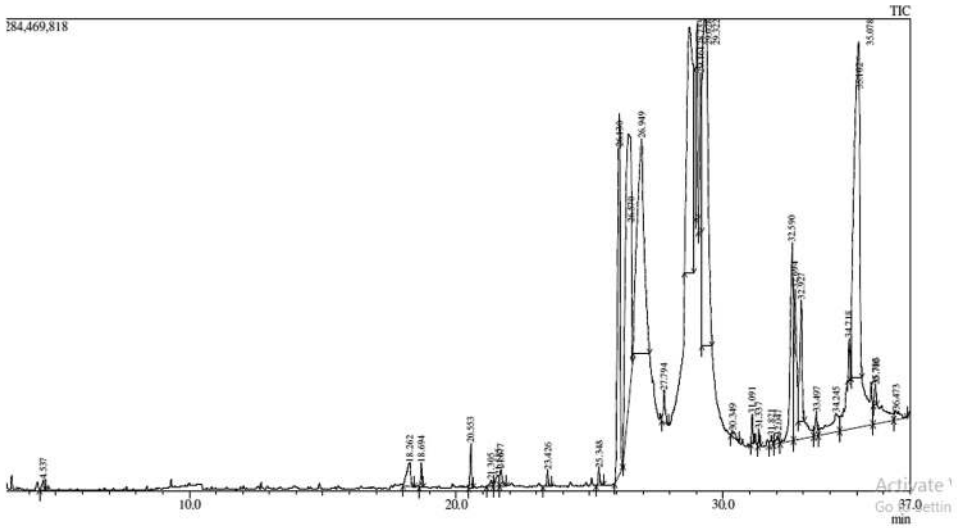

Fig. 1. Gas chromatography–mass spectroscopy spectra of ethanolic extract of *Pistacia atlantica var. kurdica* fruits.

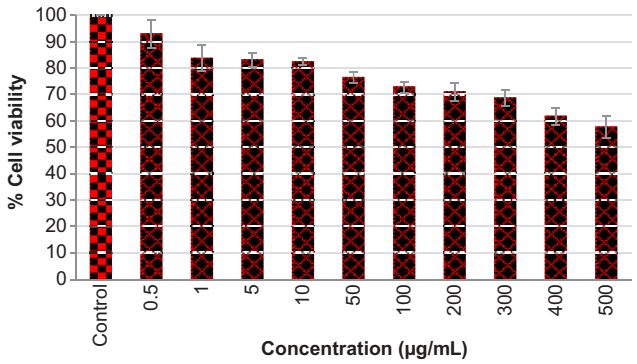

Fig. 2. The cell cytotoxicity produced by ethanolic extract of Pistacia atlantica var. kurdica fruits (represented as % cell viability) (data were presented as mean of triplicate determinations ± SD).

β-pinene (1.09–13.12%), *p*-cymene (0.39–10.19%), and terpinene-4-ol (0.42–15.97%) as major chemical constituents. Mecherara-Idjeri, et al. (2008), studied the chemical composition of leaf, fruit, and gall essential oils of *P. atlantica* Desf. from Algeria, and the major chemical constituents were found as α-pinene (32.6–54.7%) and *β*-pinene (8.0–20.2%). The above research studies were performed on *P. atlantica var. mutica* and other subspecies of it, and also plants were studied from different geographical locations such as Iran and Algeria. The current study is the first study on *P. atlantica var. kurdica* growing in Iraqi Kurdistan and shows the presence of isospathulenol, spathulenol, α-terpineol, limonene, terpinolene, *β*-myrcene, ethyl pentadecanoate, *β*-pinene, and caryophyllene oxide as major chemical constituents. The variation in chemical constituents and their amounts may be due to differences in geographical locations, altitude, soil, rainfall, etc. (Ahamad and Uthirapathy, 2021a and b).

B. Cytotoxic Activity of P. atlantica var. kurdica

The cytotoxic activity of *P. atlantica var. kurdica* was assessed using A549 (human lung cancer) cell lines by MTT test. Figs. 2 and 3 show the results of the MTT assay.

Table I
Chemical Composition of Ethanolic Extract of *Pistacia atlantica var. kurdica* Fruits

Name of chemical compound	RT	RI	% composition
4-Hydroxyhexan-3-one	4.537	846	0.15
Ethylene glycol monoisobutyl ether	18.262	878	0.72
Heptanal	18.694	904	0.24
Tricyclene	20.553	920	0.43
α-Thujene	21.305	925	0.12
α-Pinene	21.585	934	0.32
Camphene	21.677	946	0.27
Verbenene	23.426	960	0.16
Sabinene	25.348	976	0.20
β-Pinene	26.130	980	4.98
β-Myrcene	26.570	992	6.92
Limonene	26.949	1032	10.92
cis-Ocimene	27.794	1039	0.44
Terpinolene	28.733	1088	10.89
cis-Limonene oxide	29.028	1137	2.18
Isobutyl hexanoate	29.161	1160	2.19
α-Terpineol	29.322	1180	13.28
3Z-Hexenyl 3-methylbutanoate	30.349	1231	0.15
Tetradecane	31.091	1402	0.26
β-Caryophyllene	31.337	1432	0.14
α-Humulene	31.821	1458	0.13
β-Curcumene	32.047	1517	0.16
Caryophyllene oxide	32.590	1573	4.01
Ethyl pentadecanoate	32.694	1991	6.15
Epiglobulol	32.927	2026	2.02
Methyl elaidate	33.497	2080	0.33
Globulol	34.245	2092	1.29
Viridiflorol	34.718	2100	0.37
Spathulenol	35.078	2140	13.45
Isospathulenol	35.102	2241	14.63
(*E*)9-Hexadecen-1-ol	35.706	2413	0.24
Phytol	35.712	2620	1.90
Palmitic acid	36.473	2915	0.31

Where, RT: Retention time and KI: Kovats index

P. atlantica inhibits cell proliferation of A549 cell lines in a time (24 h) and dose (0.5–500 µg/mL) dependent manner. After 24 h of treatment with *P. atlantica* extract,

http://dx.doi.org/10.14500/aro.10868

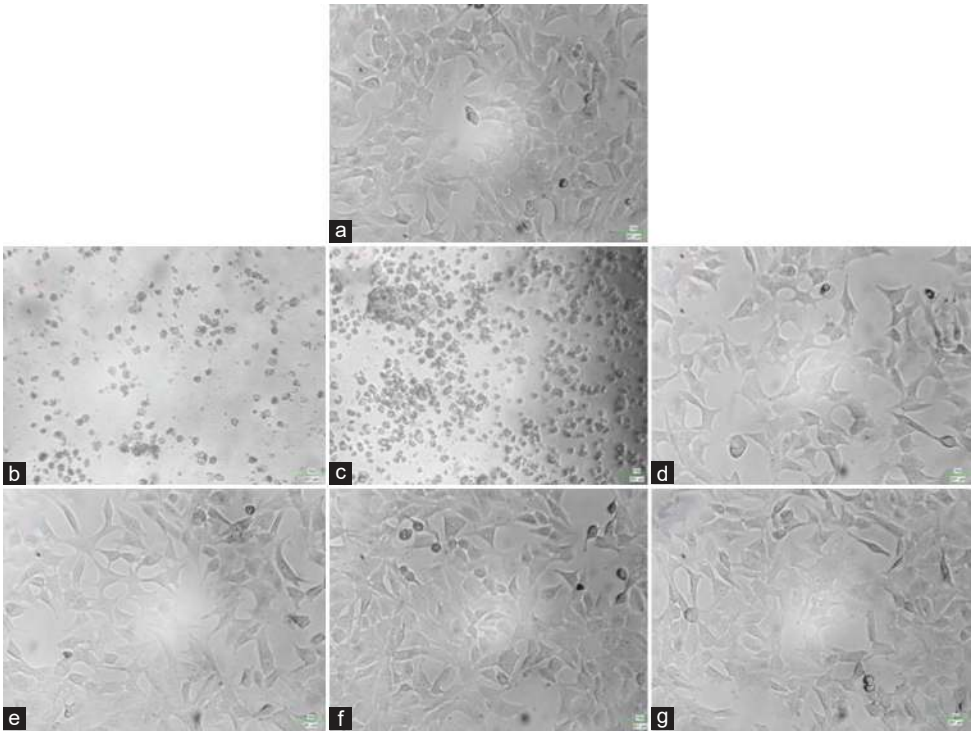

Fig. 3. Cell cytotoxicity produced by ethanolic extract of *Pistacia atlantica var. kurdica* fruits against human lung cancer A549 cell lines. Where, figure (a): Control cells; and figure b to g: *P. atlantica var. kurdica* ethanolic extract: ([b]: 500 µg/mL, [c]: 300 µg/mL, [d]: 100 µg/mL, [e]: 50 µg/mL, [f]: 10 µg/mL, and [g]: 0.5 µg/mL).

the cell viability of A549 cell lines ranged from 93.01 ± 5.24 to 57.69 ± 4.15% at concentrations of 0.5–500 µg/mL, respectively (Figs. 2 and 3). For A549 cell lines, the IC_{50} value of *P. atlantica* ethanolic extract was 21.91 µg/mL after 24 h. Even when the incubation was extended to 24 h, the untreated A549 cells maintained their original morphology and intimate contact with each other, as shown in Fig. 3A. After 24 h' treatment with ethanolic extract of *P. atlantica,* the A549 cells lost their natural form. The elongated spindle-shaped morphology of the A549 cell lines had vanished. Suspension cells (dead cells) were observed after the treatment was extended to 48 h, and more suspension cells were observed after 24 h (Fig. 3B-G). The MTT test for cell cytotoxicity has long been used to screen medicinal plants with possible anticancer activity (Ahamad, et al., 2019).

IV. Conclusion

The GC–MS analysis of ethanolic extract of *P. atlantica var. kurdica* fruits shows the presence of 33 chemical constituents, and isospathulenol, spathulenol, *α*-terpineol, limonene, terpinolene, *β*-myrcene, ethyl pentadecanoate, *β*-pinene, and caryophyllene oxide were found as major chemical constituents. The ethanolic extract of *P. atlantica var. kurdica* shows time- and dose-dependent inhibition of A549 cell lines. The present study explores the chemical composition of *P. atlantica var. kurdica* fruits and provides the scientific basis for its potential use as an anticancer medicine.

Acknowledgment

We gratefully acknowledge the Tishk International University, Erbil, Iraq, for providing research facilities. We also acknowledge Trichy Research Institute of Biotechnology Pvt. Ltd., Trichy, Tamil Nadu, India, for providing the research facilities.

References

Adams, R.P., 2007. *Identification of Essential Oil Components by Gas Chromatography/Mass Spectrometry*, 4th ed. Allured Publishing, Carol Stream, IL, USA.

Ahamad, J. and Uthirapathy, S., 2021a. Chemical characterization and antidiabetic activity of essential oils from *Pelargonium graveolens* leaves. *ARO The Scientific Journal of Koya University*, 9(1), pp.109-113.

Ahamad, J., Toufeeq, I., Khan, M. A., Ameen, M.S.M., Anwer, E.T., Uthirapathy, S., Mir, S.R., Ahmad, J., 2019. Oleuropein: A natural antioxidant molecule in the treatment of metabolic syndrome. *Phytotherapy Research*, 33(12), pp.3112-3128.

Ahamad, J., Uthirapathy, S., Ameen, M.S.M. and Anwer, E.T., 2019. Essential oil composition and antidiabetic, anticancer activity of *Rosmarinus officinalis* L. leaves from Erbil (Iraq). *Journal of Essential Oil Bearing Plants*, 22(6), pp.1544-1553.

Ahmed, H.M., 2017. Traditional uses of Kurdish medicinal plant *Pistacia atlantica subsp. kurdica* Zohary in Ranya, Southern Kurdistan. *Genetic Resources and Crop Evolution*, 64, pp.1473-1484.

Ahmed, Z.B., Yousfi, M., Viaene, J., Dejaegher, B., Demeyer, K. and Heyden, Y.V., 2021. Four *Pistacia atlantica* subspecies (atlantica, cabulica, kurdica and mutica): A review of their botany, ethnobotany, phytochemistry and pharmacology. *Journal of Ethnopharmacology*, 265, p.113329.

Ali, M., 2001. *Techniques in Terpenoid Identification*, Birla Publication,

New Delhi, India, pp.4-51.

Ben Ahmed, Z., Yousfi, M., Viaene, J., Dejaegher, B., Demeyer, K., Mangelings, D. and Vander Heyden, Y., 2016. Antioxidant activities of *Pistacia atlantica* extracts modelled as a function of chromatographic fingerprints in order to identify antioxidant markers. *The Microchemical Journal*, 128, pp.208-217.

Benhammou, N., Bekkara, F.A. and Panovska, T.K., 2008. Antioxidant and antimicrobial activities of the *Pistacia lentiscus* and *Pistacia atlantica* extracts. *African Journal of Pharmacy and Pharmacology*, 2(2), pp.22-28.

Collins, L.G., Haines, C., Perkel, R. and Enck, R.E., 2007. Lung cancer: Diagnosis and management. *American Family Physician*, 75(1), pp.56-63.

Delazar, A., Reid, R.G. and Sarker, S.D., 2004. GC-MS analysis of the essential oil from the oleoresin of *Pistacia atlantica* var. mutica. *Chemistry of Natural Compounds*, 40, pp.24-27.

Farhoosh, R., Tavakoli, J. and Khodaparast, M.H.H., 2008. Chemical composition and oxidative stability of kernel oils from two current subspecies of *Pistacia atlantica* in Iran. *Journal of the American Oil Chemists Society*, 85, pp.723-729.

Gezici, S. and Şekeroğlu, N., 2019. Current perspectives in the application of medicinal plants against cancer: Novel therapeutic agents. *Anti-Cancer Agents in Medicinal Chemistry*, 19(1), pp.101-111.

Gourine, N., Yousfi, M., Bombarda, I., Nadjemi, B., Stocker, P. and Gaydou, E.M. 2010. Antioxidant activities and chemical composition of essential oil of *Pistacia atlantica* from Algeria. *Industrial Crops and Products*, 31, pp.203-208.

Hamelian, M., Hemmati, S., Varmira, K. and Veisi, H., 2018. Green synthesis, antibacterial, antioxidant and cytotoxic effect of gold nanoparticles using *Pistacia atlantica* extract. *Journal of the Taiwan Institute of Chemical Engineers*, 93, pp.21-30.

Jones, G.S. and Baldwin, D.R., 2018. Recent advances in the management of lung cancer. *The Clinical Medicine* (*Lond*), 18(2), pp.S41-S46.

Karimi, A., Moradi, M.T. and Gafourian, A., 2020. *In vitro* anti-adenovirus activity and antioxidant potential of *Pistacia atlantica* Desf. leaves. *Research Journal of Pharmacognosy*, 7(2), pp.53-60.

Kasabri, V., Afifi, F.U. and Hamdan, I., 2011. *In vitro* and *in vivo* acute antihyperglycemic effects of five selected indigenous plants from Jordan used in traditional medicine. *Journal of Ethnopharmacology*, 133(2), pp.888-896.

Marquez, C.M.D., Garcia, J.G., Antonio, J.G., Jacinto, S.D. and Velarde, M.C. 2020. *Alangium longiflorum Merr.* leaf extract induces apoptosis in A549 lung cancer cells with minimal NFκB transcriptional activation. *Asian Pacific Journal of Cancer Prevention*, 21(8), pp.2453-2461.

Mecherara-Idjeri, S., Hassani, A., Castola, V. and Casanova, J., 2008. Composition of leaf, fruit and gall essential oils of Algerian *Pistacia atlantica* Desf. *The Journal of Essential Oil Research*, 20, pp.215-219.

Najibullah, S.N.M., Ahamad, J., Aldahish, A.A., Sultana S. and Sultana, S., 2021b. Chemical characterization and α-glucosidase inhibitory activity of essential oil of *Lavandula angustifolia* flowers. *Journal of Essential Oil Bearing Plants*, 24(3), pp.431-438.

Sharifi, M.S. and Hazell, S.L., 2012. Isolation, analysis and antimicrobial activity of the acidic fractions of Mastic, Kurdica, Mutica and Cabolica gums from genus *Pistacia*. *Global Journal of Health Science*, 4, pp.217-228.

Sharifi, M.S., 2014. Chapter five *Pistacia atlantica* Kurdica. In: *Perspectives on Kurdistan's Economy and Society in Transition*. Vol. 2. Cambridge Scholars Publishing, United Kingdom, pp.64-83.

http://dx.doi.org/10.14500/aro.10859

A Review of the Development and Applicability of Double-Skin Facades in Hot Climates

Aare N. Abtar

Department of Architecture, College of Engineering, University of Sulaimani, Sulaimani, Kurdistan Region – F.R. Iraq

Abstract—**A double-skin façade (DSF) is a multilayered skin that was initially designed for the cold climate of European countries with noticeable success. Since then, countries in different climates started looking into the possibility of adopting DSF through the use of computer simulations to avoid any unforeseen problems in real life. This study aims to look into the possibility and level of success in using DSF in the Middle East's hot-arid climate, making it a challenge compared to European countries. The study utilized a quantitative investigative approach in analyzing the results of some studies done in different countries in the Middle East. After looking into the results from different papers, careful considerations have to be made for the building due to its location and microclimate to determine specific parameters (e.g., combination of transparent and opaque materials, proportion between floor level and screen height, orientation and cavity depth), these would lead to a significant impact on reducing a building's cooling loads and energy efficiency. It is worth noting that mechanical ventilation (e.g., supplying all return cool air from internal spaces into the DSF cavity or integrating the building's heating, ventilation, and air-conditioning system with the façade) is necessary for DSF in hot climates to cool and maintain its cavity's temperature to function properly. However, this increases cooling loads, energy consumption, and running costs of the building which architects have to consider to determine the most efficient and economical solution in material and equipment.**

Index Terms—**Arid regions; Double-skin Façade; Hot climate; Middle East**

I. Introduction

Double-skin façade (DSF) is a technology designed in Europe (for cold climates) to save energy on heating and enhance indoor comfort in a building that is identified as a multilayered structure composes of an outer skin, a cavity, and an inner skin (Streicher, et al., 2005; Zhou and Chen, 2011), illustrated in Fig. 1.

The DSF system has taken its present form over a number of years of its application, predominantly seen in the European countries; it is now picking up in the USA and other countries, and has become synonym with the applications of transparent and glass architecture. It is also becoming an efficient environmental design strategy for energy savings and life cycle costs (Boake, 2001).

In this age, DSF is becoming a common architectural feature of commercial buildings. "The challenge for DSF buildings is to maintain a balance between the esthetic, acoustics insulation, and visual benefits against the performance of the building from energy point of view" (Yagoub, Appleton and Stevens, 2010).

After its successful application in the European region, many other countries of different climates are starting to consider studies and researches about DSF to try adapting it into different weathers to be able to maintain a good comfort zone and reduce energy consumption as much as possible.

II. Classification of DSF

DSF can be identified into the following types: (Knaack, et al., 2007).

A. Box Window

Each box is enclosed horizontally and vertically and has its own air circulation, Fig. 2.

B. Shaft Box

This type extracts air from its own cavity into special adjacent shafts that extend over several stories for stack effect, Fig. 2.

C. Corridor

Partitioned at each floor level or may extend over several floors. Air vents on external skin should be located near the floor and ceiling for each level. Natural, mechanical, and hybrid are three possible ventilation types, Fig. 2.

D. Multistorey

Cavity space between inner and outer skins extends over the entire façade or in some cases by a number of rooms and floors without any dividers. Vent openings are located near the ground and the roof, Fig. 2.

III. Advantages of DSF

According to a study by Ghasemi and Ghasemi, 2017, double-skin facades have a wide range of properties and

ARO-The Scientific Journal of Koya University
Vol. IX, No.2 (2021), Article ID: ARO.10859, 11 pages
DOI: 10.14500/aro.10859
Received: 22 August 2021; Accepted: 22 November 2021
Regular research paper: Published: 20 December 2021
Corresponding author's e-mail: ari.abtar@univsul.edu.iq

advantages that can be fully utilized to improve the overall performance and esthetics of our buildings, some of these advantages are the following:

- Reduction of heating energy
- Sunlight radiation control
- Possibility of natural air conditioning.

IV. Considerations in Hot Climate Regions

It has been claimed that DSF should have low thermal transmission (U-value) and low solar heat gain coefficient (G-value) to function properly (Kragh, 2000), as shown in Fig. 3. Therefore, it is necessary to design a system that decreases solar gain and air temperature inside the cavity during the summer season, this would decrease the internal surface temperature which leads to a reduction in cooling loads. A proper combination of the type of DSF and geometry, size of openings, type, and positioning of shading devices can improve building performance.

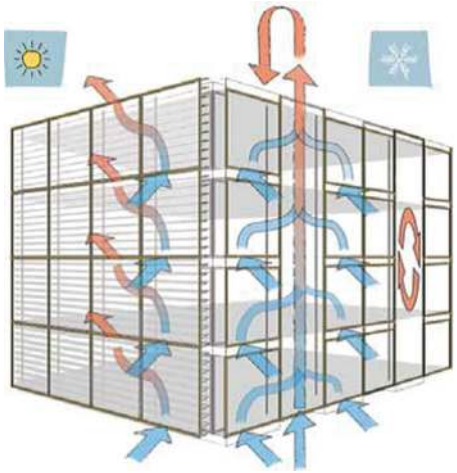

Fig. 1. Components and work mechanism of a double-skin façade (Poirazis 2004).

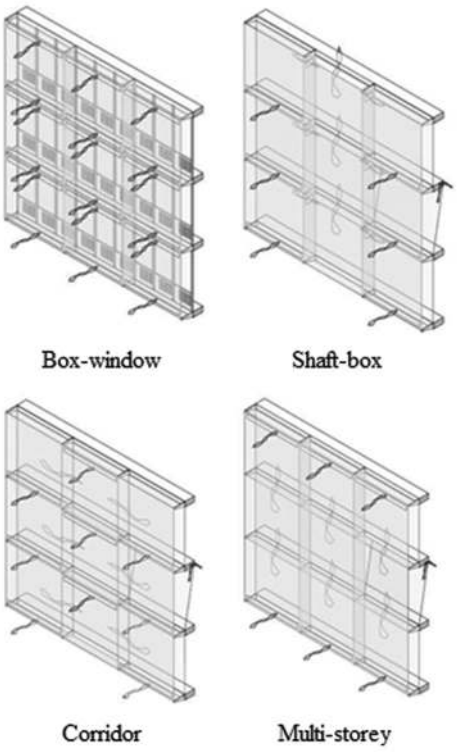

Fig. 2. Illustrations of the four types of DSF (Knaack 2007).

In addition, DSF has the potential of providing acceptable internal thermal comfort levels through natural ventilation. Considering the climate, the building's orientation can be decided based on the prevailing wind, which can make natural ventilation possible in summer (Azarbayjani, 2011).

However, application of DSF in hot climates will not be as easy as it is in cold and temperate climates, as several things must be considered to implement solutions and improvements into the envelope, such as:

- High external temperature in summer; this will greatly affect the external layer and the cavity.
- Sand storms in the region; affecting designs and mechanism for the cavity.
- Maintenance and cleaning of the cavity due to dust and sand.
- Complexity of the building shape; due to the above factors, how much can be done in terms of its shape.

V. Methodology

This study will utilize a quantitative investigative approach, by looking into the previous studies on DSF in similar climates to Iraq using the Köppen-Geiger classification system, as shown in Fig. 4, that divides Iraq into the three following regions; (Csa) [warm temperate, summer dry, and hot summer] in the north, (Bsh) [arid, summer dry, and hot arid] in the middle, and (BWh) [arid, desert, and hot arid] in the southern regions. Besides, discussing and comparing their findings through computer simulations are undertaken to better understand their local climate, regulations, software and technological capabilities, and approach to utilizing DSF.

VI. Review: Case Studies and Application Analysis

Multiple studies and analyses have been made to find out how much DSF is effective in temperate, hot, and arid

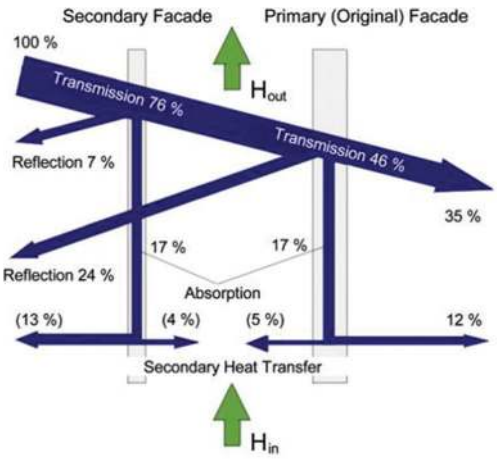

Fig. 3. Heat transfer phenomena in a double-skin façade (Blumenberg, et al., 2006).

http://dx.doi.org/10.14500/aro.10859

climates (especially within the Middle East) and looking for different possibilities to modify and adapt its current form (for Europe and cold regions) for the hot regions.

A. Case Study: Cairo World Trade Center in Cairo, Egypt

In a research (Hamza, 2008), the author mentions that understanding the performance of DSF configurations in extreme hot-arid climates is little. Therefore, her investigation adopted an analytical approach using a dynamic simulation software (IESVE). Afterward, the author attempted a comparative analysis of cooling loads on a single skin base case which is based on the third tower of the Cairo World Trade Center (to the left in Fig. 5) by Skidmore, Owings, and Merrill (SOM), compared against three possible changes to the physical properties of the external layer of the DSF.

Fig. 6 shows that the physical attributes of the base case model are a square plan and not surrounded by other buildings. Besides, the parameters listed in Table I are used for the default walls and the DSF layers. The majority of office buildings in Cairo were built the same way, this is shown in Fig. 6, which appears to have been used in constructing other base case morphologies in different climates to easily calculate the influence of changing façade configurations on its cooling loads (Lam, 2000).

The simulation's results in Fig. 7 predict an increase in annual cooling loads due to the low direct solar radiation reflection properties of clear glazing, showing that a transparent DSF has poor thermal performance compared to a well-designed single skin. The results also predict that cooling loads on the East, West, and South orientations will be 12% lower than a benchmark single skin. Hamza suggested that the heat trapped in the channel would encourage natural buoyancy which, in turn, would reduce heat gain (Hamza and Underwood, 2005).

Moreover, the results indicate that using a reflective DSF can achieve better energy savings compared to a single skin with reflective glazing, as the selective reflective glass on the outer layer of the DSF shows the highest possible decrease in cooling loads (approximately 30%). Furthermore, using glazing with lower shading coefficient and g-value (total solar energy transmittance) should be considered rather than transparent glass on the external layer to provide the first line of defense against the direct solar radiation in hot-arid climates.

B. Case Study: National Holding Headquarters in Abu Dhabi, UAE

A simulation analysis research was done by Yagoub, Appleton and Stevens, 2010, on the National Holding Headquarters' building shown in Fig. 8, which is designed by Zaha Hadid Architects and located in Abu Dhabi (which has a hot and arid climate similar to the southern regions of Iraq) to determine its effectiveness. In this paper, the data in Tables II and III were considered as the properties of the DSF glazing and the thermal parameters.

Initial results in Fig. 9 show that due to high outdoor temperatures, the DSF's gap had very high temperatures,

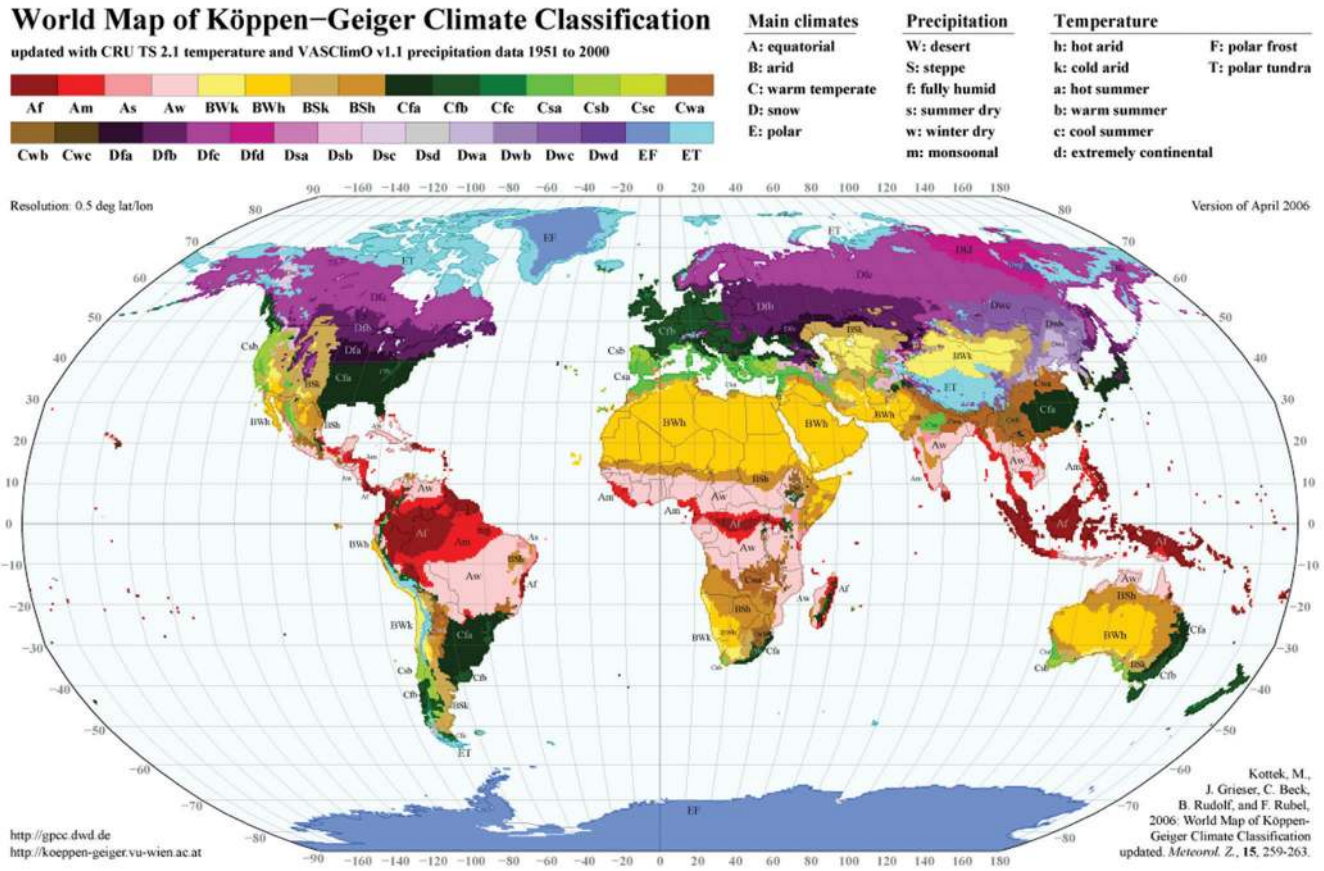

Fig. 4. Köppen-Geiger Climate Classification Map (Rubel and Kottek, 2010).

Table I
Glazing and Thermal Properties for the Outer Leaf of the Double-Skin Façade (Hamza, 2008)

Glazing thickness	Window-to-wall ratio		Wall	U-value (Wall)			
6 mm panel	40%		Single brick, uninsulated, plastered on both sides	1.4 W/m² K			
Exterior leaf glazing type	U-value (W/m² K)	Solar coefficient (SC)	g-Value	Thickness (mm)	Transmittance (%)	Reflection (%)	Absorption (%)
Clear glazing	5.6	0.85	0.87	10	73	7	20
Body tinted green	5.6	0.59	0.51	10	35	5	60
Reflective glazing active blue	5.6	0.27	0.42	10	21	12	67
Glazing properties for internal glazing 40% WWR of the double-skin façade							
Clear glazing	5.6	0.95	0.82	6	79	7	14
Single glazing type	U-value (W/m² K)	Solar coefficient (SC)	g-Value	Thickness (mm)	Transmittance (%)	Reflection (%)	Absorption (%)
Glazing properties simulated for the sing skin base case façade (BC)							
Clear glazing	5.6	0.95	0.82	6	79	7	14
Reflective glazing	5.6	0.6	0.47	6	37	5	58

Table II
Properties of the Glazing (Yagoub, et al., 2010)

Exterior leaf glazing type	External skin	Internal skin external glass	Internal skin internal glass
Thickness (mm)	10	8	8.76
Conductivity (W/m K)	1	1	1
Type of glass	Pyrolytic coating with gold appearance on outer Surface	Clear glass with low-E coating	Clear laminated glass Uncoated
Light transmittance	38%	87%	87%
Light reflectance (outside)	35%	5%	8%
Light reflectance (inside)	45%	4%	8%
Solar transmittance	46%	56%	70%
Solar reflectance (outside)	21%	20%	6%
Solar reflectance (inside)	30%	30%	6%
Outside emissivity	0.84	0.84	0.84
Inside emissivity	0.84	0.04	0.84
U-value (W/m² K)	5.56	3.2	5.6
Refractive Index	1.5	1.5	1.5

Table III
Input Parameters for the Thermal Model (Yagoub, et al., 2010)

Element	Value
Humidity in the offices space	Minimum 40% and maximum 60%
Temperature of the internal office space	24°C (constant)
Miscellaneous internal gains (e.g., small power)	15 W/m²
Lighting internal gains	18.75 W/m²
Occupancy density	9m² per person
Infiltration	0.25 air change per h
Simulation period	Whole year round

this would affect greatly what the indoor surface temperature was required to be at. Thus, solutions were sought to reduce the temperature of the DSF skins and try to maintain it at a below level. It was suggested that the DSF gap's temperature to be either maintained at 45°C or 60°C, as 45°C was the assumed external temperature for the design and 60°C was the maximum operating temperature for the shading blind motors.

Considering energy efficiency, it is beneficial to maintain the DSF cavity's temperature at the same external air

Fig. 5. Cairo World Trade Center designed by SOM (Hamza, 2008).

temperature (~45°C); however, this requires all the internal spaces' return cool air to be supplied to the cavity in addition to the extra cooling load. For example, the author stated that each floor had an estimated ventilation flow rate of 1500 l/s and cooling load of 192.6 kW. However, to be able to lower and maintain at 45°C, additional air (3000 l/s) will be needed leading to an additional cooling load of 44 kW. Whereas maintaining the cavity at 60°C needs an estimated 800 l/s

http://dx.doi.org/10.14500/aro.10859

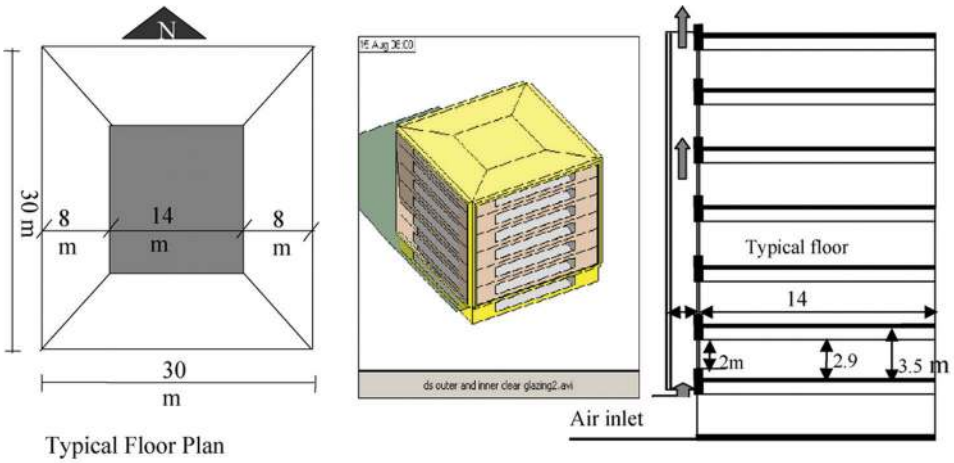

Fig. 6. Physical attributes of the base case model, showing the location of the air inlet (Hamza, 2008).

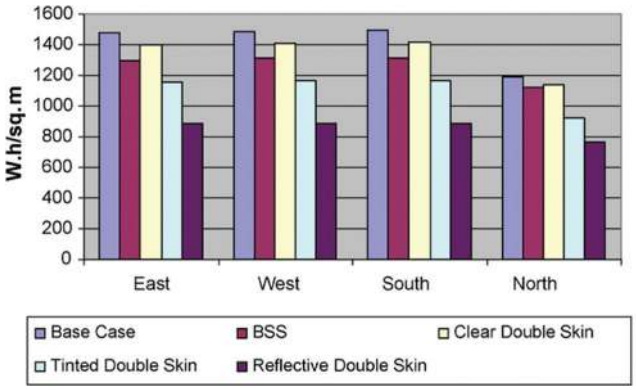

Fig. 7. Comparison between single skin and double skin on annual total cooling loads (Hamza, 2008).

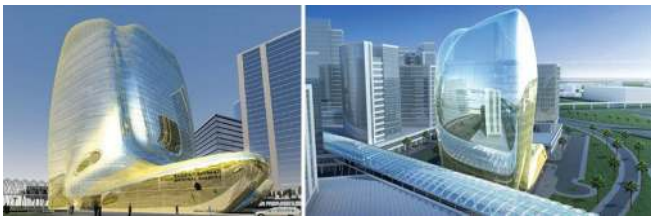

Fig. 8. External views of National Holding's building (right: Yagoub, Appleton and Stevens, 2010) (left: Wallner and Pottman, 2011).

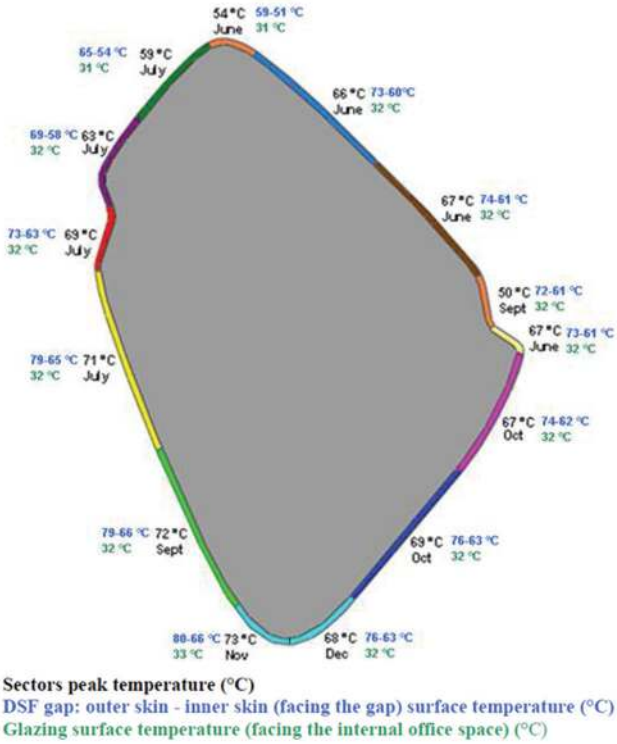

Fig. 9. Air and glazing surface temp. variation along the double-skin gap (Yagoub, Appleton and Stevens, 2010).

which is 20.6 kW worth of additional cooling load, this allows partial heat recovery which lets the motorized blinds to operate with minimum risk, as shown in Fig. 10.

Based on the results, it is possible to achieve comfortable internal conditions using DSF. However, it is unavoidable to allow for an element of energy consumption dedicated to maintain the cavity's temperature. This impacts the overall building energy consumption leading to higher running costs in the long run.

C. Case Study: Office Buildings in Riyadh

In another research (Alahmed, 2013), the author referenced the previous study's findings and tried to move it further to get improved and better solutions by conducting simulations on a hypothetical building model seen in Fig. 11, which is based on multiple existing office buildings in Riyadh, Saudi Arabia, which uses the country's specific building regulations and specifications listed in Table IV.

Buildings that were considered as case studies were not energy efficient at all, and their facades were proposed to be changed into DSF to improve their performance, as shown from Fig. 12. Moreover, for the simulation, the given information in Table V was used.

Preliminary simulations and analyses were made to find out the most important variables, for example, determining the most effective cavity depth of the DSF on the energy consumption as shown in Fig. 13. The author also looked

Table IV
Saudi Regulations for Glazing Areas in Buildings (Alahmed, 2013)
Window and Glazed Door Area Greater than 40% but not Greater than 50% of Above-Grade Wall Area

Element	Condition/Value		
Skylights (U-factor)	4.542		
Slab or below-grade wall (R-value)	R-1.409		
Windows and glass doors	Solar heat gain factor (SHGC)	U-factor	
PF<0.25	0.4	2.271	
0.25≤PF<0.50	0.5	2.271	
PF≥0.50	0.6	2.271	
Roof assemblies (R-value)	Insulation between framing	Continuous insulation	
All-wood joist/truss	R-5.284	R-4.051	
Metal joist/truss	R-5.284	R-4.227	
Concrete slab or deck	NA	R-4.051	
Metal purlin with thermal block	R-6.692	R-4.227	
Metal purlin without thermal block	R-6.692	R-4.227	
Floors over outdoor air or unconditioned space (R-value)	Insulation between framing	Continuous insulation	
All-wood joist/truss	R-4.403	R-3.170	
Metal joist/truss	R-4.403	R-3.346	
Concrete slab or deck	NA	R-3.346	
Above grade walls (R-value)	No framing	Metal framing	Wood framing
Framed: R-value cavity	NA	R-2.289	R-1.937
R-value continuous	NA	R-3	R-0
Concrete masonry units (CMU) > 200 mm:			
R-value cavity	NA	R-1.937	R-1.937
R-value continuous	R-0.881	R-0	R-0
Other masonry walls:			
R-value cavity	NA	R-1.937	R-1.937
R-value continuous	R-0.881	R-0	R-0

DD (F)=DD (C)*1.8; 1 W/m^2 K=0.1761 BTU/(hr.ft 2°F); 1 m^2 K/W=5.678 h.ft^2 °F/BTU

Table V
Input Details for the Glazing and Construction Materials (Alahmed, 2013)

Elements	Materials	Thickness	U-value (W/m^2 K)
Walls	Insulated concrete	45.5 cm	0.25
Roof	Insulated reinforced concrete	42.5 cm	0.23
Floors	Reinforced concrete ceilings	30 cm	2.4
Internal Walls	Concrete blocks	13 cm	1.16
Location	Description	U-value (W/m^2 K)	Total R-value (m^2 K/W)
Single skin facades	Double-glazed windows reflective coating	2.92	0.17
Double skin facades (external skin)	Single-glazed windows reflective coating	5.41	0.0057
Double-skin facades (internal skin)	Double-glazed low-E windows	1.67	0.33

into the possibility of replacing heating, ventilation, and air-conditioning (HVAC) systems with DSF, but this would not be ideal in hot climates due to the cavity's hot air. Thus, the cavity may be utilized as a part of the HVAC system instead of replacing it entirely. The end variables that were selected for the study were the following in Table VI.

Table VI
Simulation variables selected for study (Alahmed, 2013)

Installation type	Orientations	Cavity depth	Ventilation in cavity
Multistorey	South	100 cm	Natural
Corridor	North	150 cm	Mechanical
Box window	East		
	West		

After extensive simulations and analysis, the study showed that most DSF scenarios had significant energy use reduction compared to baseline cases of the same building. The most effective type of DSF was found to be the box window type with effective configurations when the cavity was located on the western and eastern facades and used wider cavity depth with mechanical ventilation, as it provided extra protection compared to single skin facades and reduced solar gains in rooms next to the cavity. Consequently, cooling loads were decreased. In addition, inner surface temperatures were dropped due to the injected exhaust air from the HVAC system, as shown in Fig. 14. In turn, it reduced energy consumption by 8.05% and 4.78%, respectively, in comparison to the baseline without and with shading.

The study's results give us a better picture regarding orientation and mechanical options when DSF is considered

http://dx.doi.org/10.14500/aro.10859

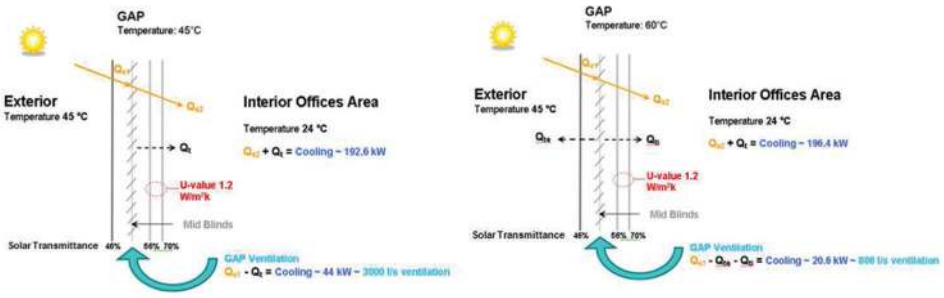

Fig. 10. Section of DSF shows cooling requirements for the gap at 45°C and 60°C (Yagoub, Appleton and Stevens, 2010).

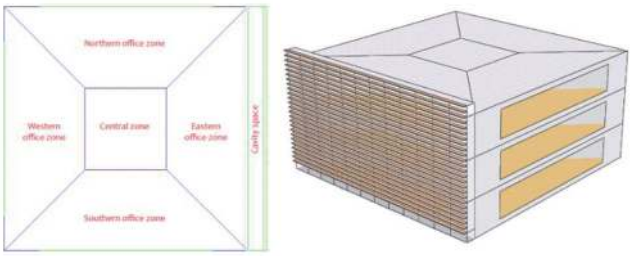

Fig. 11. Simulation building layout and model (Alahmed, 2013).

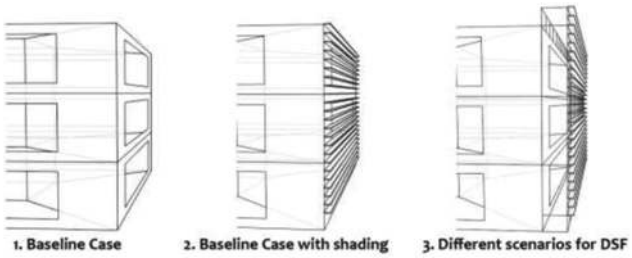

Fig. 12. Illustrations of the different cases for the simulation (Alahmed, 2013).

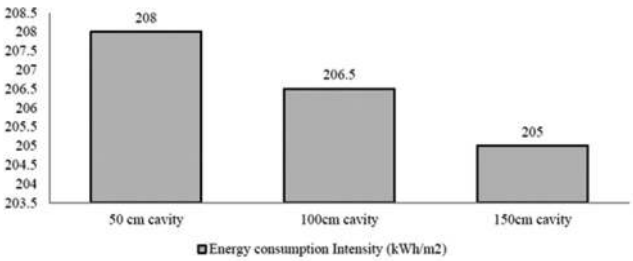

Fig. 13. Energy use intensity (kWh/m^2) for different cavity depths for cavity facing east (Alahmed, 2013).

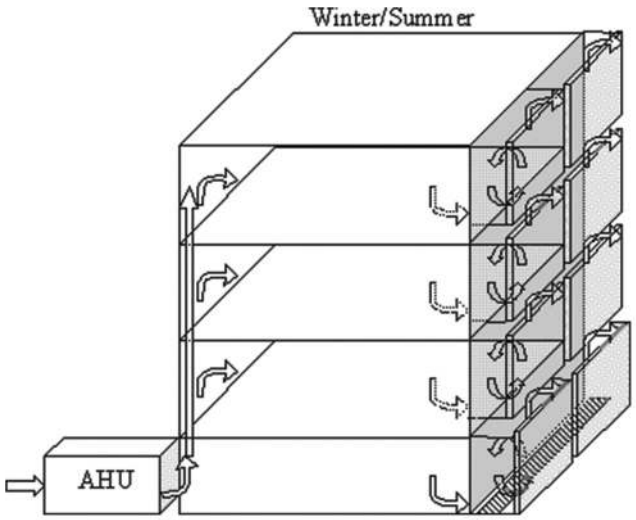

Fig. 14. DSF as an exhaust duct for the heating, ventilation, and air-conditioning system (Poirazis, 2004).

Fig. 15. Arch. Engineering Department in UAE University, Al-Ain City (Radhi, Sharples and Fikiry, 2013).

for retrofitting and rehabilitation purposes. However, this approach needs further readings from different locations to get suitable solutions for local buildings.

D. Case Study: Arch. Engineering Department in Al-Ain City, UAE

In another study (Radhi, Sharples and Fikiry, 2013) in which instead of running computer simulation on base case models, the author simulated an educational building with a multi-façade system within the UAE University campus in Al-Ain City (approximately 100 km away from Dubai), Figs. 15 and 16 show the exterior of the building and a cross-section of its external skin consecutively.

The author aimed to assess the impact of a climate interactive façade system (CRFS) compared to classical single façade system (CSFS) on cooling energy within fully glazed buildings using building energy simulation and computational fluid dynamics (CFD) as listed in Table VII to establish boundary conditions and also develop geometrical models based on a new constructed multistorey building.

The initial result presented in Fig. 17 shows that using a CRFS can reduce solar gain within internal spaces, but increases the temperature within the cavity. Regarding cooling loads on a typical summer day in the UAE, the simulation shows that between 17 and 20% of cooling energy required can be saved. The author states that this range varies from one orientation to another and depends greatly on the level of irradiance and angle of incidence.

From the research's final results, the parameters that have the most impact on cooling loads are floor level related to screen's height, followed by glazing properties and cavity depth, respectively. These results offer a reliable indicator of how a climate interactive facade system can have a substantial impact on energy savings, especially for multistorey glazed buildings in hot-arid climates such as in the Middle East.

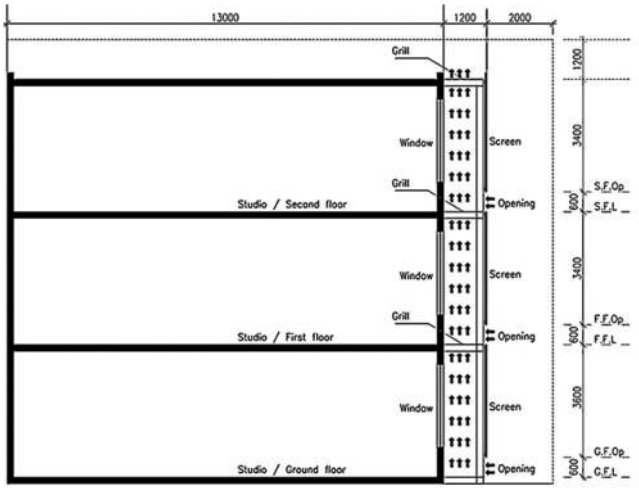

Fig. 16. Cross-section of the studios showing the cavity and air inlet through the DSF (Radhi, Sharples and Fikiry, 2013).

It is worth noting that in another research (Hashemi, Fayaz and Sarshar, 2010), the author performed field measurements instead of relying on computer simulation for base model predictions for a building with DSF for 2 weeks in summer and 2 weeks in winter in Tehran, Iran (which the country, in general, has a climate more similar to Iraq). That was to observe the behavior of the system in hot and cold conditions. Initial results showed an increase in temperature inside the cavity (reach to 1°C–10°C higher compared to outside temperature) due to direct solar radiation. It was also noticed that the cavity temperature could be 12°C less than the outside, if the façade was in a shade. The final results showed that this temperature difference between the cavity and the skins can significantly impact heating energy in winter. However, to reduce cooling loads in summer, the author suggested that it was essential to implement additional techniques such as night ventilation and shading devices for the cavity. This aligned with the results from both Yagoub, Appleton and Stevens, 2010, and Alahmed, 2013, works that some form of mechanical ventilation is necessary for DSF in hot-arid climates.

VII. Discussion: Technical Specifications

From the aforementioned researches, it has been found that in every situation of DSF, careful considerations have to be made

Table VII
Boundary Conditions of the Base Case Building (East Direction) (Radhi, *et al.*, 2013)

	Screen in-surface		Screen out-surface		Win in-surface		Win out-surface	
	Temp. (°C)	Co (W/m² K)	Temp. (°C)	Co (W/m² K)	Temp. (°C)	Co (W/m² K)	Temp. (°C)	Co (W/m² K)
Thermal boundary conditions								
09:00–10:00	50.9	2.2	44.6	6.9	42.4	1.7	43.1	1.9
12:00–13:00	50.6	1.9	46.2	5.2	45.6	1.7	46.1	1.7
15:00–16:00	46.1	1.4	43.3	5.6	43.5	1.4	43.9	1.1
18:00–19:00	40.5	1.4	37.1	7.7	41.9	0.7	42.0	1.6
	Ambient temperature (°C)		Direct radiation (kW)		Diffuse radiation (kW)		Direction	
09:00–10:00	31		0.27		0.12		East	
12:00–13:00	39		0.79		0.17		South	
15:00–16:00	43		0.86		0.14		South-west	
18:00–19:00	37		0.51		0.15		West	
Flow rate (L/S)								
Ground floor cavity	3379							
First floor cavity	4572							
Second floor cavity	6718							
Specification of glazing			Screen		Win		Wall	
U-value (W/m² K)			5.7		2.79		0.52	
Solar Transmission (ST)			0.78		0.60		-	
Light Transmission (LT)			0.88		0.78		-	
Solar heat gain coefficient (SHGC)			0.82		0.70		-	
Emissivity			0.96		0.92		0.84	

 http://dx.doi.org/10.14500/aro.10859

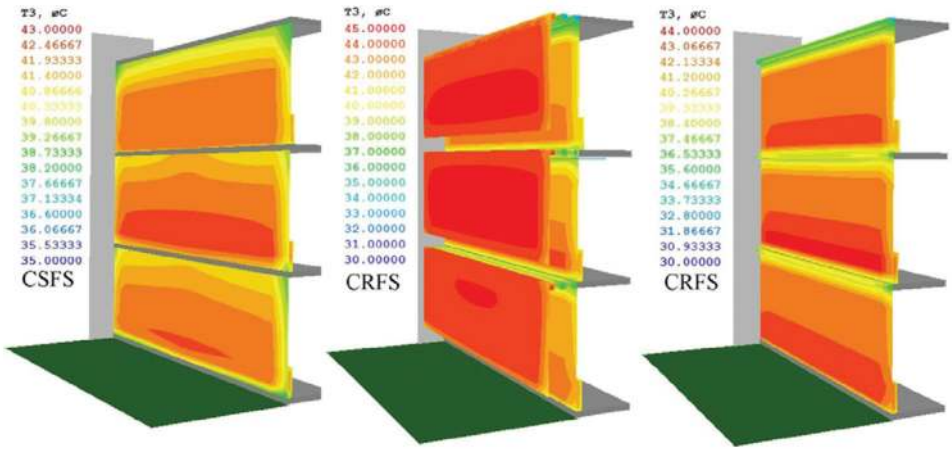

Fig. 17. Comparison of surface temperatures (Radhi, Sharples and Fikiry, 2013).

as each building and its location has its specific requirements and parameters (combination of used materials, using the right proportion and the appropriate orientation) to make DSFs an energy-efficient strategy (Cetiner and Ozkan, 2005). A set of effective guidelines have been proposed for the application of DSF in hot climates, which are the following:

A. Material

Use materials with a high R-value (thermal resistance) so that there is minimum heat gain, this should not be at the expense of using a vast amount of energy for acquiring them.

B. Glazing Material

It's necessary to determine how much glass is used, along which façade it is used and if it is appropriately shaded as this can help in reducing the internal temperature of the cavity, therefore, the DSF system wouldn't rely heavily on the mechanical ventilation components, leading to a reduction in the running cost of the system. Additionally, using locally manufactured glass in two layers for the glazed areas may be more cost-effective than using a highly advanced glazing technology that has to be imported.

C. Nature of Layers

Layers should not be completely transparent on any of the facades, except the north orientation. The opaque layers may be of the same thickness, or for better insulating effect, the outer layer can be thicker than the inner layer.

D. Dimensions

The width of the cavity between the two layers may be decided based on the required need to facilitate ventilation of trapped air and space required for maintenance of the cavity because the U-value of the air space is almost constant after 20 cm of thickness. Some studies have shown that the cavity can include plants and vegetation to cool the air in the cavity.

E. Nature of the Cavity

The cavity space between the two layers can be continuous for low-rise structures. It can be partitioned horizontally at each floor level for ease of movement of air for taller buildings.

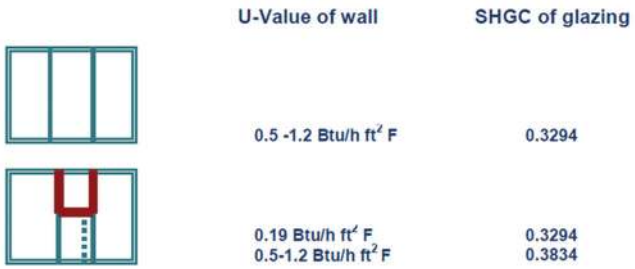

Fig. 18. Comparison of U-values and SHGC (Yellamraju, 2004).

F. U-value

The overall U-value (thermal transmission) of façade should be reduced for maximum benefit. From simulations, it has been seen that a U-value of ~1.08 W/m^2.K ≈ 0.19 Btu/h.ft^2.F is more efficient than an existing glazed double skin's with a U-value of around 2.8–6.8 W/m^2.K, which can be reduced depending on the type of glass and shading devices within the cavity, Fig. 18.

G. Solar Heat Gain Coefficient

The solar heat gain coefficient (SHGC) of a glazed double skin is based on the type of glass used on both the inside and outside, as it is the product of the two layers. Lesser solar heat gain coefficient makes the façade more efficient, Fig. 18.

H. Orientation

Façades should be designed in such a way that maximum transparency would be on the north orientation and minimum on the south orientation, east and west can have about half the transparency of the north façade. Horizontal shading devices are preferred on the north and south side, and vertical shadings devices on the east and west sides to block off direct sun and glare, Fig. 19.

New shading systems have been devised that are derived from the traditional Islamic Mashrabiya, which is a wooden mesh screen that allows some air circulation while also

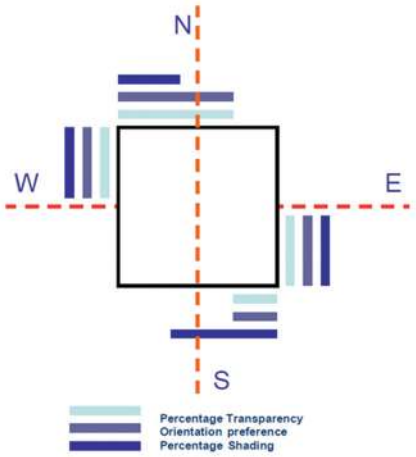

Fig. 19. Design guideline for transparency and shading of the DSF in relation to orientation (Yellamraju, 2004).

Fig. 20. Modern interpretations of the Islamic Mashrabiya. Left, The Souk and right, Masdar City, located in Abu Dhabi, UAE. By Foster + Partners. (Boake, et al., 2014).

blocking significant solar radiation and providing visual privacy. This vernacular-based feature can be seen to naturally extend as a second layer to create a new type of double façade system. Fig. 20 shows an example of said feature implemented in the buildings of Masdar City in Abu Dhabi.

VIII. Conclusion

The first thing to note from the studies is that analytical simulations are of utmost importance before starting to implement the DSF in real life, as to reach the most suitable, reasonable, and economic decision on how to appropriately implement them, thus reducing the chances of having a failed project in hand.

As it is common wisdom in taking advantage of building orientation in the design process to provide suitable indoor thermal comfort, as this will heavily influence the cooling loads and running cost of our buildings. From the hypothetical building case study (Alahmad, 2013), east and west orientations in Riyadh were to be avoided whenever possible as they result in the highest cooling loads. However, for Iraq, orientations should be reexamined alongside the southern orientation to see if their effect is similar to countries such as Saudi Arabia or the UAE. For instance, this will be necessary later on in determining the cavity depth and choosing the most appropriate mechanical ventilation solution for the DSF system.

Regarding the most important component of the DSF, the glazing; results from the studies showed that their optical properties (such as SHGC, U-value, reflectivity, and opacity) are the most effective way to select the most appropriate material for the skins. However, sufficient studies are needed to be done on the local glazing industry in Iraq. This is to see if the available materials are up to the standards in both property and price for an efficient DSF, or we should rely on importing them from other countries.

Moreover, using vernacular elements (as seen in Masdar city's Mashrabiya screens) can be considered good practice in attempting to utilize a region's specific vernacular architecture that is efficient in shading performance. However, duplicating Mashrabiya method without preliminary studies can lead to the emergence of unforeseen problems, especially in Iraqi cities, as the northern regions have a different climate compared to the southern regions. Therefore, further investigations are needed to be done regarding other vernacular architectural features to have options about DSF designs that can be protected and maintained easily during the building's lifetime.

IX. Future Studies

Regarding future studies, it is recommended to start studying aspects of the local context such as the climate, resources, and technologies available in Iraq, to get a better understanding of how ready we are in implementing DSF in our buildings and if there is a need to establish new guidelines and regulations regarding the use of DSF in the buildings. Furthermore, another aspect that can be utilized is building monitoring and model simulations for existing case studies that have significant social or cultural values in Iraq to look into the possibility of rehabilitating the buildings that have poor energy performance and thermal comfort.

References

Alahmed, Z.A., 2013. *Double-Skin Façade in Hot-Arid Climates Computer Simulations to Find Optimized Energy and Thermal Performance of Double Skin Facades*, *MSc Thesis*, University of Southern California, Los Angeles.

Azarbayjani, M., 2011. Climatic based consideration of double skin façade system: Natural ventilation performance of a case study with double skin façade in Mediterranean climate. In: *13th Conference of International Building Performance Simulation Association*, IBPSA France, Chambéry.

Blumenberg, J., Spinnler, M. and Sattelmayer, T., 2006. Double skin façade systems-a comprehensive review on thermal and energetic behavior. In: *International Conference on Recent Advances in Heat Transfer*, Technische Universität München, Munich.

Boake, T.M., 2014. Hot climate double façades: Avoiding solar gain. In: *Facade Tectonics*, University of Waterloo, Canada.

Boake, T.M., Harrison, K., Collins, D., Balbaa, T., Chatham, A., Lee, R. and Andre, B., 2001. *The Tectonics of the Double Skin: Green Building or Just More Hi-Tech Hi-Jinx? What are Double Skin Facades and How Do They Work? Case studies*, University of Waterloo, Waterloo.

Cetiner, I. and Ozkan, E., 2005. An approach for the evaluation of energy and

cost efficiency of glass facades. *Energy and Buildings*, 37, pp.673-684.

Ghasemi, N. and Ghasemi, F., 2017. Double-skin façade technology and its aspects in field of aesthetics, environment and energy consumption optimization. *International Journal of Scientific Study*, 5, pp.293-307.

Hamza, N. and Underwood, C., 2005. CFD assisted modeling of double skin facades in hot arid areas. In: *9th International Building Performance Simulation Association Conference (IPBSA)*, *Montreal*.

Hamza, N., 2008. Double versus single skin facades in hot arid areas. *Energy and Buildings*, 40, pp.240-248.

Hashemi, N., Fayaz, R. and Sarshar, M., 2010. Thermal behaviour of a ventilated double skin facade in hot arid climate. *Energy and Buildings*, 42, pp.1823-1832.

Knaack, U., Klein, T., Bilow, M. and Auer, T., 2007. *Façades: Principles of Construction*. Birkhauser Verlag AG, Berlin.

Kragh, M., 2000. Building Envelopes and Environmental Systems – Permasteelisa R&D and the increasingly required integral design approach. In: *Modern Façades for Office Buildings*. Delft Technical University, Netherlands.

Lam, J., 2000. Energy analysis of commercial buildings in subtropical climates. *Building and Environment*, 35, pp.19-26.

Poirazis, H., 2004. *Double Skin Façades for Office Buildings*, *Literature Review*, Lund University, Lund.

Radhi, H., Sharples, S. and Fikiry, F., 2013. Will multi-facade sysems reduce cooling energy in fully glazed buildings? A scoping study of UAE buildings. *Energy and Buildings*, 56, pp.179-188.

Rubel, F. and Kottek, M., 2010. Observed and projected climate shifts 1901-2100 depicted by world maps of the Köppen-Geiger climate classification. *Meteorologische Zeitschrift*, 19, pp.135-141.

Streicher, W., Heimrath, R., Hengsberger, H., Mach, T., Waldner, R., Flamant, G., Loncour, X., Guarracino, G., Erhorn, H., Erhorn-Kluttig, H., Santamouris, M., Farou, I., Duarte, R., Blomsterberg, A., Sjöberg, L. and Blomquist, C., 2005. *BESTFACADE-Best Practice for Double Skin Facades*, *Report No*. *WP1*.

Wallner, J. and Pottmann, H., 2011. Geometric computing for freeform architecture. *Journal of Mathematics in Industry*, 1, p.4.

Yagoub, W., Appleton, S. and Stevens, W., 2010. Case study of double skin façade in hot climates. In: *Adapting to Change: New Thinking on Comfort*, Network for Comfort and Energy Use in Buildings, London.

Yellamraju, V., 2004. *Evaluation and Design of Double-Skin Facades for Office Buildings in Hot Climates*, *MSc Thesis*, Texas A&M University, College Station.

Zhou, J. and Chen, Y., 2011. A review on applying ventilated double-skin facade to buildings in hot-summer and cold-winter zone in China. *Renewable and Sustainable Energy Reviews,* 15(3), pp.1468-1475.

Flood Modeling on Koya Catchment Area Using Hyfran, Web Map Service, and HEC-RAS Software

Anwer H. Dawood[1,2], Dana K. Mawlood[1], Nadhir Al-Ansari[3]

[1]Department of Civil Engineering, College of Engineering, Salahaddin University-Erbil, Kurdistan Region – F.R. Iraq

[2]Department of Geotechnical Engineering, Faculty of Engineering, Koya KOY45, Kurdistan Region – F.R. Iraq

[3]Department of Civil, Environmental and Natural Resources Engineering, Lulea University of Technology, Lulea, Sweden

***Abstract*—This research uses a new engineering approach in the management of rainfall storms in the Koya basin to delineate the inundation boundaries for the floods that occur in the study area. This covers some agricultural lands and residential areas in the countryside. According to this approach, it is possible to determine the best sites for building small dams and water collection basins for water harvesting. The above-mentioned approach consists of a meteorological and morphological study, soil classification, flood hydrograph modeling, and demarcation of inundation boundaries, to find the depth and velocity of flood flow. The average runoff depth was based on curve number (CN) values. These values were determined based on soil cover types and soil class according to the Harmonized World Soil Database program. Accordingly, the soil class in the study area is Group B alluvial silt and the CN value is determined to be 71. The results showed that the runoff potential varied with land use and soil characteristics. Hydrological modeling is performed by HEC-HMS software (Army Corps of Engineers Hydrologic Engineering Center – Hydrologic Modeling System), which simulates runoff precipitation process using a SCS Soil Conservation service CN model. A flood hydrograph generates at the catchment area outlet, and the delineation of the floodplains is verified by HEC-RAS software (US Army Corps of Engineers Hydrologic Engineering Center – River Analysis System). Furthermore, the results showed that the flood return period of 100 years could reach sensitive areas such as urban, agricultural, and residential areas. According to the results of this study, there were suitable sites in the catchment area for the establishment of small dams and ponds for water harvesting.**

***Index Terms*—Catchment area management; Flood delineation; Flood modeling; Hydrologic process; Hyfran and Web Map Service software.**

ARO-The Scientific Journal of Koya University
Vol. IX, No.2 (2021), Article ID: ARO.10824, 5 pages
DOI: 10.14500/aro.10824
Received: 01 June 2021; Accepted: 15 December 2021
Regular research paper: Published: 25 December 2021
Corresponding author's email: anwer.hazim@koyauniversity.org

I. Introduction

Water is one of the most important natural resources for countries and a fundamental basis for their growth and development. In the same time, flooding is one of the most devastating natural disasters on the planet. Floods take place due to extensive rainfall in short time duration, incorrect land use, and deforestation in headwater zones (Abdelshafy, et al., 2020). Various parts of the world are at risk of flooding, causing great loss of life and property. These large losses resulting from natural hazards such as floods are the main impetus for research, investigation, and scientific understanding of the nature of flooding and the resulting wastes. This indicates that natural hazards are a challenge. Since floods threaten life and the environment, which made researchers in dire need to find and choose the best ways, methods and procedures to protect humans and environment through such hydrological study to indicate the flood risk area and safe area for planning of urban extension. In addition, protection measures can turn the equation by converting the flood from a disaster to blessing through building infrastructure projects for flood utilization, water storage, and reuse in the dry season.

The studied area is located in East of Erbil province and west of Dokan district. It is approximately 70 km from Erbil (the capital of Kurdistan region), approximately and 50 km from Dokan, the Koya city (latitude 36 05N, longitude 44 37E, altitude 610M) (Fig. 1). The climate of the study area is classified as arid and semi-arid region.

II. Methodology

To get the maximum storm rainfall depth value, rainfall daily data were obtained from Koya meteorology station and were statistically analyzed using the model proposed by Hyfran Plus software, and then, the morphological study was carried out using geographic information system (GIS), Web Map Service (WMS), Global Mapper, and Google Earth for the determination of the boundary of the catchment area.

http://dx.doi.org/10.14500/aro.10824

The next step was runoff calculations which were carried out using the curve number (CN)-SCS model, Harmonized World Soil Database (HWSD) Viewer, HEC-HMS for Soil classification, and Determination of Peak flow according to SCS-CN. The final step was using the HEC-RAS model for drawing the flood plain.

III. Results And Discussion

A. Maximum Daily Rainfall Through the Year

The rainfall maximum daily data are available from 2001 to 2021 for Koya station. Table I shows the maximum daily rainfall data in Koya station.

For planning and design purposes of various hydrological projects, the best fit of rainfall data is used (Khalid, et al., 2016). For this purpose, the available data for the study area were treated statistically for return period (2–200) years using different methods to find the maximum daily rainfall storm depth as shown in Table II (Kurdistan Regional Government, Ministry of Agriculture and Water Resources, Directorate of Koya Irrigation; Directorate of Koya Agriculture, 2021, rainfall data).

To describe the amount of daily rainfall data, it is necessary to identify the distribution which is the best fit of the data. This was achieved using different statistical methods such as exponential distribution, GEV generalized extreme value distribution, normal distribution, lognormal distribution, and gamma distribution methods. The results are tabulated in Table III.

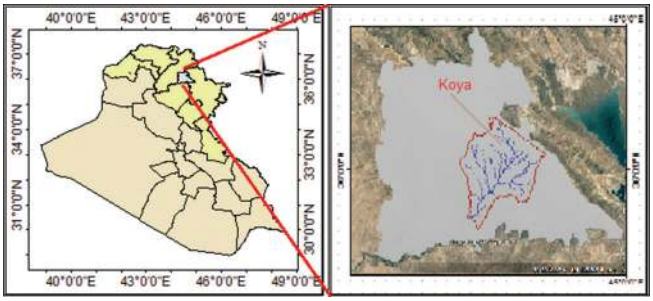

Fig. 1. Location map of study area Koya basin.

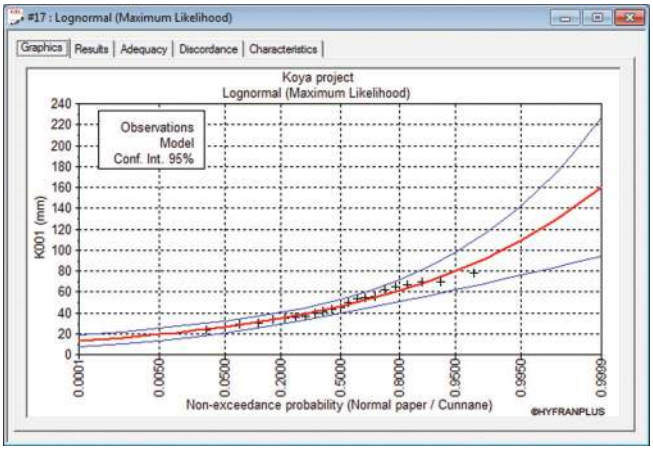

Fig. 2. Probability distribution curve of Koya basin using lognormal distribution.

According to the tests, the best distribution is one when lognormal method was used (Chow, et al., 1988). Accordingly, when the data given in Table II were used, the results of the maximum rainfall data at different return periods in Table II lognormal distribution daily rainfall data were obtained, as shown in Fig. 2.

B. Morphological Study

Physical parameters of the catchment area are very significant for hydrological study such as length of longest flow path and mean slope. Using DEM 30 m accuracy by global mapper for the study area and drawing the boundary of the catchment, the catchment characteristics were determined using WMS (Al Kalbani, 2021) (Table IV and Fig. 3).

C. Runoff Calculations Using SCS-CN Model

One of the most common techniques model of SCS-CN is for the measurement of amount of direct surface runoff for a given period during a rainfall event. The SCS model is an

Table I
Maximum Daily Rainfall Depth Record in Koya station

Year	Max. daily (mm)	Year	Max. daily (mm)
2001	35.5	2012	70
2002	55.5	2013	78.5
2003	70	2014	35
2004	65	2015	36.5
2005	55	2016	29.3
2006	40	2017	54
2007	50	2018	66.6
2008	30	2019	45
2009	33.5	2020	43
2010	62	2021	23.6
2011	41		

Table II
Design Storm Depth Resulting from Statistical Analysis of Maximum Daily Rainfall Record Using Serval Distribution Methods

	Predicted design storm resulted from Hyfran					Graphical
Dist.	Exp.	GEV	Normal	Lognormal	Gamma	
Return period (Year)						
2	40.5	47.4	48.5	46.1	46.9	44.2
5	64.5	60.8	61.8	61.1	60.9	61.0
10	82.6	68.3	68.7	70.8	69.2	73.8
25	107	76.4	76.1	82.9	78.8	90.6
50	125	81.6	80.8	91.7	85.5	103.3
100	143	86.2	85.1	101	91.7	116.1
200	161	90.2	89.1	109	97.7	128.8

Where: Exp.=Exponential distribution, GEV=General extreme value distribution, Normal=Normal distribution, Lognormal=Lognormal distribution, Gamma=Gamma distribution

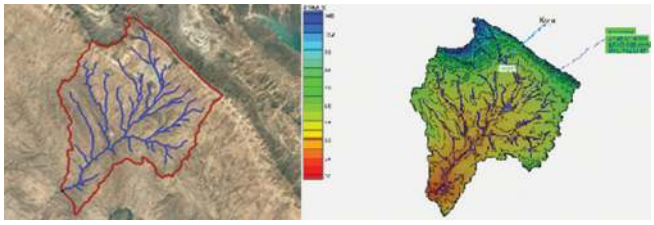

Fig. 3. Koya catchment area boundary with drainage lines.

empirical model and only includes a single parameter, the CN, which incorporates the hydrological effects of land use (Ara and Zakwan, 2018).

To apply the model, the following data required for this model: Catchment area in Km^2, calculate the time of concentration in hours, CN, and maximum daily rainfall depth in mm through return period (Sc, 1986).

The main challenge of hydrology in estimating the volume of surface runoff is how to estimate the surface runoff coefficient resulting from an effective rainfall storm in basins where no measurement stations are available. The surface runoff curve (CN) is a major factor in determining the runoff in the SCS hypothesis, which takes into account land use, soil type, geological structure, vegetation, and rainfall (USDA-SCS, 1972).

According to the HWSD viewer, the soil type in the studied area is divided into two zones which are loam and light loam so the soil class is type B silt loam or loam (Harmonized World Soil Database – HWSD – 2021).

Now for determining CN, the check land use is to be checked, so the best description for the study area it is: Oak-aspen – mountain brush mixture of oak brush, aspen, mountain mahogany, bitter brush, and other brush, plus the urban developed area in Koya city and villages. Runoff CNs for arid and semi-arid rangelands and hydrologic condition are poor so the best CN for class B is 71 (Sc, 1986) (Figs. 4 and 5).

According to the information of classification land use bare land and urban area, soil type it is considered as silt loam Group B, hydrologic condition poor.

Based on the above results, the SCS CN is 71for the catchment area.

SCS runoff equation:

$$Q = \frac{(P - Ia)^2}{(P - Ia) + S} \quad (1)$$

Where

Q=Runoff (mm)

P=Rainfall (mm)

S=Potential maximum retention after runoff begins (mm) and

Ia=Initial abstraction (mm)

$$Ia = 0.2S \quad (2)$$

$$Q = \frac{(P - 0.2S)^2}{(P + 0.8S)} \quad (3)$$

$$S = \frac{1000}{CN} - 10 \quad (4)$$ (USDA-SCS, 1972).

CN=Curve number: Unitless number has range (0–100) depend on the soil group, land use, and land cover, and determinate from table provided by the SCS (USDA-SCS, 1972).

D. Hydrological Modeling

As a start, the catchment is to be analyzed using HEC-HMS Hydrologic Engineering Center, Hydrologic Modeling System (Gebre, 2015; Scharffenberg, et al., 2010) and then for more accuracy analysis of the catchment will be divided to number of sub-catchments as shown in Fig. 6.

The modeling method was used in the program HEC-HMS for 100-year return period for drawing outlet Hydrograph at end of catchment area. Now, the runoff data were used by

Table III
Goodness of Fit Results for Different Distribution Methods

	Statistical distribution methods					Criterion for success	Best method
Test name	Exp.	GEV	Normal	Lognormal	Gamma		
Chi-squared	5.00	2.71	3.86	2.71	3.29	Min.	GEV, Lognormal
RMSE	19.29	21.03	21.7	10.86	17.09	Min.	Lognormal
IOA	0.924	0.779	0.757	0.952	0.864	Max.	Lognormal
Nash	0.769	0.973	0.970	0.998	0.989	Max.	Lognormal

Where: Chi-squared=Chi-squared goodness of fit test, RMSE=Root mean square error test, IOA=Index of agreement test, Nash=Nash-Sutcliffe coefficients test

Table IV
Koya Catchment Area Characteristics

Area km^2	Perimeter km	Mean slope	Longest flow path km	Highest El.	Lowest El.
324.27	121.66	0.1136	35.2	975	309

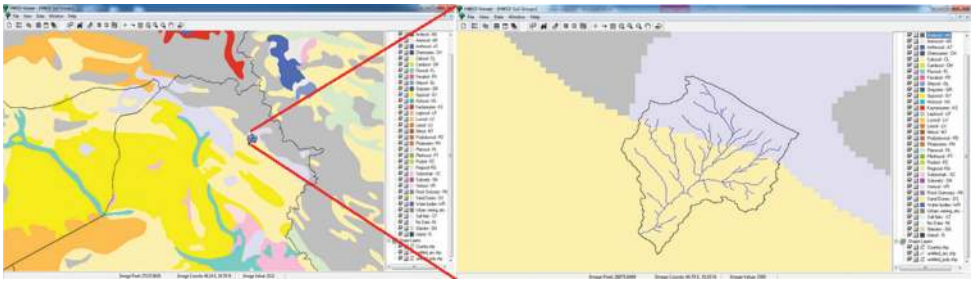

Fig. 4. Study area soil class location by Harmonized World Soil Database viewer.

http://dx.doi.org/10.14500/aro.10824

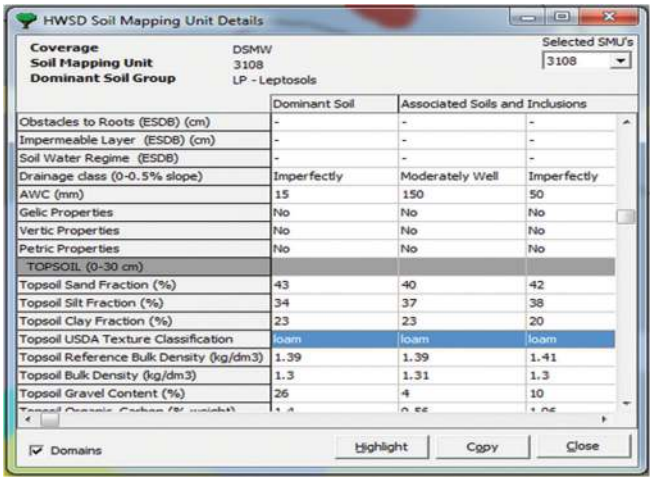

Fig. 5. Study area soil class properties by Harmonized World Soil Database viewer.

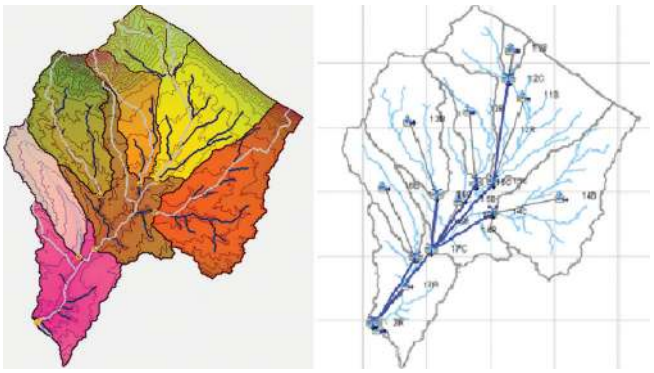

Fig. 6. Dividing catchment area by HEC-HMS Hydrologic Engineering Center, Hydrologic Modeling System into eight subcatchments.

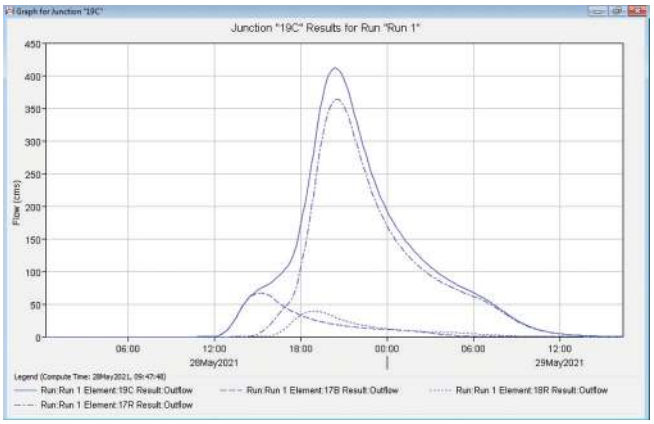

Fig. 7. Outlet subcatchment hydrographs created by HEC-HMS for 100-year return period.

Hec-Ras 5.07 (Hydrologic Engineering Center, River Analysis system) software for flood modeling. This program is capable of modeling water basins, drawing flood boundaries, flood depth, and flow velocity. Thus, the necessary precautions can be taken to determine the areas to which the flood reaches, to evacuate activities and projects before the flood occurs. The plan that was followed in this research to model the flooding of the Koya basin was to download a digital elevation model using the GIS program for the Koya area with an accuracy of

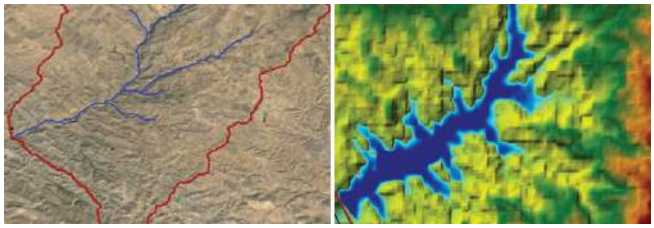

Fig. 8. Flood waters depth and flooded areas simulated by HEC-RAS model for 100-year flood event in Koya basin stream.

up to 5 m. Then, the area of the catchment and the paths of the valleys were determined using Global Mapper and WMS programs. Finally, the completed model was transferred to the Hec-Ras program (Salajegheh, et al., 2009) where the data were processed and the flood graph, whose frequency is 100 years, was drawn. The modeling of eight subcatchments flow is shown in Fig. 7.

E. Flood Modeling

According to the procedure of hydrological modeling explained in (Tate, 1999) Floodplain Mapping Using HEC-RAS and ArcView GIS, flood modeling by HEC-RAS model has been done with depth of rainfall for return period every 100 year, and the result shows the flood plain area are cover agriculture and urban area, as shown in Fig. 8.

IV. Conclusion

The morphological characteristics of the Koya basin using WMS and Global Mapper program indicated that the basin contributed significantly to the floods, due to the increase in the value of the CN as a result of the increase in the urban area, the decrease in vegetation cover, and the change of land uses. The value of the CN 71 was found adjusted according to the type of soil and land use. The rainfall runoff was simulated using the CN SCS model. Flood hydrography was investigated in the process of delimitation of floodplains by the Hec-Ras model. These results showed that a 100-year return period flood more than 420 m^3/s can invade critical areas such as urban area (villages), agricultural area, and public roads in the outlet of the catchment.

This study is very important in the decision-making process for the local authority so that they can benefit from the results in applying measures for the economic and social development of the Koya catchment.

The study shows that the measured water flow and volume can be stored in ponds by building small dams on the valley streams for water harvesting. The model can be further utilized to predict water storage based on precipitation and evapotranspiration results.

V. Acknowledgments

The authors would like to thank the Kurdistan Regional Government Ministry of Agriculture and Water Resources, Directorate of Koya Irrigation, Directorate of Koya Agriculture for their

Support and providing rainfall data, where their support is highly appreciated.

References

Abdelshafy, M., Mostafa, A. and Seleem, E.M., 2020. Flash Flood modeling on wadi reem in the Western Region, Kingdom of Saudi Arabia. *Journal of the Egyptian Academy of Environmental Development*, 21(1), pp.11-24.

Al Kalbani, K., 2021. 3D city model for monitoring flash flood risks in Salalah, Oman. *International Journal of Engineering and Geosciences*, 7(1), 17-23.

Ara, Z. and Zakwan, M., 2018. Estimating runoff using SCS curve number method. *International Journal of Emerging Technology and Advanced Engineering*, 8(5), 195-200.

Chow, V. Te, Maidment, D. R., & Mays, L. W. (1988). Applied Hydrology. McGraw Hill, Inc., New York.

Gebre, S.L., 2015. Application of the HEC-HMS model for runoff simulation of upper Blue Nile River Basin. *Journal of Waste Water Treatment and Analysis*, 6, 2.

Harmonized World Soil Database, 2021. *Land and Water Food and Agriculture Organization of the United Nations Land and Water Food and Agriculture Organization of the United Nations*. Available from: https://iiasa.ac.at/web/home/research/researchPrograms/water/HWSD.html. [Last accessed on 2021 Dec 22].

Khalid, K., Alib, M.F., Manc, N.F., Rahmanb, N.F.A., Yaccob, A.A., Noor, N.A.M. and Rosli, S.H., 2016. Rainfall data analysis in langat river basin using hyfran-plus. *Journal of Engineering and Applied Sciences*, 11(11), 2360-2365.

Kurdistan Regional Government, 2021 *Ministry of Agriculture and Water Resources, Directorate of Koya Irrigation, Rainfall Data*, Kurdistan Regional Government.

Kurdistan Regional Government, 2021 *Ministry of Agriculture and Water Resources, Directorate of Koya Agriculture, Rainfall Data*, Kurdistan Regional Government.

Salajegheh, A., Bakhshaei, M., Chavoshi, S. and Hajivar, M.N., 2009. Floodplain mapping using HEC-RAS and GIS in semi-arid regions of Iran. *Desert* (*Biaban*), 14(1), 83-93.

Sc, 1986. *Urban Hydrology for Small. Soil Conservation, Technical Release, 55* (*TR-55*)*, No. 164*. Available from: https://www.nrcs.usda.gov/Internet/FSE_DOCUMENTS/stelprdb1044171.pdf

Scharffenberg, W., Ely, P., Daly, S., Fleming, M. and Pak, J., 2010. *Hydrologic Modeling System* (*Hec-Hms*): *Physically-Based Simulation Components*. 2nd Joint Federal Interagency Conference, No. 8.

Tate, E.C., 1999. *Floodplain Mapping Using HEC-RAS and ArcView GIS. Technical Report University of Texas at Austin*, Center for Research in Water Resources.

USDA-SCS, 1972. *Part 630 Hydrology National Engineering Handbook Chapter 10 Estimation of Direct Runoff from Storm Rainfall*, National Engineering Handbook.

http://dx.doi.org/10.14500/aro.10845

Contact Geometrical Study for Top Emitting 980 nm InGaAs/GaAsP Vertical-Cavity Surface Emitting Lasers

Faten A. Chaqmaqchee

Department of Physics, Faculty of Science and Health, Koya University, Koya KOY45, Kurdistan Region - F.R. Iraq

Abstract—***Geometrical*** **contacts of a double mesa structure with a 16 rows × 15 columns arrays of top emitting GaAs-based 980 nm vertical-cavity surface emitting lasers (VCSELs) are fabricated and characterized. In this paper, five strained $In_{0.22}Ga_{0.78}As/Ga_{0.9}AsP_{0.1}$ quantum wells within λ/2 thick cavity have been employed. The top and the bottom epitaxially grown mirrors are based on the linear graded $Al_{0.9}Ga_{0.1}As/GaAs$ distributed Bragg reflectors with 20.5 and 37 periods, respectively. Static parameters including threshold currents, rollover currents, maximum optical output power, and wall-plug efficiency are extracted from light out power-current-voltage (*LIV*) of VCSELs with fixed oxide aperture diameter of ∅~ 6 μm and various mesa2 diameters. In addition, spectral emission for 980 nm VCSELs of oxide aperture between ∅~ 6 and 19 μm and with fixed ∅~ 6 μm and different bias currents are analyzed. The highest optical output power of around 33 dBm is observed at bias current of 0.8 mA for short-reach optical interconnect applications.**

Index Terms**—Vertical-cavity surface emitting laser; AlGaAs Distributed Bragg reflectors; InGaAs/GaAsP quantum wells; Static characterization.**

1. Introduction

Today, thousands of optical interconnects (OIs) based on oxide-confined vertical-cavity surface emitting lasers (VCSELs) and multimode fibers (MMFs) are generally mounted in high-performance computers (Choquette, et al., 1994). VCSELs at 980 nm have recognized as key components in short-reach MMF applications and dominantly deployed in OIs in datacenters, supercomputers, and data storage systems to meet requirements of high modulation bandwidth and energy efficiency (Taubenblatt, 2011; DeCusatis, 2013; Haghighi and Lott, 2021). VCSELs are semiconductor lasers with unique geometry of low threshold current, low divergent angle, and circular beam that reduce electrical power conversion and emitted single longitudinal mode at desired wavelengths (Iga, 2000; Chaqmaqchee, 2020). The design of the VCSEL structure can achieve low resistance distributed Bragg mirrors (distributed Bragg reflectors [DBRs]) and low optical loss by optimization of doping concentration of top mirrors. When the oxide layer has larger aperture diameters, it reduces the capacitance. When the aperture is small, it slows down the laser speed (Castro, et al., 2015). However, VCSELs have higher electrical resistance due to their small top contact area and high resistive of DBRs mirrors (Chaqmaqchee, 2021). The contact geometry of the two-mesa VCSEL allows a combination of low electrical parasitics and high thermal conductivity of VCSELs (Ou, et al., 2009; Mutig and Bimberg, 2011). VCSELs at short emission wavelengths are formed from compressively strained InGaAs quantum wells (QWs) lattice matched to GaAs and surrounded by GaAs, AlGaAs, or GaAsP barrier layers to achieve high differential gain (Healy, et al., 2010). VCSELs have been motivated by the market demand, as a result of demonstrating of VCSELs at high modulation bandwidth (Blokhin, et al., 2009; Haghighi, et al., 2020) and possibility with the highest wall-plug efficiency (WPE) to help dissipate heat and to help lower series resistance (Haghighi, et al., 2020).

In this study, we have focused on a geometrical study of 980 nm VCSEL at various top mesa diameters. The sizes of double mesa high-speed VCSELs are arranged in a 16 rows × 15 columns arrays. Static characteristics with different top mesa diameters give information on VCSELs performance, including threshold currents, maximum output powers, and rollover currents that extracted from the light output power-current-voltage (*LIV*) and WPE. In addition, optical emission spectra measurements were measured at fixed column of B and at row diameters from 0 to F. VCSELs with aperture diameter of ∅~ 6 μm at 25°C were designed to reduce the order modes with the current confinement profile. Low threshold current of ~ 0.5 mA with top mesa diameter of 18 μm was achieved for almost all the diameters of rows 0, 9, B, D, and E. Maximum WPE of 12% with top mesa diameter of 26 μm and diameters of rows B and maximum output power of 33 dBm at bias current of 0.8 mA for fixed column of B and at row diameters of 0 were obtained.

II. Materials and Method

In this study, the epitaxial structure of VCSEL was grown on a semi-insulating of 1.5857 μm thick (n+) GaAs (100) substrate by metal-organic chemical vapor deposition and

ARO-The Scientific Journal of Koya University
Vol. IX, No.2 (2021), Article ID: ARO.10845, 5 pages
DOI: 10.14500/aro.10845
Received: 02 August 2021; Accepted: 13 December 2021
Regular research paper: Published: 26 December 2021
Corresponding author's email: faten.chaqmaqchee@koyauniversity.org

designed to emit at wavelength of 980 nm (Chaqmaqchee and Lott, 2020). To reduce the device capacitance, two oxide layers, a thick layer of benzocyclobutene (BCB), are used under the p-bond pad and an undoped substrate (Lau and Yariv, 1985; Hofmann, 2010). VCSELs at 980 nm require a lower drive voltage and are possible to design with deeper and more strained QWs that improve differential gain and thus the intrinsic and thermally limited bandwidths (Chaqmaqchee, 2020). Resistance and optical loss in the DBRs are minimized using modulation doping and graded interfaces, and thermal impedance is lowered using binary alloys in DBR, which all ease operation at high temperatures (Moser, et al., 2014). Fig. 1(a) depicts the schematic cross-section of the 980 nm VCSEL structure. VCSELs were fabricated through standard processing techniques including optical lithography, dry etching, wet oxidation, and metal contact deposition. Reactive ion etching is applied to form top and bottom DBRs mesas. VCSELs show single mode and multimode behaviors with smaller and larger aperture diameters, respectively. Two 20 nm thick $Al_{0.98}Ga_{0.02}As$ layers are separated by half wavelength to increase the optical confinement factor and reduce the carrier transport times (Nagarajan, et al., 1992; Westbergh, et al., 2012). The double oxide apertures are placed as close to the QWs as possible to confine the current and the optical fields, and it is formed by high selectivity of wet oxidation with controlled oxidation furnace. Active region includes five strained $In_{0.22}Ga_{0.78}As/Ga_{0.9}AsP_{0.1}$ QWs for high differential gain. The top mirror consists of 20.5 pairs p-doped $Al_{0.9}Ga_{0.1}As$/GaAs DBRs and 37 pairs n-doped $Al_{0.9}Ga_{0.1}As$/GaAs top mirrors.

The VCSELs have a double mesa structure and uniformly distributed with a 16 rows ×15 columns arrays. The top mesa diameters are varied from 18 μm in row 0 to 31 μm in row F, whereas the bottom mesa diameters is varied from 0 in column 0 to 60 μm in column E. The VCSEL set is differ in the double mesa design and the geometric design and the position of the bottom contact. Fabrication procedure begins with etching of top mesas surface and then selectively oxidized to form 6 μm diameter apertures. A cathode contact is formed by etching a bottom mesa to the b-contact layer. Finally, the structure is planarized with bis(benzocyclobutane) (BCB) and deposited with bond pads. Fig. 1(b) shows part of an optical microscope image of the fabricated VCSEL array together with a zoomed view of a VCSEL with the unit cell of 33 and the top mesa diameter of 22 μm (with fixed column of 4 and variable row of 6). Devices that fabricated with small aperture diameters exhibited stable bandwidths than bigger aperture diameter at room temperature.

The static characteristics output light-current-voltage (*LIV*) is automatically determined and evaluated using homemade mapping system. The output light from the VCSEL is coupled into a MMF connected using an optical spectrum analyzer Ando model AQ6317C to analyze the optical emission spectra over ~780–1180 nm, where the VCSELs are driven by the digital source meter Keithley model 2400-LV and the measurements are controlled by LabVIEW program running on a Microsoft Window-based personal tower computer.

III. Results and Discussion

We performed static optical output power-current-voltage (*LIV*) and optical spectral emission for VCSELs at room temperature with different mesa and fixed oxide aperture diameter of 6 μm showed various threshold current, rollover current, and output powers. Fig. 2 shows the threshold current versus top mesa diameters between 18 and 31 μm. With increasing mesa diameters, the threshold current increased linearly from 18 to 31 μm, where the diameters are almost constant for 18 μm diameters of row E, D, B, 9, and 0, whereas the diameters are between 1.89 for row 0 and 8.58 of row E of 31 μm diameters. The lowest threshold currents were recorded between 0.48 and 1.89 μm in row 0 for 31 μm diameter. Fig. 3 presents maximum output power of VCSELs with different diameter and fixed oxides aperture diameter. The output power increased linearly as a result of increasing the top mesa diameters from 18 μm (P_{out} Max. from 0.47 of row 9 to 0.86 mW of row D) to 31 μm (P_{out} Max. from 2.98 of row E to 5.98 mW of row B). In addition, the maximum current (*I*) point is extracted from the light output power-current (*LI*) rollover for various mesa diameters. Fig. 4 illustrates the maximum rollover currents of VCSELs that varied for top mesa diameter from 18 to 31 μm between 9.70 mA to 26.55 mA of row 9 and between 14.72 and 32.95 mA for row 0.

In addition, WPE as a function of top mesa diameters is depicted in Fig. 5. LabVIEW program was used to swept the

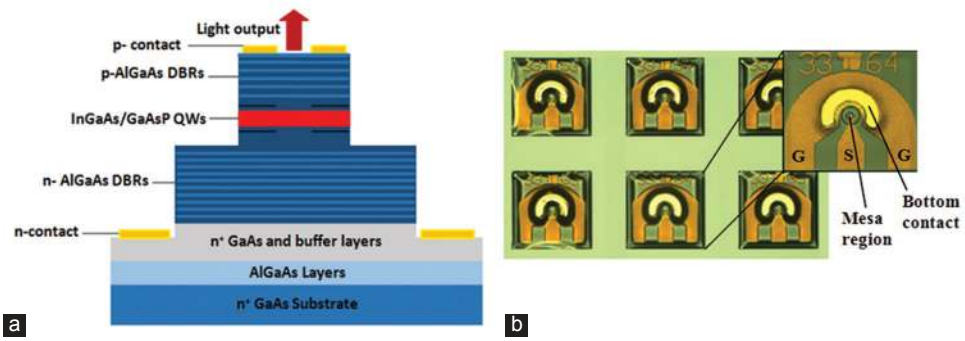

Fig. 1. (a) Schematic cross-section of 980 nm GaAs-based vertical-cavity surface emitting lasers (VCSELs) features an active region sandwiched between top and bottom DBRs mirrors, (b) optical microscope image of the fabricated array of VCSELs including an expanded top-down view of a device.

http://dx.doi.org/10.14500/aro.10845

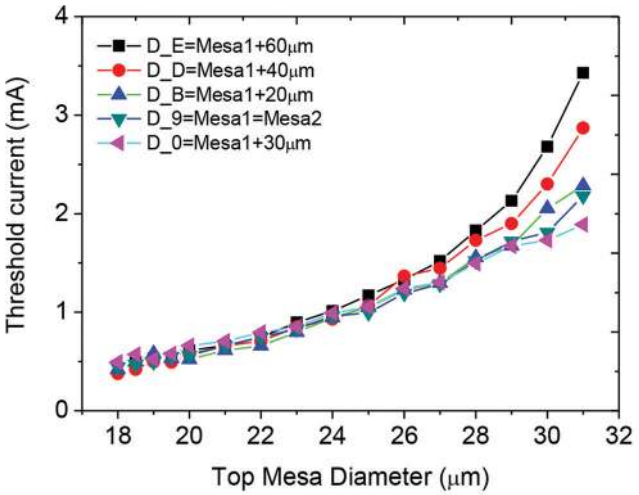

Fig. 2. Threshold current versus top mesa diameter for vertical-cavity surface emitting lasers diameters of rows 0, 9, B, D, and E.

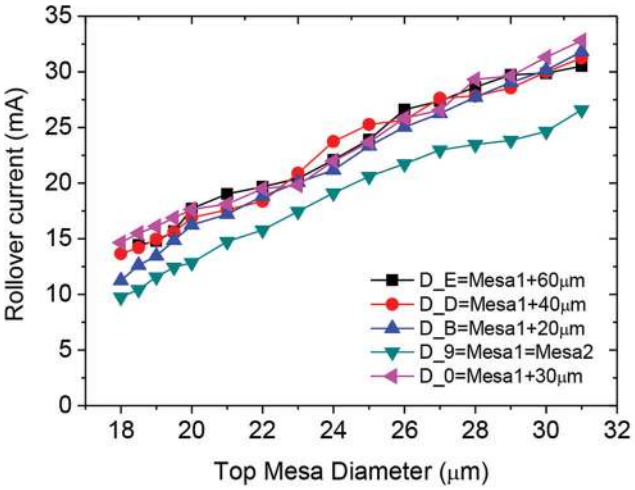

Fig. 4. Rollover current versus top mesa diameter for vertical-cavity surface emitting lasers diameters of rows 0, 9, B, D, and E.

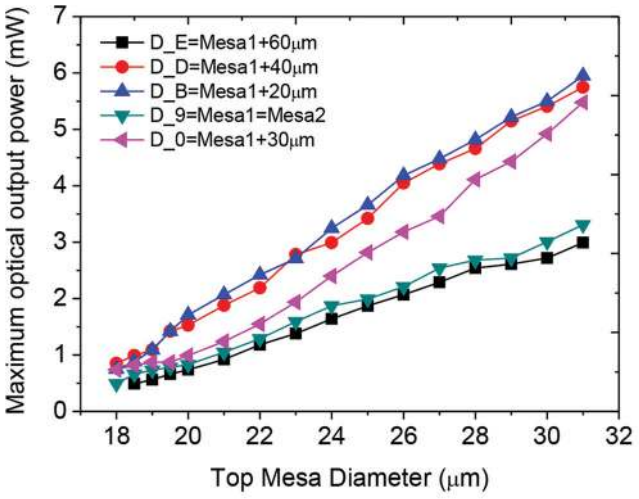

Fig. 3. Maximum output power versus top mesa diameter for vertical-cavity surface emitting lasers diameters of rows 0, 9, B, D, and E.

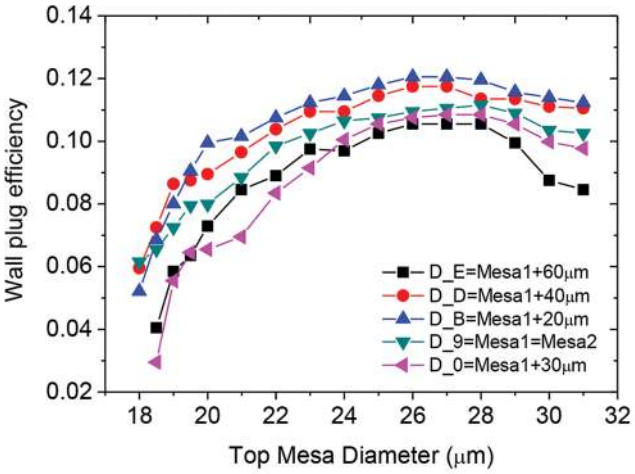

Fig. 5. Wall-plug efficiency versus top mesa diameter with vertical-cavity surface emitting lasers diameters of rows 0, 9, B, D, and E at 25°C.

bias current (I) with a Keithley 2400-LV and measuring the static light output power (L), current (*I*), and voltage (V). The WPE (WPE = 100×L/(I×V) as a percentage) versus top mesa diameters were extracted from the maximum value of WPE with current increasing then decreases with increasing current for different Rows. The WPE is bended as a result of increasing the top mesa diameters from 18 to 26 μm and reaches maximum values of 0.12 in row B and 0.10 in row E. Thus, a large WPE allows more power to convert into potentially useful optical power (Choquette, et al., 1997).

The optical spectra at fixed column of B and rows of 0, 1, 2, 3, 4, 5, 6, 7, 8, 9, A, B, C, D, E, and F are shown in Fig. 6. The optical spectrum at temperature of 25°C shows a typical number of around 4 to 10 transverse modes that contribute to the emitted power and the bias current is just above threshold at 1 mA. The device with a smaller aperture diameter has the fewer existed optical mode caused by the small lateral confinement aperture design. Larger aperture diameter generates further modes existed in the VCSEL due to the weak optical confinement. In Fig. 6a-c, the center wavelength of VCSELs spectra at this bias current is around 980 nm whereas in Fig. 6d, the center wavelength is in the region of 977 nm. When the device has smallest aperture diameter, the spectral width for the single mode is around 0.2 nm for oxide apertures between 6 and 11 μm as in Fig. 6(a) and (b) with an optical power of around 22.7 dBm for ∅~ 6 μm, whereas the output power for ∅~ 6.5 μm is about 16.81 dBm. However, when the aperture diameter is getting larger, the side mode suppression ratio decreases and thus the spectral width of $\Delta\lambda$ increases which is varied between 1.3 and 2.7 nm as shown in Fig. 6(c) and (d).

The spectrum of the VCSEL emission at below and above threshold currents with VCSEL aperture diameter of ∅~ 6 μm is presented in Fig. 7, where two modes are clearly visible at around 980 nm. At higher bias current, the emissions become strongly multimode and a red shift is observed. The number of transverse multiple modes of VCSEL increases when an oxides aperture diameter increases (Satuby and Orenstein, 1999). The peak emission wavelengths at lower bias current

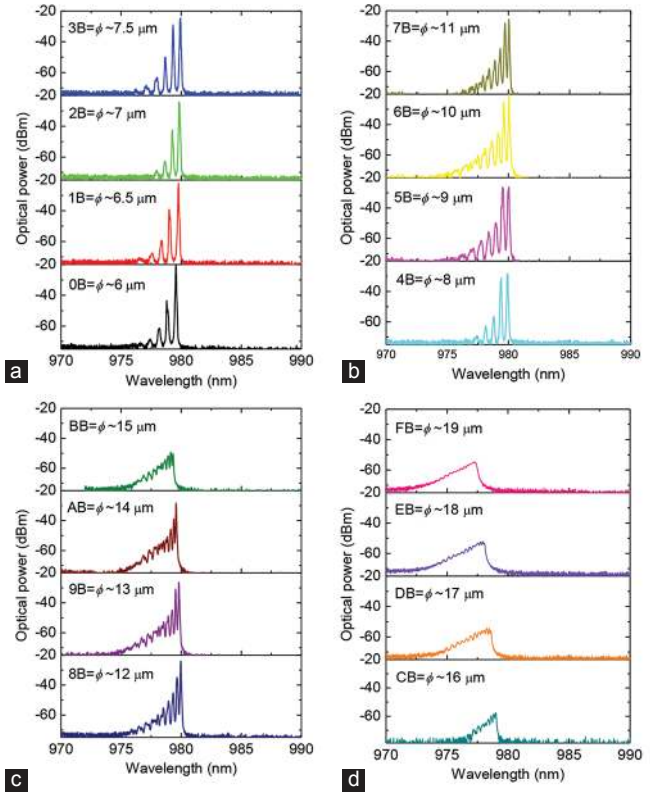

Fig. 6. Spectral emission for a 980 nm vertical-cavity surface emitting lasers with: (a, b) ∅ from 6 to 11 μm and (c, d) ∅ from 12 to 19 μm measured at fixed column of B and at row diameters from 0 to F through bias current of 1 mA at 25°C.

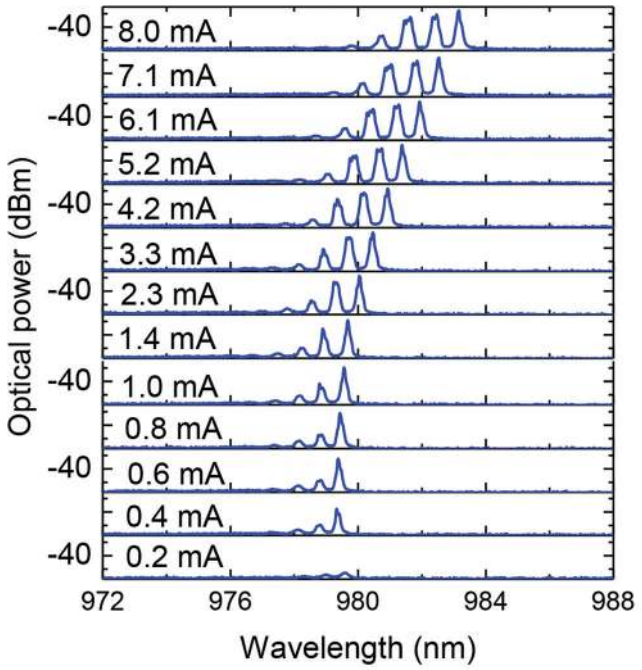

Fig. 7. Optical spectra measurements for vertical-cavity surface emitting lasers of ∅ ~ 6 μm with different bias currents.

of 0.8 mA are about 978.8 and 979.6 nm, the highest optical output power at ~33 dBm at center emission of 979.6 nm is observed. Their spectral emission width is about 0.21 nm which reduces the chromatic dispersion to send data over longer distances.

IV. Conclusion

The performances of top emitting VCSELs at room temperature have been demonstrated. Geometrical study of two mesa VCSELs with sizes of 16 rows × 15 columns arrays is fabricated and characterized including threshold currents, rollover currents, maximum optical output power' and wall-plug efficiency which are extracted from current-voltage-power of VCSELs with oxide aperture diameter of ∅~ 6 μm and various mesa2 diameters. In addition, spectral emission of oxide aperture between ∅~ 6 and 19 μm and with fixed ∅~ 6 μm and different bias currents are analyzed. At low bias current of 0.8 mA, we obtained high optical power of 33 dBm for small device of □~ 6 μm, which corresponding top mesa diameters of around 18 μm. This wavelength is suitable for future short reach OIs, particularly in high-performance computers (HPC) applications. Throughout the increasing demand for VCSELs in markets, companies and research institutions are following the development of research, optimizing VCSEL performance, and improving output power in the near future.

V. Acknowledgment

This work was supported by the MARHABA Erasmus Mundus Lot 3 with project number 2014-0653 and Funded by the European Union. FC highly appreciates the support of the TU Berlin team (Arbeitsgruppe (AG) Lott) during this work. FC also acknowledges the support of Koya University during the period of visit in Germany.

References

Blokhin, S., Lott, J.A., Mutig, A., Fiol, G., Lederntsov, N.N., Maximov, M.V., Nadtochiy, A.M., Shchukin, V.A. and Bimberg, D., 2009. Oxide-confined 850 nm VCSELs operating at bit rates up to 40 Gbit/s. *Electronics Letters*, 45(10), pp.501-503.

Castro, J.M., Pimpinella, R., Kose, B., Huang, Y., Lane, B., Szczerba, K., Westbergh, P., Lengyel, T., Gustavsson, J.S., Larsson, A. and Andrekson, P.A., 2015. 48.7-Gb/s 4-PAM transmission over 200 m of high bandwidth MMF using an 850-nm VCSEL. IEEE Photonics Technology Letters, 27(17), pp.1799-1801.

Chaqmaqchee, F.A., 2020. Long-wavelength GaInNAs/GaAs vertical-cavity surface-emitting laser for communication applications. *Aro-the Scientific Journal of Koya University*, 8(1), pp.107-111.

Chaqmaqchee, F.A., 2021. A comparative study of electrical characterization of p-doped distributed Bragg reflectors mirrors for 1300 nm vertical cavity semiconductor optical amplifiers, *Aro-The Scientific Journal of Koya University*, 9(1), pp.89-94.

Chaqmaqchee, F.A.I. and Lott, J.A., 2020. Impact of oxide aperture diameter on optical output power, spectral emission, and bandwidth for 980 nm VCSELs. *OSA Continuum*, 3(9), pp.2602-2613.

Chaqmaqchee, F.A.I., 2020. Gain analysis of vertical-cavity surface-emitting laser for long optical fiber communication. *Journal of Optoelectronics and Advanced Materials*, 22(7-8), pp.339-343.

Choquette, K., Schneider, R.P., Lear, K.L. and Geib, K.M., 1994. Low threshold

voltage vertical-cavity lasers fabricated by selective oxidation. *Electronics Letters*, 30(24), pp.2043-2044.

Choquette, K.D., Chow, W.W., Hadley, G.R., Hou, H.Q. and Geib, K.M., 1997. Scalability of small-aperture selectively oxidized vertical cavity lasers. *Applied Physics Letters*, 70(7), pp.823-825.

DeCusatis, C., 2013. Optical interconnect networks for data communications. *Journal of Lightwave Technology*, 32(4), pp.544-552.

Haghighi, N. and Lott, J.A., 2021. Electrically parallel three-element 980 nm VCSEL arrays with ternary and binary bottom DBR mirror layers. *Materials*, 14(2), pp.1-17.

Haghighi, N., Moser, P. and Lott, J.A., 2020. 40 Gbps with electrically parallel triple and septuple 980 nm VCSEL arrays. *Journal of Lightwave Technology*, 38(13), pp.3387-3394.

Haghighi, N., Moser, P., Zorn, M. and Lott, J.A., 2020. 19-element vertical cavity surface emitting laser arrays with inter-vertical cavity surface emitting laser ridge connectors. *Journal of Physics: Photonics*, 2(4), pp.04LT01.

Healy, S.B., O'Reilly, E.P., Gustavsson, J.S., Westbergh, P., Haglund, A., Larsson, A. and Joel, A., 2010. Active region design for high-speed 850-nm VCSELs. *IEEE Journal of Quantum Electronics*, 46(4), pp.506-512.

Hofmann, W., 2010. High-speed buried tunnel junction vertical-cavity surface-emitting lasers. *IEEE Photonics Journal*, 2(5), pp.802-815.

Iga, K., 2000. Surface-emitting laser-its birth and generation of new optoelectronics filed. *IEEE Journal of Selected Topics in Quantum Electronics*, 6(6), pp.1201-1215.

Lau, K. and Yariv, A., 1985. Ultra-high speed semiconductor lasers. *IEEE Journal of Quantum Electronics*, 21(2), pp.121-138.

Moser, P., Lott, J.A., Wolf, P., Larisch, G., Li, H. and Bimberg, D., 2014. Error-free 46 Gbit/s operation of oxide-confined 980 nm VCSELs at 85 C. *Electronics Letters*, 50(19), pp.1369-1371.

Mutig, A. and Bimberg, D., 2011. Progress on high-speed 980nm VCSELs for short-reach optical interconnects. *Advances in Optical Technologies*, 2011, pp.1-15.

Nagarajan, R., Ishikawa, M., Fukushima, T., Geels, R.S. and Bowers, J.E., 1992. High speed quantum-well lasers and carrier transport effects. *IEEE Journal of Quantum Electronics*, 28(10), pp.1990-2008.

Ou, Y., Gustavsson, J.S., Westbergh, P., Haglund, A., Larsson, A. and Joel, A., 2009. Impedance characteristics and parasitic speed limitations of high-speed 850-nm VCSELs. *IEEE Photonics Technology Letters*, 21(24), pp.1840-1842.

Satuby, Y. and Orenstein, M., 1999. Mode-coupling effects on the small signal modulation of multi transverse-mode vertical-cavity semiconductor lasers. *IEEE Journal of Quantum Electronics*, 35(6), pp.944-954.

Taubenblatt, M.A., 2011. Optical interconnects for high-performance computing. *Journal of Lightwave Technology*, 30(4), pp.448-457.

Westbergh, P., Safaisini, R., Haglund, E, Kögel, B. Gustavsson, J.S., Larsson, A., Geen, M., Lawrence, R. and Joel, A., 2012. High-speed 850 nm VCSELs with 28 GHz modulation bandwidth operating error-free up to 44 Gbit/s. *Electronics Letters*, 48(18), pp.1145-1147.

General Information

ARO's Mission: ARO seeks to publish those papers that are most influential in their fields or across fields and that will significantly advance scientific understanding. Selected papers should present novel and broadly important data, syntheses, or concepts. They should merit the recognition by the scientific community and general public provided by publication in ARO, beyond that provided by specialty journals.

We welcome submissions from all fields of natural science and technology, and from any source. We are committed to the prompt evaluation and publication of submitted papers. ARO is published biannually; selected papers are published online ahead of print.

Submission

Manuscripts should be submitted by the correspondent authors of the manuscript via the on-line submission page. Regardless of the source of the word-processing tool, only electronic Word (.doc, .docx, .rtf) files can be submitted on-line. There is no page limit. Only online submissions are accepted to facilitate rapid publication and minimize administrative costs. Submissions by any other one but the authors will not be accepted. The submitting author takes responsibility for the paper during submission and peer review. If for some technical reason submission through the email is not possible, the author can contact aro.journal@koyauniversity.org for support. Before submitting please check ARO's guide to authors thoroughly to avoid any delay in the review and publication process.

Authors are explicitly responsible for the language of their texts. Paper should be submitted in a well written in understandable English. Authors should not expect the editor or editorial board to rewrite their paper. Prior to submission, authors should have their paper proofread by a possible academic native speaker of English.

- Submit the Article with contact Information
- File name should be your article tittle
- Don't submit your article in multiple journal, we are taking only minimum time for review process. please don't waste our time
- Once the paper is accepted, it can't be withdrawn
- Please follow publication ethics and regulation
- Avoid plagiarism and copied material
- Strictly Follow ARO's Template

Terms of Submission

Papers must be submitted on the understanding that they have not been published elsewhere and are not currently under consideration by another journal or any other publisher. ARO accepts original articles with novel impacts only. Post conference papers are not accepted "as is", however, regular papers on the same topic but with a different title can be submitted. The new paper should contain significant improvements in terms of extended content, analysis, comparisons with popular methods, results, figures, comments, etc. Please do not forget that the publication of the same or similar material in ARO constitutes the grounds for filing of an (auto) plagiarism case.

The submitting author is responsible for ensuring that the article's publication has been approved by all the other co-authors. It is also the authors' responsibility to ensure that the articles emanating from a particular institution are submitted with the approval of the necessary institution. Only an acknowledgement from the editorial office officially establishes the date of receipt. Further correspondence and proofs will be sent to the author(s) before publication unless otherwise indicated. It is a condition of submission of a paper that the authors permit editing of the paper for readability. All enquiries concerning the publication of accepted papers should be addressed to aro.journal@koyauniversity.org.

Peer Review

All manuscripts are subject to peer review and are expected to meet standards of academic excellence. Submissions will be considered by an editor and "if not rejected right away" by peer-reviewers, whose identities will remain anonymous to the authors.

Guide to Author

We welcome submissions from all fields of science and from any source. We are committed to the prompt evaluation and publication of submitted papers. Selected papers are published online ahead of print. Authors are encouraged to read the instructions below before submitting their manuscripts. This section arranged into an overview speedy guidelines below and more detailed at the bottom section of this page

Manuscript Preparation

Submitting your manuscript will be in two stages namely before final acceptance and after.

Stage one:

At the first stage manuscript needs to be prepared electronically and submitted online via the online submission page in a Word (.doc, .docx, .rtf) format of one column double-spaced page, Times New Roman font type, and 12 p font size. A pdf version of the submitted manuscript should be submitted too. All authors' names, affiliations, e-mail addresses, and mobile phone numbers should be typed on a cover page, indicating the correspondent author.

Stage two:

- File type: MS-Word version 2003 or later.
- Format: The preferred format of the manuscript two-column template with figures and captions included in the text. This template can be downloaded via the following link. Please follow instructions given in the template; http://aro.koyauniversity.org/about/submissions#onlineSubmissions
- Text: All text is in Times New Roman font. The main text is 10-point, abstract is 9-point font and tables, references and captions are 8-point font.
- Figures: Figures should be easily viewed on a computer screen.

Units of Measurement

Units of measurement should be presented simply and concisely using System International (SI) units.

Title and Authorship Information

The following information should be included;

- Paper title.
- Full author names.
- Affiliation.
- Email addresses.

Abstract

The manuscript should contain an abstract. The abstract should be self-contained and citation-free and should not exceed 200 words.

Introduction

This section should be succinct, with no subheadings.

Materials and Methods

This part should contain sufficient detail so that all procedures can be repeated. It can be divided into subsections if several methods are described.

Results and Discussion

This section may each be divided by subheadings or may be combined.

Conclusions

This should clearly explain the main conclusions of the work highlighting its importance and relevance.

Acknowledgements

All acknowledgements (if any) should be included at the very end of the paper before the references and may include supporting grants, presentations, and so forth.

References

References must be included in the manuscript and authors are responsible for the accuracy of references. Manuscripts without them will be returned. ARO is following Harvard System of Referencing. (Learn how to import and use Harvard Styling in your Microsoft Office by following this link:
http://bibword.codeplex.com/releases/view/15852)

Preparation of Figures

Upon submission of an article, authors are supposed to include all figures and tables in the PDF file of the manuscript. Figures and tables should be embedded in the manuscript. Figures should be supplied in either vector art formats (Illustrator, EPS, WMF, FreeHand, CorelDraw, PowerPoint, Excel, etc.) or bitmap formats (Photoshop, TIFF, GIF, JPEG, etc.). Bitmap images should be of 300 dpi resolution at least unless the resolution is intentionally set to a lower level for scientific reasons. If a bitmap image has labels, the image and labels should be embedded in separate layers.

Preparation of Tables

Tables should be cited consecutively in the text. Every table must have a descriptive title and if numerical measurements are given, the units should be included in the column heading. Vertical rules should not be used.

Copyright

ARO Reviewer/Associate Editor Application Form

ARO is a scientific journal of Koya University (p-ISSN: 2410-9355, e-ISSN: 2307-549X) which aims to offer a novel contribution to the study of Science. The purpose of ARO is twofold: first, it will aim to become an ongoing forum for debate and discussion across the sciences and Engineering. We hope to advance our problem solving capacity and deepen our knowledge regarding a comprehensive range of collective actions. Second, ARO accepts the challenges brought about by multidisciplinary scientific areas and aspires to expand the community of academics who are able to learn from and help to produce advances in a variety of different disciplines.

The Journal is seeking reviewers who can provide constructive analysis of papers thus enhancing overall reputation of the Journal. If any expert is interested in participating of the review process, we highly encourage you to sign up as a reviewer for our Journal and help us improve our presence in domain of your expertise. Appropriate selection of reviewers who have expertise and interest in the domain relevant to each manuscript are essential elements that ensure a timely, productive peer review process. We require proficiency in English.

How to apply

To apply for becoming a reviewer of ARO, please submit the application form by following the link:
http://aro.koyauniversity.org/user/register
To apply for becoming a member of the Editorial Board of ARO, please submit the application form by following the link: http://aro.koyauniversity.org/pages/view/AEB

Both Associate Editor and Reviewers should specify their areas of research and expertise. Applicants must have a doctorate (or an equivalent degree), and if Master degree they need to have significant publishing experience. Please note that;

- You will need to write your full official name.
- Please provide an email which reflects your official name, such as nameOne.NameTwo@... , or your institute's official email.
- All data need to be written in English.

Note: For more information, kindly visit the following websites:

1. aro.koyauniversity.org.
2. http://libweb.anglia.ac.uk/referencing/harvard.htm.
3. http://bibword.codeplex.com/releases/view/15852.


INDEXED IN
EMERGING SOURCES CITATION INDEX
CLARIVATE ANALYTICS


PRESERVED IN
CLOCKSS


PRESERVED IN
LOCKSS


PKP
PUBLIC
KNOWLEDGE
PROJECT


DOAJ
SEAL


INDEXED IN
DOAJ


Journal
TOCs
The latest Journals Tables of Contents


ingenta


Dimensions


ZDB
ZEITSCHRIFTEN
DATENBANK


SHERPA
RoMEO


scinapse


Scilit


ScienceGate


ROAD
DIRECTORY
OF OPEN ACCESS
SCHOLARLY
RESOURCES


ResearchGATE
scientific network


OAJSE


Microsoft
Academic


OCLC
WorldCat


Google
Scholar


Crossref


BASE


publons


ACADEMIA

Koya University is a young University established in 2003 and it is located in the city of Koya (Koysinjaq), short distance to the East of regional capital city of Erbil (Arbil, Hewlêr) in Kurdistan Region of Iraq. It is on the foothills of beautiful High Mountain. Its campus has been carefully laid out to embrace the beautiful mountainous nature. The Koya University has a Faculty system which enhances the interactions between similar academic fields. Today, Koya University has four Faculties: Engineering, Science and Health, Humanities and Social Sciences and Education in addition to the School of Medicine, which all consist of twenty-five scientific departments in different fields, such as Petroleum Engineering, Geotechnical Engineering, Software Engineering, Physics, Chemistry, Clinical Psychology, Social Science, Medical Microbiology and Sport Education.

ARO-The Scientific Journal of Koya University is a biannual journal of original scientific research, global news, and commentary in the areas of Science and Technology. ARO is a Peer-reviewed Open Access journal with CC BY-NC-SA 4.0 license. It provides immediate, worldwide and barrier-free access to the full text of research articles without requiring a subscription to the journal, and has no article processing charge (APC). ARO Journal seeks to publish those papers that are most influential in their fields or across fields and that will significantly advance scientific understanding. ARO Journal is a member of ROAD and Crossref agencies and has got ESCI, DOAJ seal, SHERPA/RoMEO deposit policy, and LOCKSS archiving policy.

ARO
The Scientific Journal of Koya University

Koya University (KOU)
University Park
Danielle Mitterrand Boulevard
Koya KOY45, Kurdistan Region - Iraq

DOI: 10.14500/2307-549X p-ISSN: 2410-9355 e-ISSN: 2307-549X